A Laser Spark Plug Ignition System for a Stationary Lean-Burn Natural Gas Reciprocating Engine

Dustin L. McIntyre

Dissertation submitted to the College of Engineering and Mineral Resources at West Virginia University in partial fulfillment of the requirements for the degree of

Doctor of Philosophy
in
Mechanical Engineering

Mridul Gautam, Ph.D., Chair
John M. Kuhlman, Ph.D.
Michael H. McMillian, Ph.D.
Gary J. Morris, Ph.D.
Gregory J. Thompson, Ph.D.
Steven D. Woodruff, Ph.D.

Department of Mechanical and Aerospace Engineering

Morgantown, West Virginia
2007

Keywords: Laser Ignition, Diode Pumped Solid State Laser, Passively Q-switched Laser, Natural Gas Engine Ignition, Laser Design

Abstract

A Laser Spark Plug Ignition System for a Stationary Lean-Burn Natural Gas Reciprocating Engine

Dustin L. McIntyre

To meet the ignition system needs of large bore, high pressure, lean burn, natural gas engines a side pumped, passively Q-switched, Nd:YAG laser was developed and tested. The laser was designed to produce the optical intensities needed to initiate ignition in a lean burn, high compression engine. The laser and associated optics were designed with a passive Q-switch to eliminate the need for high voltage signaling and associated equipment. The laser was diode pumped to eliminate the need for high voltage flash lamps which have poor pumping efficiency. The independent and dependent parameters of the laser were identified and explored in specific combinations that produced consistent robust sparks in laboratory air. Prior research has shown that increasing gas pressure lowers the breakdown threshold for laser initiated ignition.

The laser has an overall geometry of 57x57x152 mm with an output beam diameter of approximately 3 mm. The experimentation used a wide range of optical and electrical input parameters that when combined produced ignition in laboratory air. The results show a strong dependence of the output parameters on the output coupler reflectivity, Q-switch initial transmission, and gain media dopant concentration. As these three parameters were lowered the output performance of the laser increased leading to larger more brilliant sparks. The results show peak power levels of up to 3MW and peak focal intensities of up to 560 GW/cm^2.

Engine testing was performed on a Ricardo Proteus single cylinder research engine. The goal of the engine testing was to show that the test laser performs identically to the commercially available flashlamp pumped actively Q-switched laser used in previous laser ignition testing. The engine testing consisted of a comparison of the in-cylinder, and emissions behavior of the engine using each of the lasers as an ignition system. All engine parameters were kept as constant as possilbe while the equivalence ratio (fueling), and hence the engine load, was varied between 0.8, 0.9, and 1.0.

The test laser was constructed with a 30% output coupler, 32% Q-switch initial transmission, and a 0.5% Nd concentration rod all pumped by approximately 1000 Watts of optical power. The test laser single mode output pulse had an energy of approximately 23 mJ, with a pulsewidth of approximately 10 ns, and an M^2 value of 6.55. This output produced focal intensity of approximately 270 GW/cm^2 with the modified on-engine optical arrangement. The commercial laser had similar output parameters and both laser systems operated the engine with similar results. Due to the shortening of the focal length of the on-engine optical setup both laser systems produced a spark well within the optical transfer cavity of the laser optics to spark plug adaptor. This shrouded spark led to a very long ignition delay and retarded combustion timing for all three values of equivalence ratio. This was evidenced by the in-cylinder pressure traces and the HRR waveforms. The emissions data indicate that both lasers produced very similar combustion. The ignition delay caused

by the shrouded spark cause most of the combustion to happen after TDC which lead to poor combustion that produced high levels of CO and THC.

The novelty of this work lies in the combination of the laser parameters to create a single high peak power laser output pulse for use as a spark ignition source. Similar configurations have been investigated in the literature but for different applications such as multiple output pulse trains for various industrial and communications applications. Another point of novelty is the investigation of the laser medium concentration on the output characteristics of a passively Q-switched laser system. This work has shown that lowering the Neodymium concentration in the active media within a passively Q-switched laser produces higher output energy values. This is significant because an actively Q-switched laser shows the opposite affect when the active ion concentration is varied.

Acknowledgements

I would first of all like to acknowledge and thank the grand architect of the universe for the breath of life and the manifold blessings and wonders that surround everyone, everywhere, every moment of every day. I would also like to thank Mridul Gautam and his family for helping a weary traveler on a cold January evening in 2002, your acts of kindness and understanding toward a stranger were and are the most valuable things that one person could offer another in this life.

I would also like to thank Mike McMillian and Steve Woodruff for making this research opportunity available and within reach, without these two this chapter of my life would have never been written much less completed and closed. I would like to thank Greg Thompson, Gary Morris, and John Kuhlman for their encouragement, support, advice, and most importantly their heavy boots to keep me motivated. I must express my deepest gratitude to the United States Department of Energy and the National Energy Technology Laboratory for the opportunity, the infrastructure, and support to ensure the completion of this work.

Words cannot describe my feelings for my family who have supported me in every imaginable way through all the good times and the bad times throughout my life, for them I am thankfull. My mother, Dorinda McIntyre, my father, Donald McIntyre, and my sister Regina McIntyre, I love and cherish you. Dad-I I think of you each time I see a solitary bird or butterfly dancing through the sky.

The following is a list of people who I have relied on as both friends and family and whom without I would not have had the strength to complete this undertaking. The list is as follows and is no particular order. Debbie Willis, JoAnn Yuill, Jim Poston, David Huckaby,

Clark Robinson, Todd Worstell, Rich Eddy, Doug Horton, Brad Linton, Al Shoaf, Rich and Kathy Pineault, Ben and Amy Chorpening, Narasimharao Ayyalasomayajula, Chris and Jean Garman, Fred and Jean Turnley, John and Becky Finch, Erik and Crystal Nantz, Randy and Donna Martin, Pete Turner, Harold Facemeyer, Ryan Stichweh, Diane Newlon, Dave Houdyschell, Dan Haynes, Bob and Deb Stevens, Jason Trembly, Grant Bromhal, Judy and Stacey Sneed, John and Carol Mathews, Steve Richardson, Buster (The Bad Kitty), Tommy and Kelly Johnson, Don Rogers, Sandy Boggess, Sandy Lunsford, Margie Barrett, and all of their families.

And last but certainly not least I must thank my brothers at Putnam Lodge #139 A.F.& A.M., Morgantown Union Lodge #4 A.F.& A.M. for aiding me in discovering the correct path to travel in life.

Dedication

You are missed.

Natalie Nicole Smith

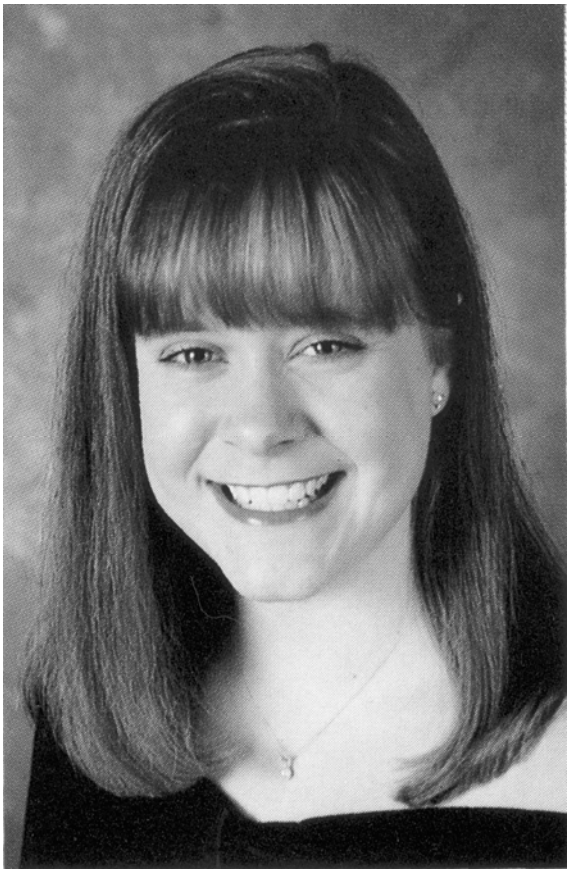

August 3, 1976

-

September 16, 1998

Laura Danielle Turley Carder

June 21, 1979

-

October 4, 2006

Table of Contents

List of Figures

List of Tables

Nomenclature

Ar	- Argon
A	- Output beam cross sectional area (cm^2)
ASE	- Amplified spontaneous emission
AR	- Antireflection (coating)
BMEP	- Brake mean effective pressure (bar)
CO_2	- Carbon dioxide
CO	- Carbon monoxide
CH_4	- Methane
CFR	- Code of Federal Regulations
Cr	- Chromium
CW	- Continuous wave
c	- Speed of light in a vacuum (3×10^8 m/s)
C_v	- Specific heat at constant volume
C_p	- Specific heat at constant pressure
D_2	- Deuterium
DPSS	- Diode pumped solid state (laser)
δ	- Ionization fraction
e^-	- Free electron
ε_i	- Ionization potential (eV)
E_{stored}	- Stored energy (J)
E_{loss}	- Energy loss (J)
E_s	- Saturation energy (Saturable absorber) (J/cm^2)
ESA	- Excited state absorption
E_o	- Output pulse energy (J)
F	- Photon flux
FWHM	- Full width half maximum
G_{rt}	- Round trip gain
g	- small signal gain coefficient (cm^{-1})
$GaPO_4$	- Gallium orthophosphate
γ	- Inversion reduction factor (γ =1 for a four level laser)
γ_{SH}	- Ratio of specific heats
Hg	- Mercury
$h\upsilon$	- Photon energy (J)
h	- Planck's constant (6.626076×10^{-34} J-sec)
H_2	- Hydrogen
I_{th}	- Threshold breakdown flux intensity ($Watts/cm^2$)
I_s	- Laser medium materials parameter
IMEP	- Indicated mean effective pressure (bar)
κ	- Polytrophic coefficient
k	- Boltzmann's constant (1.388066×10^{-23} J/K)
KTP	- Potassium Titanyl Phosphate
l	- Gain medium length (cm)
l_s	- Path length (Saturable absorber) (cm)
L	- Bulk optical losses

m_t - Total mass of thermodynamic system (g)
MPI - Multiphoton ignition
m - Integer number of ionization photons
M - Neutral molecule or atom
m_e - Electron mass (g)
MBT - Maximum brake torque (ft-lbs)
MFB_θ - Mass fraction burned with respect to crank angle
M^2 - Beam quality
n - Polytrophic index
N_g - Active media ground state population
N_f - Final excited state population density (excited states/cm^3)
N_{th} - Threshold excited state population density (excited states/cm^3)
N_i - Initial excited state population density (excited states/cm^3)
N_e - Excited state population density (excited states/cm^3)
N_{es} - Excited state population density (Saturable absorber) (excited states/cm^3)
N_{gs} - Ground state population density (Saturable absorber) (ground states/cm^3)
N_{so} - Total states population (total states/cm^3)
Nd - Neodymium
N_{oe} - Initial free electron concentration (e^-/cm^3)
N_{fe} - Free electron concentration (e^-/cm^3)
N_{ce} - Critical electron population for breakdown (e^-/cm^3)
NO - Nitrogen monoxide
NO_2 - Nitrogen dioxide
NO_x - Oxides of nitrogen
N_2O - Nitrous oxide
O_2 - Oxygen
OC - Output coupler
O_3 - Ozone
PQSW - Passive Q-switch
p - Gas pressure
P_{out} - Output power (Watts)
P - Output power (Watts)
PW - Pulse width (s)
P_{max} - Maximum pressure
P_{in} - Input power (Watts)
P - Pressure
Φ - Photon density (photons/cm^3)
$\Phi_{F/A}$ - Fuel to air ratio
Q - Quality factor
Q_{chem} - Incremental chemical energy release
Q_i - Incremental heat release
Q_{wall} - Heat loss to cylinder walls
R - Output coupler reflectivity
R_r - Ratio of connecting rod length to crank radius
R_{ave} - Average gas constant
r_c - Compression ratio

SF_6 - Sulfur hexafluoride
SA - Saturable absorber
σ - Absorption cross section (Laser gain medium) (cm^2)
σ_{gas} - Absorption cross section (Laser gain medium) (cm^2)
σ_{gs} - Ground state cross section (Saturable absorber) (cm^2)
σ_{es} - Excited state cross section (Saturable absorber) (cm^2)
τ - Free electron lifetime (s)
TDC - Top dead center
T - Temperature (K)
T_o - Initial transmission (Saturable absorber)
T_{max} - Maximum transmission (Saturable absorber)
t_r - Cavity round trip time (s)
τ_s - Excited state lifetime (Saturable absorber) (s)
t_p - Output pulse width (s)
THC - Total hydrocarbons (ppm)
θ_{max} - Crank angle where maximum pressure occurs (degrees)
UV - Ultraviolet radiation
VIS - Visible radiation
υ - Photon frequency (Hz)
V - Focal volume (cm^3)
V_d - Displaced volume (cm^3)
V_c - Clearance volume (cm^3)
V_{cyl} - Cylinder volume (cm^3)
ω - Optical angular frequency (rad/s)
W_p - Excited state production rate (excited states/cm^3/s)
W_c - Work per cycle
Xe - Xenon
YAG - Yttrium aluminum garnet ($Y_3Al_5O_{12}$)

1 Introduction

With increasing restrictions being placed on stationary reciprocating engine emissions and increasing demands for energy efficiency [1-3], the traditional spark ignition system is quickly reaching its practical durability limit, as well as its effectiveness in igniting ultra-lean fuel/air mixtures [3,4] (see also Appendix A). A durable high-energy electrode-less ignition system is a desirable option for overcoming this limitation in higher efficiency, ultra lean mixture, reciprocating engines [5-7]. Current technology, however cheap and relatively efficient, cannot meet the performance and emissions guidelines to be mandated by the federal government in the next five years [1-3].

By shifting to leaner fueling conditions, cooler combustion can be maintained; dramatically reducing the amount of NO_x produced by the engine [8-13]. Higher thermal efficiency can also be achieved due to lower heat loss and higher compression efficiency [10-12]. Increasing the in-cylinder pressure at the time of ignition allows the engine designer to increase the engine efficiency by increasing the power per unit piston area, which increases the specific power/heat loss ratio. Increases in both the in-cylinder pressure and leaning of the fuel/air mixture are currently limited by the durability of the ignition system and its ability to ignite the leaner mix at higher pressures.

The electric spark systems perform well at normal operating conditions. However, when the engine parameters are modified for increased BMEP or leaner operation current electric spark plugs cannot deliver the needed amount of energy to the combustible mixture to initiate or sustain smooth combustion without significant durability problems. The solution so far has been to dramatically increase the amount of energy delivered to the spark plug. This method of stabilizing lean combustion has a few serious consequences concerning

the life of the spark plugs. The electrodes act as a thermal energy sink, robbing the discharge of a considerable portion of its energy thereby reducing the amount of energy that is transferred to the gas for ignition [8-12]. Further, electrode erosion and the inherent increase in maintenance cost incurred by users quickly negates any benefits gained.

There are several attractive aspects to the proposed laser ignition system. The laser ignition system will offer a spark source with no electrodes inside the combustion chamber. This will allow a higher energy transfer to the gas and eliminate flame kernel heat losses to electrodes. The introduction of laser energy into the combustion chamber will allow for the tailoring of spark size, location and energy density within the initiating spark. Also, for equivalent amounts of system input energy delivered to the spark, the laser ignition system provides a much larger initiating spark volume as compared to an electrical spark.

Laser ignition has the potential to advance large bore lean burn natural gas fueled engine technology by improving ignition system durability and ignitability and also promises improved efficiency and lower emissions. Laser ignition has been shown to extend the lean limit of operation of natural gas fueled engines [8-14]. The breakdown threshold for laser ignition has been shown to be an inverse function of gas pressure unlike electrical discharges [15-19]. Therefore, the higher the gas density, the easier it becomes to induce breakdown with a high peak power laser pulse. Although laser ignition shows promise as a durable high-energy ignition system for future high efficiency internal combustion engines it currently suffers from issues such as large size, high cost, low efficiency, and system complexity as compared to the traditional electrical ignition system. The development of a miniaturized, low cost, laser ignition system could enable great advancement in the

development and commercialization of highly efficient ultra low emission large bore natural gas fired engines.

The present study focuses on the design and analysis of a miniature, diode pumped, solid state, passively Q-switched laser for use as a high energy spark plug in a natural gas fueled, single cylinder, reciprocating engine. Design indicators were drawn from the theoretical and experimental literature regarding lasers of this type. A literature study in conjunction with preliminary experimentation was employed to establish a suitable test plan emcompassing a variety of independent variables. The test laser was characterized according to the combinations of independent variables and the most appropriate setup was used as an ignition source for a natural gas fueled, single cylinder research engine. It is expected that the laser spark plug can eventually be packaged in a manner similar to the current electrical spark plug technology.

2 Objectives

The overall objective of this research is to improve the efficiency and ignition system durability of large bore, stationary, natural gas, reciprocating engines. This will be accomplished by researching current diode pumped, passively Q-switched laser designs and extending the operational envelope through design improvement, testing and evaluation. The end product will be a compact, diode pumped, passively Q-switched laser capable of providing an ignition source for a large bore, stationary, natural gas engine. The specific objectives are given below and are accompanied by a brief discussion of how each relates to the overall research objective.

- **Examine literature:**

The published literature is reviewed to determine the feasability of designing and implementing a diode pumped, passively Q-switched, laser spark plug. Information about the laser geometry, optical component characteristics, and arrangement as well as electrical and optical power requirements for practical operation can be gained from the literature and incorporated into the design and implementation of the laser spark plug.

- **Validate assumptions and "rules of thumb" with preliminary experimentation:**

Optical components and optical input power levels are selected to validate, complement, and extend the literature to gauge component and input relationships required to accomplish the ultimate goal of designing and operating a laser spark plug. By performing the preliminary experimentation the designer is better able to assess the fine details of the construction and implementation of the laser system and identify and avoid potential pitfalls with full scale experimentation. Preliminary experimentation will allow for the design of a

full scale experiment that will produce the most information from the minimal amount of data points and analysis.

- **Design, execute, analyze, and report full scale test plan:**

The information gained in the previous step was used to properly design an experiment to explore the optical component combinations and optical input that will produce sufficient output for laser spark production.

- **Use information gained to establish prototype parameters for engine testing:**

Use the information gained in the previous section to establish the laser design for testing the laser ignition system on a stationary natural gas fueled engine.

- **Design, execute, analyze, and report engine testing:**

Integrate the laser system with the engine ignition system and attempt to operate the natural gas fueled engine with the diode pumped passively Q-switched laser as the ignition source at nominal engine conditions to verify operation.

3 Literature Review

3.1 Impetus for the Development of a Durable Laser Ignition System

This study was primarily driven by durability issues stemming from tightening government regulations concerning emissions reduction and efficiency improvement in stationary natural gas engines [2,20]. The foremost goals of the regulations are NO_x reduction and improvement of engine efficiency. The reduction of NO_x, as well as CO, can be achieved by diluting the combustable mixture with excess air for leaner engine operation. The leaner mixture provides cooler combustion which lowers NO_x emissions [21,22]. The leaner mixture provides excess oxygen for the oxidation of CO into CO_2, thus significantly lowering the CO concentrations. The CO_2 concentrations in the exhaust are primarily a function of the hydrogen and carbon composition of the fuels and not a function of the equivalence ratio. The leaner/cooler combustion also produces a higher thermal efficiency due to lower heat losses [10,21]. Increases in engine efficiency can be realized because the excess air increases the ratio of specific heats of the burned gases which in turn increases the work output of the engine during the expansion stroke [21]. Subsequent efficiency gains are realized due to a reduction of the pumping losses that result from the higher intake pressures used to dilute the fuel mixture [21,23]. This increased operating pressure acts to offset the loss of power density due to lean operation [12].

Regardless of the gains in efficiency or emissions reduction as the fuel/air mixture is diluted it becomes more difficult to ignite with modern ignition systems [21]. Therefore in order to ignite the leaner mix, designers have had to increase the ignition discharge energy. This has an adverse affect on the spark plug electrode erosion and hence the useful lifetime of the ignitor. The shortening of the plug lifetime increases the maintenece costs of replacing

the worn plugs. Another negative affect of accelerated electrode erosion is the cost of downtime needed to replace the worn plugs and the increasing frequency of this mantenence. If an ignition system could be developed that could ignite the lean, or leaner, mixtures and have increased durability, allowing for longer ignitor lifetime it would be to the benefit of consumers and manufacturers to employ this technology.

3.2 Electrical Ignition Systems for Stationary Natural Gas Engines

Large bore stationary natural gas fueled reciprocating engines generally employ capacitive discharge ignition (CDI) systems primarily because of their simplicity, low cost, ease of use and high energy output. The CDI system is attractive to engine manufacturers because it has no moving parts, is electronically controllable and renders a very precise and robust ignition spark over a wide range of engine speeds and operating conditions [22]. A general circuit diagram of a CDI system is shown if Figure 3.1 [24].

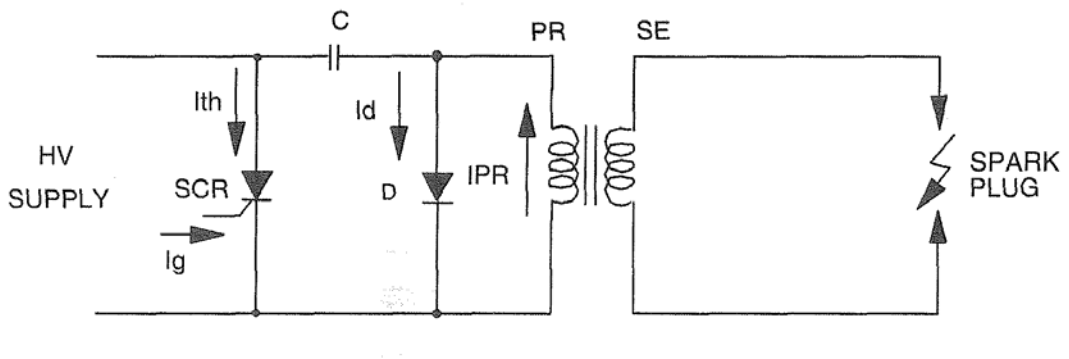

Figure 3.1: Capacitive discharge ignition (CDI) system [24]

In between ignition pulses the high voltage source charges the capacitor. When an ignition pulse is desired current is driven into the gate of the switch (Silicon Controlled Rectifier – SCR or Triac). The gate current causes the switch to conduct current thereby grounding the charged capacitor. The capacitor voltage induces a current through the switch

to ground. The current from the capacitor to ground induces a current within the primary winding of the step up transformer. This induces a large voltage (~400-1000V) on the transformer primary due to the change in the current flow through the primary [22,24]. This voltage causes the freewheeling diode to conduct and allows the current to continue flowing through the diode and primary coil. The voltage present on the primary coil is stepped up by the secondary coil to several thousand volts (~5-25kV) [22,24]. This high voltage induces an electrical breakdown across the spark plug electrodes.

Typically a CDI system has a dwell time of approximately 2 milliseconds or less [22,24]. Although a CDI system can deliver higher ignition energies in a more precise manner than a common inductive ignition system, the short ignition pulse can lead to ignition failure when operating with lean mixtures [22]. Therefore in order to secure ignition with a leaner mixture at higher pressures, a considerable amount of ignition energy must be added. Such is the case with modern large bore stationary natural gas reciprocating engines. Designers are utilizing leaner mixtures for pollution control and higher pressures for increased thermal efficiency. This operational regime has led to the increased erosion of the spark plug electrodes which has become a major maintenance and downtime issue.

3.3 Spark Plug Erosion Mechanisms

The electrical discharge produced across the electrodes of a spark plug is composed of three distinct phases: breakdown, arc discharge, and glow discharge [25,26]. Each phase of the spark discharge involves a different physical process, therefore each phase has a different effect on electrode erosion [25,26]. This section will discuss each phase of the electrical spark discharge and how each mechanism contributes to electrode wear.

The discharge begins with the elevation of the voltage between the electrodes. As the breakdown voltage is reached, the free electrons in the electrode gap gain enough energy from the electric field to ionize, via collisions, the gas molecules in the gap [25-27]. The ionization produces new electrons and an electron avalanche ensues between the anode and cathode. During the breakdown phase the charge carriers are supplied by the cathode via photo emission and at later stages supplied by field emission [25-27]. The breakdown is characterized by a low voltage drop in concert with thin high current conductive channel between the electrodes [25-27]. The high current (>>100mA) produced by the breakdown phase only lasts a few nanoseconds and forms hot spots at the discharge/conductor interface creating molten pools of metal [25,26].

Breakdown is then followed by the arc regime whose charge carriers are largely supplied by thermionic emission concentrated in and around the molten hot spot [25,26]. The conductive channel expands radially, yet concentrated current density can reach values of approximately 10^8-10^{10} A/m^2 [25,26]. During the arc phase the elevated current density can heat the small area of molten cathode material to its boiling point making the cathode susceptable to erosion due to evaporation and/or splashing of the molten cathode material [25,26]. This process is sustained as long as the arc current is above approximately 100mA [25,26].

The final phase of the electrical breakdown process is the glow discharge. This phase begins as the available current from the ignition system begins to drop (below ~ 100mA) and the hot spot can no longer be sustained [25]. The electrons are then supplied by a much more inefficient process, ion impact emission, that induces a large voltage drop and spreads the discharge across the entire electrode face significantly lowering the current density [25].

Although the glow discharge is the mechanism by which the majority of the spark energy is delivered to the gap, it has no erosional effects on the electrodes due to the decreased current density [25].

The gas pressure in which a spark is produced in can have a significant affect on the discharge production and development as well as the electrode erosion progression. Studies have shown that spark production at or near atmospheric pressure (1 bar) only involves the breakdown and glow discharge phases [25]. This regime produces a low current density while still delivering substantial energy to the gas thereby limiting and in some cases eliminating cathode erosion [25]. However in an engine the gas pressure is substantially higher and research has shown a distinct difference in the spark formation and development at in-cylinder pressures. At higher pressures all three phases of the spark breakdown process occur. For electrical arcs produced in a gas, Paschen's Law states that the threshold breakdown voltage for a given spark gap is proportional to the gas pressure within the spark gap [28,29]. Figure 3.2 shows breakdown voltage as a function of pressure according to Paschen's Law for a 1 mm electrode gap.

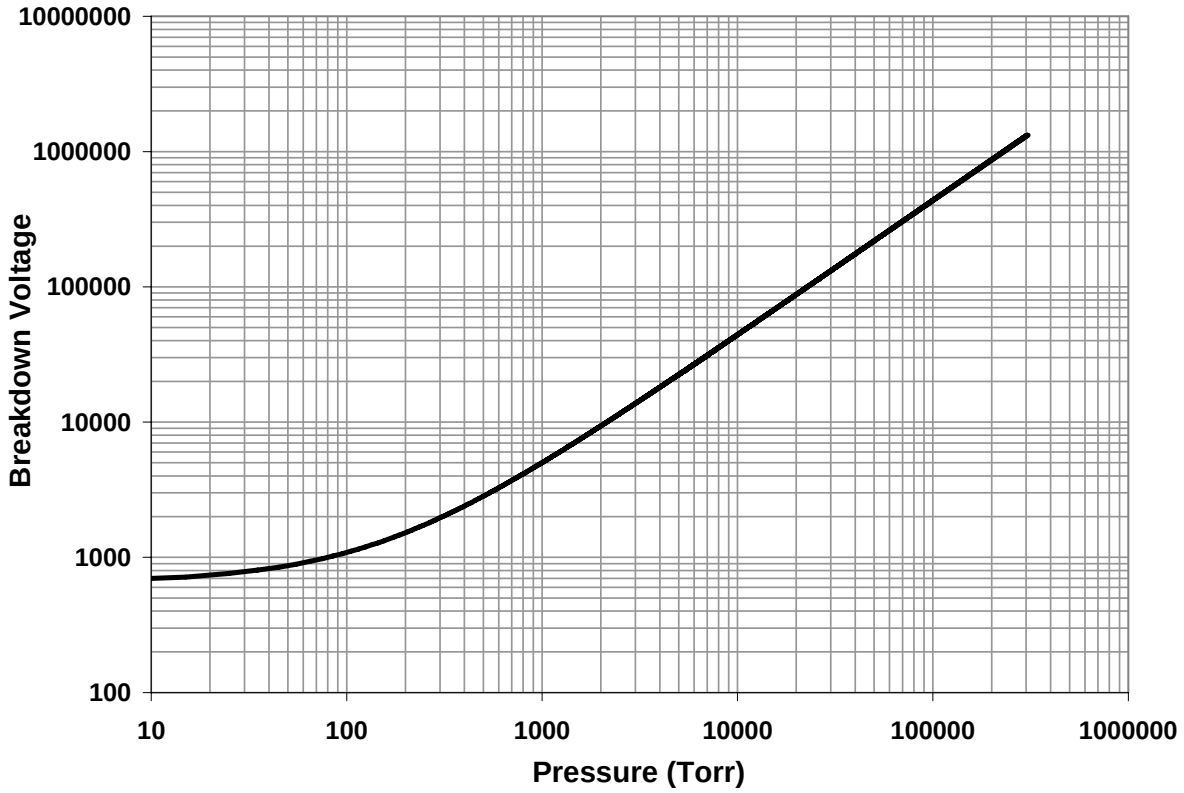

Figure 3.2: Minimum breakdown voltages for a 1 mm electrode gap according to Paschen's Law [28,29]

As the pressure is increased, the voltage of the system must be increased to induce breakdown, the increased voltage in conjunction with the fixed capacitance causes the system to store more energy. The increased energy storage produces a larger and hotter spark when breakdown ensues. This leads to larger cratering and accelerated erosion due to the larger hot spots created by the increased ion flow. Figure 3.3 illustrates cathode cratering produced by one spark at elevated pressure (9 bars) in air [25].

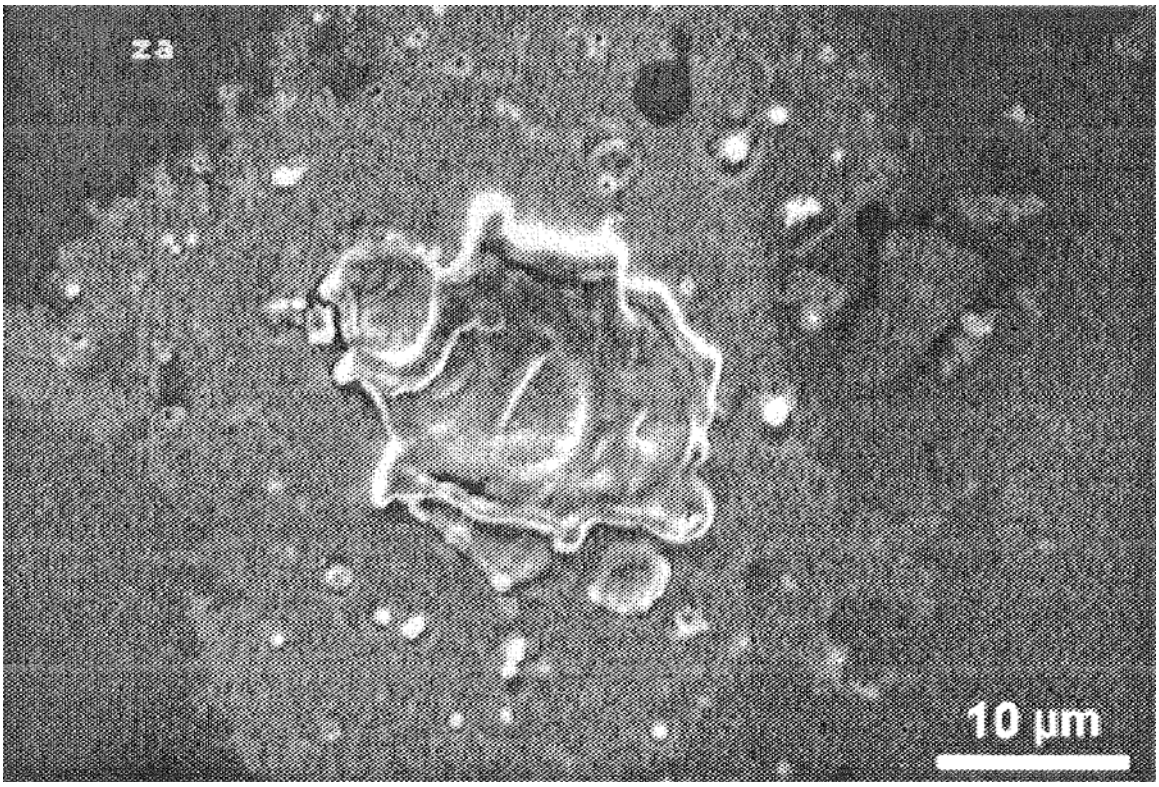

Figure 3.3: Cratering produced by a discharge across a 1 mm gap at 9 bars in air with a Platimum cathode [25]

It was estimated that the volume of material lost from the cratering shown in Figure 3.3 was approximately 1.4 μm^3 [25]. Considering the volume of material eroded from one spark in Figure 3.3, if an engine were operated at 1800 rpm for two weeks continuously more than 25 million sparks would have been generated and eroded approximately 0.025 mm^3. The erosion appears small, however it would be desirable to have an ignition system that would not degrade with each ensuing ignition event. Laser ignition offers this possibility by inducing ignition without electrodes and free from any surfaces that would reduce the durability or lifetime of the laser igniter.

3.4 Laser Induced Spark Ignition Theory

Laser induced ignition has been of interest ever since the invention of the high peak power, Q-switched laser and the production of the first laser spark in air. Laser induced ignition has been used for a wide variety of applications including, ignition of gaseous fuels for internal combustion engines [30-44]; ignition of high explosives [45-48]; ordnance/pyrotechnics [49-69] and rocket motors [70-72]; initiation of chemical reactions [73-75]; ignition of liquid fuel sprays [76-89] as used in turbines [90-94], boilers [95,96], and jet engines [97]; initiation of nuclear fission/fusion reactions [98-100]; initiation of plasma discharges for materials processing [101-103]; triggering of high voltage switches [104]; and lightning protection/diversion systems [105-110]. It is clear that laser-induced breakdown has many potential industrial applications; however, this work will focus on a laser ignition system for large bore, stationary, natural gas fueled, lean burn, reciprocating engines that are typically used for electrical power generation and gas pipeline pumping. The physical processes by which laser energy can induce ignition in a combustible gaseous mixture have been divided into four groups: thermal ignition, non-resonant ignition, resonant ignition, and photochemical ignition [38,41].

3.4.1 Thermal Ignition

Thermal ignition is initiated when low energy (long wavelength > 1μm [16]) laser radiation is incident on a target material that is a strong absorber, solid [85,111,112] or gaseous [113-115], in a gaseous combustible mixture. Thermal initiation utilizes infrared (IR) laser energy to vibrationally and/or rotationally excite a specific highly absorbing species within the combustible mixture to induce ignition. Ignition takes place when the target absorber transfers sufficient energy to the combustible mixture to cause autoignition

[116]. Numerous studies [85,111-115] have been published stating that thermal laser ignition has been accomplished by using a CO_2 laser source operating at 10.6 μm. Lavid et al. [113] published a set of experiments where natural gas mixtures were thermally ignited with a CO_2 laser. A study of the absorption properties of natural gas indicated that the CH_4 component was practically transparent to the laser radiation; however, the butane and propane components were found to be highly absorbent [113]. An illustration of the thermal ignition concept is shown in Figure 3.4.

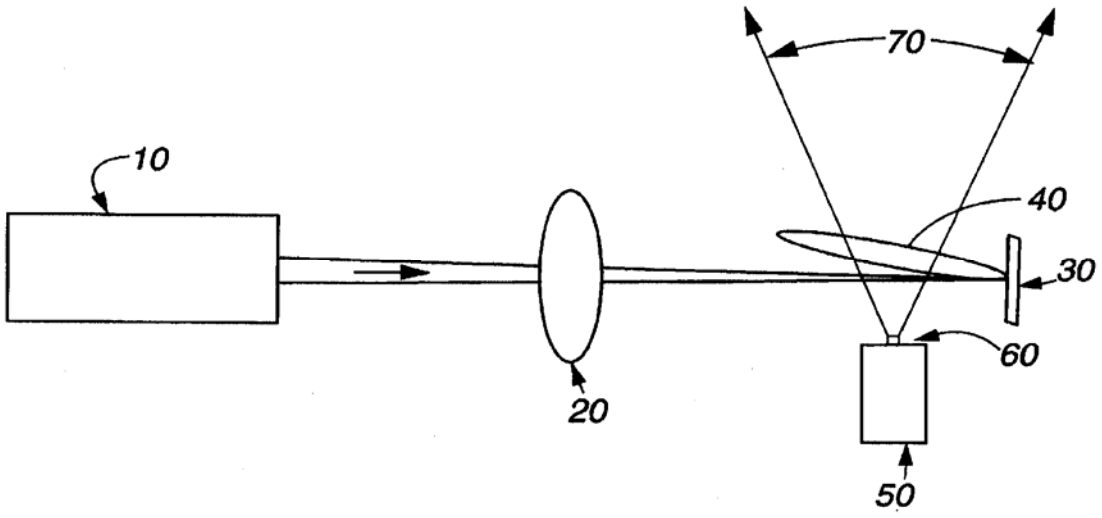

Figure 3.4: Laser Ablation Based Fuel Ignition Concept 1 [117]

The laser, focusing lens, and target are denoted by the numbers 10, 20, and 30 respectively. The hot plume of material is denoted by the number 40 and the fuel spray to be ignited is labeled number 70.

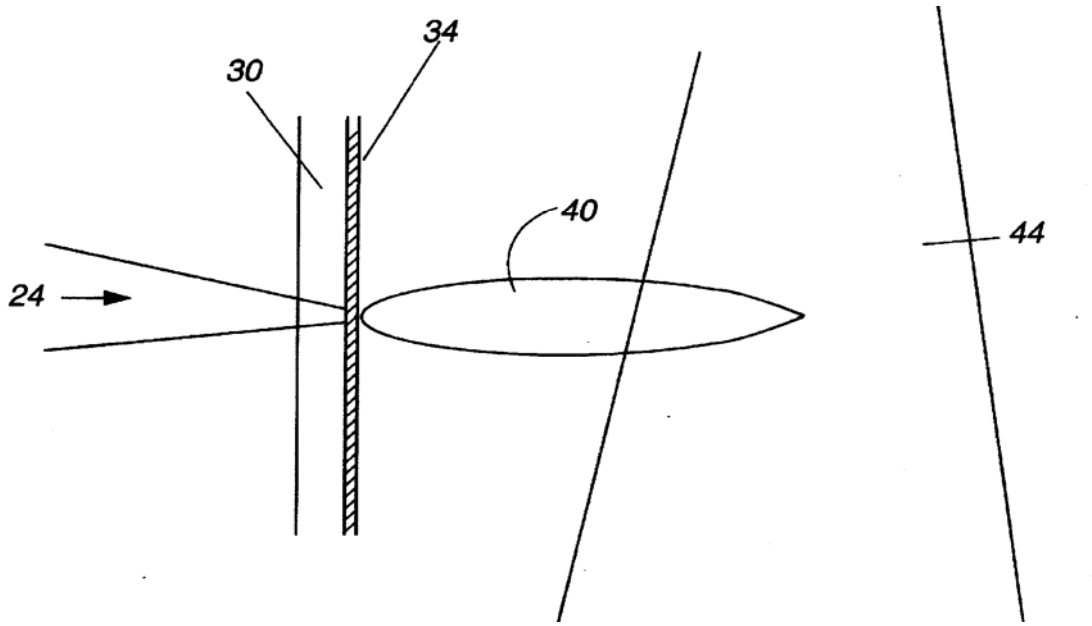

Figure 3.5: Laser Ablation Based Fuel Ignition Concept 2 [117]

Continued work by Early and Lester [117] describes a variation of the thermal laser ignition method and is shown in Figure 3.5. This variation makes use of a physical barrier between the laser source and the fuel spray. The laser radiation (24) is focused on the barrier, which is constructed of a transparent medium (30) with a sacrificial coating (34) on the fuel spray side of the barrier. The coating (34) is rapidly heated producing a jet of hot particles (40) that are exposed to the fuel spray (44) inducing ignition [117].

Although the laser equipment is readily available for a thermal ignition system it is rather unpractical because it requires a portion of the system to be sacrificial (like spark plug electrodes), whether it be a fuel additive or a part of the engine.

3.4.2 Photochemical Ignition

Photochemical ignition occurs when a high energy photon dissociates a molecule allowing the ionized constituents to react with the surrounding gases [38,41,116]. This type of ignition mechanism is similar in concept to the thermal ignition regime, however the

primary difference is the photon energy of the incident radiation and the fact that the absorber is the gas to be ionized and not a secondary solid or gas. Thermal initiation utilizes IR laser energy to vibrationally and/or rotationally excite specific noncombustible yet highly absorbing species within the combustible material to induce combustion. The photochemical process employs ionizing radiation in the ultraviolet (UV) wavelength range or higher [115,118]. Neither the IR nor visible (VIS) photons contain sufficient energy to photo ionize most molecules and require multiple photons to ionize the combustible gas molecules [119]. This high energy radiation is denoted ionizing because a single photon contains sufficient energy to overcome the ionization potential of certain molecular species and can directly initiate a sustainable chemical reaction. This laser ignition method has been used for the ignition of hydrocarbon/air [115,120], H_2/O_2 [121-123], and H_2/Air [122,123] mixtures. It has been reported that due to high reactive radical production rates the minimum laser ignition energy for certain mixtures is shown to be below a millijoule [115,120,122,123]. This is an attractive method for initiating combustion however the equipment needed for such a system is extremely cost prohibitive.

3.4.3 Resonant Breakdown Ignition

Resonant laser ignition is initiated by the dissociation of target molecules or atoms by the non-resonant multiphoton ionization process [124-126]. The dissociated atoms or molecules are then resonantly ionized via multiphoton ionization by continued laser illumination [124-126]. The electrons generated by the resonant ionization gain energy via the inverse Bremstrahlung photon absorption process and induce breakdown via the electron cascade process [124-126].

A limited number of experimental studies have been published concerning resonant laser ignition. The studies published to date have indicated the feasibility of this technique and the distinct advantage of greatly reducing the required ignition energy when the proper laser wavelength is applied to a specific gas mixture. The literature has reported that resonant laser ignition has been applied to gaseous mixtures of H_2/O_2 [124-126], D_2/O_2 (Deuterium/Oxygen) [124-126], and CH_4/N_2O [126] with relative success in reducing the minimum ignition energy of the mixtures. Figure 3.6 shows the wavelength dependence of the breakdown energy that is possible when applying the resonant laser ignition technique to CH_4/N_2O mixtures [126].

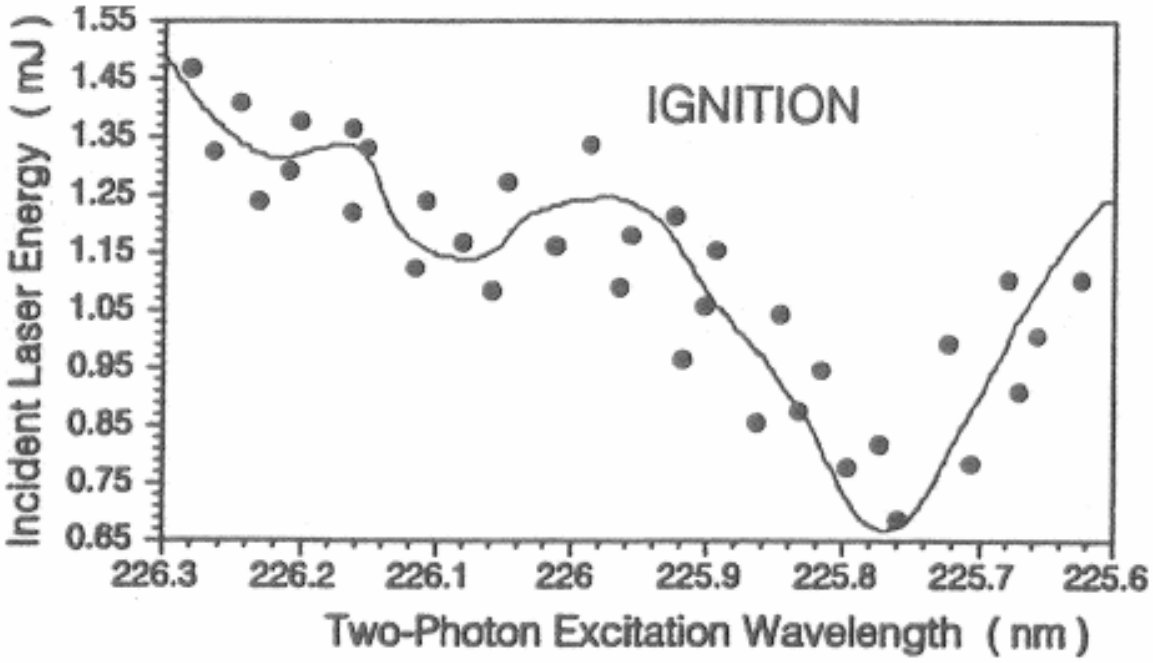

Figure 3.6: Minimum ignition energy as a function of laser wavelength [126]

The resonant laser ignition technique is very attractive, however the construction and operation of laser systems that produce the needed output wavelength is difficult and expensive at this point in time.

3.4.4 Non-Resonant Breakdown Ignition

Non-resonant breakdown occurs when a laser pulse of sufficient peak power is focused to a sufficiently small spot whereby the electrical field component of the focused light is strong enough to influence the gas molecules and initiate the electrical breakdown of the gas [38,41]. Depending on the characteristics of the laser energy and the gaseous medium there are two different mechanisms that dominate the initiation of the breakdown, which are multiphoton ionization (MPI), and electron cascade breakdown [127, 16].

3.4.4.1 Multiphoton Ionization Breakdown

Multiphoton ionization involves the simultaneous absorption of a sufficient number of photons by a gas molecule or atom to cause ionization [127]. The absorption of (m) photons induces the ejection of a valence electron into the conduction band where the electron is considered free of the atomic or molecular system and gains energy from the time varying electromagnetic field produced by the focused laser radiation [127]. The free electrons also absorb kinetic energy from the incident radiation via the inverse Bremstrahlung process and are then able to ionize the molecules or atoms within the focal volume producing an even greater number of free electrons [16, 128, 129]. The free electrons grow exponentially in number until the local electric field potential exceeds the breakdown potential of the gas. Once the local breakdown potential is exceeded a plasma discharge ensues that can produce localized temperatures of approximately 10^6 K [16, 128, 129] and localized pressures of approximately 10^3 kPa [16,128]. Multiphoton ionization can be described by the reaction in Equation 3.1 [127].

$$M + mh\nu \rightarrow M^+ + e^- \qquad \text{if } m \geq \frac{\varepsilon_i}{h\nu} + 1 \tag{3.1}$$

From Equation 1, M is a neutral molecule or atom, m is the integer number of photons plus one required to ionize a particular gas species. The parameter ε_i is the ionization potential of the specific gas atom or molecule and $h\nu$ is the photon energy of the laser radiation.

The multiphoton breakdown threshold is defined as the minimum intensity per unit area (Watts/cm^2) that releases a critical number of electrons during a given laser pulse to induce breakdown [128, 129]. The MPI breakdown threshold intensity is given in Equation 3.2 [127].

$$I_{th} = \left[\frac{\nu}{\sigma_{gas}}\right]\left\{\frac{N_{ce}(m-1)!}{N_{oe}PVt_p\nu}\right\}^{1/m} \tag{3.2}$$

From Equation 3.2, N_{ce} is the critical electron population required for breakdown, N_{oe} is the initial free electron population, P is the gas pressure, V is the focal volume of the laser flux, t_p is the full width half maximum (FWHM) pulse width of the laser pulse, ν is the frequency of the laser radiation and σ_{gas} is the photon absorption cross section for a particular gas. The expression for the breakdown threshold intensity can be simplified by assuming that a certain fraction, $\delta \sim 10^{-3}$, of the $PN_{oe}V$ atoms within the focal volume V are ionized at the initiation of breakdown [128, 129]. A simplified expression of the breakdown threshold intensity for MPI can be found in Equation 3.3.

$$I_{th} = \left[\frac{\nu}{\sigma_{gas}}\right]\left\{\frac{\delta(m-1)!}{t_p\nu}\right\}^{1/m} \tag{3.3}$$

The number of electrons freed by multiphoton ionization due to the application of a constant uniform photon flux, F, incident upon a focal volume, V, over the FWHM duration of the laser pulse is expressed by Equation 3.4 [128, 129].

$$N_{fe}(t) = \frac{N_{oe} P V t_p F^m \sigma_{gas}{}^m}{\nu^{m-1}(m-1)!} \tag{3.4}$$

The MPI model has a limited range of validity depending on the operating gas pressure and laser wavelength. At higher pressures, atomic and molecular collisions quench the photon flux driven ionization production and limit the ion production to a level well below that which could induce breakdown by this model alone. Breakdown strictly due to multiphoton ionization has only been observed for gas pressures below 10 Torr and laser wavelengths shorter than 1 μm [128]. However, at elevated pressures MPI can provide the small amount of free electrons to initiate electron cascade ionization (ECI) [130].

3.4.4.2 Electron Cascade Ionization Breakdown

Electron cascade ionization involves the absorption of laser energy by free electrons via the inverse Bremstrahlung process and subsequent energy transfer to the gas by elastic electron collisions with neutral molecules [15,17,126,128129]. The more energetic electrons can ionize the gas molecules if sufficient energy is gained as described by the reaction in Equation 3.5 [127].

$$M + e^- \rightarrow M^+ + 2e^- \tag{3.5}$$

The electron concentration will increase exponentially, described by Equation 3.6, resulting in a cascade breakdown [17,131].

$$N_{fe} = N_{oe} e^{t_p/\tau} \tag{3.6}$$

The electron cascade process is dependent on two necessary conditions. The first condition requires that an initial electron must be within the focal volume irradiated by the laser energy to initiate the process [127,131]. The second condition requires that the electrons must acquire an energy level greater than the ionization energy of the gas for the cascade to take place [127,131].

The breakdown threshold intensity for the electron cascade process is dependent on the gas pressure and the laser pulse width and can be found in simplified functional form in Equation 3.7 [128,129].

$$I_{th} \cong \frac{m_e \varepsilon_i \omega^2}{4\pi e^2 t_p \alpha P} \tag{3.7}$$

From Equation 3.7, m_e is the electron mass, ε_i is the ionization potential of the gas, ω is the angular frequency of the incident laser light, e is the electron charge, α is a coefficient that depends on the geometry of the optics used to focus the light beam and t_p is the FWHM laser pulse width. The electron cascade process is the dominant breakdown mechanism for short pulse durations under high pressures [128,129]. In both circumstances the electron diffusion losses are minimized and the energy transfer between the free electrons and the neutral gas molecules is maximized [128,129]. ECI is considered the primary ignition mechanism for laser induced ignition in natural gas fueled engines due to the high in-cylinder pressure.

3.4.5 Non-Resonant Laser Spark Breakdown Threshold

An important advantage of laser spark ignition over traditional electrical spark ignition is the direct pressure dependence of spark breakdown threshold. As opposed to the electrical spark breakdown threshold the intensity required for laser breakdown decreases as a function of the gas pressure at the focal volume [15-19].

The laser breakdown threshold can be significantly lowered by the addition of impurities into the gas being irradiated. Strongly absorbing impurities such as aerosols and low ionization potential organic vapors can produce a large number of initial electrons and invariably lower the photon flux needed to induce breakdown [15,16,131]. This is the case in laboratory air where dust is present. This is also expected to hold true in the case where laser energy is applied as an engine ignition source. Figure 3.7 shows the laser breakdown thresholds produced from multiple experimental studies with various gases to indicate the degree of variation of the threshold [15-19]. It can be seen that regardless of the gas being tested the laser breakdown threshold decreases as a function of pressure.

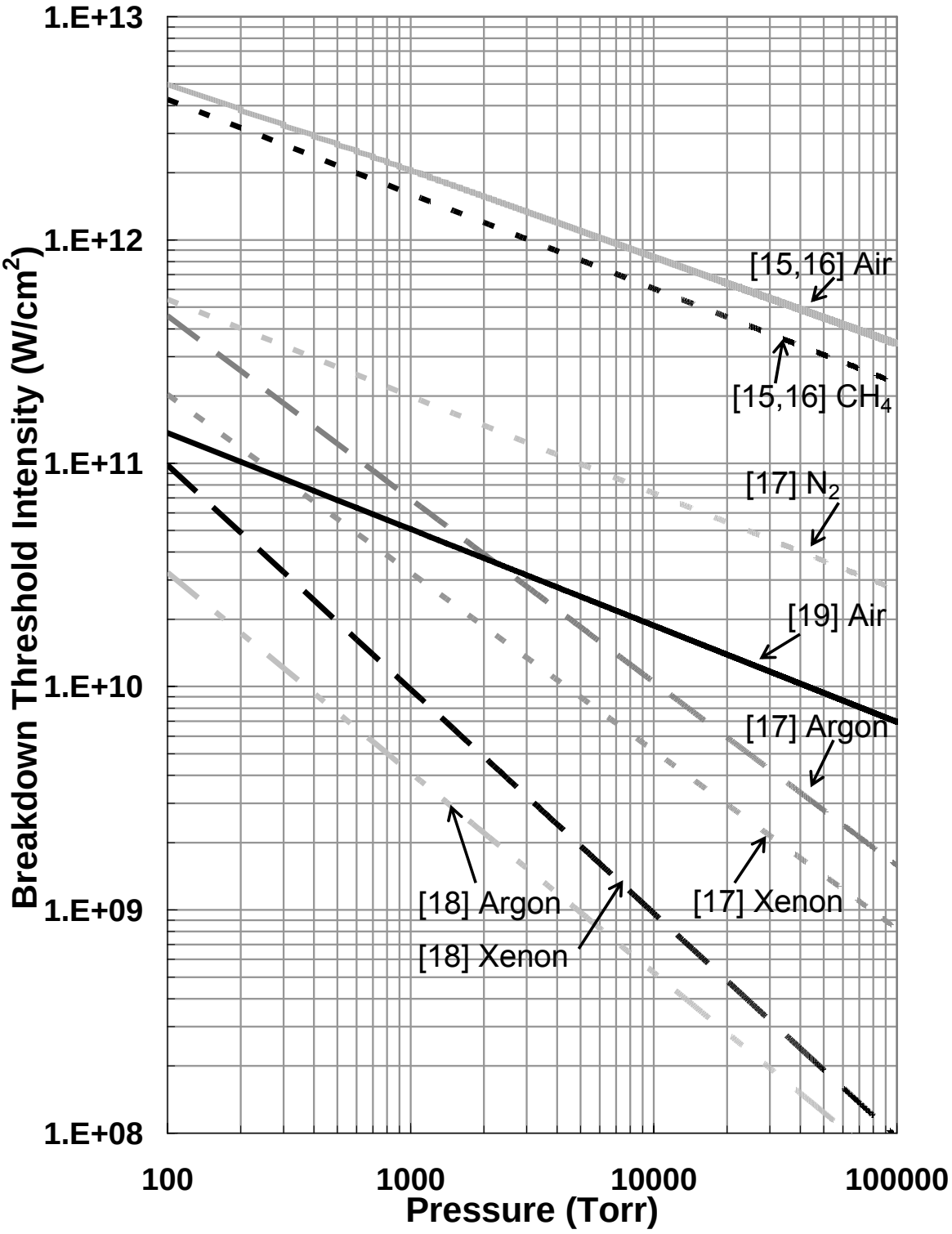

Figure 3.7: Experimental laser breakdown thresholds for Argon, Xenon, Nitrogen, Air and Methane [15-19]

The difference in behavior of the electrical and laser spark breakdown thresholds, as a function of gas pressure, is relatively straightforward. For the electrical spark, when the pressure is increased, more gas molecules or insulators are forced in between the electrodes greatly increasing the dielectric strength of the gap. The greater the density of the insulators, gas molecules, the larger the required breakdown voltage. For laser breakdown when the pressure is increased more gas molecules or absorbers are forced into the focal volume. The increase in the density of the absorbers, or gas molecules, allows for the more efficient transfer of energy from the photons to the gas.

3.5 Initial Flame Kernel Development of Electric Sparks and Laser Sparks

Laser ignition has been shown to produce larger and more consistent initial spark and flame kernels, when studied at identical conditions as an electric spark [132]. This is primarily due to the insensitivity of the laser energy deposition to variations of local equivalence ratios, species concentrations, or turbulence. The laser energy is also delivered to the mixture more efficiently due to inverse Bremstrahlung absorption and subsequent ionization. The electrical spark production process requires much more overall energy input to achieve the same effects due to considerable energy losses to the electrodes and the relatively small size of the spark channel as compared to the initial laser spark kernel. Figure 3.8 illustrates this point with a series of shadowgraphs of sparks produced by an electrical high energy ignition (HEI) system and laser sparks of two different output energy levels.

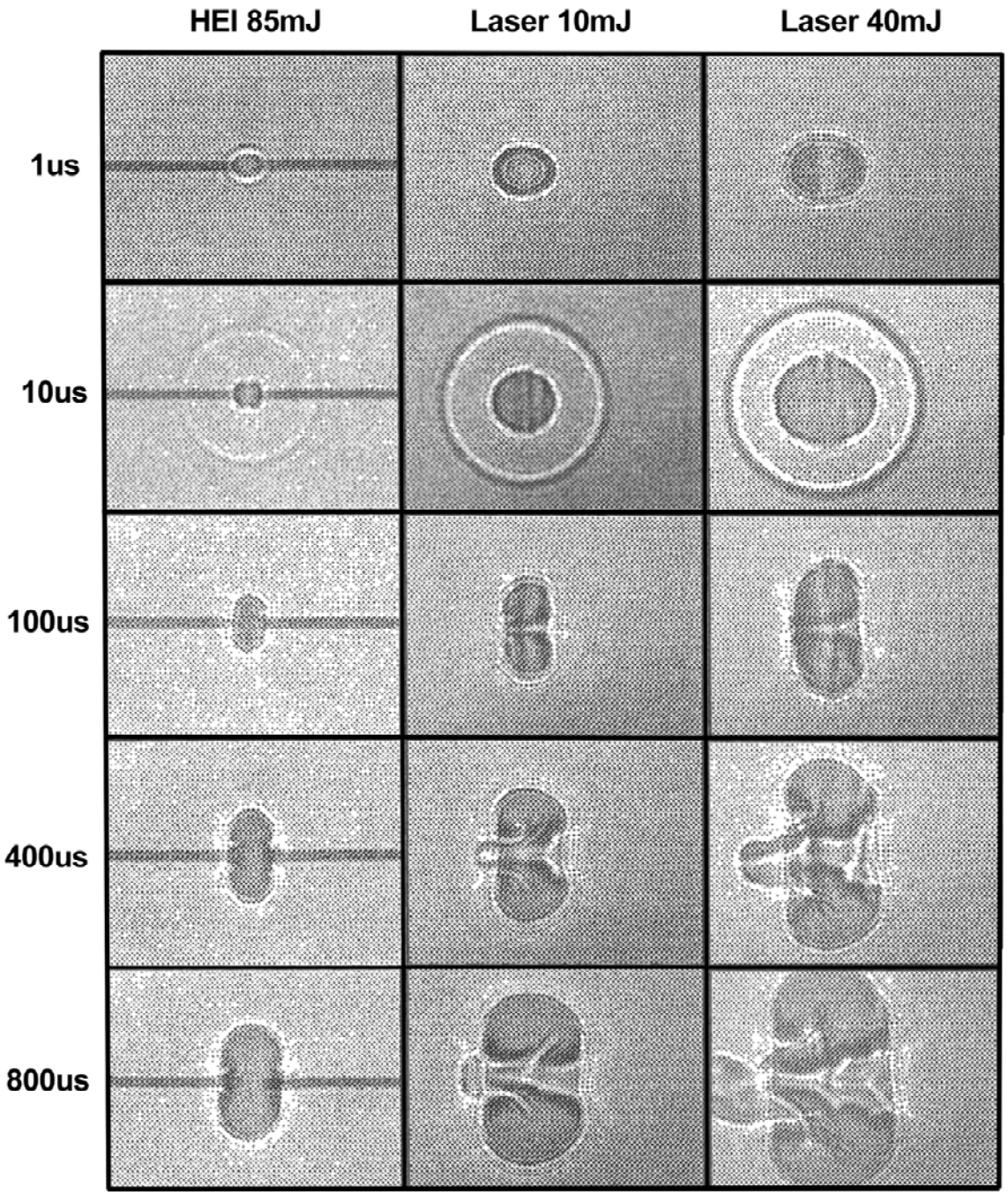

Figure 3.8: Shadowgraphs of the spark formation over time for electrical and laser ignition systems reported by Ho [132]

It can be seen in Figure 3.8 that the laser sparks produce a larger initial spark kernel and a more rapidly expanding flame kernel with less than half of the input energy. Figure 3.9

shows various electrical spark induced ignition kernel flows reported throughout the literature. The flow field characteristics of the electrically produced sparks were found to vary depending on the mixture properties, electrical properties and preceding flow fields. It is not clear why the electrical spark flow fields shown in Figure 3.8 most resemble the flow field shown in Figure 3.9 part (f).

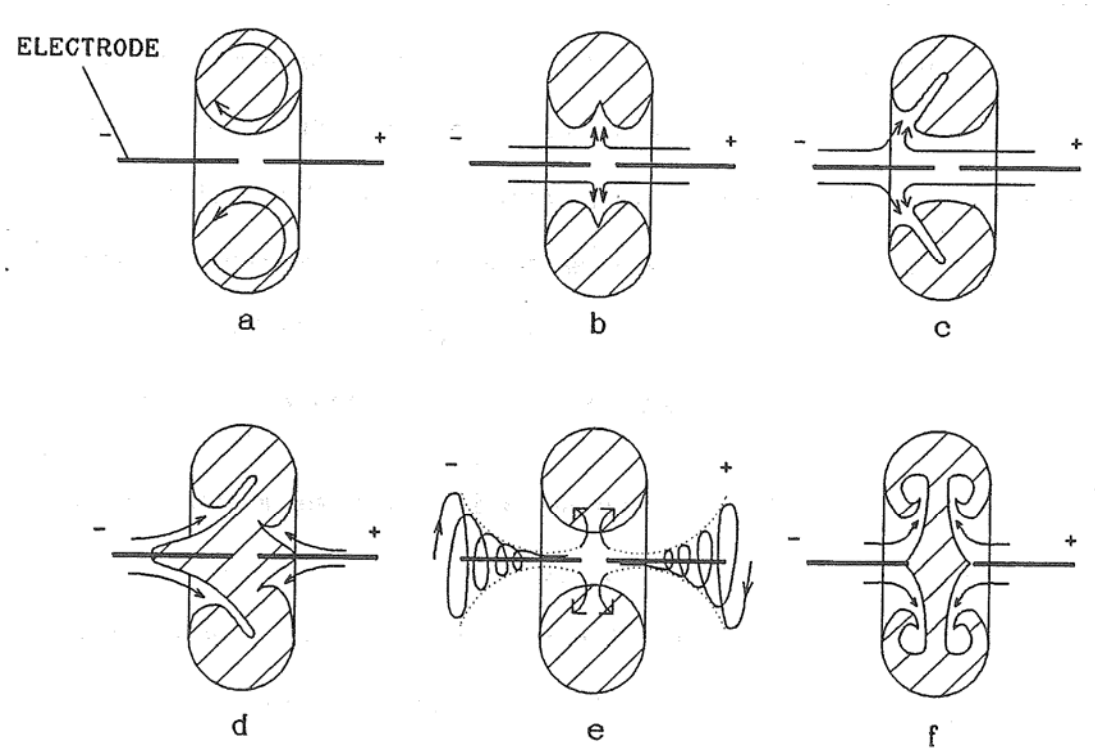

Figure 3.9: Various electrical spark induced flow fields reviewed by Ho [132]

Figure 3.10 shows the initial laser spark kernel before shock wave separation (a), the developed spark kernel after shock wave separation for the 10mJ laser pulse (b), and the developed spark kernel after shock wave separation for the 40mJ laser pulse (c) reported by Ho [132]. The laser energy was delivered from left to right. The flow fields for the laser induced sparks are in part due to the extremely high absorption of the ionized species produced by the initial breakdown. The plasma formed at breakdown is so highly absorbent

of the incoming laser energy that the plasma propagates toward the incoming laser energy creating the flow patterns that are seen in Figures 3.8 and 3.10.

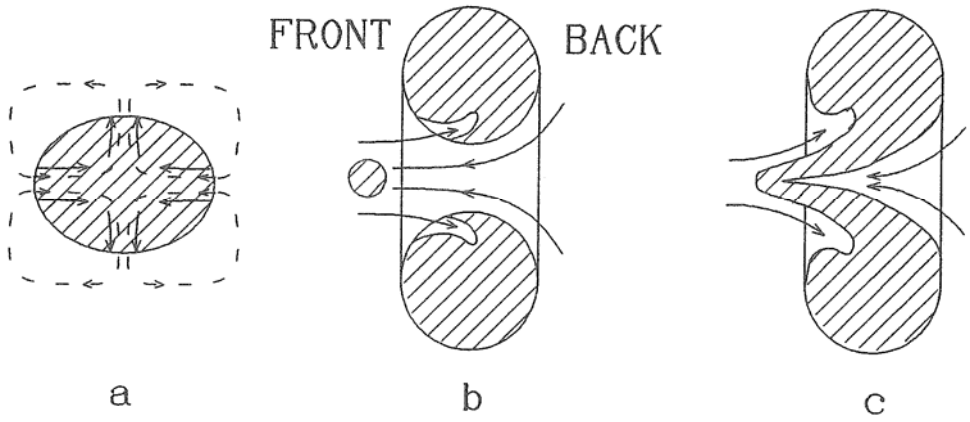

Figure 3.10: Laser spark kernel formation reported by Ho [132]

3.6 Laser Ignition Engine Studies

Internal combustion engine operation utilizing laser ignition has been the subject of a number of research efforts since the late 1970's. To date, the published research indicates the use of varying laser systems and delivery methods, multiple fuels, and overall improvement of engine operation and emissions production.

Dale et al., [133] employed a pulsed repetitive CO_2 laser operating at 10.6 μm with a pulse width of 300 ns and a pulse energy of approximately 1 J [133]. This provided a peak power of approximately 3.3 MW which readily ignited the test fuels, regular grade leaded and unleaded gasoline [133]. This approach utilized a zinc selenide window, with external focusing optics, adapted to the existing 18 mm spark plug hole of an ASTM-CFR single cylinder engine [133]. Additional engine and operational details were not reported.

Researchers at the National Energy Technology Laboratory used a flashlamp pumped actively Q-switched Nd:YAG laser operating at 1064 nm with a pulse width of 5 ns and a pulse energy of 50 mJ [9-12]. This laser output produced a peak power of approximately 10 MW which ignited a lean, $\Phi_{F/A}$ = 0.513, mixture of air and domestic natural gas at a BMEP of 12 bar [10,11]. The laser was focused into the combustion chamber by a sapphire window lens that was adapted to the existing 14 mm spark plug hole of a Ricardo Proteus single cylinder engine with a displacement of 1.99 liters [9-12]. The same laser and engine setup was used to explore the effects of blending hydrogen with natural gas on the engine performance and emissions [21].

Researchers at the Technical University of Vienna (TUV) and the Technical University of Graz (TUG) in collaboration with GE Jenbacher [134,135] used a diode pumped actively Q-switched Nd:YAG laser operating at 1064 nm with a pulse width of 5 ns and pulse energies varying from 4-30 mJ [134,135]. This laser output produced peak power levels in the range of 0.8-6.0 MW which were found to adequately ignite a lean mixture of air and domestic natural gas [134]. One study focused the open beam laser energy through a 5 mm thick sapphire window and into the combustion chamber [134]. This study used one cylinder of a 1 MW reciprocating engine using domestic natural gas with a BMEP of 18 bars [135]. A subsequent study used a miniaturized diode pumped laser that was directly connected to the engine [135]. This subsequent study found that with a very high beam quality and an output pulse energy of 1.5 mJ (the output pulse width was not reported) sufficient ignition the fuel/air mixture was possible for a short time. However window fouling was a significant issue [135]. This study did not report detailed information concerning the test engine.

Alger et al., used a flashlamp pumped Nd:YAG laser operating at 1064 nm with a pulse width of 6 ns and a pulse energy of 50 mJ [136]. This laser output produced a peak power of 8.3 MW which ignitied a lean mixture of air and propane/iso-butane [136]. A one inch thick fused silica window was used as a pressure barrier and optical access in combination with external optics [136]. The engine used in this study was a modified Tecumseh L-Head single cylinder engine with a displacement of 0.455 liters [136]. Additional engine and operational details were not reported.

Researchers at Colorado State University have performed both open beam path and fiber optic delivery tests using flashlamp pumped Nd:YAG lasers operating at 1064 nm [8,137]. The open beam path laser system had a pulse width of 8 ns and a pulse energy range of 10-31 mJ [137] whereas the optical fiber delivery test laser had a pulse width of 8 ns and a pulse energy of 47 mJ [138-140]. The open beam testing peak power range was 1.25-3.8 MW and ignited a lean, $\Phi_{F/A} = 0.73$, mixture of air and domestic natural gas [137]. The open beam testing used a sapphire window with external optics that was adapted to both the spark plug hole and the air start port of one cylinder of a Cooper-Bessemer GMV-4TF 4-cylinder two-stroke engine to examine the effects of spark location on engine operation [137]. The fiber optic delivery tests produced a peak power of 5.8 MW and ignited a lean mixture of air and domestic natural gas [138]. The fiber optic testing used one cylinder of an inline 6-cylinder Waukesha VGF turbocharged natural-gas engine with a displacement of 18 liters [138]. Additional engine and operational details were not reported.

Smith [141] employed a frequency doubled flashlamp pumped Nd:YAG laser operating at 532 nm with a pulse width of 10 ns and pulse energies in the range of 30-100 mJ. This laser output produced peak powers in the range of 3-10 MW which ignited a lean,

$\Phi_{F/A}$ = 0.8, mixture of air and propane [141]. This study did not report detailed information regarding the optical pressure barrier or the test engine.

Bihari et al., used a frequency doubled flashlamp pumped Nd:YAG laser operating at 532 nm with a pulse width of 8 ns and a pulse energy of 33.5 mJ [20]. This laser output produced a peak power of 4.1 MW which ignited a lean, $\Phi_{F/A}$ = 0.52, mixture of air and domestic natural gas at a BMEP of 15 bar. A similar laser ignition test was reported by the same authors where the laser energy was coupled to a hollow core optical fiber before being delivered to the engine for ignition. The details of the optical fiber experimentation were not reported, however ignition was obtained at $\Phi_{F/A}$ = 0.6 and a BMEP of 10 bar. The engine used in these studies was a Bombardier BSCRE-04 single cylinder research engine with a displacement of 2.7 L [20].

Regardless of the laser system, an extension of the lean limit of operation was reported [9-12,20,133-136] as well as significant reduction of NOx emissions [11,135] and reduction of ignition delay [10,12,137,141]. Longer burn duration [10,12,141], increased combustion stability [10,12,135], improved performance [10,12, 133,135], and laser spark ignition location insensitivity [13,141] were also reported in the literature.

3.7 Laser System Fundamentals

3.7.1 Introduction

The word laser is an acronym for **L**ight **A**mplification by **S**timulated **E**mission of **R**adiation (LASER). This section will discuss the basic components and operation of laser systems and will lead into the design and operation of high energy lasers capable of producing the peak power required for laser induced breakdown.

3.7.2 Optical Storage

Laser gain materials can take the form of solids, liquids, gases, and plasmas. Laser gain material contains atoms and/or molecules which can be excited to a higher energy state for a short time and produce photonic energy when the higher energy states are stimulated to a lower state. The ability to store optical energy and release via stimulated emission is the fundamental quality of a laser material.

Atomic systems can only exist in discreet states or energy levels [142]. A change, or transition, from one energy level to another involves the absorption or emission of a photon [142]. Bohr's frequency relation defines the transition frequency of the radiation that is absorbed or emitted and is shown in Equation 3.8 [142-144].

$$E_2 - E_1 = h\nu_{21} \tag{3.8}$$

E_2 and E_1 are discreet electronic energy levels, h is Planck's constant, and ν_{21} is the photon frequency. External electromagnetic radiation with an energy of $h\nu_{21}$ can interact with the energy gap (E_2-E_1) of the atomic system [142]. When a photon interacts with an atomic system and is absorbed this induces a transition of the ground state atom to a higher energy or excited state. The atomic system will remain in an excited state for a period of time and then decay to a lower state or to the ground state. The relaxation time of an excited material is defined as the length of time it takes for 63.2% {(1-1/e)} of the originally excited states to naturally decay. Once a number of excited states are produced the excited states will spontaneously decay at a rate defined by Equation 3.9 [142, 145].

$$N_2(t) = N_2(0)\exp\left(\frac{-t}{\tau_{21}}\right), \tag{3.9}$$

where $N_2(0)$ is the initial excited state population density, t is time, and τ_{21} is the relaxation time or time constant between levels E_2 and E_1. When a photon induces a transition from a higher state to a lower state this is termed a stimulated transition and subsequent emission and produces an additional photon with a wavelength equal to the difference in the transition energy levels. The key aspect to stimulated emission is that the original photon is not absorbed and the emitted photon travels in the same direction as the original photon and has the same phase and polarization; this overall process is termed optical amplification [142]. This process illustrates the concept of excited state production (optical storage) and stimulated emission (controlled release) and is shown graphically in Figure 3.11 [145].

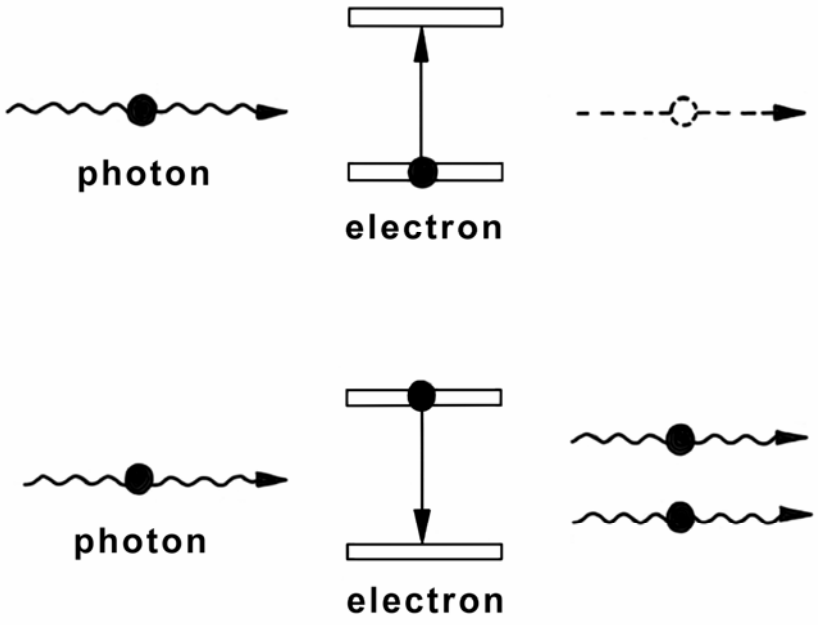

Figure 3.11: Photonic absorption producing excited electonic energy state, photonic interaction producing stimulated emission of secondary photon [145]

The relative density of discrete electronic energy states in thermal equilibrium within a large volume of laser material can be described by the Boltzmann Principle in Equation 3.10 [142-144].

$$\frac{N_2}{N_1} = \exp\left(-\frac{(E_2 - E_1)}{kT}\right) \tag{3.10}$$

Equation 3.10 defines the ratio of excited state densities between two energy levels when the atomic system is in thermal equilibrium [142]. This is illustrated in Figure 3.12 by the dashed line.

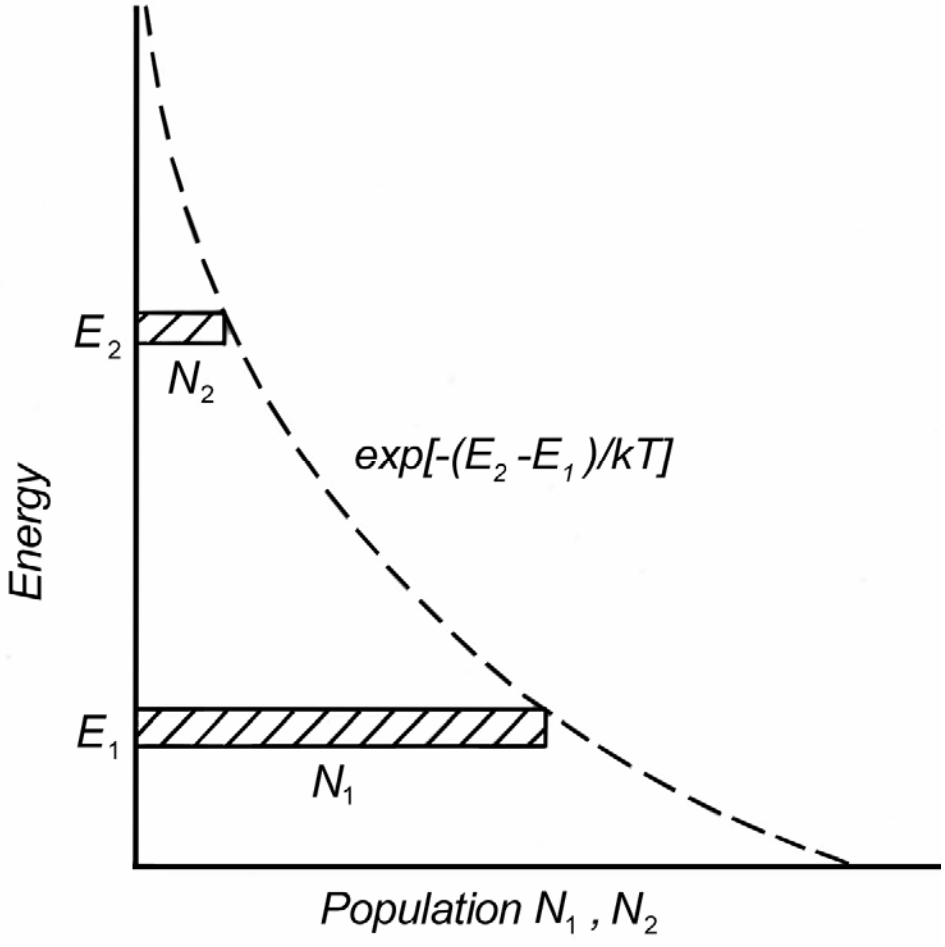

Figure 3.12: Energy level population density distribution for an atomic system in thermal equilibrium [142,145]

For atomic systems with large energy gaps such that E_2-E_1 = $h\nu_{21}$ >> kT, the ratio of energy state densities will be close to zero and virtually all atoms will be in the ground state [142]. This is especially true of the near infrared and visible spectral frequencies where due to the scale of the photon energy virtually all of the atoms will be at the ground state energy level [142].

Thermal equilibrium requires that all lower energy states be more populated than higher energy states [142]. This means that the ratio from Equation 3.10, N_2/N_1, will always be less than one and indicates that optical amplification is not possible while the atomic system is in thermal equilibrium [142]. For a laser material to store optical energy it must be driven out of thermal equilibrium. This is achieved by the application of an external energy source (or pump) that is readily absorbed by the gain media and induces a number of the ground states into one or more of the upper electronic states. The depopulation of the ground states into an overpopulation of one or more of the upper energy states is defined as a population inversion and is shown graphically in Figure 3.13. The creation and maintenance of a population inversion is the optical storage mechanism within the active media of a laser system.

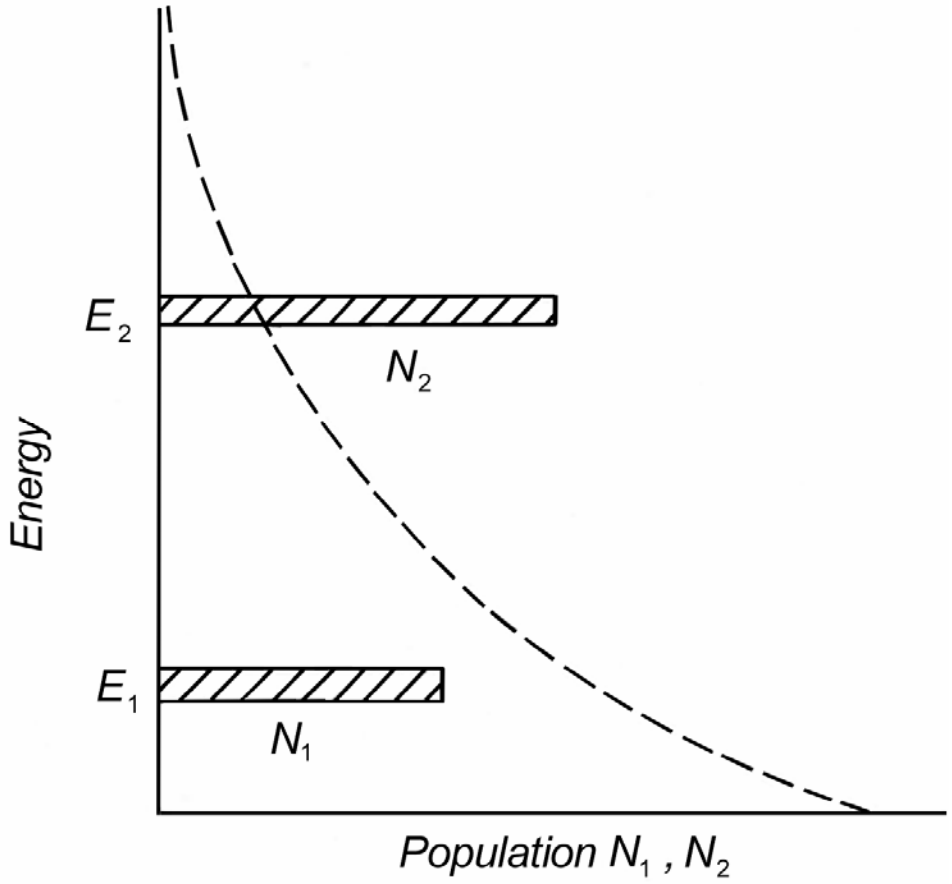

Figure 3.13: Energy level diagram showing a population inversion [142,145]

Depending on the material used and the pumping regime, a population inversion may only be short lived, while with other materials may be able to maintain an inversion indefinitely with continuous pumping [142]. Materials that only support a transient inversion are more suitable for pulsed laser applications [142]. Materials that support continual inversion are more suitable for continuous wave (CW) operation [142].

3.7.3 Four Level Laser Medium

To this point only a simple two energy level atomic system has been discussed, to better understand the energy transfer mechanisms within an actual high energy laser system the discussion must move on to slightly more complicated energy level schemes. The four-

level laser material, such as Nd:YAG is the most practical for storing large amounts of optical energy. A four-level system is composed of a ground level (E_0), a pump band (E_3), a laser level or metastable optical storage level (E_2), and terminal laser level (E_1) all of which are shown in Figure 3.14.

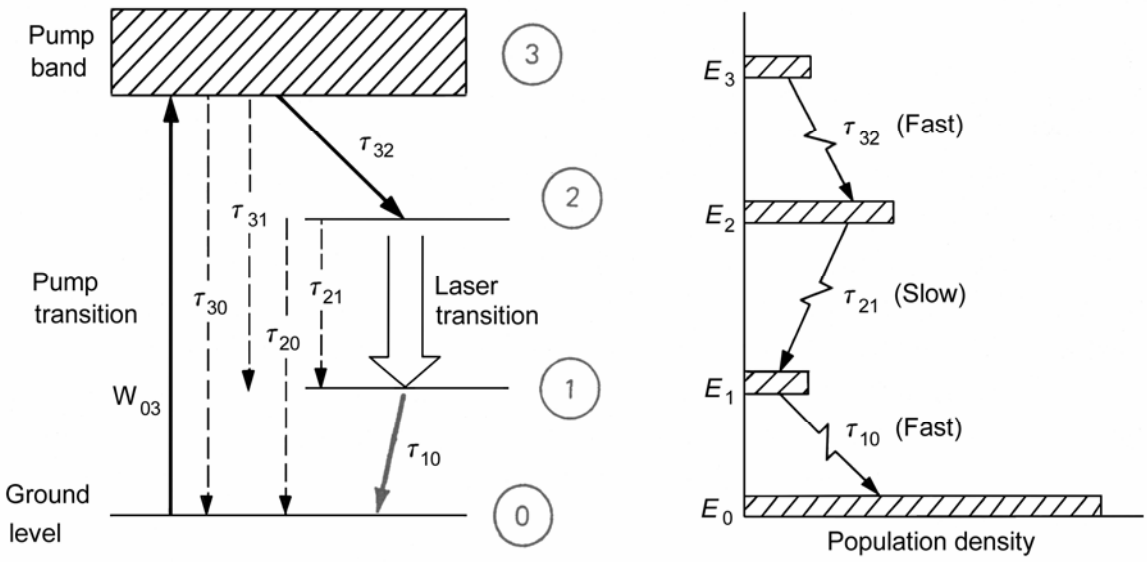

Figure 3.14: Energy level diagrams for a four-level laser atomic system [142]

When pumped the active ions are excited into a wide pump band, E_3, where most of the excited states quickly decay (non-radiative) to the upper laser level, E_2. Due to the relationships of the atomic energy levels the excited states can remain in this metastable energy level for hundreds of microseconds. When the excited states spontaneously decay or are stimulated by external radiation to the terminal laser level, E_1, a photon is emitted whose energy is equal to the energy gap between the initial, E_2, and terminal laser level, E_1. Once the excited state reaches the terminal laser level, E_1, it quickly decays to the ground state, E_0. A four level laser material has a relaxation rate between the ground level and terminal laser levels, τ_{10}, that is fast compared to the upper laser level relaxation rate, τ_{21} [142,145]. The terminal laser level must also be far enough above the ground level so that its thermal

population is small as compared to the ground level [142,145]. This ensures that the relaxation rate τ_{10} will be as fast as physically possible [142, 145]. The population inversion for the working energy levels within a spatially uniform laser material can be described by a pair of coupled differential equations. This can be accomplished with two equations if it is assumed that the relaxation rate from the pump band to the upper laser level (τ_{32}) is very fast, which assumes that the pump band is relatively empty ($N_3 \approx 0$) for any given period of time [142, 145]. The coupled rate equations are shown in Equations 3.11, 3.12, and 3.13 [142-146]:

$$\frac{dN_2}{dt} = W_p N_g - \left(N_2 - \frac{g_2}{g_1} N_1 \right) \sigma \Phi c - \left(\frac{N_2}{\tau_{21}} + \frac{N_2}{\tau_{20}} \right) \tag{3.11}$$

$$\frac{dN_1}{dt} = \left(N_2 - \frac{g_2}{g_1} N_1 \right) \sigma \Phi c + \frac{N_2}{\tau_{21}} - \frac{N_1}{\tau_{10}} \tag{3.12}$$

$$N_{tot} = N_g + N_1 + N_2 , \tag{3.13}$$

where W_p is the pump rate, N_g is the ground state population, N_1, N_2, and N_3 are the respective energy level populations, σ is the stimulated emission cross-section, Φ is the photon density, c is the speed of light in a vacuum, τ_{ij} is the relaxation rate between two energy levels where i indicates the initial energy level and j indicates the terminal energy level, g_1,g_2 are the level degeneracy factors. The right hand terms of Equation 3.11 represent the mechanisms that populate the upper laser level N_2. The first term is the pumping term and is the population mechanism for the upper laser level. The population of pump level N_3 is neglected as zero because the relaxation from the pump band to the upper laser level, τ_{32}, is orders of magnitude faster than the relaxation from the upper laser level to the lower laser

level, τ_{21}. This allows a large number of atoms to remain in the upper laser level for a relatively long period of time as compared to the pump band and lower laser level. For most solid state laser materials the relaxation rate for the upper laser level is on the order of microseconds whereas the relaxation time for the pump band and lower laser level are on the order of picoseconds to nanoseconds [142].

The other two terms of Equation 3.11 represent the stimulated and spontaneous emission processes respectively. The stimulated emission term includes the photon density within the pumped material and the stimulated emission cross section. The stimulated emission cross section represents the relative interaction cross section of an excited state atom. The excited atom has a smaller interaction cross section as compared to a ground state atom. This makes the excited atom less "visible" to the pump and stimulating radiation. This term can be thought of as a probability that the stimulating photons will interact with the excited state atom and induce stimulated emission. The spontaneous term of Equation 3.11 relys on the population of the upper laser level and the relaxation rates between that level and the lower laser level and the ground level. It is clear by this term that all of the spontaneously emitted photons will not have the same energy because they are not all decaying across the same energy gap.

3.7.4 Optical Pumping

Laser pump systems include many different mechanisms for producing excited states for optical amplification. For instance certain types of CO_2 laser uses a low pressure time varying electrical discharge (plasma) to excite the CO_2 molecules into a higher vibrational energy state. Some laser designs use solar energy while some use chemical reactions or even explosions to excite and store optical energy. Crystalline solid state lasers typically use

flashlamps as a pump source to excite electronic states of a particular atomic constituent of the material.

Although flashlamp pumped laser systems exist that are compact and produce the desired output, the flashlamp pumping of a laser system exhibits several distinct disadvantages for cost, efficiency, compactness and/or portability. Flashlamp pumping requires a high voltage drive signal which has to be properly enclosed to avoid arcing to other sensitive equipment or operators. It is also a highly inefficient radiation source, losing most of the energy used to produce the discharge to thermal radiation that does not contribute to the pumping of the laser gain medium [142]. A laser rod has relatively narrow pumping bands that need to be excited in order to produce excited states [142]. A flashlamp discharge typically produces a strong emission at the laser pump wavelength however this energy usually accounts for only a few percent of the overall optical output of the flashlamp [142].

High power laser diode arrays have recently become an efficient and economically viable alternative to flashlamp pumping. They are able to be packaged in relatively small footprints with relatively simple electronics. Laser diode arrays are typically packaged as 1 cm long strips 100 microns thick. The nature of the laser diode and the characteristics of the mounting geometry make the diode arrays very directional devices as compared to flashlamps. The typical divergence of a laser diode is 40° along the fast axis and 10° along the slow axis. Even with the divergence of the output radiation, the large degree of directionality allows the designer to more closely arrange the pump source and the laser medium. Some diode pumping arrangements can induce nearly all of the pump radiation to enter the laser crystal without the use of a reflecting cavity or correcting optics greatly improving the pump energy to gain medium coupling efficiency.

The laser diode pump arrays operate at approximately two volts per array connected in series. The electrical-to-optical efficiency of a laser diode array is between 40-55%. This is in stark comparison to the electrical-to-optical efficiency of the flashlamp which is typically on the order of 3-5% [142]. The final advantageous difference between the laser diode pump arrays and the flashlamp pumps is the pump energy emission band. Figure 3.15 shows the flashlamp discharge spectra for two different current densities along with the laser diode emission.

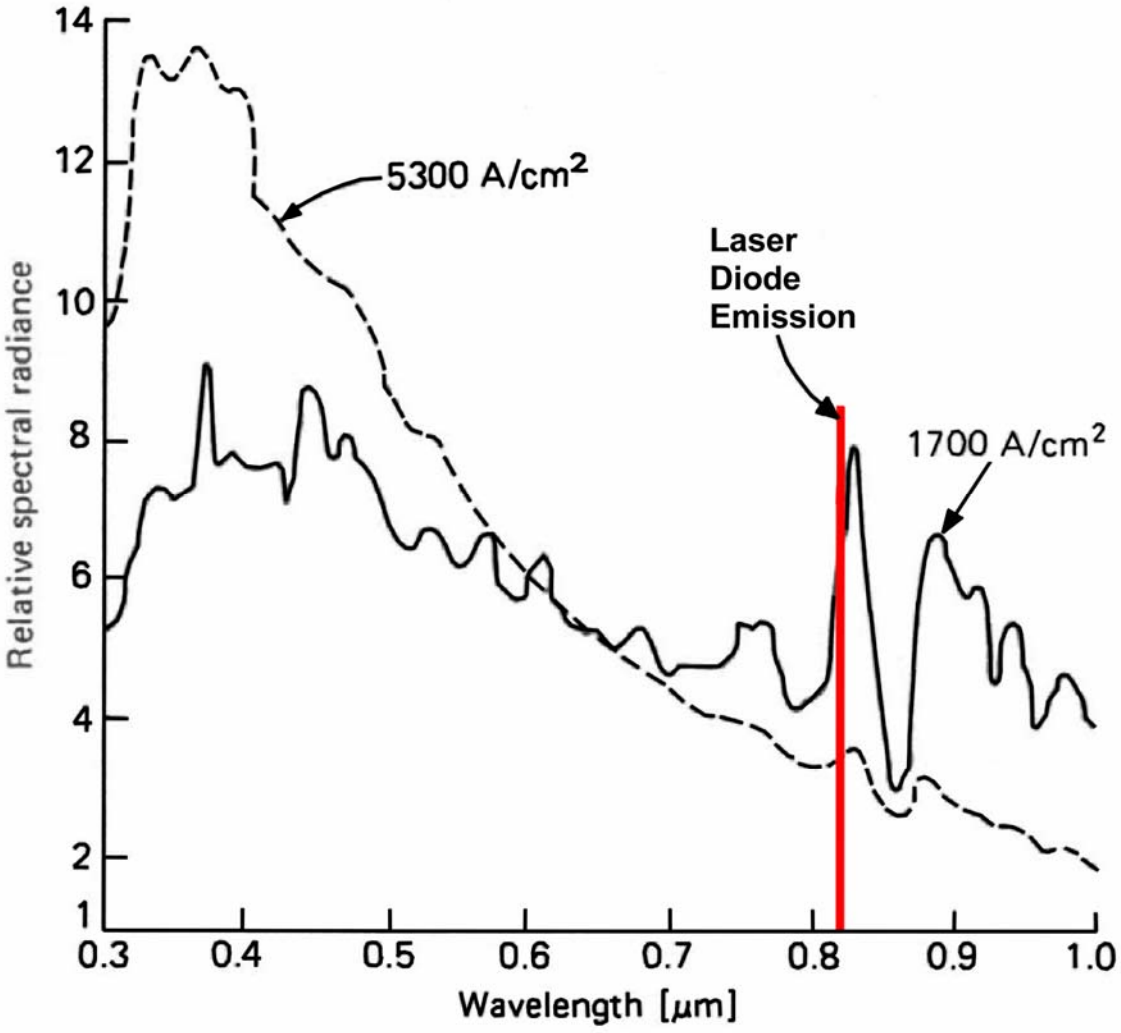

Figure 3.15: Flashlamp and Laser Diode pump emission spectra [142]

The nature of the flashlamp discharge is the emission of radiation in a very wide band from the mid-infrared to ultraviolet. The Nd:YAG laser material has only a few discreet absorption bands that efficiently populate the upper laser level. The balance of the pump energy is wasted by exciting alternate states or simply being delivered as waste heat. In contrast the laser diode arrays emit pump radiation at a discreet energy level or wavelength with a very narrow bandwidth, typically +/- 2 nm FWHM. This allows for a marked increase in the absorption and quantum efficiencies in a laser system per unit pump radiation. This is evident in Figure 3.16 where the Nd:YAG absorption spectra is overlaid with the laser diode emission spectra.

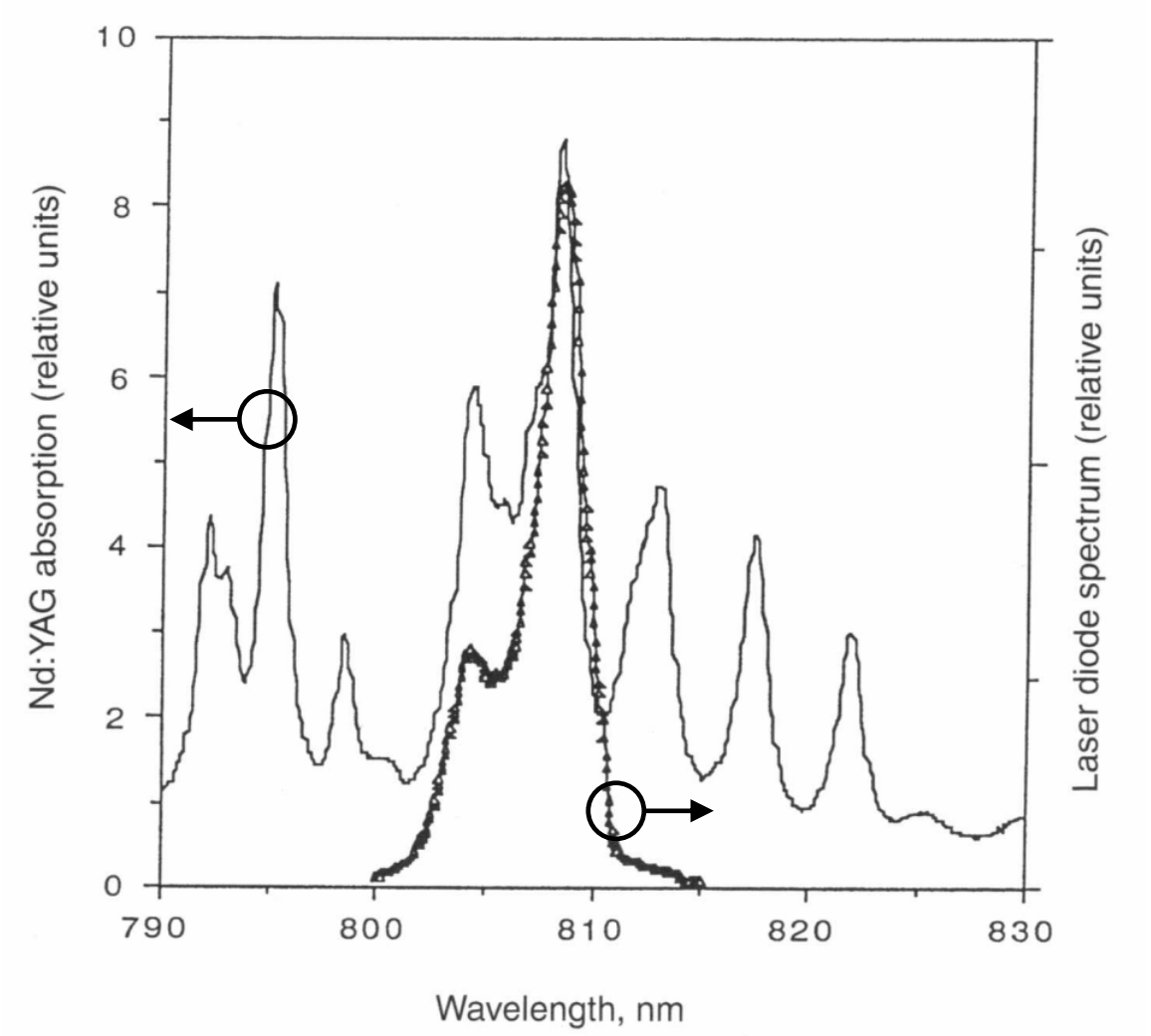

Figure 3.16: Nd:YAG absorption spectra with Laser Diode emission spectra overlay [142]

3.7.5 Continuous Wave Laser Systems

The continuous wave (CW) laser system is the simplest form of laser system consisting of feedback mirrors arranged around an inverted gain medium. This section will explain the basics of CW laser oscillation.

3.7.5.1 Feedback and Amplification

The basic elements of a CW laser system are the gain medium, pump mechanism, high reflection mirror and the partially reflecting mirror. The arrangement of these parts is

illustrated in Figure 3.17 part (a). The pump source acts to excite the active atoms into the upper laser level. Once in the upper laser level the excited states tend to spontaneously decay. When spontaneous decay takes place the released photon is emitted in a random direction. A portion of the spontaneously emitted photons are released that are colinear with the laser optical axis. These photons are reflected between the two mirrors where some are allowed out of the cavity by the output coupler. The photons that are retained within the cavity interact with additional excited atoms and induce stimulated emission. In this process the incoming photon has the same energy as the laser transition and induces the premature decay of the excited state and the consequental release of a photon. The released photon is emitted in the same direction as the stimulating photon and has the same phase and energy level. As groups of photons travel back and forth through the gain medium their numbers grow exponentially as illustrated in Figure 3.17 part (b). The losses in the system are predominantly found at the air/media interfaces. The output coupler and the high reflection mirror provide the largest losses to the intracavity photon density. The interface between the air and the gain medium also provides a substantial loss that can be greatly reduced with the use of antireflection coatings.

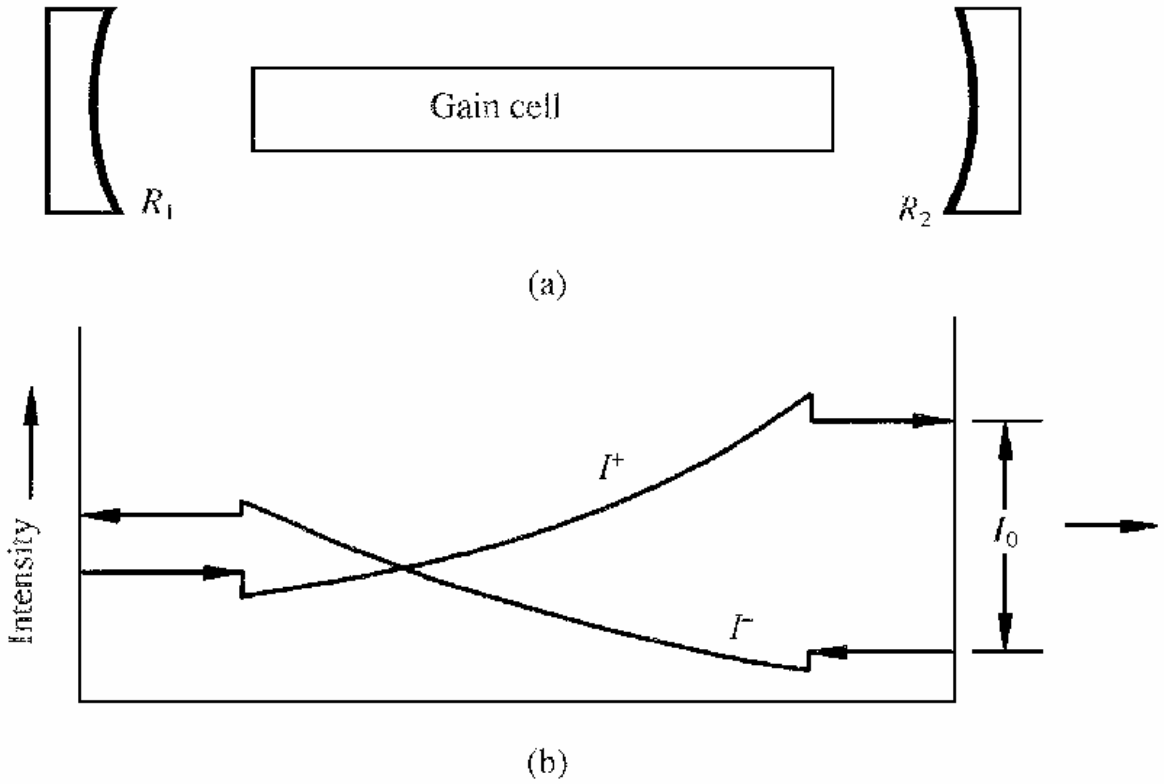

Figure 3.17: CW laser construction and intracavity intensity relationships [146]

The round trip gain of the laser system in Figure 3.17 can be modeled by Equation 3.14 [142].

$$G_{rt} = R_1 R_2 e^{(2gl)} \tag{3.14}$$

R_1 and R_2 are the mirror reflectivities and represent the losses of the resonator, g is the gain coefficient, and l is the length of the inverted laser gain material. If the laser is pumped beyond the threshold condition, where $G_{rt} > 1$, the gain will exceed the losses and radiation of the lasing wavelength will rapidly grow within the cavity. The intensity within the cavity will increase exponentially with each round trip as shown in Figure 3.17. I^- denotes the exponential gain due to stimulated emission by a packet of photons traveling from right to left, I^+ denotes the exponetial gain in the opposite direction. The sharp drops in intensity are

due to losses at the optical interfaces. The laser will produce a spiking behavior as the output rapidly depletes the population inversion to where the output momentarily ceases. The continued pumping will again build the population inversion while the photon density is low. This process is repeated many times at the initial stages of CW laser operation until the damped oscillation reaches a steady state. The oscillations are damped depending on the combination of the pumping of the gain medium and the reflectivity of the output coupler. This behavior is illustrated in Figure 3.18.

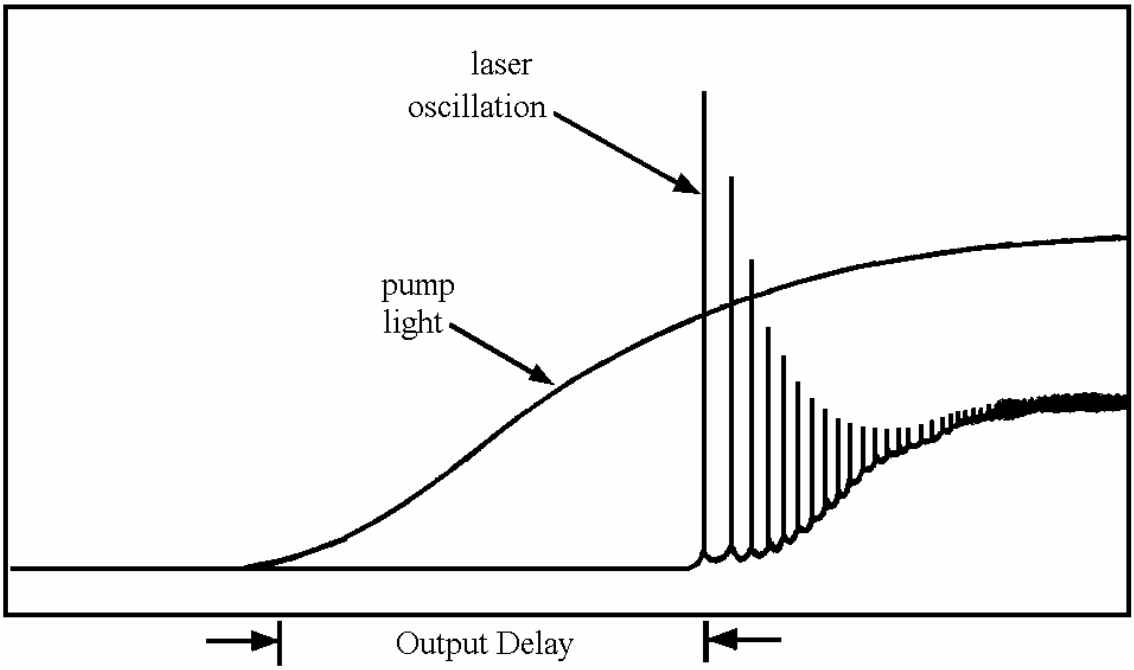

Figure 3.18: Laser spiking at the initial stages of CW operation [145]

3.7.5.2 Continuous Wave Laser Operation and Output

The output of a laser oscillator is governed by a number of different parameters involving both the gain medium and the resonant cavity. Many of the laser parameters are externally measurable such as output power and system efficiency. However, many of the system parameters are not measurable such as internal resonator and optical material losses

which must be estimated. Equation 3.15 combines the gains, losses, material properties and laser geometry to describe the power output of a CW laser system pumped beyond threshold and after spiking has ceased [142]:

$$P_o = A\left(\frac{1-R}{1+R}\right)I_s\left(\frac{2gl}{\delta - \ln R} - 1\right), \tag{3.15}$$

where A is the cross-sectional area of the laser rod, R is the output coupler reflectivity, l is the laser rod length, I_s is a materials parameter for the laser rod, g is the small signal gain coefficient, and δ is the optical resonator losses.

3.7.6 Q-switched Laser Systems

Until this point all discussions of laser operation and output characteristics have concerned contiuous wave or long pulse laser operation. High peak power laser pulses are produced by adding a Q-switch to the laser cavity that allows for the modulation or switching of the energy storage capacity, or Q, of the laser cavity. The cavity Q is defined as the ratio of the energy stored to the energy lost while pumping, as shown in Equation 3.16 [145].

$$Q = \frac{E_{stored}}{E_{loss}} \tag{3.16}$$

If the natural onset of lasing is stopped by blocking one of the cavity mirrors with a Q-switch the energy storage capability can be greatly increased. The stored energy within the laser cavity changes substantially throughout the pumping process due to spontaneous emission, stimulated emission and gain material saturation. When the Q-switch is in the opaque mode it prevents the onset of lasing and acts to bolster the population inversion within the gain medium. The inversion then grows to a much higher level than would be achievable in a CW

laser system. The optical energy stored by the excited states greatly increases the gain of the active media. When the Q-switch is switched to the high transmission mode the high gain of the laser media begins lasing and quickly depletes the excited states which induces a rapid increase in the intracavity photon flux. The high transmission mode of the Q-switch acts to lower the Q of the cavity by several orders of magnitude. The large photon flux causes the laser system to dump a large portion of the stored energy thereby creating a high energy output pulse. The peak power of the high energy pulse is typically several orders of magnitude larger than that of the CW output of the same laser system. Comparisons of the development of both a Q-switched pulse and continuous wave output from a laser system can be seen in Figure 3.19.

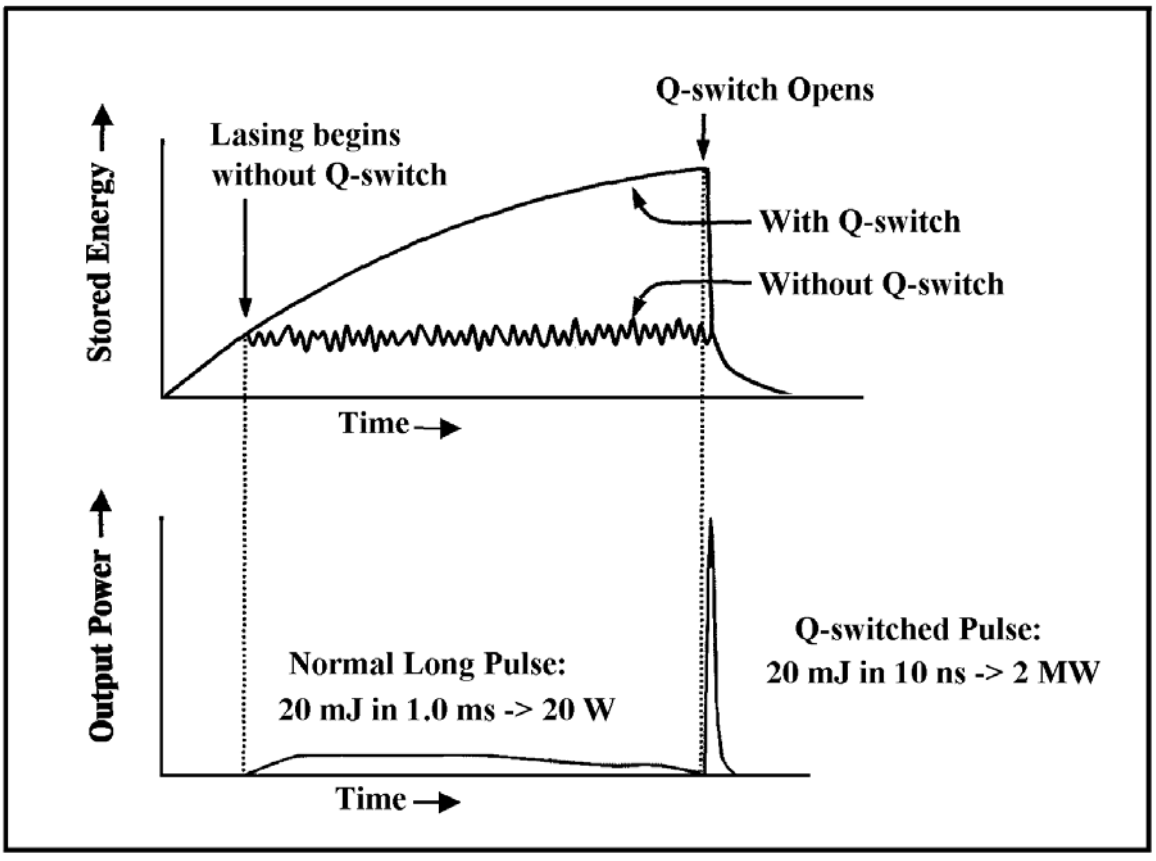

Figure 3.19: Continuous wave and Q-switched pulse development [147]

The upper part of Figure 3.19 illustrates the energy stored within the laser system as a function of time. It can be seen that the Q-switched laser continues to store energy beyond what would typically be possible with a CW laser system. The lower portion of Figure 3.19 shows the output power of the respective laser systems as a function of time. In this example both laser systems deliver 20 mJ of energy. The difference arises in the time period over which the energy is delivered.

As illustrated in Figure 3.19 this mode of operation can produce the peak power that is required for spark breakdown. For the long laser pulse example if a 20 mJ pulse is delivered over 1.0 ms, the peak power of the pulse is 20 W. With a Q-switched pulse the same 20 mJ pulse with a 10 ns width produces peak power of 2 MW. If this same output had an M^2 (beam quality factor) of 5.5 and was focused through a 10 mm plano convex lens the approximate focal intensity would be 412 GW/cm^2. A focused laser pulse of this magnitude would easily induce spark breakdown in air at atmospheric pressure.

The diffraction limited focal spot diameter of a Gaussian laser beam can be expressed as [148]:

$$d_o = \frac{4\lambda f_L}{\pi D}, \tag{3.17}$$

where f_L is the focal length of the focusing lens, D is the diameter of the laser beam at the input to the lens, and λ is the operating wavelength. This value represents the absolute physically smallest spot diameter that can be produced with a given lens at a given wavelength for a given beam diameter. The M^2 factor relates the diffraction limited beam diameter to the actual beam diameter that is produced by focusing an imperfect laser beam through an imperfect lens. The closer the M^2 value is to one, the better the beam quality and

the smaller the spot size. The smaller the focal spot size the higher the intensity and the easier it is to produce a spark. M^2 can be expressed as [148]

$$D_m = M^2 d_o \tag{3.18}$$

Where d_o is the diffraction limited spot diameter and D_m is the real spot diameter. The real spot diameter can be used for calculation of the focal intensity with units of power per area. The relationship between the focusing of a real laser beam and a diffraction limited laser beam is shown in Figure 3.20.

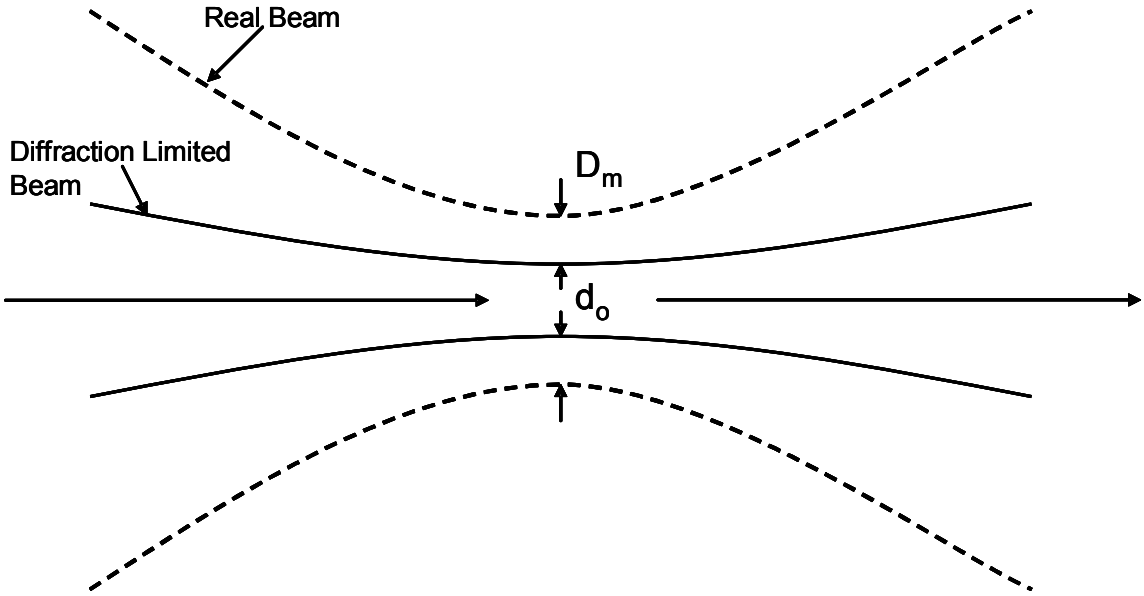

Figure 3.20: Comparison of the focused beam waist sizes of a real laser beam and a diffraction limited laser beam

3.7.6.1 Passive Q-switching

There are two types of Q-switches, active and passive. Active Q-switching involves the addition of an externally timed and controlled variable transmission device to the laser cavity. Passive Q-switching involves the addition of a material whose transmission is dictated by the intracavity photon density in the laser cavity. In other words, the switching is

an open loop feedback system that relies on the interdependencies of the input pump power and the cavity optical parameters, such as the output coupler reflectivity, Q-switch initial transmission, and cavity optical losses. The experimental work described in this dissertation will deal only with a passive Q-switch.

A passive Q-switch, or saturable absorber, is a material whose transmission characteristics can be varied as a function of the photon flux density of a particular wavelength. The variation of the transmission properties of a saturable absorber is a process very similar to excited state production and retention within a laser gain medium. A specific wavelength of radiation induces an excited state, the excited state is retained for a long period of time as compared to the other physical processes within the laser sytem. The difference between the laser media and saturable absorber process arises with the particular use of the material. Both the saturable absorber and the laser medium behave the same way as far as the storage of excited states while having a reduced interaction cross section of the excited atom. In fact some of the more effective saturable absorber Q-switches were first used as laser materials. A key difference between the two is that the effective laser material typically has an excited state decay time that is at least an order of magnitude longer than that of an effective saturable absorber. A desirable property of the two cyrstals is the overlap of suitable emission and absorbtion bands between the laser material and the saturable absorber respectively. For example Nd:YAG can be used as a laser material in conjunction with Cr:YAG as a saturable absorber. The Nd:YAG excited state lifetime is approximately 230 microseconds, whereas the Cr:YAG excited state lifetime is approximately 4.1 microseconds. Nd:YAG is commonly pumped at 808 nm and produces output at 1064 nm, Cr:YAG has a wide absorption (pump) band centered around 1050 nm and the emission occurs at 1300 nm.

This is a good example where laser diodes can be used to pump a laser material and the laser output can be used to bleach a saturable absorber for it to act as a Q-switch.

Solid state saturable absorbers have become increasingly popular due to the fact that they do not degrade over time with use, have a very high damage threshold and have very good thermal and structural properties provided by crystalline substrates. The saturation of a passive Q-switch is dependent on the amount of energy incident upon the crystal per unit area. This relationship is demonstrated by Equation 3.19 [142]:

$$E_s = \frac{h\nu}{\sigma_{gs}}, \tag{3.19}$$

where E_s is the saturation energy, $h\nu$ is the energy of the pumping radiation, σ_{gs} is the ground state cross section of the active ions within the solid state absorber. Equation 3.19 is the energy incident upon the approximate cross sectional area of a ground state active atom needed to excite the atom into an elevated energy state. Figure 3.21 illustrates a typical transmission characteristics of a saturable absorber material as the incident energy approaches and surpasses the saturation energy.

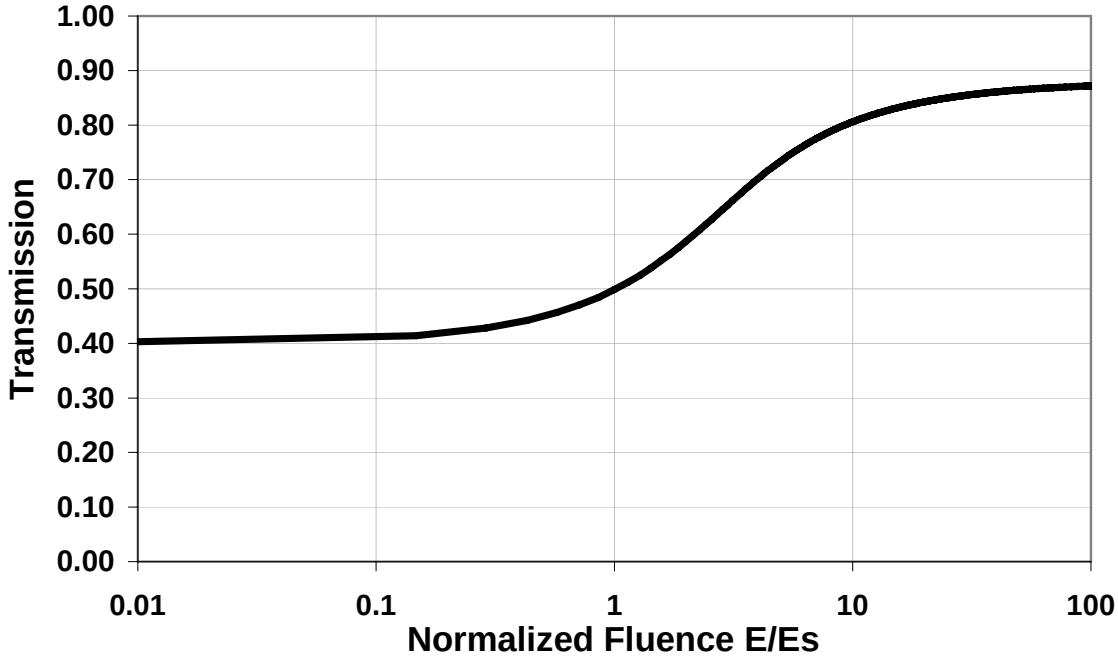

Figure 3.21: Passive Q-switch transmission as a function of the normalized incident energy density

The saturation energy appears as unity on the normalized scale and is the energy density at which the transmission of the Q-switch begins so saturate significantly as a consequence of the incident energy. In Figure 3.20 the initial transmission of the passive Q-switch is 40% and the final transmission approaches 90%. The transmission characteristics of a passive Q-switch (PQSW), that is, the initial and final transmission values can be accurately modeled by Equations 3.20 and 3.21 [142]:

$$T_o = e^{-N_{gs}\sigma_{gs}l_s} \tag{3.20}$$

$$T_{\max} = e^{-N_{gs}\sigma_{es}l_s}, \tag{3.21}$$

where T_o and T_{max} are the initial and final transmissions of the SA respectively, l_s is the path length through the SA, N_{gs} is the ground state population density of the absorbing atoms in

the SA, and σ_{gs} and σ_{es} are the ground state and excited state cross sections of the absorbing atoms. The initial transmission dictates the amount of light that is allowed to pass through the SA during the very early stages of laser action. The higher the initial transmission the quicker the absorber saturates and the lower the overall optical energy storage that is attainable in the laser crystal. The maximum transmission of the PQSW is dictated by the excited state cross section, the ground state population density and the length of the crystal and is limited by the excited state absorption (ESA) in the Q-switch crystal. Therefore the actual transmission of the SA will approach the maximum transmission asymptotically and will never reach 100% transmission due to the loss mechanism imposed by the excited state absorption. The basic operation of a SA as well as the ESA losses can be more easily understood by an examination of an energy diagram. Figure 3.22 depicts the energy level diagram of a Cr:YAG saturable absorber.

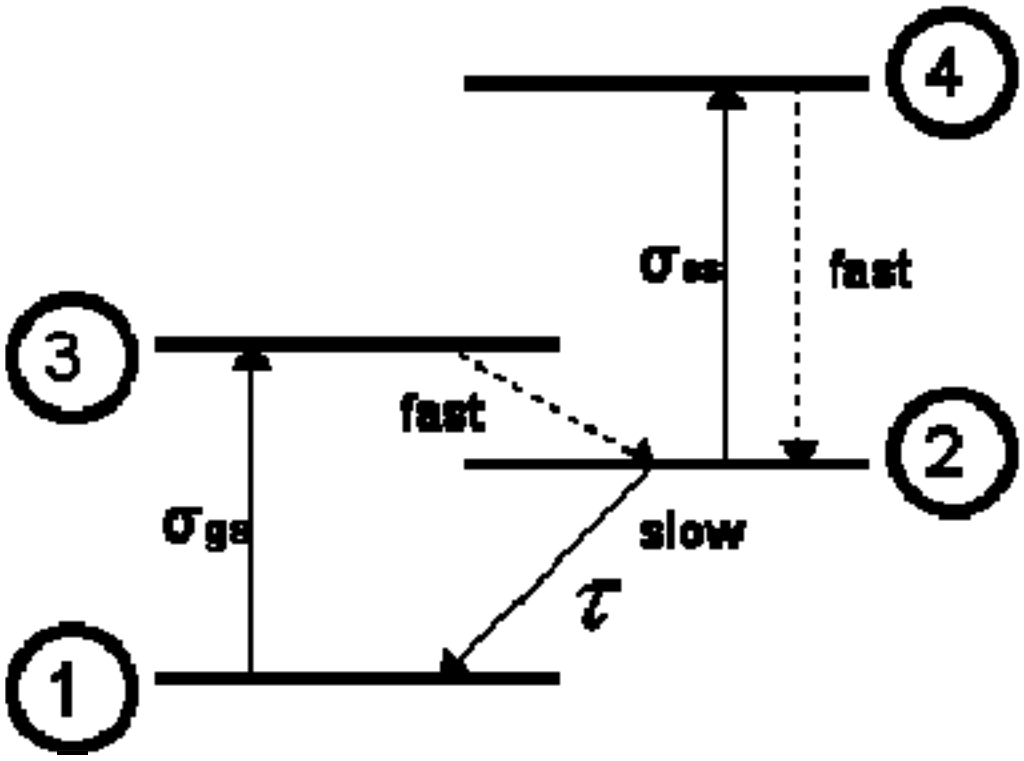

Figure 3.22: Saturable absorber (Cr:YAG) energy level diagram [142]

The operation of the crystal as a saturable absorber primarily concerns itself with the transitions from energy levels 1 to 3 to 2 and back to level 1. When a Cr atom in the SA interacts with a photon that has an energy level corresponding to emission at 1064 nm an electron in the outer shell of the Cr atom is induced into an excited state and this process is represented by the transition from 1 to 3. Energy level 3 is not a stable energy level (short lifetime) for this atom and the electron quickly decays to a lower energy state (2), which is more stable (longer lifetime). With an electron excited to energy level 2 the atom of Cr has a much smaller interaction cross section and is nearly invisible to further incoming radiation at 1064 nm. Energy level 2 with its long lifetime, ~4.1 μs [142], provides an optical storage mechanism for the system and allows the SA to maintain a large amount of bleached atoms for a long period of time as compared to the laser output pulse.

The ESA takes place when an excited Cr atom with an electron at energy level 2 interacts with a second pump photon, at 1064 nm, and is induced to energy level 4. The difference in this process is that this secondary absorption does not contribute to any optical storage of the excited state. This process reduces the number of useful photons that would normally be used for exciting ground state Cr atoms into level 2. Prior research has found that the excited state absorption level 4 lifetime is approximately 0.55 ns [142], which is much shorter than the output pulse width and thus is not a suitable storage mechanism for the excited states. Therefore this process is considered a loss. The ability of the chromium ion to store excited states and provide higher transmission for a time period longer than the output pulse width makes Cr:YAG a desirable choice for a solid state crystalline passive Q-switch.

3.7.6.2 Passively Q-switched Laser Operation and Output

The intracavity optical and electronic processes within a passively Q-switched solid state laser can be modeled by a set of coupled nonlinear differential equations. Equations 3.22-3.24 describe the cavity photon density (Φ) [149-152], the laser media excited state density (N_e) [150], and passive Q-switch ground state population density (N_{gs}) [150]. Equation 3.25 acts as a continuity equation for the totals states density (N_{so}) within the passive Q-switch.

$$\frac{d\phi}{dt} = \frac{\phi}{t_r}\left(2\sigma N_e l - 2\sigma_{gs} N_{gs} l_s - 2\sigma_{es} N_{es} l_s - \ln\left(\frac{1}{R}\right) - L\right) \tag{3.22}$$

$$\frac{dN_e}{dt} = -\gamma\sigma c\phi N_e - \frac{N_e}{\tau} + W_p \tag{3.23}$$

$$\frac{dN_{gs}}{dt} = -\sigma_{gs} c\phi N_{gs} + \frac{N_{so} - N_{gs}}{\tau_s} \tag{3.24}$$

$$N_g + N_{es} = N_{so} \tag{3.25}$$

Here, t_r is the cavity round trip time, σ is the laser material excited state cross section, l is the length of the gain material, σ_{gs} is the saturable absorber ground state cross section, l_s is the saturable absorber transmission path length, σ_{es} is the saturable absorber excited state cross section, R is the output coupler reflectivity, L represents the bulk optical losses, τ is the laser material excited state lifetime, W_p is the excited state production rate or pump rate, c is the speed of light in a vacuum, τ_s is the saturable absorber excited state lifetime.

Equation 3.22 models the cavity photon density as a function of time and consists of a series of gains and losses that contriubute to the overall photon density. The first term of

Equation 3.22 models the contribution of photons from the stimulated emission process within the laser material. The next two terms model losses associated with the production of excited states within the saturable absorber and ESA within the absorber respectively. The final two loss terms in Equation 3.22 concern the output coupler loss and the bulk optical losses within the cavity.

Equation 3.23 models the excited state popluation density within the laser material with respect to time and contains two loss and one gain term. The loss terms describe reductions in the excited state density due to both stimulated and spontaneous emission respectively. The gain term is the excited state production rate or pump rate. Equation 3.24 models the saturable absorber ground state population density and consists of a gain and a loss term. The loss term concerns the excited state population production within the absorber material. The gain term concerns the repopulation of the ground state due to spontaneous decay within the absorber excited states. The behavior of the photon density, excited state population density, and the saturable absorber ground state population density for a passive Q-switching event is shown in Figure 3.23.

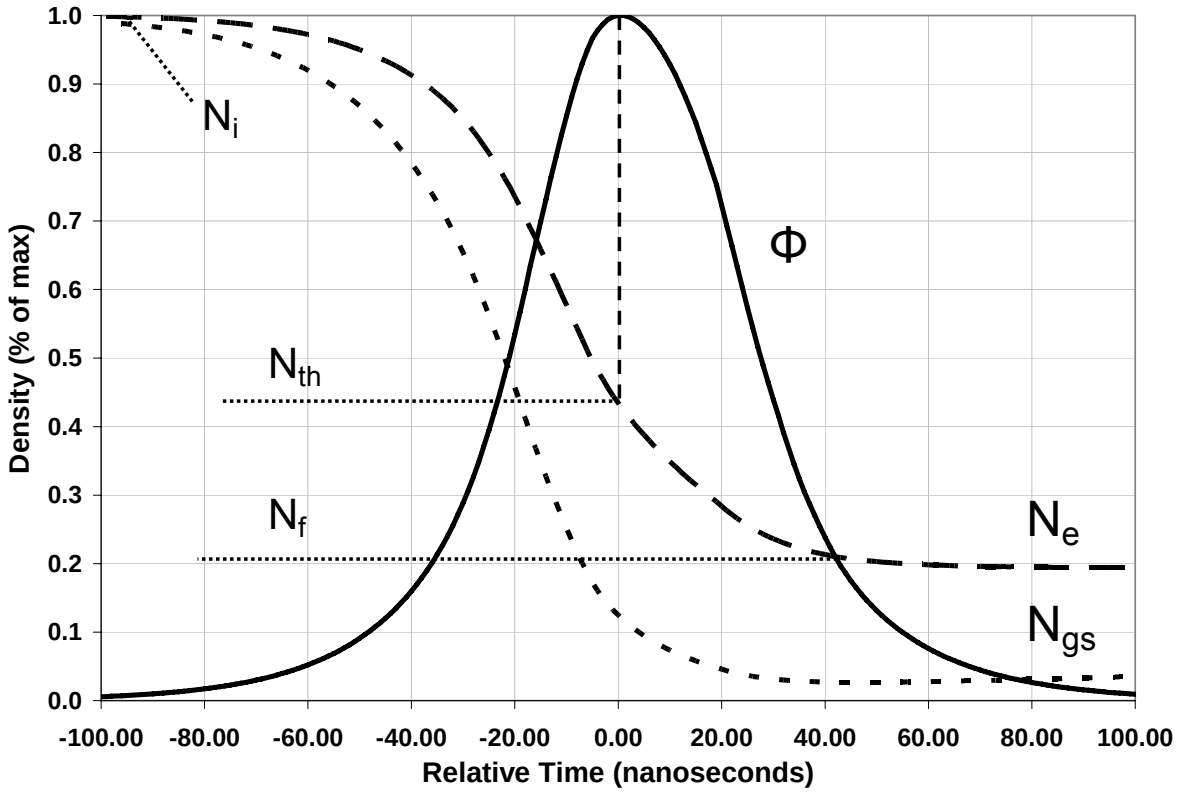

Figure 3.23: Time dependent behavior of the photon density (Φ), laser material excited state density (N_e), and the saturable absorber ground state density (N_{gs}) for passive Q-switching

Figure 3.23 begins with the initial conditions for N_e, N_{gs}, and Φ, which are $N_e=N_i=100\%$, $N_{gs}=100\%$, and $\Phi=0\%$. N has just reached a maximum where spontaneous emission and small scale lasing has limited any further growth for a given pump rate and with a given combination of optical parameters. At this point excited state production within the saturable absorber causes N_{gs} to drop indicating a signficant increase in the saturable absorber transmission. The laser excited state density and the SA ground state density both fall rapidly causing an avalanche type increase in the photon density. The growth of Φ further depletes both N_e and N_{gs}. This depletion takes place on a time scale that is orders of magnitude shorter than the pumping process so new excited state production can be ignored during the switching process. The time scale used in Figure 3.23 is relative and is only used

for demonstration purposes. In general the entire switching process takes place in less than 50 ns.

Equations 3.26-3.28 approximate the output pulse energy, output peak power, and output pulse width with respect to the excited state population densities, laser optical parameters, laser geometry, and photon energy. Equation 3.26 approximates the output pulse energy of a Q-switched laser by using the initial to final excited state population density ratio, along with other optical and geometric parameters [149-152]. Equation 3.27 approximates the output pulse peak power using the initial, threshold, and final excited state density values [150]. Equation 3.28 simply divides the output pulse energy by the output peak power to obtain a measure of the output pulse width [150,152].

$$E_o = \frac{h\nu A}{2\sigma\gamma}\ln\left(\frac{1}{R}\right)\ln\left(\frac{N_i}{N_f}\right) \tag{3.26}$$

$$P = \frac{h\nu Al}{\gamma t_r}\ln\left(\frac{1}{R}\right)\left[N_i - N_{th} - N_{th}\ln\left(\frac{N_i}{N_{th}}\right)\right] \tag{3.27}$$

$$t_p \approx \frac{E_o}{P} \tag{3.28}$$

3.8 Diode Pumped Solid State Passively Q-Switched Laser Prior Research

Diode pumping of solid state laser materials was first introduced in the early 1970's [153-155]. This technology was abandoned due to high costs and low output efficiency obtainable at that time. Great improvements in laser diode technology as well as a reduction in cost have allowed researchers to develop compact highly efficient diode pumped laser packages. These research efforts coupled with the development of new solid state passive Q-

switch materials have allowed for the development of highly efficient, rugged, all solid state laser systems.

Recent studies have shown dramatic improvements in the overall output and operation characteristics of DPSS PQSW lasers. Table 3.1 lists the optical parameters and optical output characteristics of recent published research efforts utilizing diode pumping of Nd:YAG as an active media and Cr:YAG as a passive Q-switch.

Table 3.1: DPSS PQSW laser parameters reported in the literature

	OC (%)	To (%)	Pump Power (W)	Eo (mJ)	tp (ns)	Rep. Rate (Hz)	Peak Power (W)	References
1	30	57	300	5.0000	10.00	-	500000	[156]
2	88	82	10	0.2200	30.00	15000	7333	[157]
3	90	89	25	0.1750	48.00	24000	3646	[158]
4	64	71	7	0.0296	3.70	-	8000	[159]
5	85	82	10	0.2000	17.00	-	11765	[157]
6	60	55	100	1.5000	3.90	-	384615	[160]
7	80	90	15	0.1140	19.00	-	6000	[161]
8	65	60	60	0.6500	2.60	120	250000	[162]
9	70	80	15	0.2100	10.00	-	21000	[161]
10	85	83	15	0.1000	36.00	-	2778	[161]
11	85	86	15	0.1670	21.00	-	7952	[161]
12	80	74	1	0.0032	0.40	2000	8000	[162]
13	90	80	26	0.3260	25.50	9200	12784	[158]
14	26	26	15	0.2500	0.38	5500	565000	[164]

The output parameters of the above systems presented in the literature are plotted as a function of the optical component parameters and can be found in Figure 3.24. This plot was developed in an attempt to understand what parametric trends might aid in the development of a DPSS PQSW laser that could produce the output needed to be used as a laser spark plug.

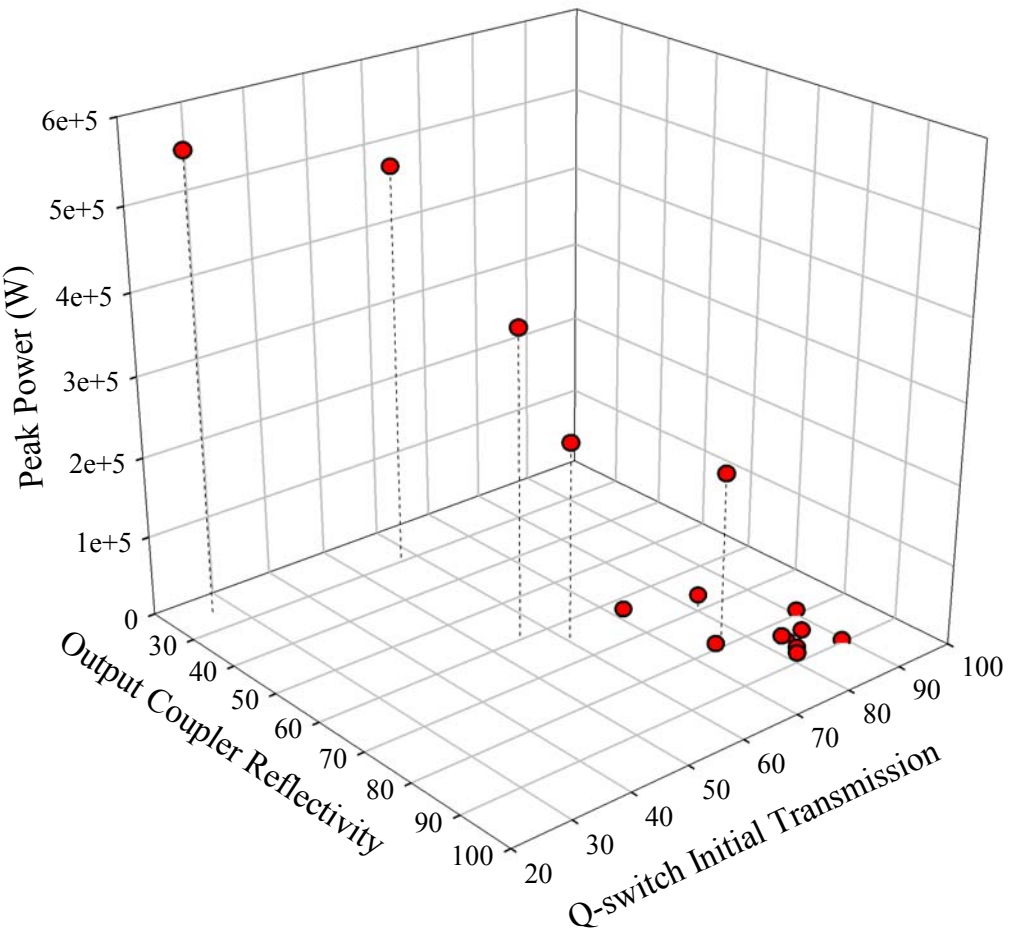

Figure 3.24: Output peak power of reported literature as a function of the output coupler reflectivity and Q-switch initial transmission

It can be seen from Figure 3.24 that as the output coupler reflectivity and the Q-switch initial tranmission are lowered that the output peak power tends to increase. Figure 3.25 shows the output pulse energy of the literature data as a function of the reported input power. The pattern of the data suggests that the output of such a laser system may be strongly dependent on the input power. Therefore input power levels exceeding 300 Watts should be examined if the desired output pulse energy is to exceed 5 mJ.

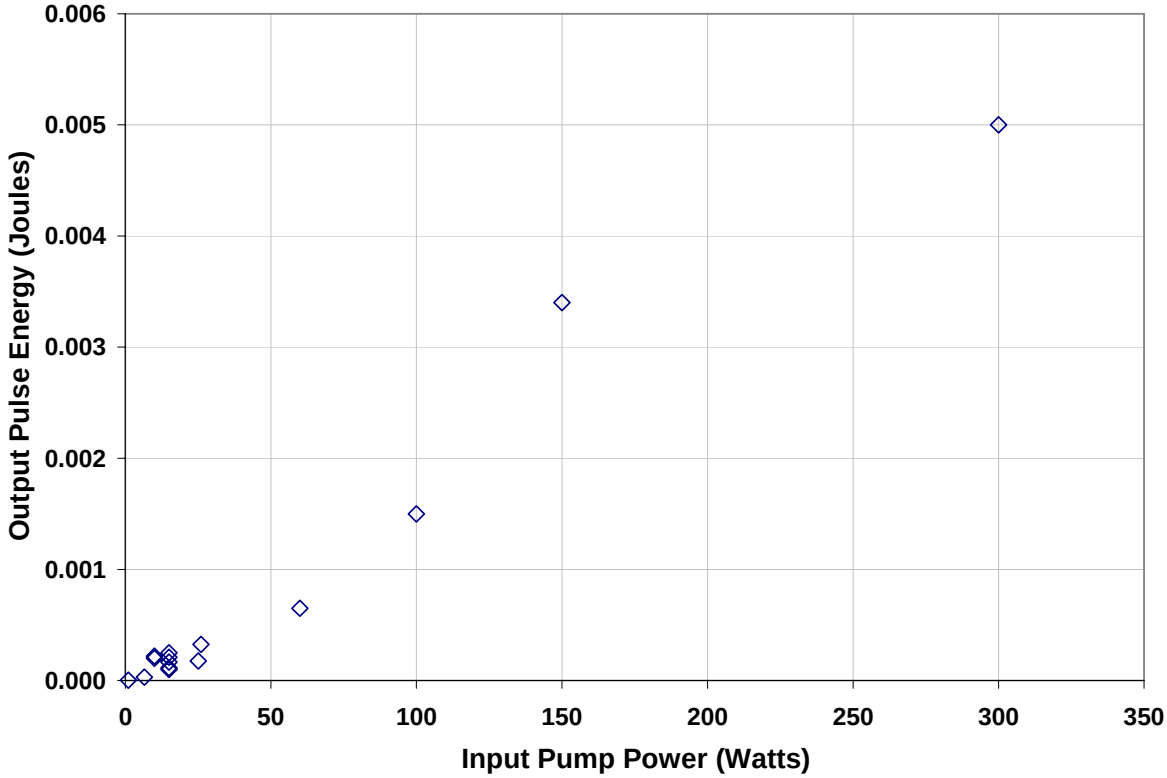

Figure 3.25: Output pulse energy from the literature as a function of input power

Figure 3.26 shows the output peak power of the literature data as a function of the reported input power. The pattern of the data suggests that the input power has very little effect on the output peak power. The optical parameters and laser geometry are likely to have a more significant effect on the output peak power. To some Figure 3.26 may seem to show a system that produces more power than what is added but, this is not the case. Power is defined as energy per unit time, and in this case the difference in time scales plays a role in the apparent output. The input power consists of energy delivered over hundreds of microseconds whereas the output power consists of energy released over a period of nanoseconds. In this and all other cases where output power data is displayed as a function of input power, the amount of energy input far exceeds the amount of output energy.

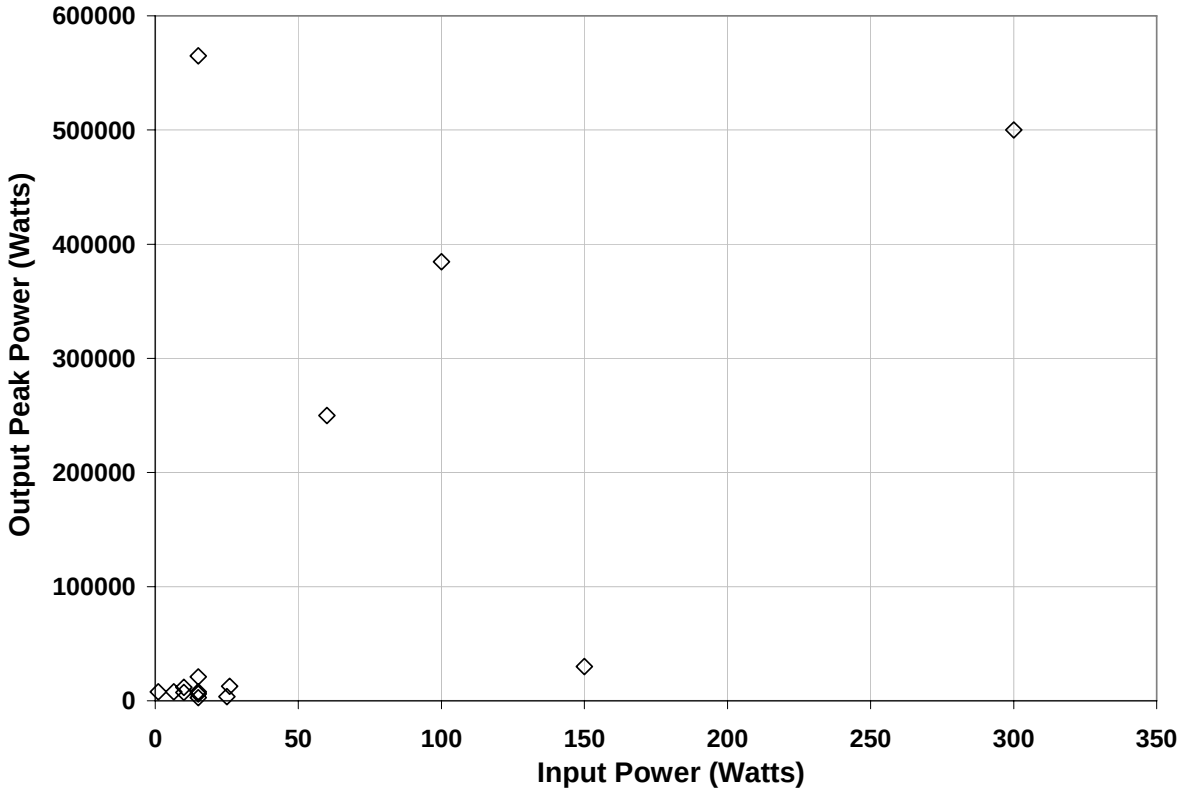

Figure 3.26: Output peak power from the literature as a function of input power

4 Experimental Setup and Procedure

The primary objective of this work was to develop design parameters and guidelines for a compact laser system that could be coupled to a natural gas fueled engine to act as the ignition source. Preliminary experimentation was performed to answer questions about the finer points of the laser design as well as the broader aspects of the operational characteristics. A discussion is presented regarding the selection of a number of the laser components and their characteristics, such as the selection of the active media material and geometry, Q-switch material, basic resonant cavity geometry and pumping arrangement. A portion of this chapter is devoted to describing the outcomes of the preliminary experiments which were designed to answer specific questions about the design and operation of the laser system. The preliminary experimentation was used in conjunction with a mathematical model to produce data that would allow for the design of an efficient experimental procedure that could reveal the most information about the system with minimal data sets. The optical experimental design and data collection techniques are outlined and discussed. Engine testing procedures and techniques are outlined and discussed in the final section of this chapter.

4.1 Laser Arrangement and Component Selection

The Nd:YAG active media was chosen primarily due to its cost and availability. The maturity of this active material in the literature and in industry was the key to its selection. It is well known that the YAG host material has superior mechanical and thermal properties as compared to other popular host materials, e.g. glass, yttrium orthovanadate, and yttrium fluoride. High quality Nd:YAG is also widely produced at low cost due to its academic and industrial maturity. Nd was chosen as the active ion because of its excellent suitability as an

optical amplifying medium as compared to other trivalent rare earth ions typically used in laser applications. Nd has strong absorption bands in the near infrared. High power laser diodes are readily manufactured in quantity specifically for pumping these strong absorption bands. It has been incorporated into over 100 different host materials and has obtained higher power levels than any other four level material [142].

Nd:YAG produces a strong fluorescence emission at 1064 nm when pumped at 808 nm. This emission at 1064 nm is captured and amplified by the resonant cavity in conjunction with the passive Q-switch. As discussed in Chapter 3 the shorter the wavelength the higher the photon energy. Laser systems are currently in production that produce output with significantly shorter wavelengths which accordingly require far less laser output to induce a gaseous medium spark. Unfortunately these laser systems are not suitable for diode pumping or passive Q-switching and are typically designed and built with newer less-well-known and expensive technologies. The 1064 nm output from Nd:YAG can be frequency doubled or tripled. This is attractive due to the higher photon energies for ignition purposes. However frequency multiplying requires precision alignment of optically pure non-linear crystals. For example when frequency doubling 1064 nm using a Potassium Titanyl Phosphate (KTP) crystal, two photons at 1064 nm are required to produce one photon at 532 nm. This process is generally 20-50% efficient thereby requiring many additional 1064 nm photons to produce the same output at 532 nm. The doubling process also requires high quality high intensity laser output in order to efficienly (~50%) produce the higher energy photons. This generally entails the reduction of the 1064 nm beam waist within a KTP crystal, and this can damage or destroy a crystal if it has any defects or if the 1064 nm output beam is not uniform.

A cylindrical geometry was examined for the active media for several reasons. The primary reason was the excellent suitability of the rod for diode array side pumping within a linear cavity. Many of the other active media geometries, such as slab or disk lasers, do not easily lend themselves to efficient side pumping or integrate easily into a linear cavity. The rod geometry is readily available from many manufacturers with a wide variety of lengths and radii at a low cost as compared to other geometric configurations. The length of the laser rod was designed to accommodate two 1 cm diode arrays lengthwise as well as to provide mechanical support for the rod within the pump chamber chassis.

The linear laser cavity was examined for two reasons: ease of assembly (fabrication), and ease of alignment and use. This resonator configuration type was weighed against bent cavities, multiple reflection cavities, and ring oscillator cavities and was found to be the most appropriate for this application. This resonator type has the simplest construction, fewest parts and the simplest alignment procedure.

The cavity length used for this study was examined for several reasons. The length of the cavity was chosen primarily for convenience of manufacture, component installation and relative size as compared to a common natural gas engine spark plug. Another reason for the overall size of the resonator cavity has to do with the output pulse width as a function of cavity length. The output pulsewidth is primarily dictated by the overall depletion of the excited state population density over the lifetime of the output pulse. The output pulse width is also dependent on the resonator decay time. The decay time is proportional to the length of the cavity divided by the speed of light corrected for optical and resonator losses. Therefore the shorter the cavity the shorter the decay time and the shorter the pulse width. A shorter cavity would have been beneficial, producing shorter pulses thereby creating higher

peak power levels. The current cavity was designed to produce approximately 10-15 ns pulses. In practice the cavity produced 7-12 ns output pulses depending on the pump rate, alignment, and the optical component combinations.

The side pumped geometry was used because laser diode arrays were used as the pumping mechanism. The array geometry is conducive to efficient side pumping of a laser rod because they can be arranged in close proximity to the laser rod thereby coupling a majority of the diode output into the active media. The side pumped geometry was the most immediate solution to diode pumping a laser rod with 300-1000 Watts. Diode end pumped laser systems produce superior output beam quality and laser performance in general. However, the end pumped systems have major disadvantages that stem from the difficulty in coupling the light from multiple high power diode arrays into a fiber optic for efficient delivery. Previously, manufacturers were only capable of delivering approximately 30 Watts of pump power through an optical fiber. Recent technical advancements have allowed for the delivery of up to one kilowatt of diode array energy through an optical fiber. The hurdle involves the transformation of the periodic linear emission, from multiple diode arrays, into a geometrically coherent light beam that can be efficiently coupled to an optical fiber and subsequently coupled into the laser system. The fiber coupled pump system required to end pump a laser system of this scale would need to deliver between 300 and 1000 Watts and would cost in excess of $140 per Watt. In comparison the diode modules required to side pump the same system would have the same output and cost approximately $8 per Watt.

End pumping creates a symmetric and uniform pump distribution that perfectly overlaps the active resonator volume within the active media. Side pumping produces a non-uniform pump distribution concentrated at the edges of the absorbing gain media. This non-

uniform pump distribution can produce highly variable non-symmetric spatial and temporal output mode features. This type of operation is undesirable because it makes focusing the energy to a sufficiently small area for spark production difficult. The temporal mode features limit the effectiveness of a given pulse because it is delivered in multiple packets instead of one large pulse. The desired laser output would consist of pulses that are spatially and temporally uniform such that sufficient energy can be delivered to a small volume at one time to "pack the biggest punch" for spark production.

These problems can be overcome in side pumped systems through several strategies described below. One strategy involves increasing the number of diode arrays and equally spacing them around the circumference of the laser rod to more uniformly illuminate the active media. Another strategy involves increasing the power input which will act to saturate more of the crystal in a given amount of time. More light is available to saturate the active ions and in consequence the pump light penetrates deeper into the rod producing a more uniform pump distribution. Another strategy involves reducing the path length within the laser rod by reducing the rod diameter. This gives the pump energy shorter distance to travel thereby producing a more uniform pump distribution. Another strategy involves modifying the active media absorption (Nd concentration) so the pump light penetrates further into the crystal thereby producing a more uniform pump distribution.

Cr:YAG was used as the passive Q-switch medium for several key reasons. A primary reason for its selection was the solid state YAG substrate and its similarity to the active media host material. Cr:YAG is a well developed technology for passive Q-switching, is readily available and is relatively inexpensive. Unlike other saturable absorber materials Cr:YAG does not degrade with use, it is not poisonous like gaseous SF_6 and it is not a

suspected carcinogen such as dye cell saturable absorber liquids. Its optical and physical properties are very similar to and complimentary of Nd:YAG. Cr:YAG has a high damage threshold, a wide absorption band to accommodate the Nd emission, and acts as a fast Q-switch when properly pumped by the Nd emission.

4.2 Preliminary Experimentation

4.2.1 Pump Radiation Distribution

4.2.1.1 Laser Rod Radius

Early experimentation showed that a 5 mm diameter 1.0% Nd laser rod pumped symmetrically from three sides produced three distinct output beams. This output mode production was caused by the excellent absorption of the Nd atoms. The pump light was so readily absorbed that sufficient pump light never penetrated more than 1-1.5 mm. This problem was found to have two solutions. The first solution involved the reduction of the rod diameter from 5 mm to 3 mm while keeping the Nd concentration constant. This strategy shortened the transmission path so that the pump light was able to penetrate at least halfway through the rod diameter to create a more uniform pump distribution. This correction allowed for lower order mode production and an improvement in output beam quality. The second solution involved the modification of the Nd ion concentration and is discussed in a following section. The 3 mm diameter laser rod geometry was adopted for the full scale testing.

4.2.1.2 Barrel Finish

The laser rod barrel finish was found to influence the pump light distribution within the active media. A preliminary experiment was designed to determine whether a polished barrel or a ground barrel produced better pump light distribution and subsequently better

laser output. Two identical laser rods were procured, the barrel of one was sanded and polished by hand until it was smooth and transparent and the other was left with the opaque factory finish. Identical tests were performed on each rod. The ground barrel was found to produce a more uniform output both temporally and spatially. Although the ground barrel laser rod produced three distinct output beams, they were nearly coherent temporally and they were approximately of equal size and intensity. The polished barrel laser rod produced lower output levels which consisted of multiple nonsymmetric spatial and temporal output modes. The polished rod acted like a cylindrical lens when the pump light entered and it acted like a cylindrical mirror when the light reached the opposing side. The focusing and reflection of the pump light seemed to foster a larger degree of amplified spontaneous emission (ASE) than the diffuse ground barrel finish. Whether the ASE was collected and amplified by the cavity or not, it did act to significantly deplete the available excited states leading to a lower and more erratic laser output. The ground barrel finish acted to diffuse the pump light producing larger and more uniformly pumped "hot spots" for laser action to take place. The ground or frosted barrel finish was adopted for the full scale testing.

4.2.1.3 Rod End Treatment

Temporal mode control was a problem during the early stages of laser development. It was hypothesized and tested as to whether the laser rod end faces, and anti-reflection (AR) coatings, were contributing to this problem. It was thought that the flat parallel faces of the laser rod were acting like a weak resonator, within the main cavity, inducing ASE laser action prior to the whole system reaching the proper threshold. This was thought to be the cause of the randomly spaced multitude of output pulses under most operating conditions during preliminary assembly and testing. To investigate this issue identical 3 mm diameter

laser rods were procured with 0.5˚ antiparallel wedged end faces. The ends were AR coated for 1064 nm just as the flat parallel rod end faces. The addition of the antiparallel wedge was found to significantly reduce and/or eliminate the multi-temprotal mode output when the cavity was properly aligned. Therefore the 0.5˚, antiparallel, wedge end treatment was adopted for the full scale testing.

4.2.1.4 Ion Concentration

Through preliminary experimentation the Nd ion concentration of the active media was found to have a significant influence on the Q-switch delay and the laser output characteristics. Not only does the ion concentration influence the pump energy distribution, as previously noted, it also affects the output pulse energy and output pulse delay time. For a given pump power the Nd concentration defines the degree of energy storage that a particular laser rod can obtain. This was evident during the preliminary experimentation where both the 1.3% Nd and the 1.0% Nd laser setup produced a lower pulse energy than the 0.5% Nd laser setup. This happened because the gain is much higher in the 1.0% rod and as a consequence had a greater degree of spontaneous emission losses that trigger lasing much quicker than the other laser setup. These losses act to cap the storage capability of the laser system. Aside from the increase spontaneous emission that triggers passive Q-switching sooner, the ions are "closer" together, relatively, to where the spontaneous decay is more likely to stimulate subsequent emissions not contained by the cavity creating a greater loss. The lower concentration setup produces more energy because more energy is available in the crystal when the lasing threshold is reached. Since the spontaneous emission that triggers lasing is smaller, the crystal ends up being pumped for a slightly longer time. The increased distance between the ions makes it less likely that a spontaneous emission will deplete as many or any

other excited states. Also as the average distance between the ions is increased by lowering the concentration the coherence length between the ions is modified. The coherence length refers to the crystal lattice theory involving the high loss sharing of energy between two identical ions. When the ions are within the coherence length they can share the excited state energy through phonon interactions with losses. By lowering the concentration the likelihood of ions being close enough to share energy falls dramatically. Because of the reduced concentration more excited states are available for laser output at the time of Q-switching.

The active ion concentration also affects the Q-switch delay. With higher concentrations more spontaneous emissions are present to induce the early stages of bleaching within the Q-switch. Therefore the higher the concentration the faster a given Q-switch will trigger. This phenomenon will be studied more in depth in the full scale experimentation.

The ion concentration also affects the overall beam quality. As the concentration is lowered the pump light is able to penetrate further into the active media. This results in a more uniform pump distribution and a large degree of overlap between the pumped regions. The more uniformly the rod is illuminated the better the beam quality. Another aspect of the ion concentration affecting the beam quality concerns the thermal distortions caused by high absorption of the pump radiation. The higher the absorption of the material, (the higher the concentration) the more thermal energy is deposited in the crystal which causes slight variations in density and refractive index. The higher concentration crystals are more prone to have poor beam quality because of beam distortions induced by thermal lensing. Since the ion concentration affects so many aspects of the laser operation, four different ion

concentrations were selected for the full scale experimentation, 0.35%, 0.5%, 0.75%, and 1.00%.

4.2.1.5 Diode Spacing

The spacing between the diode pumps and the laser rod was varied during the initial development to determine what effect the output divergence of the diode pumps had on the operational characteristics of the laser. The testing showed that as the diode pumps were positioned closer to the laser rod the laser output increased. However when the Nd concentration was increased the proximity of the diode pumps induced multiple output pulses as well as a degraded beam quality. The diodes were finally positioned approximately 1 mm from the rod surface for the full scale experimental testing.

4.2.2 Output Coupler Reflectivity

The preliminary experimentation concerning the output coupler reflectivity qualitatively agreed with the theoretical and experimental work in the literature. In brief, as the output coupler reflectivity was lowered the passive Q-switched pulses increased in energy and the Q-switch delay grew in length. The primary goal of this experimentation was to define a range of combinations of output coupler reflectivity and Q-switch initial transmission that would assist in the design of a full scale experiment that would provide the most useful data. Overall as the output coupler reflectivity was lowered the output pulse energy increased as well as the Q-switch delay. The increase in the output pulse energy was caused by the excess build up of stored excited states that was allowed due to the decreased 'feedback' the lower reflectivity output coupler provides. The lower reflectivity does not retain as many lasing photons within the cavity as the higher reflectivity output coupler. Therefore the active media is pumped longer and more effectively with fewer losses induced

by prelasing before the lasing threshold is reached. This is the reason why the Q-switch delay is longer with a lower reflectivity output coupler, it simply takes more time for a sufficient photon density to build up before the lasing threshold is reached. The preliminary experimentation tested the laser output of five different output coupler reflectivities 90%, 80%, 70%, 60%, and 50%. Figure 4.1 shows the output pulse energy data for five output coupler values and with fixed Q-switch initial transmission of 50%. It can be seen in Figure 4.1 that the lower output coupler reflectivity values produce the highest output pulse energy. Figure 4.2 shows the output peak power data for five output coupler values and fixed Q-switch initial transmission of 50%. Figure 4.2 also indicates that lower output coupler reflectivity values produce the highest output peak power levels. Accordingly the output coupler reflectivities chosen for the full scale experimentation were 30%, 40%, and 50%.

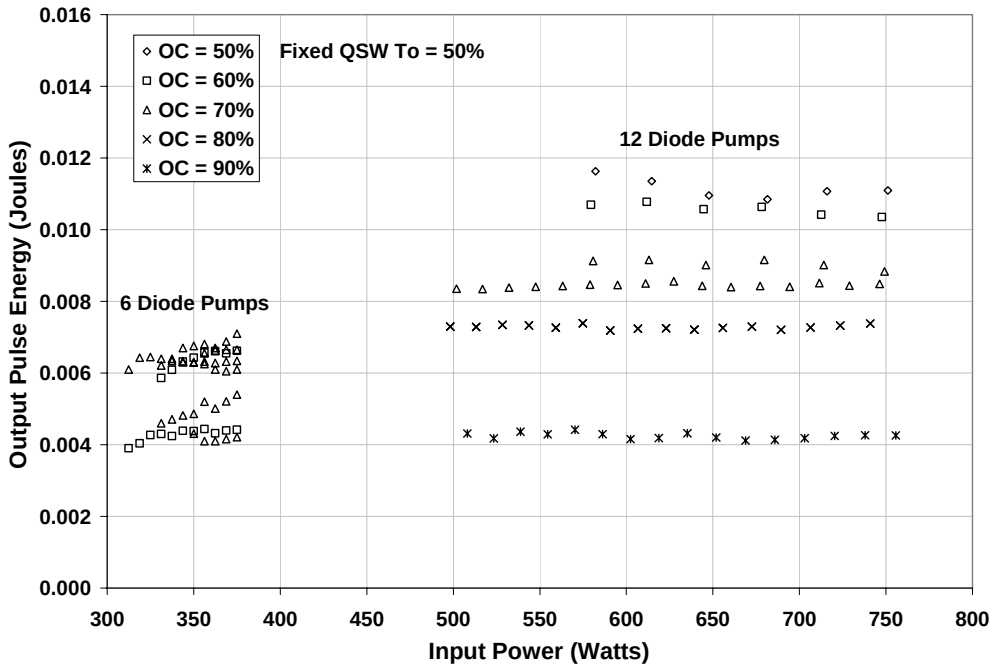

Figure 4.1: Preliminary output pulse energy data for five output coupler reflectivity values with a fixed Q-switch initial transmission of To = 50%

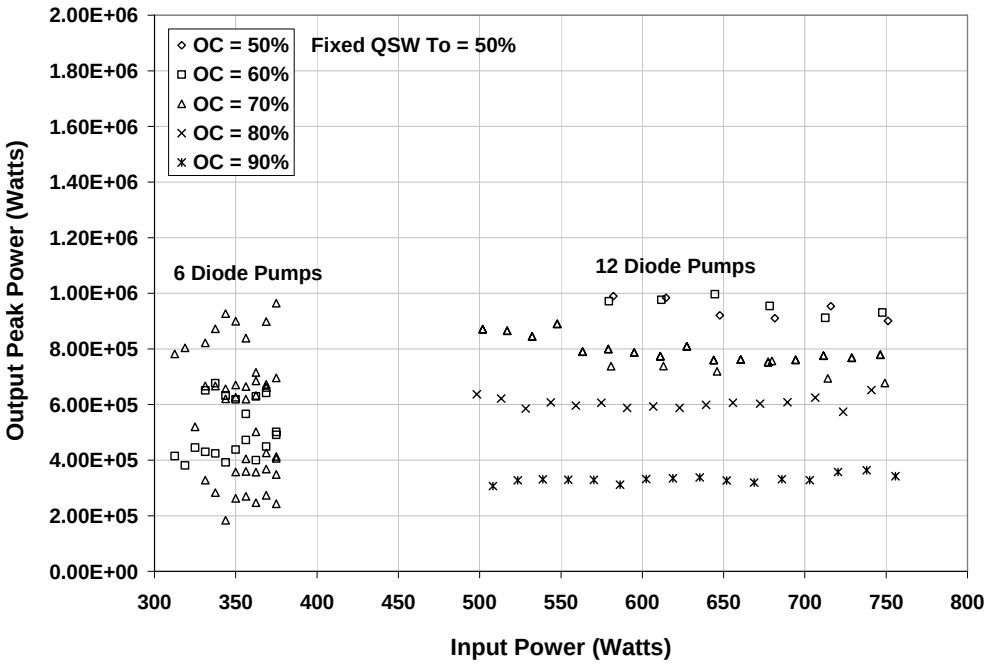

Figure 4.2: Preliminary output peak power data for five output coupler reflectivity values with a fixed Q-switch initial transmission of To = 50%

4.2.3 Q-switch Initial Transmission

The preliminary experimentation regarding the Q-switch initial transmission agreed well with the theoretical and experimental data in the literature. In short as the initial transmission was reduced, for a given output coupler reflectivity, the output pulse energy increased and the Q-switch delay increased as well. This experimentation was very similar to that of the output coupler reflectivity and had the goal of defining a suitable range of initial transmission values for full scale testing. The output pulse energy increase was due to the increased energy storage capability of the system. Therefore more excited states are available for lasing as when the threshold is reached. The passive Q-switch acts to partially block the laser cavity and slow down the intracavity build up to the lasing threshold condition. The hold-off introduced by the passive Q-switch also acts to increase the delay time between the start of pumping to the attainment of the lasing threshold. The preliminary experimentation

tested the laser output of three different Q-switch initial transmission values 50%, 60%, and 70%. The analysis of the preliminary data indicated that the goals of the overall research could be more closely met by exploring even lower values of the Q-switch initial transmission. The initial transmission values chosen for the full scale experimentation were 32%, 36%, and 40%. Figure 4.3 shows the output pulse energy data for four Q-switch initial transmission values and with fixed output coupler reflectivity of 60%. It can be seen in Figure 4.3 that the lower Q-switch initial transmission values produce the highest output pulse energy. Figure 4.4 shows the output peak power data for four Q-switch initial transmission values and fixed output coupler reflectivity of 50%. Figures 4.4 also indicates that lower Q-switch initial transmission values produce the highest output peak power levels. The Q-switch initial transmission values chosen for the full scale experimentation were 32%, 36%, and 40%. These values were chosen due to trends found in the literature and experience gained during the preliminary experimentation. The values chosen for the full scale experimentation were also found to be the lowest initial transmission values that produced laser output at the lowest optical input power level.

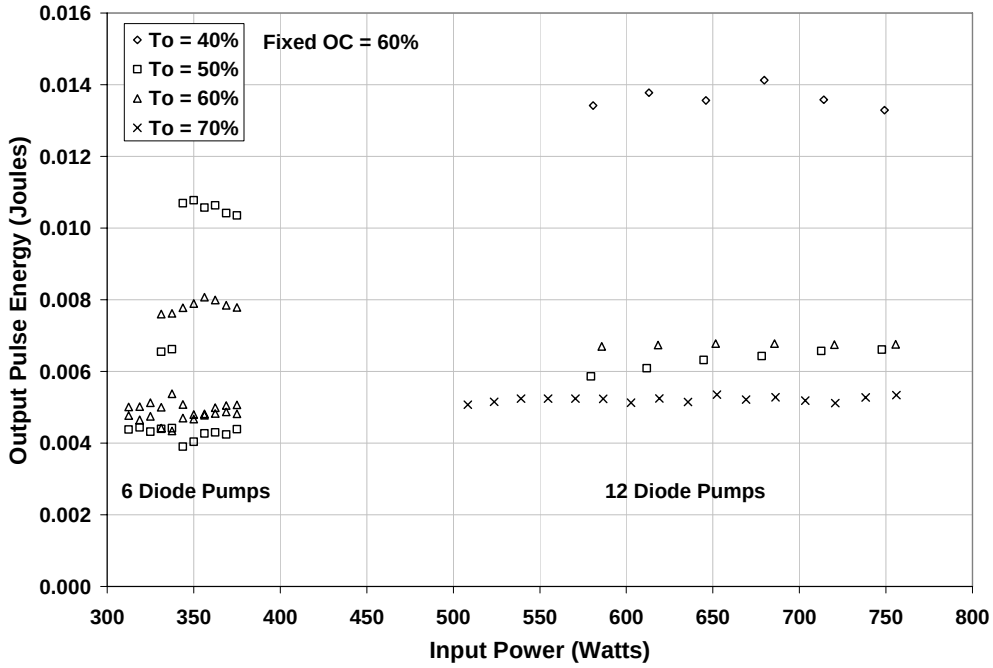

Figure 4.3: Preliminary output pulse energy data for four Q-switch initial transmission values with a fixed output coupler reflectivity of OC = 60%

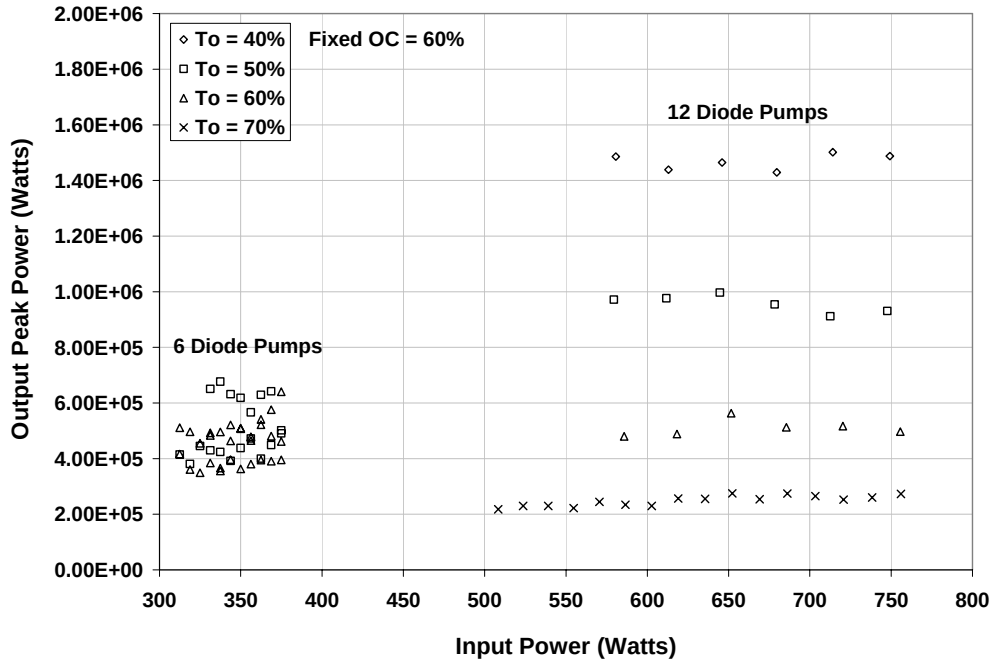

Figure 4.4: Preliminary output peak power data for four Q-switch initial transmission values with a fixed output coupler reflectivity of OC = 60%

4.2.4 Resonator Geometry

Two different resonator configurations were considered for use in the laser spark plug experimental testing. Preliminary testing was able to distinguish which resonator design was most appropriate and more conducive to producing the desired output. The plane-parallel and hemispherical resonators were evaluated by the preliminary experimental testing. The plane-parallel resonator consists of two flat and parallel mirrors forming an optical cavity. The hemispherical resonator consists of a flat mirror and a concave mirror with a radius of curvature that is less than or equal to the cavity length. Two hemispherical resonators were considered: 0.5 m and 1.0 m radius of curvature mirrors were used. The cavity length was approximately 125 mm which was significantly less than the radius of curvature of either concave mirror being tested. The 0.5 m mirror produced highly multimode spatial and temporal output patterns. The output pulse energy was lower than both the plane-parallel and the 1.0 m mirror resonators. The 1.0 m mirror resonator produced the highest output pulse energy however the poor beam quality and unpredictable multimode output made this cavity unsuitable for use in the laser spark plug. It was initially thought that the concave mirrors would allow for the focusing of the intracavity flux into the pumped areas of the laser rod to increase the extraction efficiency. The higher output energy may be an indication of this effect but the seemingly uncontrollable spatial and temporal output modes made this resonator less attractive. The plane-parallel resonator produced low order spatial output modes as well as single temporal mode output. With the improvements in the output modes the higher output pulse energy is not needed. The plane-parallel optical resonator was chosen for the full scale experimental testing.

4.2.5 Input Power

Two sets of preliminary tests were performed to find a sufficient input power level that would produce laser sparks. The first set of tests were performed with six laser diode arrays arranged around a 3 mm laser rod. The nominal laser output was approximately 300 Watts. The output from this line of tests did not produce sparks although the output peak power was near one megawatt. This phase of testing did allow for the characterization of many of the other parameters addressed in the preliminary experimental testing. The second set of tests used twelve laser diode bars arranged around the same 3 mm laser rod. The nominal laser output was approximately 600 Watts. Under strictly controlled conditions this input arrangement and power level produced laser sparks sporadically. The increase in the pump power allowed for the continuing study of the other laser parameters examined in the preliminary testing as well as in the full scale testing. The final test used 18 laser diode bars and had a nominal output of approximately 900 Watts. All phases of input power testing indicated shorter Q-switch delays, overall stepwise increase in output energy, and an overall decrease in output pulse width, all with increasing input power.

4.3 Design of the Experiment

The experimental design was based on the information gathered from both the literature survey and the preliminary experimentation. Between the two sources of information a list of meaningful independent and dependent variables was developed along with suitable ranges for each of the independent variables. The four independent variables are the output coupler reflectivity, the Q-switch initial transmission, the input pump power, and the Nd concentration. A 3^4 factorial statistical design was chosen whereby each of the four variables has three test values. A single block of this design structure, for a given value

of Nd concentration, is shown in Figure 4.5. The experimental values for the output coupler reflectivity, Q-switch initial transmission, and input power are listed in Figure 4.5 as well. The complete design structure, showing the experimental values of the Nd concentration, is shown in Figure 4.6.

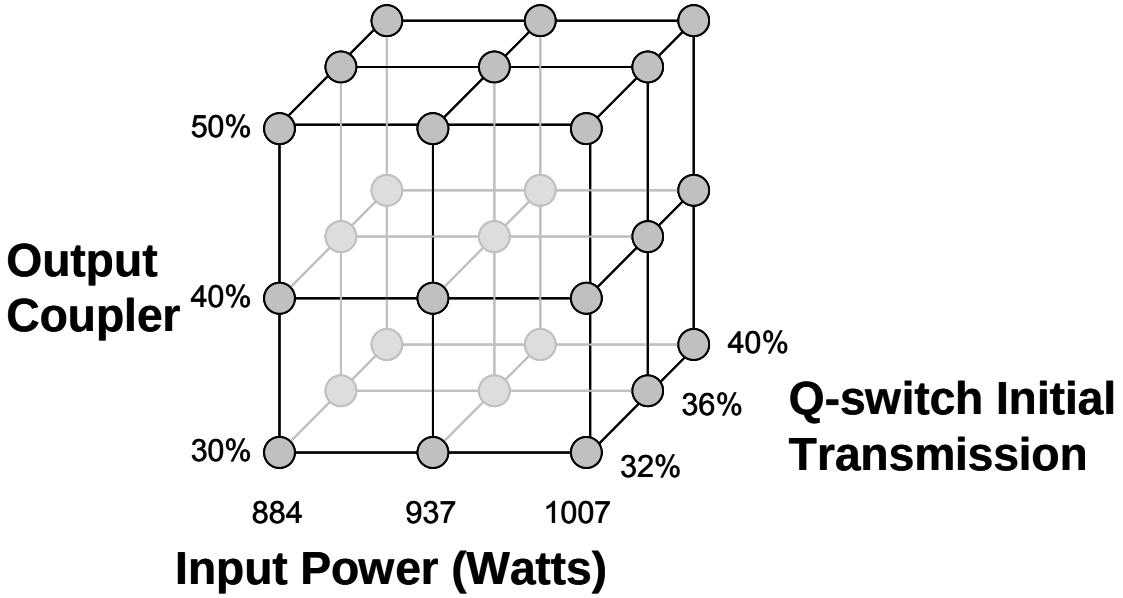

Figure 4.5: Statistical design method

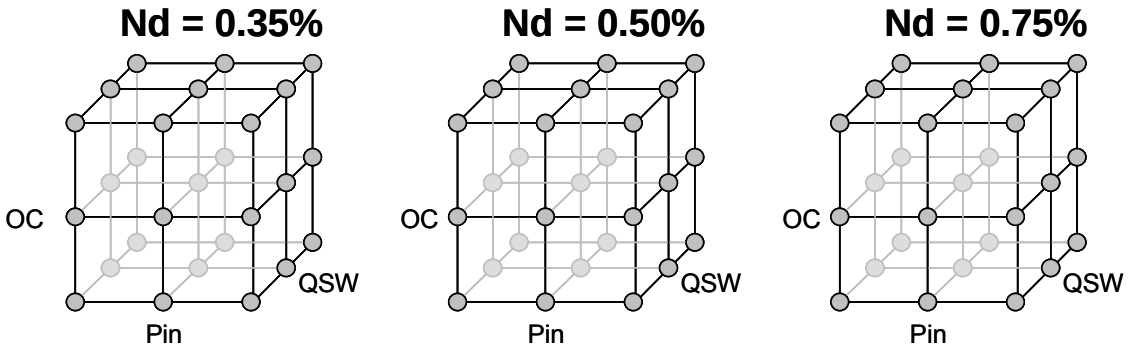

Figure 4.6: 3^4 Factorial Statistical Design

For each test point the output pulse energy, pulsewidth, output pulse delay and beam quality values were recorded. This procedure was repeated three times a an average of each

data point was calculated. A 95% confidence interval was applied to the data. The confidence interval was used to more accurately gauge the deviation of the data about the mean. The confidence interval, unlike the standard deviation, takes into account the number of data points taken for the mean. The standard deviation provides a reliable error estimate for the mean however, it will only accurately represent 86% of the data for large smaples. The 95% confidence interval provides a much more complete error estimate providing a reliable error estimate for 95% of the data over large samples. The data collection was not randomized due to timeliness issues regarding optical setup and alignment. The test plan included 81 optical combinations with three repeats each for a total of 243 individual data points.

4.4 Optical Experimental Setup and Procedure

The laboratory setup for testing the prototype lasers was designed and assembled to have the capability to measure all of the dependent variables while maintaining the optical alignment. A block diagram of the equipment setup is shown in Figure 4.7.

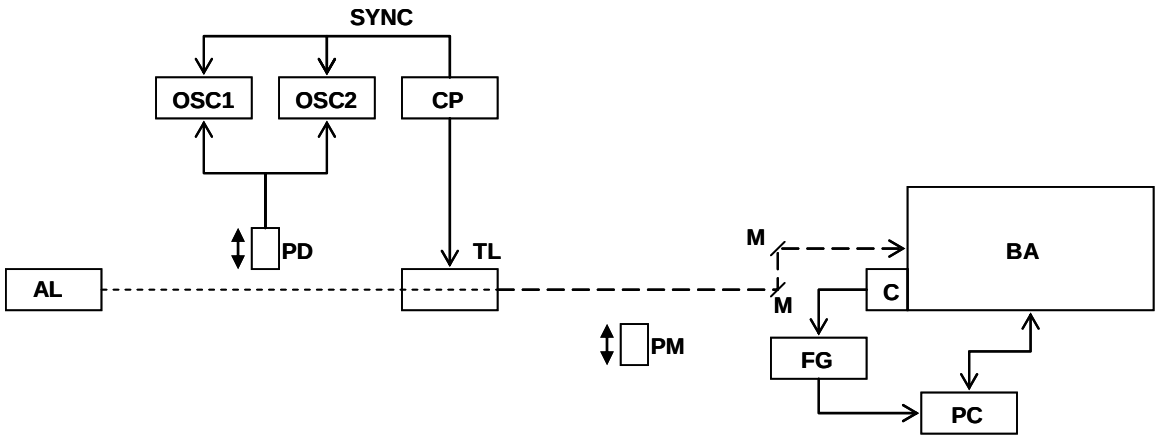

Figure 4.7: Block diagram of the laboratory experimental setup

The dashed line represents the optical axis of the setup created by the alignment laser (AL) which was a Helium-Neon laser. The AL beam was used to ensure proper alignment of

the test laser (TL) as well as to align the output of the TL with the beam analyzer (BA). Turning mirrors (M) were used to fine tune the alignment between the TL and the BA. The power meter (PM) was used to monitor the output pulse energy. The photodiode (PD) was connected to both oscilloscope number 1 (OSC1) and oscilloscope number 2 (OSC2) which were used to monitor the output pulsewidth and Q-switch delay respectively. OSC1 and OSC2 were identical, but OSC1 was set to a very short time base to monitor the output pulsewidth on a nanosecond scale, whereas OSC2 was set to a long time base to monitor the Q-switch delay on a microsecond scale. A CCD camera (C) was connected to the beam analyzer and then to a frame grabber board (FG) and finally to a laptop computer (PC). The current pulser (CP) was used to drive the pump diodes within the TL and had onboard controls for the pulse frequency, delay, and power level. The two oscilloscopes were both connected to the SYNC output of the CP which acted as a trigger source. The data sheets for all materials and equipment are listed in Appendix B.

The data for each combination was recorded by hand and transferred to a spreadsheet computer program for arrangement, plotting, and analysis. The raw optical testing data can be found in Appendix E. The test laser consisted of ten components which include the Nd:YAG laser rod, the Cr:YAG passive Q-switch, the high reflector mirror and mount, the output coupler mirror and mount, the laser chassis, and the three laser diode pump mounts. The laser chassis was designed and fabricated as one piece so that the continual assembly and disassembly during testing would have little effect on the overall laser geometry and alignment. A picture of the laser chassis is shown in Figure 4.8. A mechanical drawing of the chassis and additional components can be found in the Appendix D.

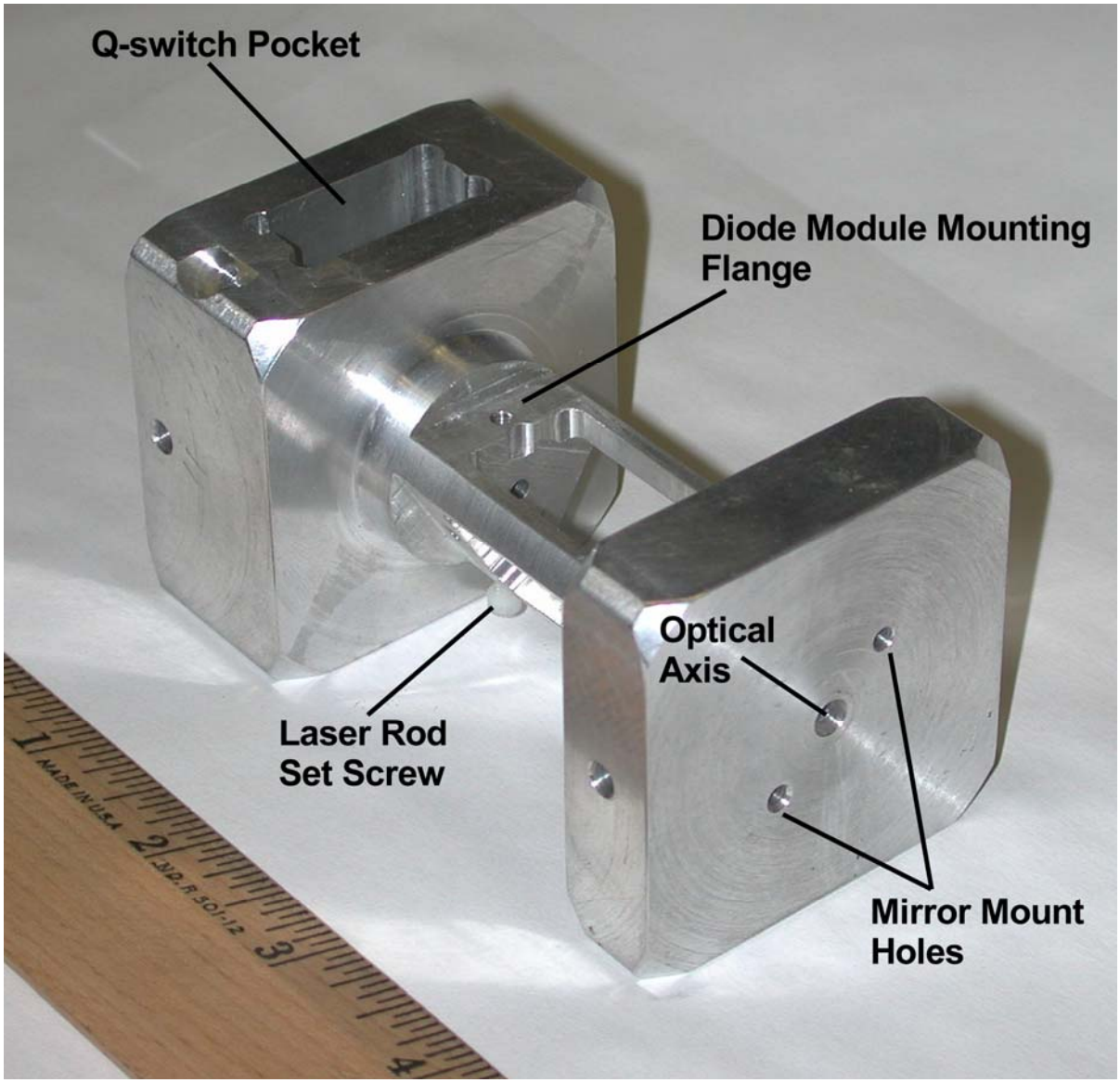

Figure 4.8: Laser chassis showing mounting surfaces for the diode pump mounts, Q-switch pocket, laser rod mounting hole and cavity mirror mounting holes

The diode pump mounts each consisted of a copper block with flanges for mounting onto the laser chassis. The laser diodes were made by Northrop Grumman Cutting Edge Optronics, model number ASM05P150. Each array submodule (ASM) consisted of three laser diode bars each rated for 50 Watts of optical output power. The laser diodes were connected in series with each diode mount module and the entire three module assembly was connected to the high voltage current pulser. The diode modules were mounted on

thermoelectric coolers (TEC). The TEC's were used to tune the temperature of the laser diode modules for operation at repetitions rates higher than one hertz. The laser diode output wavelength is highly sensitive to temperature and can shift significantly. If the output of the laser diode arrays shifts just a few nanometers the output no longer overlaps the absorption band of the Nd:YAG and the production of excited states within the laser material decreases significantly. The TEC's were primarily used during engine testing where the repetition rate was approximately 5 Hz. When a voltage is applied to a TEC the semiconductor device exhibits the Peltier effect whereby one side becomes cold and the other side becomes hot. In this way the TEC acts as a heat pump, removing heat from the laser diode arrays and dumping into the copper mounts. A picture of the diode pump mounts are shown in Figure 4.9.

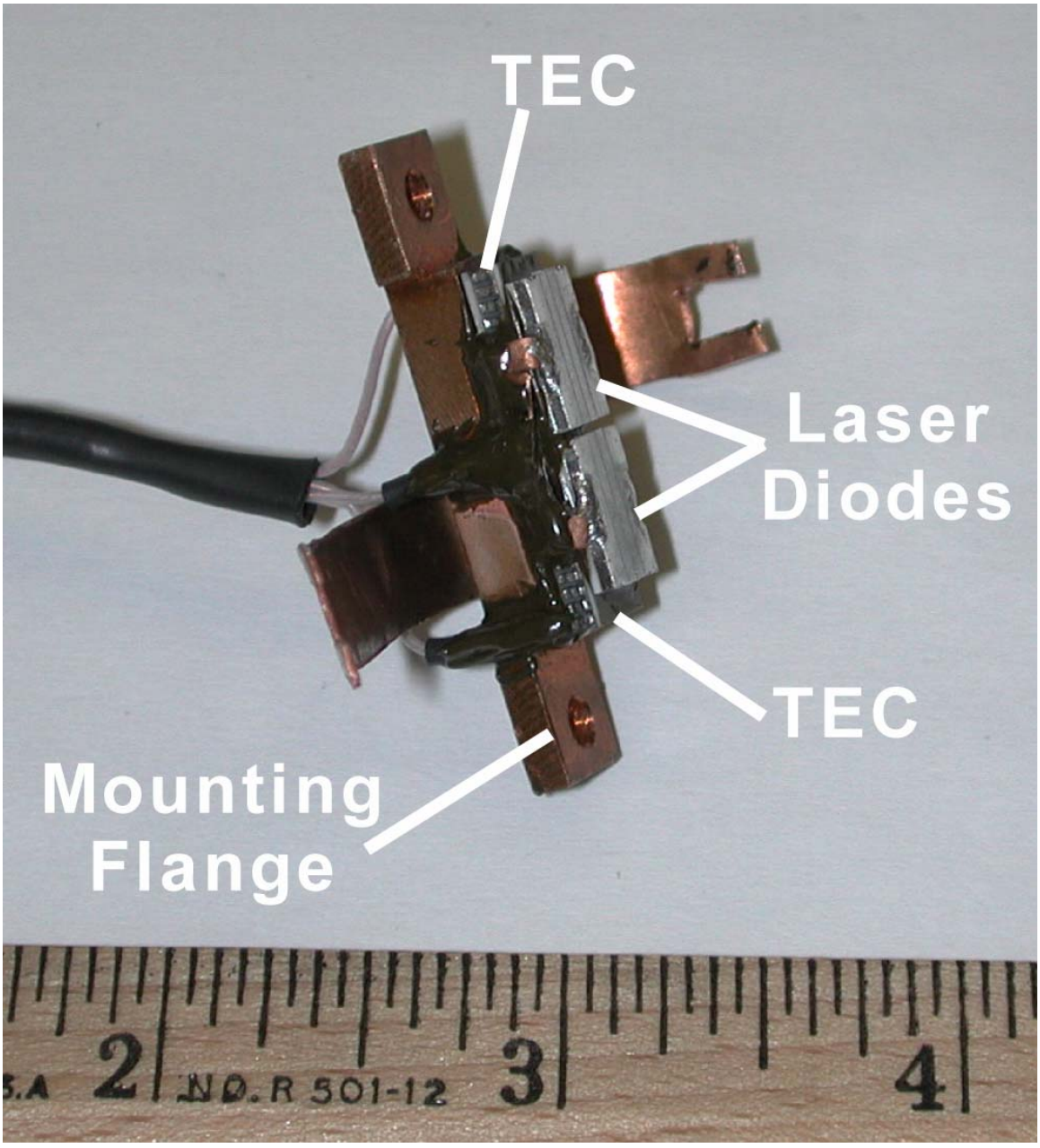

Figure 4.9: Diode pump mounts showing mounting flanges, TEC's, laser diode pumps

The Nd:YAG laser rods consisted of cylinders 3 mm in diameter and 40 mm in length. Each laser rod had a rough finish along the barrel in an attempt to scatter the pump light when it entered the crystal so that the pump light distribution would be as uniform as possible throughout. The ends of the laser rods were wedged 0.5˚ and non-parallel. The optical faces of the rods were polished to a λ/10 surface smoothness. The ends were coated

with an anti-reflection material to index match the air/crystal interface thereby enhancing the transmission of the laser energy from the air into the crystal and vice versa. Three different Nd dopant levels were used for testing, 0.35%, 0.50%, and 0.75% by atomic weight. A picture of a laser rod mounted in the laser chassis for testing is shown in Figure 4.10.

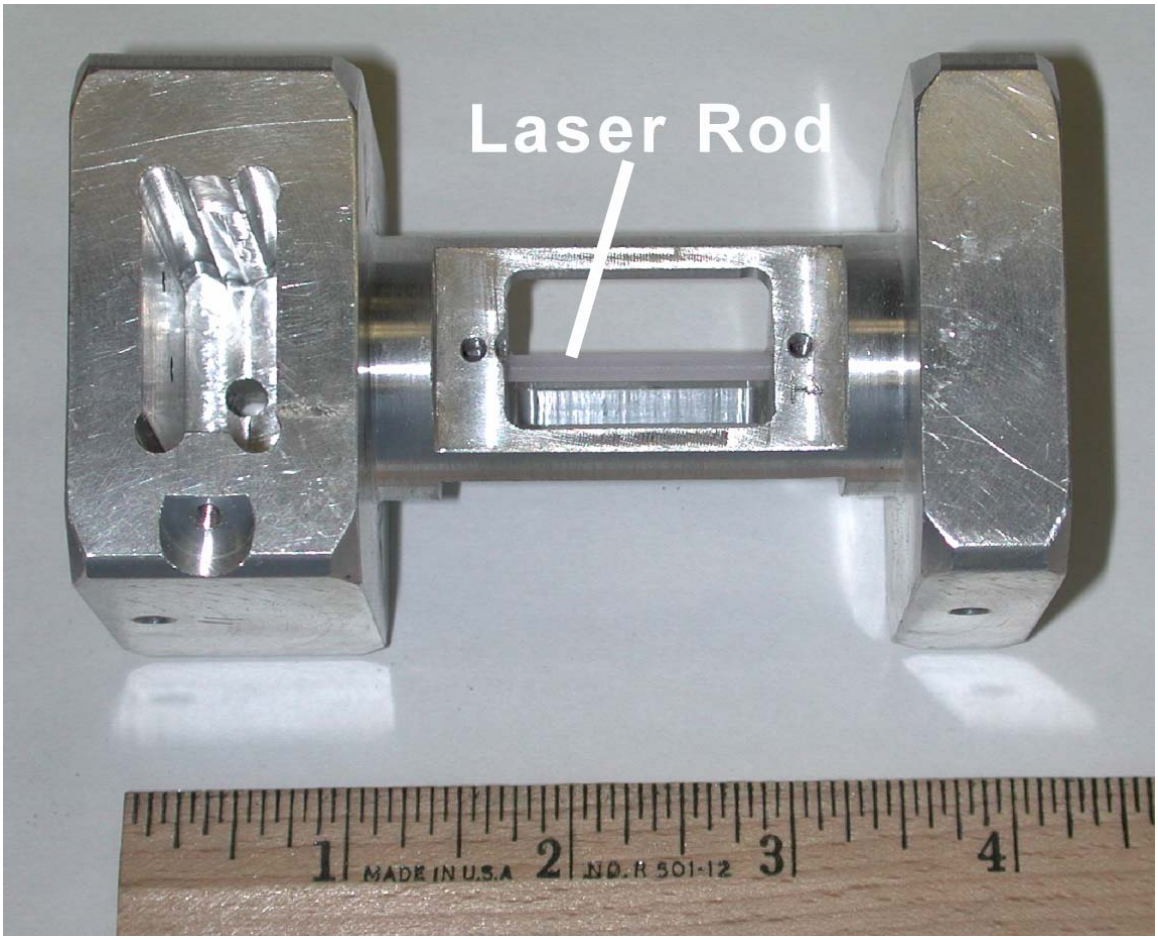

Figure 4.10: Laser rod installed into the laser chassis

The Cr:YAG passive Q-switch crystals were 5 mm x 5 mm across the optical face and between 1.5-4 mm thick depending on the Cr dopant level and the desired initial transmission value. The optical faces were polished to a surface smoothness of λ/10 and coated with an anti-reflection material to index match the air/crystal interface thereby enhancing the transmission of the laser energy from the air into the crystal and vice versa.

The Q-switch crystals were each mounted inside an aluminum disk for ease of handling and alignment. The aluminum disks were one inch in diameter and between 0.25 and 0.5 inches thick. Three different initial transmission values were used for testing: 32%, 36%, and 40%. Combinations of Q-switch crystals were used to attain the initial transmission values used for testing. The 40% initial transmission value was realized with a single crystal whereas the 36% and 32% initial transmission values were attained by combining the 40% crystal with a 90% and 80% crystal, respectively. A picture of a passive Q-switch mounted in the laser chassis for testing is shown in Figure 4.11. Figure 4.12 shows the diode pump modules mounted to the laser chassis and electrically connected to each other.

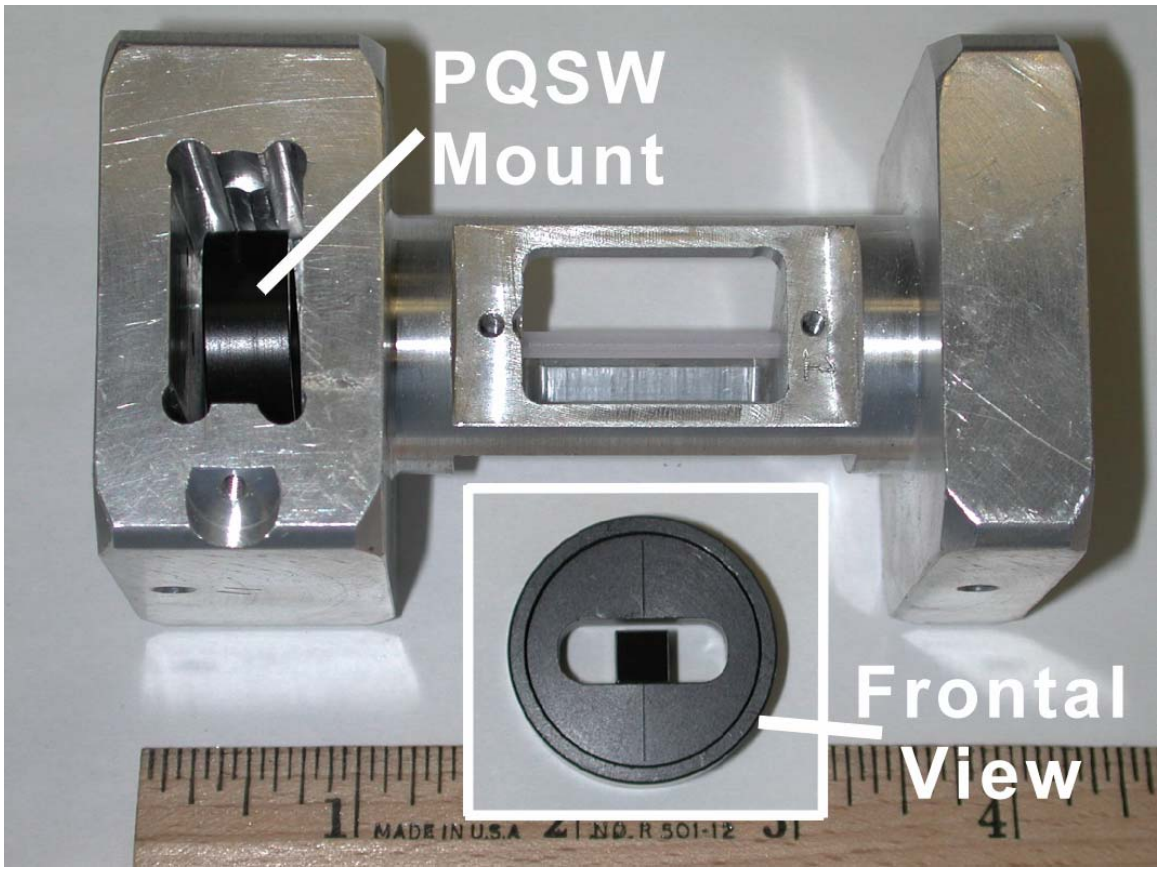

Figure 4.11: Passive Q-switch crystal installed into the laser chassis, frontal view of passive Q-switch crystal inside its mount (inset)

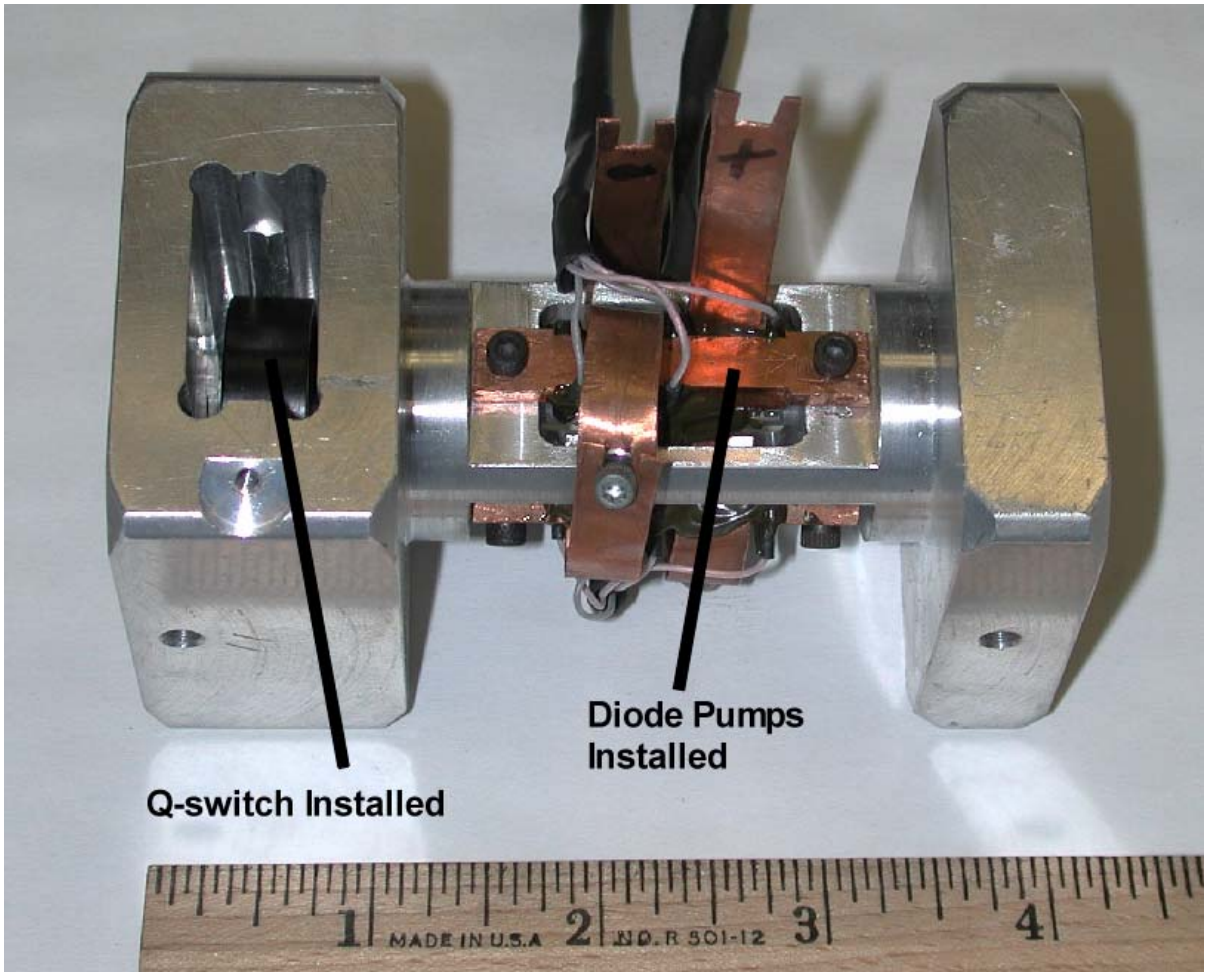

Figure 4.12: Test laser showing the installation of the laser diode mounts

The mirror mounts for the laser spark plug were industrial grade flexure mounts from Newport, model number MFM-050. The mounts were designed to accommodate 0.5 inch optics and provide rigidity and alignment stability. The output coupler and high reflector were 0.5 inches in diameter and 0.5 inches thick. The mirrors were flat first surface mirrors with vapor deposited dielectric reflective coatings. The output coupler had an antireflective coating on the output face to ensure low losses as the laser light exited the optic into free space. The mirrors were produced by CVI laser; Figure 4.13 shows the installed mirrors and mounts. The complete laser assembly and data collection procedure list can be found in the Appendix C.

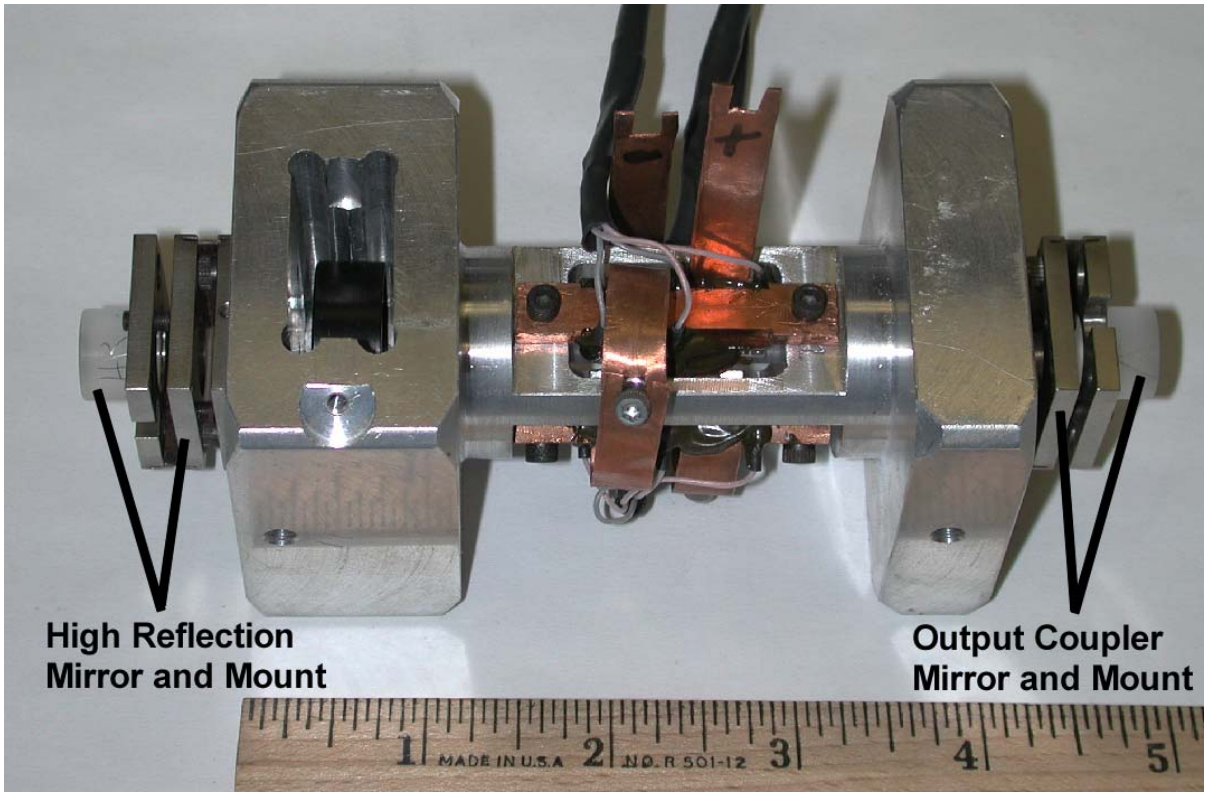

Figure 4.13: Complete test laser assembly

4.5 Engine Testing Experimental Setup and Procedure

This section describes the engine ignition testing where the test laser has been compared to a commercially available laser. The engine test cell and equipment used to control, monitor, and report the ignition testing are described. The recorded parameters are listed and explained as well as the testing procedure and required modifications to the ignition system.

4.5.1 Engine Test Cell

The test cell used for experimentation in this work is located at the U.S. Department of Energy's National Energy Technology Laboratory facility in Morgantown, West Virginia [167]. The test cell consists of a Ricardo Proteus single cylinder research engine, dynamometer, and control and instrumentation hardware for measuring and/or modifying many of the operational aspects of the engine.

The cell is outfitted with a 75 kW dynamometer manufactured by McClure [165], which is used for a host of applications for this and other engine research. The dynamometer can motor the engine for starting before fuel or spark energy is added to the system for full operation. The dynamometer is used to regulate the operational speed of the engine under fueled conditions.

The cell includes fuel flow monitors for both liquid and gaseous fuels. The cell is equipped with temperature controls for the engine coolant, oil, intake air, and the test cell. These controls are vital to the consistency of any tests that are spread over the course of days, weeks or months because they allow for the most similar test situations independent of daily or operational differences. Figure 4.14 shows a basic schematic of the engine test cell.

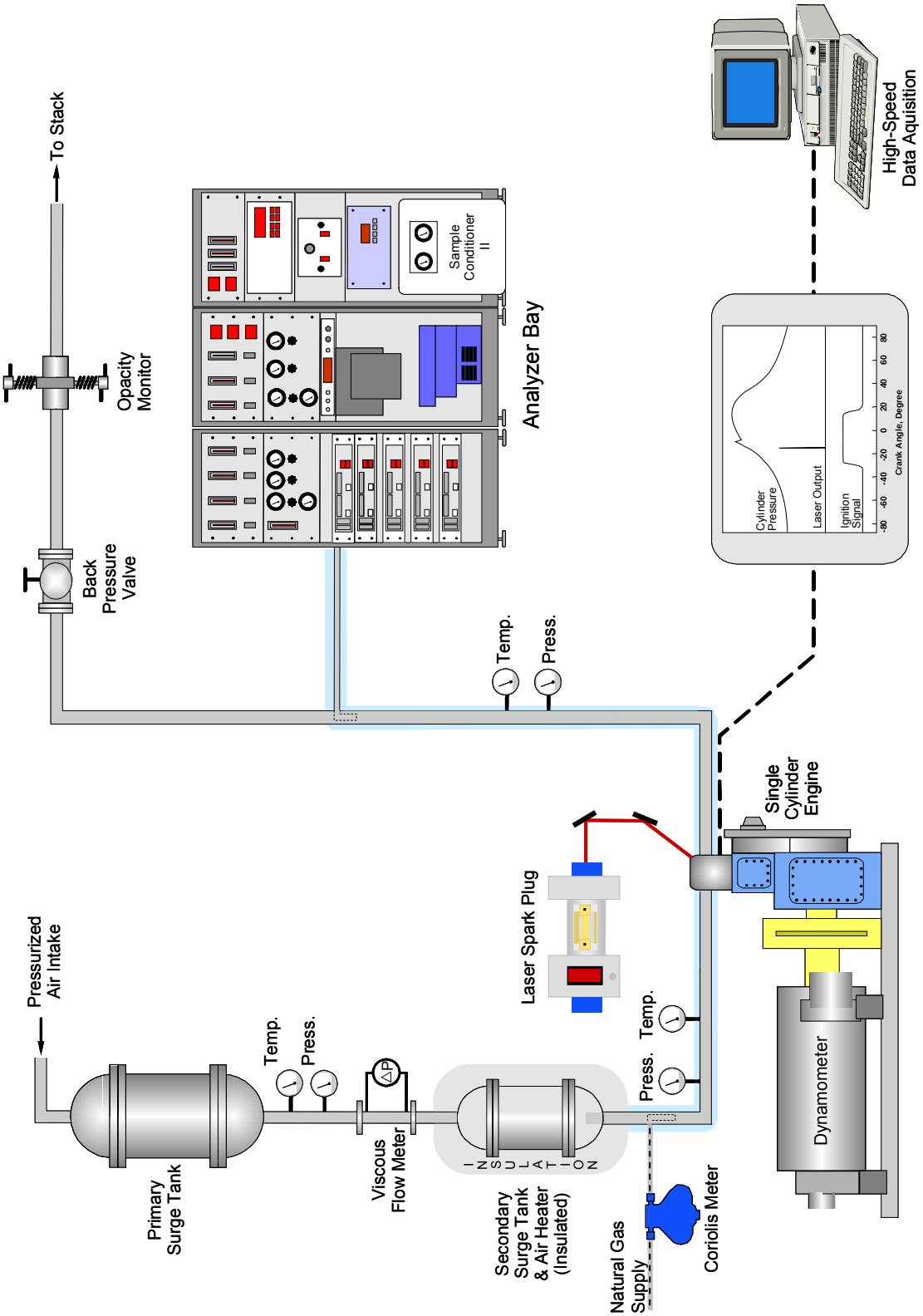

Figure 4.14: Engine test facility schematic

4.5.2 Combustion Quality Measurement

For decades researchers have been using in-cylinder pressure information to investigate the combustion processes in internal combustion engines [166]. The in-cylinder pressure data provides an effective and easy way to monitor and analyze the combustion process on a cycle-to-cycle basis. Current piezo-electric transducer technology offers fast response sensors that easily withstand the harsh environment within the combustion chamber of an internal combustion engine. Voltage signals from the piezo-electric transducer and associated charge amplifier can be sampled and recorded by high speed digital data acquisition systems that are triggered by a crankshaft mounted encoder.

The development of the cylinder pressure in an internal combustion engine is a complex process that involves the heat release from the combustion, heat transfer due to convection, conduction, and radiation, as well as the changing combustion chamber volume [166]. Parameters such as the peak or maximum combustion pressure, (P_{max}), the crank angle where the maximum pressure occurs, (θ_{Pmax}) and the indicated mean effective pressure (IMEP) can be directly inferred from the in-cylinder pressure data. These combustion parameters are based on the combination of the cylinder pressure data with thermodynamic models. Quantitative measures of the combustion quality can be developed from the use of the in-cylinder pressure data with the cylinder volume and the derivatives of these thermodynamic models [166]. The combustion data that can be extracted from the measured parameters include the heat release rate, ignition delay, and the combustion duration.

The mean effective pressure (MEP) is an important measure of engine performance, because it is relatively invariant with respect to engine size, and it is an excellent measure of the overall performance of the engine. By definition the mean effective pressure is the work

produced per unit displaced engine combustion cylinder and is shown in Equation 4.1 [166, 22]:

$$MEP = \frac{W_c}{V_d}, \tag{4.1}$$

where W_c is the work per cycle and V_d is the displaced volume of the engine. The IMEP is derived from the in-cylinder pressure data and is defined as the work delivered to the piston by the combustion gases during a given engine cycle per unit displaced volume. This quantity neglects all losses (frictional, heat losses, etc.) and measures only the PdV work delivered to the piston. Pumping losses during the intake and exhaust strokes are neglected. The net IMEP is defined in Equation 4.2 [166, 22]:

$$IMEP = \frac{\int_{-\pi}^{\pi} P dV_{cyl}}{V_d}, \tag{4.2}$$

where P is the in-cylinder pressure (gage) and dV_{cyl} is the differential change in volume. Because the cylinder pressure data is discretely sampled, the integral given in Equation 4.2 can be simplified into a summation of the pressure data collected throughout the compression and expansion strokes. This is possible because the in-cylinder pressure data is discreetly sampled as a function of the crank angle. This transformation is shown in Equation 4.3 [166].

$$IMEP = \frac{\sum_{\theta=-\pi}^{\theta=\pi} P \frac{dV_{cyl}}{d\theta} d\theta}{V_d} \tag{4.3}$$

The resolution of the encoder used to trigger the data acquisition system has been used as the differential change in crank angle, $d\theta$.

The volumetric rate of change of the combustion chamber can be derived as a function of engine geometry. The cylinder volume as a function of the crank angle is given by Equation 4.4 [22]:

$$V_{cyl}(\theta) = V_c + \frac{V_c}{2}(r_c - 1)\left[R_r + 1 - \cos(\theta) - \left(R_r^2 - \sin^2(\theta)\right)^{1/2}\right], \tag{4.4}$$

where $V_{cyl}(\theta)$ is the cylinder volume at any crank angle θ, V_c is the clearance volume of the combustion chamber, r_c is the compression ratio, and R_r is the ratio of connecting rod length to crank radius. The cylinder volume rate of change as a function of crank angle is found by differentiating Equation 4.4 with respect to crank angle. The result is shown in Equation 4.53 [166].

$$\frac{dV_{cyl}}{d\theta} = \frac{V_c \sin(\theta)}{2}(r_c - 1)\left(1 + \frac{\cos(\theta)}{\sqrt{R_r^2 - \sin^2(\theta)}}\right) \tag{4.5}$$

Substituting this expression this into Equation 3.31 gives an expression for the net IMEP as a function of the sampled in-cylinder pressure shown in Equation 4.6 [166].

$$IMEP = \frac{\sum_{\theta=-\pi}^{\theta=\pi} P(\theta)\frac{V_c \sin(\theta)}{2}(r_c - 1)\left(1 + \frac{\cos(\theta)}{\sqrt{R_r^2 - \sin^2(\theta)}}\right)}{V_d} \tag{4.6}$$

The net indicated mean effective pressure can be used as a measure of the efficiency of the combustion process and can be easily calculated for any single engine cycle (assuming adequate CA resolution).

The IMEP calculation takes the magnitude of the in-cylinder pressure into account as well as the accuracy of the phasing of the cycle with respect to the maximum brake torque timing.

MEP values are frequently estimated from dynamometer measurements of the brake mean effective pressure (BMEP). The BMEP is derived from dynamometer measurements during engine operation and takes into account all mechanical losses. The BMEP of a 4-stroke engine is measured in bar and is shown in Equation 4.7 [166].

$$BMEP = \left(\frac{Torque}{V_d}\right)\left(\frac{2rev}{cycle}\right)\left(\frac{2\pi rad}{rev}\right) \tag{4.7}$$

The combustion quality can be represented by the maximum cylinder pressure, which is a very simple means of quantifying the combustion process because it requires only measurements and no calculations. The maximum cylinder pressure for any given cycle is a function of both the total amount of energy released during combustion, and the timing of the energy release with respect to TDC. With all other parameters held constant, the maximum pressure increases as the heat release increases and as the ignition timing is advanced. As the ignition timing is advanced, the combustion heat is released earlier in the cycle, when the cylinder volume is smaller. This leads to higher maximum in-cylinder pressures.

The direct pressure measurements discussed in this section offer a simple method of quantifying the quality of combustion in an engine, however the measurements are affected by several competing phenomenon that are not always easily decoupled. For example, the IMEP describes the total heat release, the timing of the heat release, and the variation in the cycle-to-cycle heat transfer. More specific information is required concerning the parameters that compose the cylinder pressure data. These methods are based on simple combustion

models and require simplifying assumptions in order to allow calculation from only the cylinder pressure data. The two most common combustion parameters that are calculated are the heat release rate and the combustion or burn duration.

The rate of heat release is an excellent means by which to characterize the combustion process [166]. Cylinder pressure data can be used to approximate the heat release rate by treating the combustion chamber as a closed system of varying volume during combustion. By neglecting heat transfer and the effects of the crevice volumes, an energy balance on the combustion chamber volume yields the expression in Equation 4.8 [166]:

$$dQ_{chem} = m_t C_V dT + P dV_{cyl}, \tag{4.8}$$

where dQ_{chem} is the incremental amount of chemical energy released, m_t is the total mass of the system, C_v is the specific heat at constant volume of the gas, dT is the differential change in the gas temperature, P is the cylinder pressure, and dV_{cyl} is the differential change in the cylinder volume. Equation 4.8 neglects heat transfer, which accounts for approximately 15% of the total heat release. Applying the ideal gas law to Equation 4.8 gives the expression shown in Equation 4.9 [166]:

$$dQ_{chem} = \frac{C_V}{R} V_{cyl} dP + \left(\frac{C_P}{R_{ave}} + 1 \right) P dV_{cyl}, \tag{4.9}$$

where R_{ave} is the average gas constant for the cylinder constituents and C_p is the specific heat at constant pressure. Substituting the ratio of specific heats and taking the rate of change with respect to crank angle yields an expression for the heat release rate as a function of the measured pressure, volume, and the rate of change of these properties. This expression is shown in Equation 4.10 [166]:

$$\frac{dQ_{chem}}{d\theta} = \left(\frac{1}{\gamma_{SH} - 1}\right) V_{cyl} \frac{dP}{d\theta} + \left(\frac{\gamma_{SH}}{\gamma_{SH} - 1}\right) P \frac{dV_{cyl}}{d\theta}, \tag{4.10}$$

where γ_{SH} is the ratio of specific heats. The ratio of specific heats can be used as a constant or it can be estimated as a function of temperature throughout the combustion process.

The heat release rate can also be integrated and normalized to yield a measure of the burned gas fraction. The importance of the heat release rate is the direct link between the measured cylinder pressure data and the actual cycle resolved combustion events. With correction for heat transfer to the cylinder walls Equation 4.10 can be expressed as Equation 4.11 [166].

$$\frac{dQ_{chem}}{d\theta} = \left(\frac{1}{\gamma_{SH} - 1}\right) V_{cyl} \frac{dP}{d\theta} + \left(\frac{\gamma_{SH}}{\gamma_{SH} - 1}\right) P \frac{dV_{cyl}}{d\theta} + \frac{dQ_{wall}}{d\theta} \tag{4.11}$$

The number of crank angle degrees required for the combustion of the cylinder charge is an important parameter for the operational analysis of internal combustion engines. The burn duration can be estimated using the heat release rate. The Rassweiler and Withrow mass fraction burned (MFB) model was found to produce the best results in comparative tests (spark ignited engines) with simulated and experimental pressure data. The Rassweiler and Withrow MFB model is shown in Equation 4.12 [166]:

$$MFB_{\theta} = \frac{\sum_{i=ign}^{i=0} \Delta P_{c,i}}{\sum_{i=EEOC}^{i=ign} \Delta P_{c,i}}, \tag{4.12}$$

where, MFB_{θ} is the mass fraction burned at crank angle θ, ΔP_c is the corrected pressure rise due to combustion, i is the integer crank angle location, ign is the ignition crank angle

location and EEOC is the crank angle for estimated end of combustion. The corrected pressure rise due to combustion is calculated from the difference between the incremental measured pressure rise and the pressure rise corresponding to a polytropic compression/expansion process and then referenced to the cylinder volume at TDC and is shown in Equation 4.13 [166]:

$$\Delta P_{c,i} = \left[P_i - \left(\frac{V_{cyl(i-1)}}{V_{cyl(i)}} \right)^n P_i - 1 \right] \left(\frac{V_{cyl(i-1)}}{V_r} \right), \tag{4.13}$$

where n is the assumed polytropic index, V_{cyl} is the cylinder volume and V_r is the reference volume at TDC. Here the polytropic index is based on values calculated from least squares fits to the log pressure versus log volume data usually over a 40 degree period. The two most commonly used burn durations are the number of crank angle degrees between ignition and 2% mass fraction burned, $\theta_{0\text{-}2}$ and the duration of the bulk of combustion, between 10% and 90%, $\theta_{10\text{-}90}$ [166].

4.5.3 Engine Data Acquisition Equipment

This study employs the use of a multiple channel indicating system for recording engine operational and emissions characteristics as well as cylinder pressure as a function of crank angle. The indicating system, sensors and software are manufactured by AVL North America, Inc. An AVL GU21D uncooled gallium orthophosphate ($GaPO_4$) piezoelectric pressure transducer was used for in-cylinder pressure measurement. An AVL 3066 piezo amplifier was used to condition the output of the GU21D. The piezoelectric transducer was ranged at 200 bar with a linearity of < ±0.3% full scale output. Its thermal sensitivity shift in

the 200°C to 300°C range is < ±0.5%. Its cyclic temperature drift and IMEP stability over a 10 hour test period is less than ±0.4 bar and 2% respectively.

Engine speed and crank angle (CA) positions were measured using an AVL 364C high precision optical crankshaft encoder. The angle information is transmitted by light pulses from the encoder through an optical cable to a light-to-current converter. The signal was then conditioned and sent to the data acquisition system. Crank angle measurement resolution was selectable down to 0.05°CA.

For this study, cycle averaging of 150 cycles and 0.5°CA resolution has been employed. Filtering of cylinder pressure data is required for accurate combustion analysis as rapid changes in pressure (dP) resulting from signal noise and in-cylinder acoustical resonance are highly amplified in the resulting heat release calculations. The pressure signal conditioning was accomplished using a low-pass digital filter. The simple digital low-pass filter provided by AVL's Concerto software was used for signal conditioning in the present study. Where convenient, a spreadsheet was used to calculate the combustion parameters.

4.5.4 Exhaust Gas Analysis

A gas analysis system was used to measure the concentration of gaseous components in the exhaust gas stream. Total hydrocarbons (THC), NO_x, CO_2 and CO concentrations were measured in the raw exhaust. Three heated stainless steel probes were inserted into the raw engine exhaust to a depth of 1.5" (38 mm) in a 4" (101 mm) exhaust line. These probes were connected to heated lines which transfer the sampled exhaust to the gas analyzers. The hydrocarbon line and probe were kept at a wall temperature of 375°F±10°F (191°C ± 5.5°C) while the other probes and lines were heated to 175°F±10°F (79°C ± 5.5°C). The temperatures were kept high to prevent condensation of water or volitile organic compounds

in the sample lines for the NO_x and CO samples and hydrocarbon compounds for the THC sample.

4.5.4.1 NO_x Analysis

Prior to entering the NO_x analyzer, significant sample conditioning is required to obtain an accurate and repeatable NO_x measurement. The sample line prior to the sample conditioner heated to above the dew point of the sample gas. After traveling the length of the sample line the sample gases first pass through a Horiba Model COM11, NO_2 to NO convertor. It is important to convert the NO_2 to NO before the water condenser due to substantial NO_2 absorption by water [167]. After exiting the NO_2 to NO convertor, the sample travels a very short distance to the water condenser. The water condenser used in this study was a Baldwin Model 8210 sample conditioner designed to remove water from the sample stream. This unit is rated to remove less than 10% of any remaining NO_2 from the sample stream while removing greater than 98% of the moisture during the condensation process. After moisture removal, the sample enters the NO_x analyzer. The indicated concentration was determined to be inversely proportional to the reaction chamber pressure. It is therefore important to monitor and control the reaction chamber pressure. This is accomplished by using a needle valve at the outlet of the analyzer upstream of the vacuum pump in this study. The ThermoEnvironmental Model 42C operation is based upon the concept that nitric oxide (NO) and ozone (O_3) react to produce a characteristic luminescence with intensity linearly proportional to the NO concentration. Infrared light emission results when electronically excited NO_2 molecules decay to lower energy states [166].

$$NO + O_3 \rightarrow NO^*_2 + O_2 \tag{4.14}$$

$$NO^*_2 \rightarrow NO_2 + h\nu \tag{4.15}$$

$$NO^*_2 + M \rightarrow NO_2 + M \tag{4.16}$$

In Equation 4.14, ozone reacts with nitric oxide to produce electronically excited nitrogen dioxide. This NO_2* can reach equilibrium either through photoemission (Equation 4.15) or by collisional energy transfer (Equation 4.16), where M represents a neutral molecular constituent within the sample gas mixture. The intensity of the photoemission is given by Equation 4.17 [166]:

$$I = \frac{k_1 k_2 [NO][O_3]}{k_2 + \sum k_{3M}[M]}, \tag{4.17}$$

where k_{3M} is a function of a specific third body or carrier gas. Because chemiluminescence analyzers measure this intensity, it is advantageous to decrease the probability of collisional de-excitation. This is conventionally accomplished by operation at sub-atmospheric pressures, typically less than 10 mm of Hg. Since k_3 is a function of the third body interaction, M, the chemical composition of the carrier gas also affects the measured intensity [168].

NO_2 is converted to NO by a stainless steel NO_2 to NO converter heated to about 635°C. The sample is then drawn into the analyzer through a particulate filter, a capillary, and then to the mode selection valve. The valve routes the sample either directly to the reaction chamber when the unit is operating in the NO mode or to the NO_2 to NO converter and then to the reaction chamber when the analyzer is in the NO_x mode. The NO_x mode was used in this study. Dry filtered air enters the analyzer through a flow sensor and then through a silent discharge ozonator which generates ozone for the chemiluminescent reaction. A

cooled photomultiplier tube (PMT) detects the NO_2 chemiluminescence. The detector operates in pre-set ranges from 10 ppm up to 5,000 ppm. Response time (T_{90}) is 5 seconds. Repeatability and linearity are both less than 1% full scale. Zero drift is less than 0.05 ppm in 24 hours. Span drift is less than 1% full scale per 24 hours. The NOx concentration is transferred to the data acquisition system via 4 - 20 mA analog output.

4.5.4.2 CO and CO_2 analysis

After traveling through a heated filter and heated sample line, sample gases enter a Baldwin Environmental Model 20410 thermoelectric sample gas conditioner which lowers the sample dew point to +5°C (41°F). Particulate matter that may have made it through the upstream heated filter was removed by a Baldwin sample prefilter located downstream from the cooler. The sample once conditioned, is directed to the gas analyzers. The reported soluble gas removal rates as percent of inlet gas concentration are NO: 0% loss, NO_2: <2% loss, CO: 0% loss, and CO_2: <1% loss. There were two analyzers used in this study, one for CO and one for CO_2 in the analyzer bay. The CO and CO_2 analyzers are Horiba Model VIA-510 infrared units. They are based on infrared absorption of the measured component. By determining the amount of attenuation of an infrared beam, the component concentration can be determined. The infrared radiation from a light source is passed through a rotating chopper and into the detection cell. Infrared radiation is absorbed as it passes through the sample. The light then reaches a detection cell which generates an electric current proportional to the incident light. The current is amplified and provided as a 4 - 20 mA analog output. The Horiba VIA-510 has a reproducibility of ±0.5% of fullscale and a zero and span drift of ±1.0% of full-scale per 24 hours.

4.5.4.3 Total Hydrocarbon Analysis

The sample gases were transferred directly into the heated Horiba FIA-236 flame ionization analyzer. No other conditioning was required because cooling the gas would result in condensation and loss in sample. The analyzer employed a burner/sensor where a regulated flow of sample gas entered a flame produced by reactions of a 40% hydrogen in helium fuel and hydrocarbon free air. The hydrocarbon components of the sample stream underwent a complex ionization that produced electrons and positive ions as shown in Equations 4.18-4.20 [166].

$$CH + O \rightarrow CHO^{+} + e^{-} \tag{4.18}$$

$$CHO^{+} + H_2O \rightarrow H_3O^{+} + CO \tag{4.19}$$

$$H_3O^{+} + e^{-} \rightarrow H_2O + H \tag{4.20}$$

Polarized electrodes then collect the ions that are produced, causing current to flow through the associated electronic measuring circuitry. The current flow is proportional to the carbon atom concentration. The model FIA-236 measured in set ranges from 10 ppm up to 30,000 ppm, with a T_{90} of 1.5 seconds. Sensitivity was 0.5% of full scale on each range while repeatability and linearity were both less than 1% full scale. Zero span drift was less than 1% full scale per eight hours. The analog output was 0 -5 VDC non-isolated.

4.5.5 Engine Test Experimental Setup and Procedure

The goal of the engine testing was to study how the engine operated when ignited by the test laser and by the commercial laser and to show any similarities or differences. The commercial laser system was used in a number of previous research efforts, listed in Chapter

3, that showed improvements in engine operation and emissions production. The current engine testing is limited by the repetition rate of the test laser. If the engine testing results for the two laser systems are similar then one can assume that the test laser will produce results similar to the commercial laser at the higher repetition rate. The optical arrangements as well as the operational procedures for the ignition testing were similar. The optical arrangement for the commercial laser testing is shown in Figure 4.15.

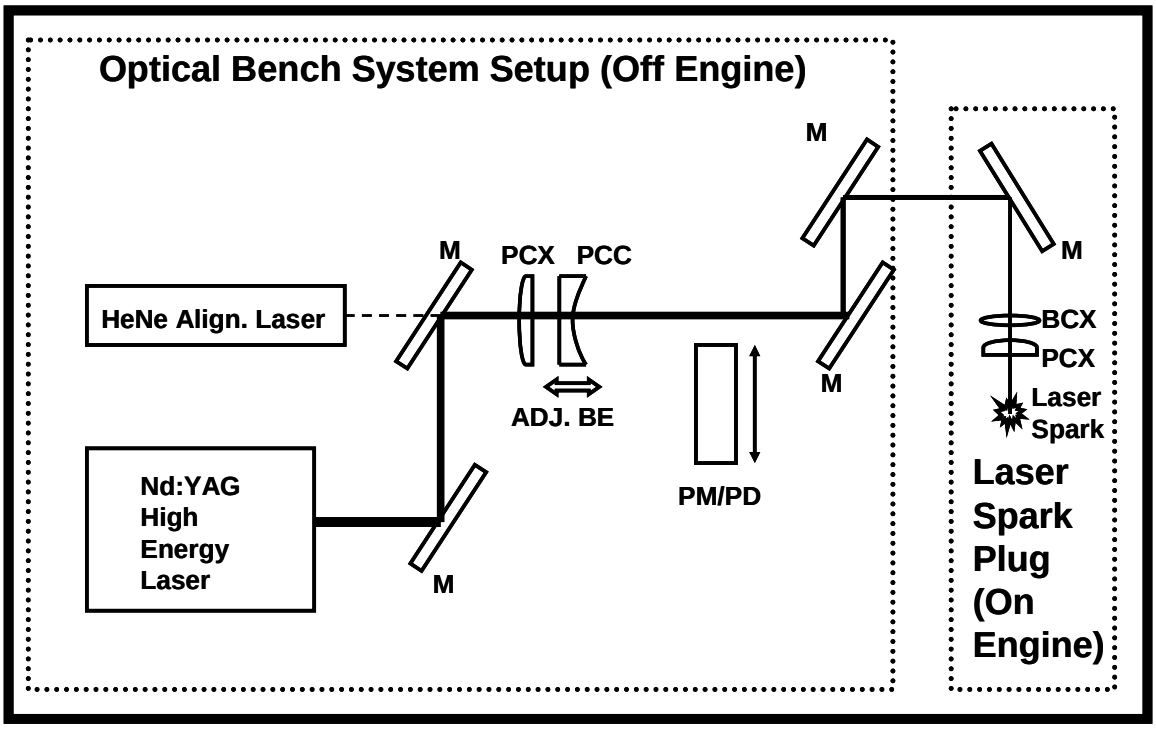

Figure 4.15: Commercial laser engine test optical setup

The commercial laser used was a New Wave Research Tempest-20 flashlamp pumped actively Q-switched laser system. The output of the commercial laser was reflected off of two mirrors (M) such that is was made coaxial with a Helium-Neon alignment laser. The laser output was then directed through a two element beam expander that consisted of a fixed plano-convex (PCX) lens with a focal length of 100 mm and a movable plano-concave (PCC) lens with a focal length of 50 mm. The output of the beam expander was then

directed through a set of two steering mirrors that pointed the laser output from the optics table to the engine optics. A movable power meter (PM) and photodiode (PD) setup was employed between the beam expander and the steering mirrors to monitor the laser output characteristics. Once the laser output reached the on-engine optics a single turning mirror directs the energy through a sapphire lens, that also acted as a pressure barrier, for focusing into the combustion chamber. A photo of the commercial laser optical setup is shown in Figure 4.16. This photo shows the optical bench setup including the commercial and alignment lasers, turning mirrors adjustable beam expander and steering mirrors.

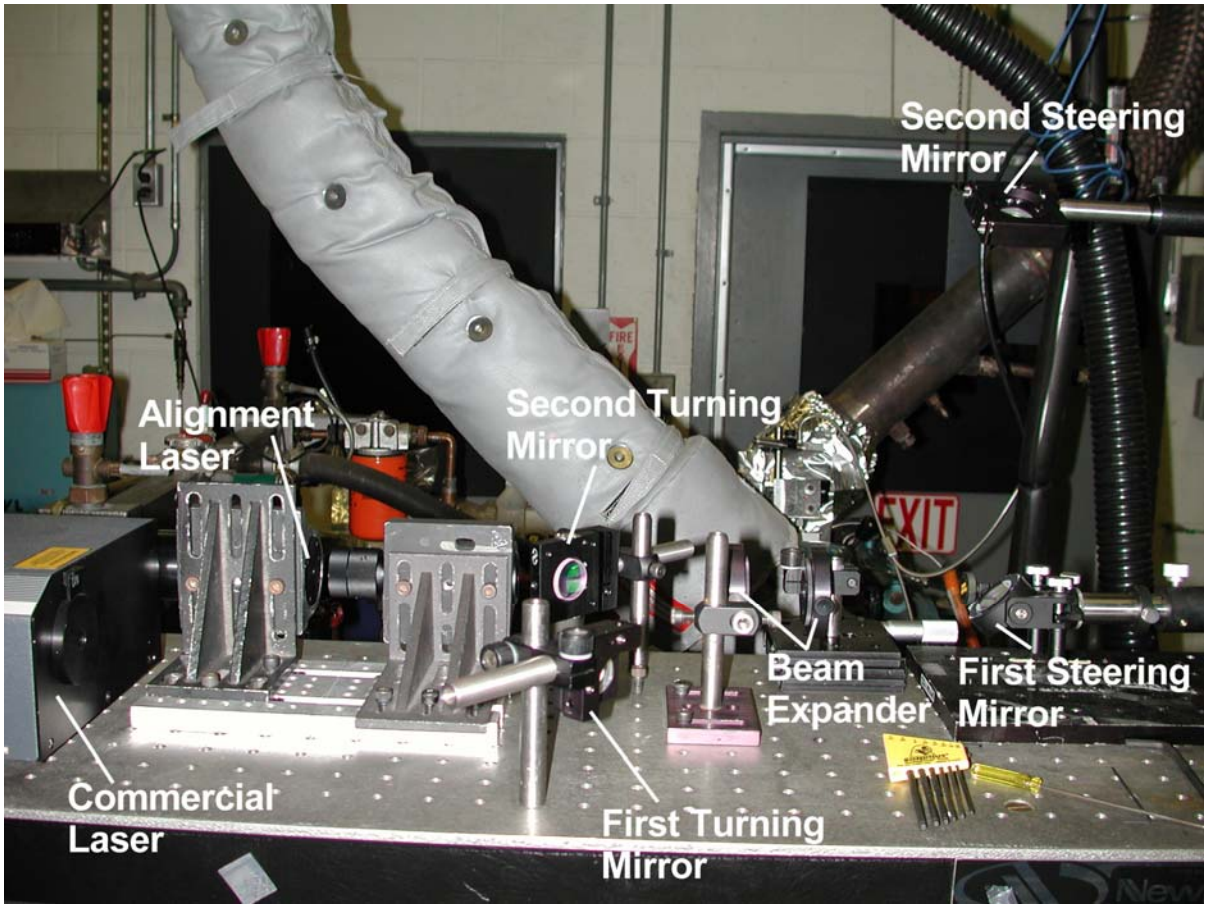

Figure 4.16: Commercial laser engine laboratory optical bench setup

The test laser (TL) was able to make use of a less complicated optical setup due to the optical access through the cavity. The alignment laser (AL) was directed through the high reflector of the test laser and continued on through the output coupler. This arrangement was used to align the laser as well as align the optical path to the engine. This setup is shown in Figure 4.17.

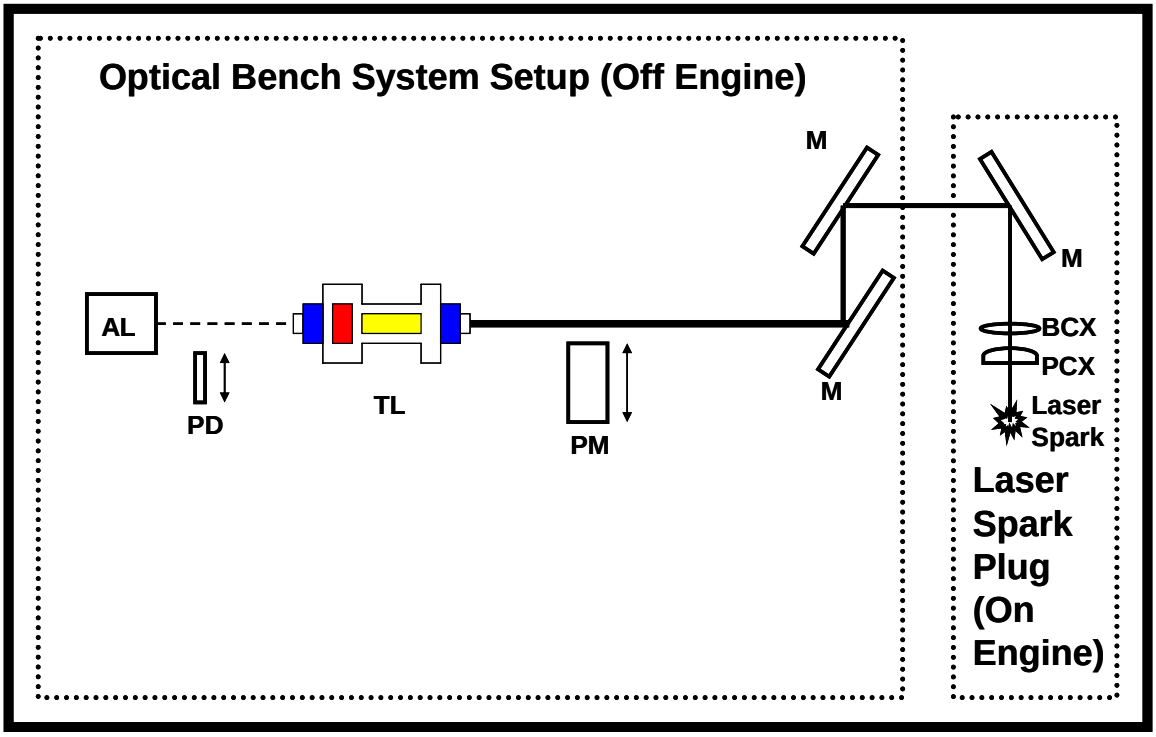

Figure 4.17: Test laser engine test optical setup

The output pulsewidth was monitored by a photodiode placed behind the high reflector. The output pulse energy was measured between the laser and the steering optics before the output is directed to the engine optics. The test laser electrical and optical setup differed slightly from the optical experimental testing. Figure 4.18 shows the functional block diagram of the test laser engine setup.

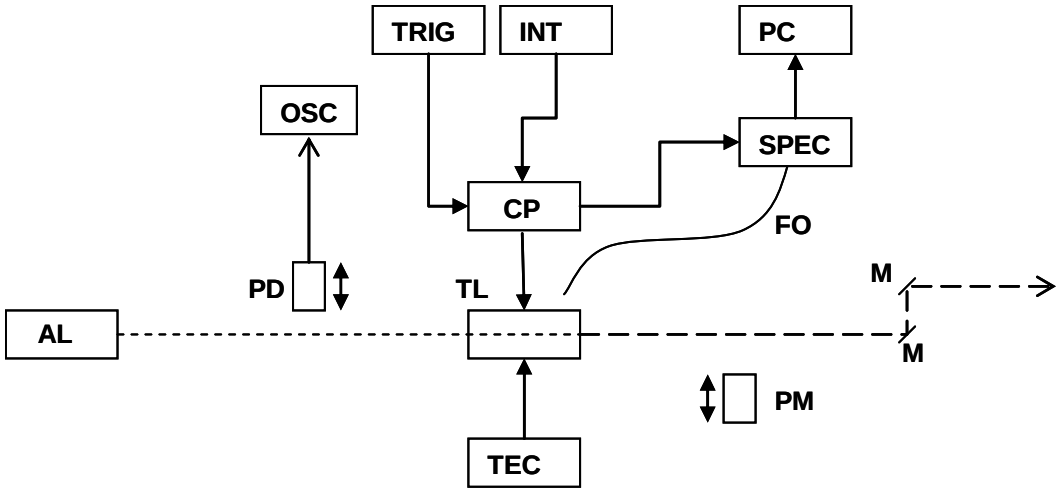

Figure 4.18: Test laser functional block diagram for engine testing

As discussed in the previous figure the alignment laser was directed through the laser and to the steering mirrors and onto the engine. The laser diode current pulser (CP) used either the interal (INT) triggering or the external triggering (TRIG) depending on whether the laser was being used with or without the engine motoring. The current pulser was synchronized with a miniature spectrometer (SPEC) used to monitor the output wavelength of the laser diode pumps. A fiber optic (FO) was used to collect the stray light from the diode pumps and direct it into the spectrometer where a PC was used to display the spectral data for feedback purposes. A thermoelectric cooler (TEC) controller was used in conjunction with the spectrometer output to adjust the temperature and subsequent output wavelength of the laser diodes operating at approximately 5 Hz. Figure 4.19 shows a photo of the test laser optical setup. The optical setup photo shows the alignment laser in line with the photodiode test laser and power meter. After the power meter the optical setup is identical to the commercial laser setup.

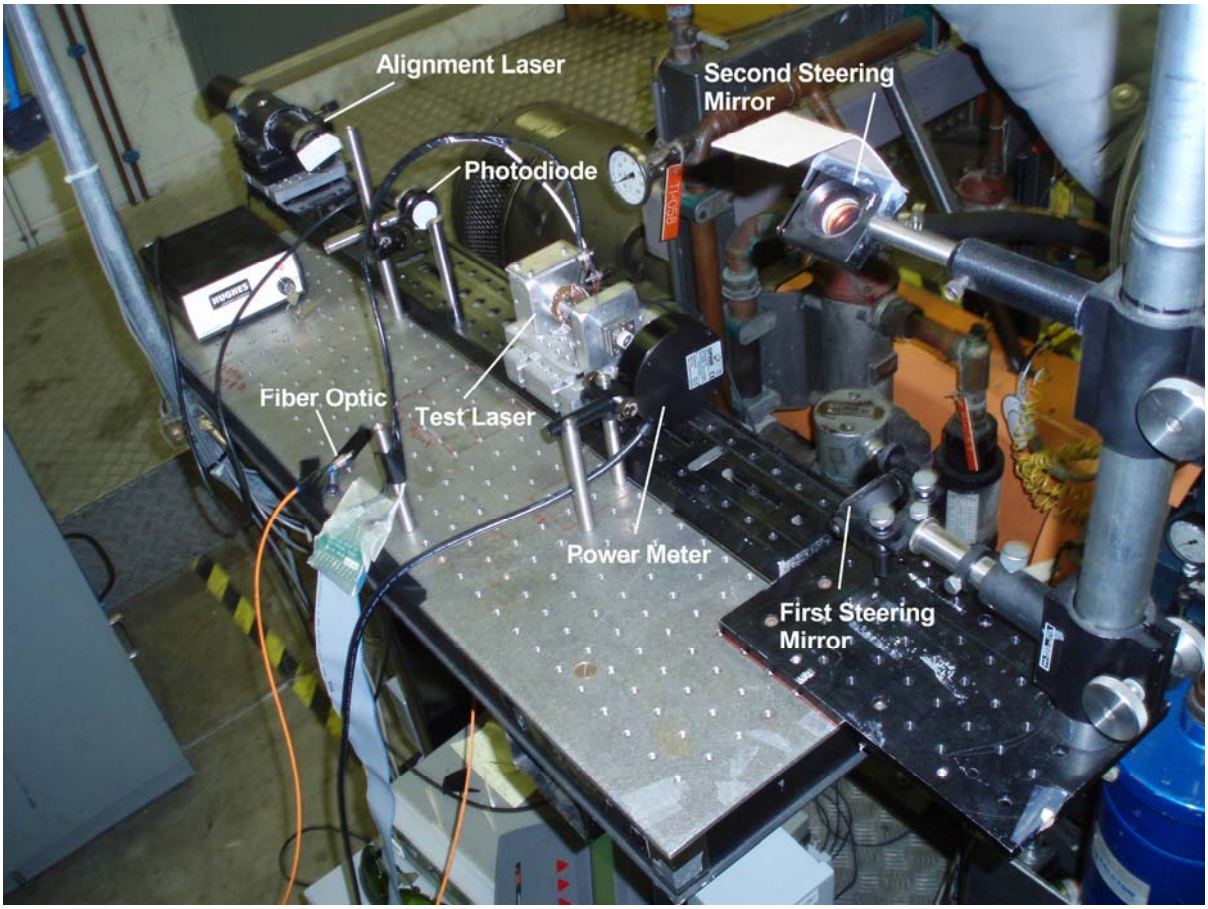

Figure 4.19: Test laser engine laboratory optical bench setup

Figure 4.20 shows the engine side of the sapphire window/lens adaptor with the spark plug hole to laser optics adaptor. Figure 4.21 shows a photo of the turning mirror arrangment connected to the sapphire window/lens adaptor. Figure 4.22 shows the assembly from Figure 4.21 installed on the engine.

Figure 4.20: View of engine side of the sapphire window/lens (left) and the spark plug adaptor showing the optical access cavity (right)

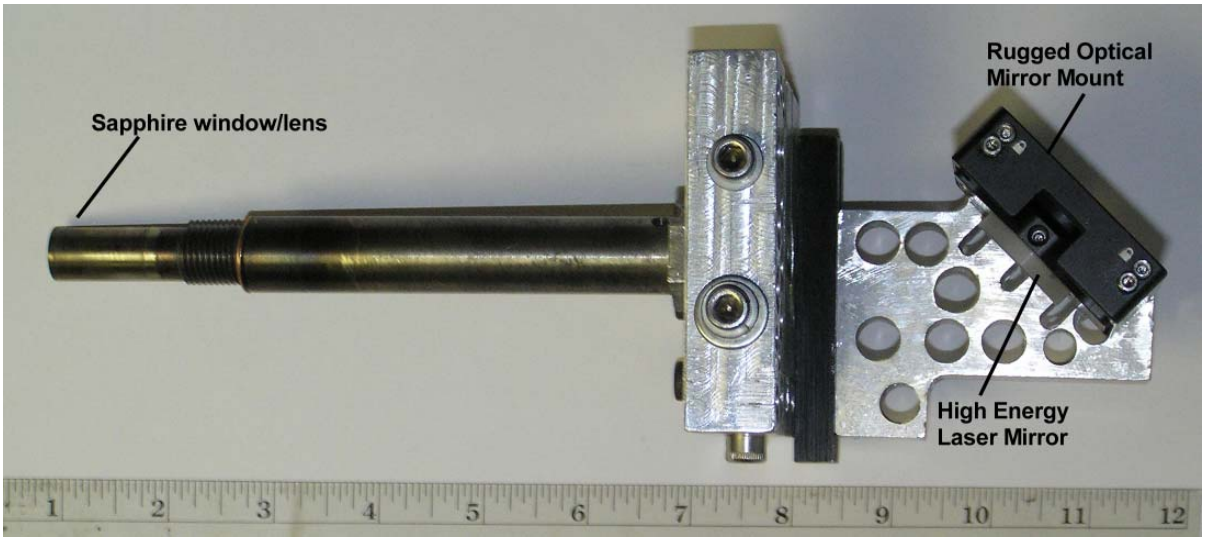

Figure 4.21: On-engine optical arrangement without spark plug adapter

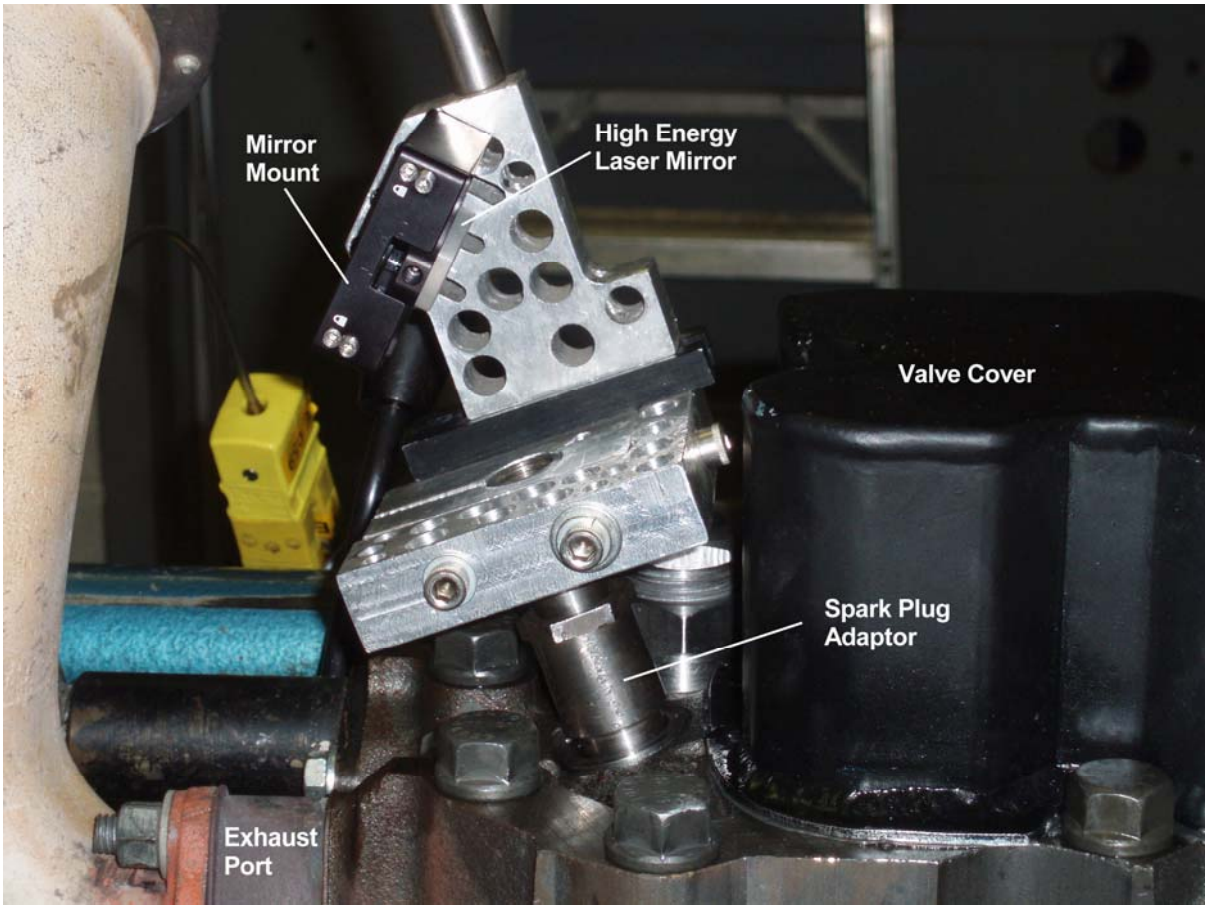

Figure 4.22: On-engine optical arrangement installed with spark plug adapter

The focusing optics were a combination of a bi-convex (BCX) lens and a plano-convex lens whose combined focal length was approximately 12mm. Previous experimentation used a single plano-convex sapphire lens with a focal length of approximately 31 mm. This lens also acted as the pressure barrier between the combustion chamber and ambient, which is illustrated in Figure 4.23 (A).

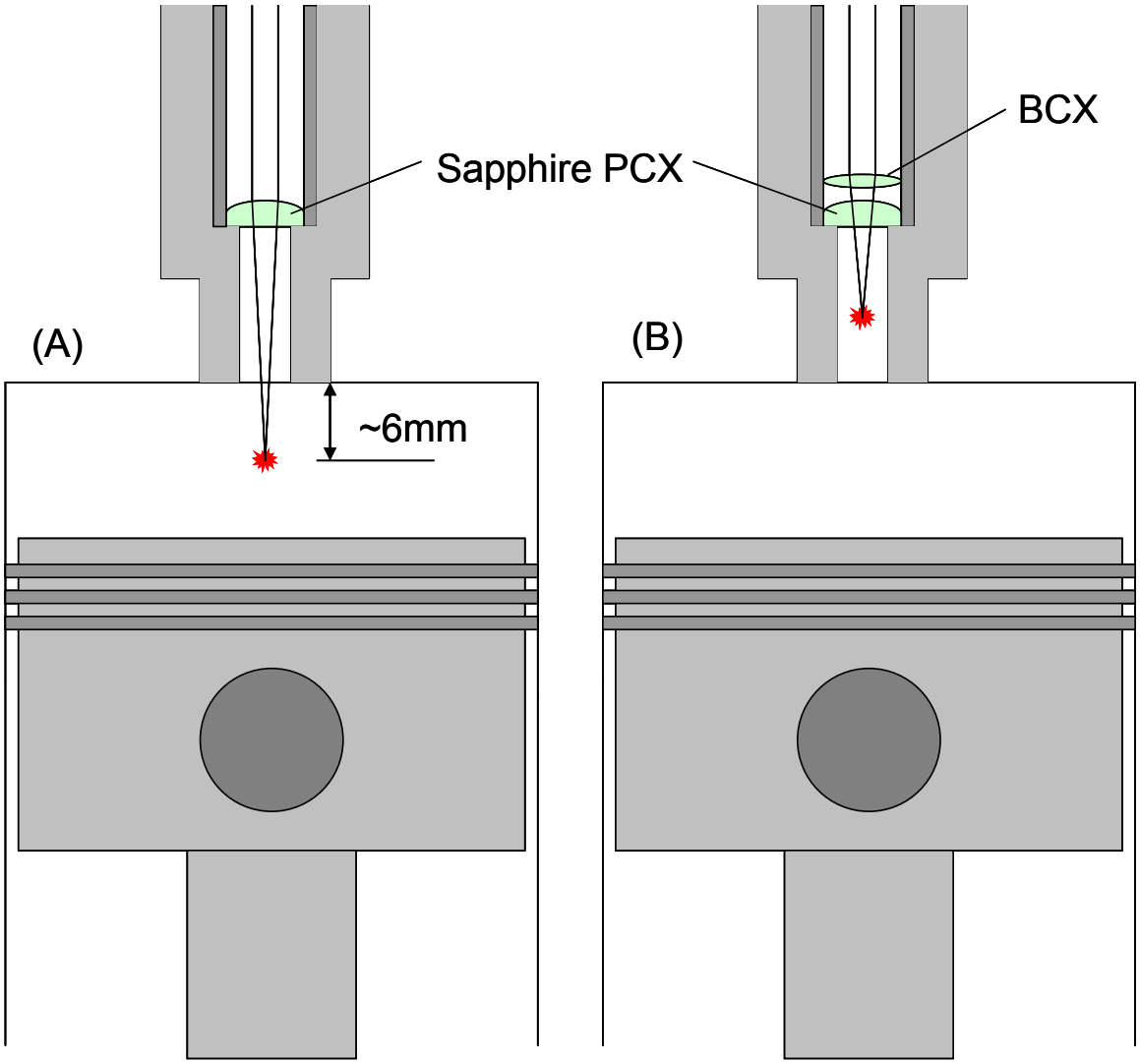

Figure 4.23: Schematic illustrating the original ignition location (A) and the new location due to the addition of the extra lens (B) [Not to scale]

Previous work [9-12,21] used only the sapphire window/lens with a focal length of approximately 31 mm such that the focal spot would produce a spark approximately 6 mm below the bottom of the head and above the piston crown. This arrangement kept the spark away from the walls of the combustion chamber to reduce quenching effects and enhance the propagation of the flame front evenly across the combustion chamber.

The current setup used an additional lens placed upstream from the sapphire lens to modify the focal length of the assembly as shown in Figure 4.23 (B). The additional lens was

a fused silica bi-convex lens with a focal length of approximately 18 mm. The addition of this lens shortened the overall focal length of the setup to approximately 11 mm. This was done to improve the spark performance of the test laser due to multimode output production. Shortening of the focal length provides a smaller focal spot which greatly increases the focal intensity of a given output pulse. Unfortunately this placed the laser spark well inside the optical access cavity shrouding the spark. This was not the preferred setup due to the adverse combustion issues that it caused, which will be discussed in the next chapter. This arrangement did however allow the sporadic multimode output of the test laser to consistently produce sparks for engine testing. This modification was the primary reason for not making an additional engine operational comparison with an electrical ignition system. It was felt that the spark location produced by the modified optics could not be sufficiently reproduced with an electrical ignition system.

Although the test laser performed well in the optics laboratory and consistently produced sparks under tightly controlled conditions this "good behavior" did not transfer into the engine laboratory. Due to design deficiencies of the test laser it was not able to properly and symmetrically reject the heat built up over prolonged operation at the higher repetition rates encountered during engine testing. The inability to sufficiently shed the proper amount of heat led to minor problems with the alignment of the laser due to thermal expansion in the chassis. Therefore the laser had to be "warmed up" slowly to ensure even heat distribution to maintain proper alignment. In addition to the problem of misalignment was the the issue of sporadic multimode output. This problem is illustrated in Figure 4.24.

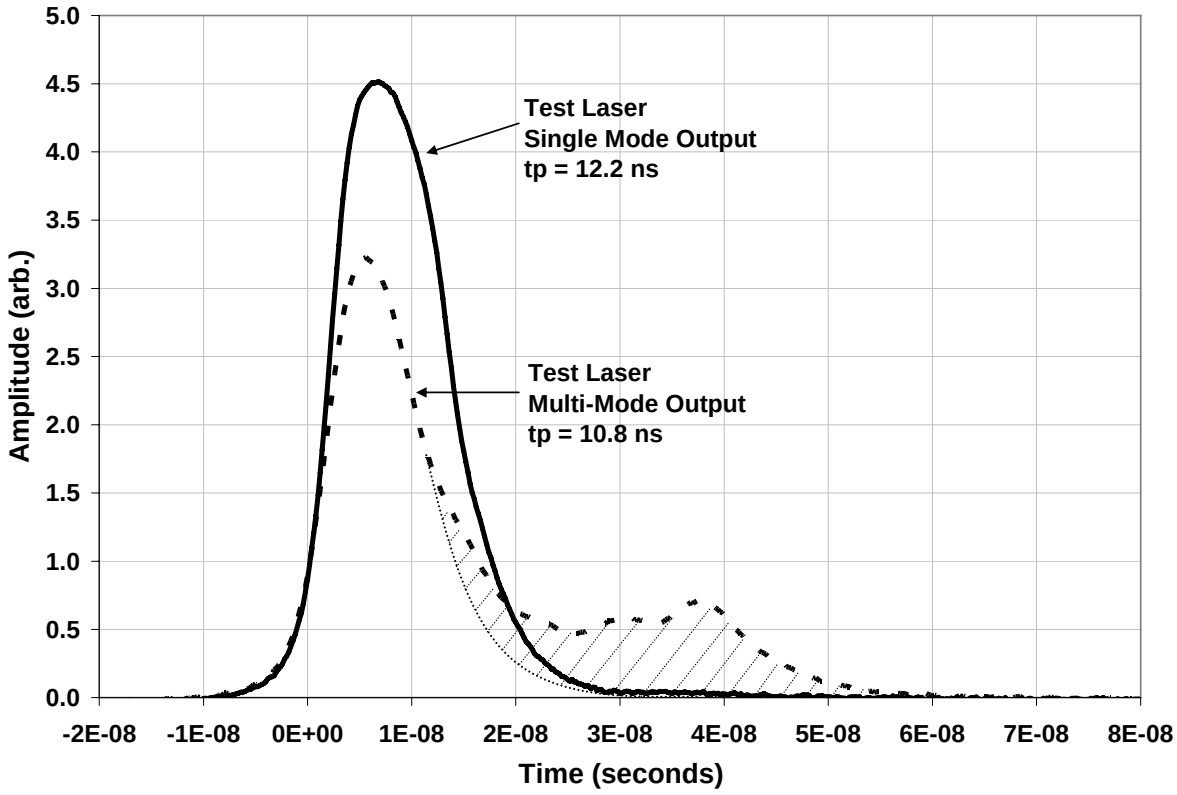

Figure 4.24: Output pulse shapes for the test laser and the commerical laser

The sporadic multimode output is thought to be caused by an uneven excited state distribution within the laser rod and subsequently the Q-switch. This is thought to cause two or more distinct areas of excitation within the cross-section of the laser rod. This is illustrated schematically in Figure 4.25 where the top laser diode array is minutely closer to the laser rod and therefore produces a broader area of excitation. Figure 4.25 is not to scale, however it serves to show how a minute degree of asymmetry can significantly affect the inner workings of the laser system. Figure 4.26 shows an optimal or preferred side pumping optical arrangement with the available equipment.

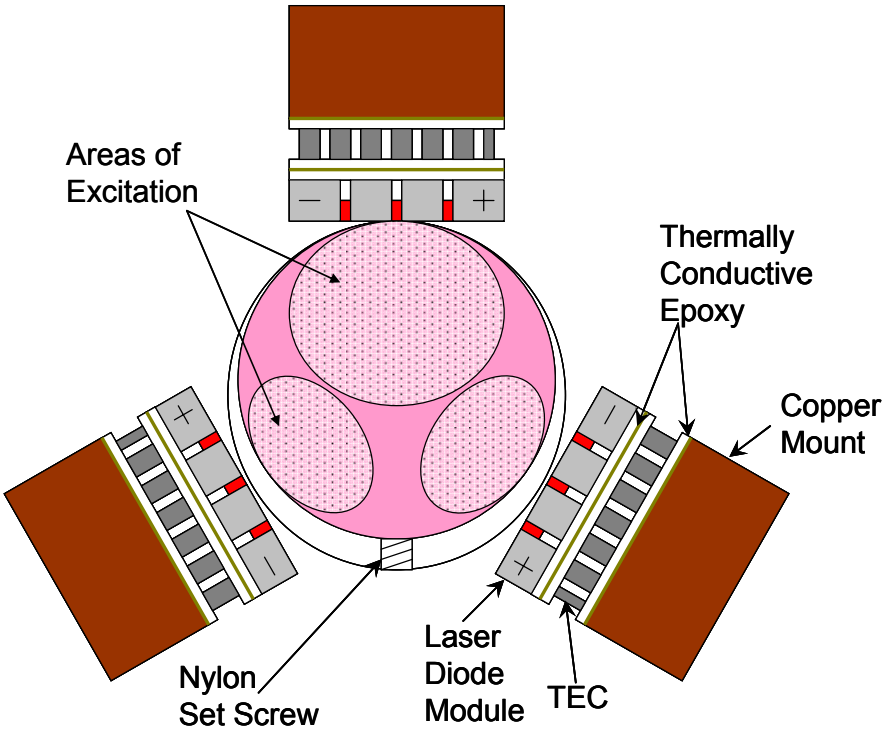

Figure 4.25: Cross section of laser pump arrangement showing uneven pump distribution [not to scale]

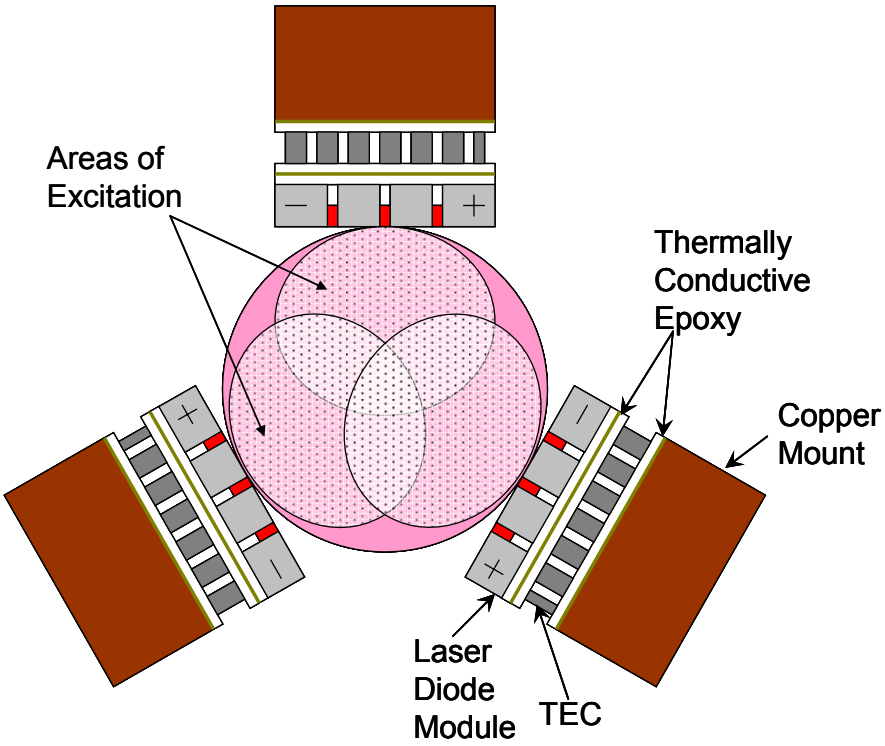

Figure 4.26: Cross section of pump arrangement showing preferred pump distribution [not to scale]

The slight asymmetry produced by the set screw produces two distinct excited regions within the laser rod cross section. The use of the set screw further compounds the problem by only allowing one avenue for heat removal from the laser rod. This asymmetry in the heat removal induces a nonuniform refractive index gradient across the cross section of the laser rod. This index gradient acts as a weak lens further distorting the laser light as it passes throught the cavity. The combination of the asymmetries with the excitation and heat flow could produce the multimode output behavior. The amount of energy contained in the cross hatched area of the multimode output pulse in Figure 4.24 is approximately a third of the total output pulse energy. Looking back at the optical preliminary experimentation section for the laser design and testing it can be seen that as the laser is pumped harder the output pulse delay becomes shorter and shorter. It is hypothesized that the geometric asymmetry provided by the set screw produces a slightly less excited region within the laser rod whose output is minutely delayed and therefore is out of synchronization with the larger more excited region of the laser rod. Under the strict operational and environmental conditions of the optics laboratory this issue could be mitigated through lower repetition rate operation and careful alignment. However under the more harsh conditions seen in the engine test laboratory with higher repetition rates, thermoelectric cooling, engine heat, etc. the laser could not be aligned to consistently produce single mode output pulses therefore the shorter focal length arrangement had to be employed. The excess heat produced by the operating the laser at higher repetition rates limited the operation of the laser system to 5 Hz, or an engine speed of approximately 600 rpm. This engine speed is typically an idling condition for large power generation reciprocating engines but, this engine speed was sufficient to demonstrate the operation of the test laser and the commercial laser for comparison.

The test laser optical components and input parameters are listed in Table 4.1. This particular combination of optics was chosen because produce the highest and most consistent output with the least amount of alignment difficulty.

Table 4.1: Test laser optical component and input parameter list

Output Coupler Reflectivity – R	30%
Q-switch Initial Transmission – To	40% + 80% = 32%
Neodymium Concentration – Nd	0.5%
Laser Diode Electrical Power	~2006 Watts
Average Electrical Power at 1 Hz 500 μs pulsewidth	~1 Watt
Average Electrical Power at 5 Hz 500 μs pulsewidth	~5 Watts
Laser Diode Optical Output	~1007 Watts
Average Optical Power at 1 Hz 500 μs pulsewidth	~0.5 Watt
Average Optical Power at 5 Hz 500 μs pulsewidth	~2.5 Watts

The laser output parameters used in the engine study are listed in Table 4.2. Two output columns are listed for the test laser one for single mode output and the other for multimode output. The commercial laser output energy was selected to match the output pulse energy. When this commercial laser system is operated so near the output threshold the output pulse width becomes much broader than at the higher output conditions and deviates significantly from the data sheet specifications. Unfortunately, this operational quality of the commercial laser system was not discovered until after the engine testing had been performed and the apparatus disassembled. This is the primary difference in the values listed in Table 4.2 between the test and commercial laser outputs.

Table 4.2: Laser output engine test parameters list

Parameter	Test Laser (Single Mode Output)	Test Laser (Multi mode Output)	Commercial Laser
Output Energy (mJ)	23	~16	23
Output Pulsewidth (ns)	10	9	18
Peak Power (MW)	2.3	1.7	1.27
Beam Quality or M^2	6.55		6.25
Beam Diameter (mm)	~3		~3
Estimated Focal Intensity (Watts/cm2) [31mm focal length]	$3.9x10^{10}$	$2.8x10^{10}$	$2.2x10^{10}$
Estimated Focal Intensity (Watts/cm2) [11mm focal length]	$2.7x10^{11}$	$1.9x10^{11}$	$1.5x10^{11}$

The engine test plan consisted of three replications of three equivalence ratios randomized for each laser ignition system. All other independent variables were to remain constant. Preliminary engine operation with the test laser allowed for the determination of an acceptable range of values for Phi that would not cause misfire or knock. Table 4.3 lists the target equivalence ratio values for each test in the sequence that they were performed.

Table 4.3: Randomized test matrix for engine study

Test Number	Test Laser Phi	Commercial Laser Phi
1	0.8	1.0
2	0.9	0.8
3	0.9	0.9
4	0.8	0.9
5	1.0	1.0
6	0.9	0.8
7	1.0	1.0
8	0.8	0.9
9	1.0	0.8

The engine test procedure begins with energizing all of the emissions and data collection equipment. The gas analyzers are then calibrated with seven to nine-point calibration curves generated using least squares regression in accordance with the requirements of CFR 40, part 86, subpart N. All calibration gases are NIST traceable with analytical uncertainty of less than ±1.0%. Leak checks on all analytical lines were performed in accordance with NETL engine research laboratory leak check procedures [169]. The engine is then rotated by hand to ensure smooth rotation before the dynomometer is energized to motor the engine. The supply air valve is opened and the engine is motored up to 10 rev/s. The output trigger to the laser is enabled and verified by switching the laser system over to external control and ensuring that the laser produces sparks in time with the engine. Optical path adjustments are made at this time if necessary. In the case of the commercial laser system the beam width entering the engine optics is checked and adjusted if needed. The fuel supply is then opened

while an operator adjusts a fine control needle valve while monitoring the output of the mass flow meter to ensure the correct equivalence ratio. Once the proper equivalence ratio is reached the system was allowed to run for at least two minutes. At the end of the two minutes the low speed data logging was recorded into a spreadsheet. The high speed data acquisition software was then activated to record one hundred consecutive engine cycles. The equivalence ratio setpoint was then changed and allowed to settle out for the next data recording cycle. This was repeated until all target equivalence ratios were examined at which time the fuel supply to the engine was closed. The ignition signal to the laser system was then disabled and the engine was stopped. Post processing of the data was then performed for analysis. The exact engine operating conditions are listed in the results section.

5 Results and Discussion

The following chapter provides a discussion of the optical experimental data and engine test data. The raw data from the optical experimental investigation is tabulated in the Appendix E.

5.1 Optical Laboratory Results

The optical laboratory results section examines the data produced from the optical laboratory testing and development of the laser spark plug. The data points represent the mean of three recorded values for each curve. The error bars for each data point represent a 95% confidence interval of the mean. The data used to produce each plot was also analyzed through multi-linear regression. This analysis was intended to show whether or not relationships existed between measured independent and dependent variables. The regression equation produced by the regression analysis was also plotted with the experimental data. The trend lines were produced from the overall regression of the plotted data in each figure, and not of the individual plotted curves. This was done to provide a visual aid whereby estimates of the variable relationships could be made depending on the orientation of the trend lines and the data. The significance of these relationships and the likely physical reasons for this behavior is discussed.

5.1.1 Output Pulse Energy

Section 5.1.1 examines the dependence of the output pulse energy on the values of the Q-switch initial transmission, the output coupler reflectivity, Neodymium (Nd) concentration, and the input power level. Figures 5.1-5.3 show the dependence of the output pulse energy on the output coupler reflectivity and the Q-switch initial transmission with

varying values of Nd concentrations of 0.35%, 0.50%, and 0.75% respectively. Figure 5.1 indicates an overall range of operation of 18.42-27.91 mJ, where all test points produced sparks.

The three levels of Q-switch initial transmission produced significantly different output pulse energy levels with respect to the 95% confidence intervals, for all levels of output coupler reflectivity except the highest level. Table 5.1 shows the results of the regression analysis of the data plotted in Figure 5.1. The adjusted R-squared value indicates that the linear model was a useful fit. Both independent variables contribute significantly to the model because of the respectively small p-values. The plotted trend lines are from the regression of the entire data set plotted in Figure 5.1 and do not represent individual regression lines of the plotted curves. This was done to produce a visual aid when examining the overall fit of the regression analysis to the data set. The coefficients of the linear regression model were combined with the test variables to produce the trend lines shown in Figure 5.1. This has been done throughout Section 5.1. The slope of the trend lines indicates the significance of the output coupler reflectivity. The greater the slope the greater the contribution of the independent variable. A large spacing of the trend lines is an indication of a significant dependence of the output on the Q-switch initial transmission value. The larger the distance between the trend lines the greater the contribution of the secondary input variable, Q-switch initial transmission (T_o).

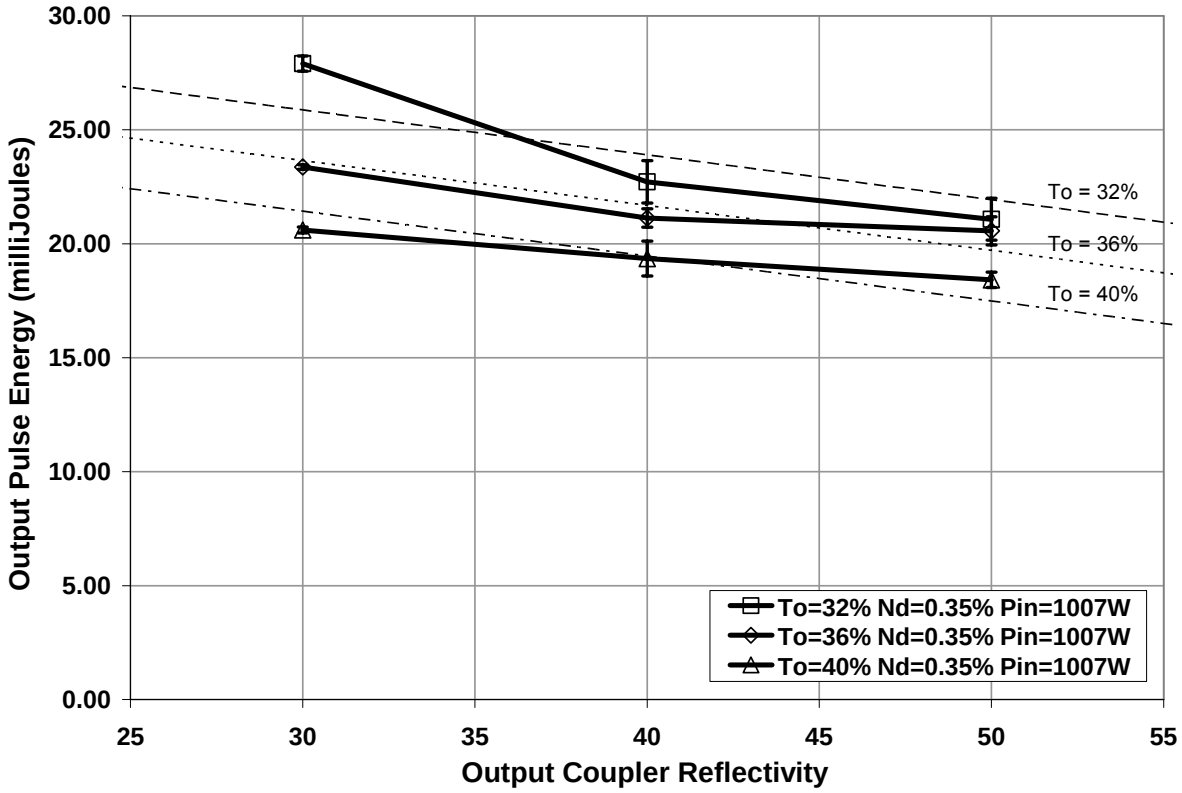

Figure 5.1: Output pulse energy response as a function of output coupler reflectivity and Q-switch initial transmission with Nd concentration of 0.35% at an input power of 1007 Watts

Table 5.1: Regression analysis of data plotted in Figure 5.1

Regression Statistics	
Multiple R	0.913
R Square	0.834
Adj. R Square	0.820
Standard Error	1.149
Observations	27

ANOVA

	df	*SS*	*MS*	*F*	*Significance F*
Regression	2	158.700	79.350	60.140	4.487E-10
Residual	24	31.670	1.319		
Total	26	190.400			

	Coefficients	*Standard Error*	*t Stat*	*P-value*	*Lower 95%*	*Upper 95%*
Intercept	49.560	2.676	18.520	1.015E-15	44.040	55.080
OC % Reflect.	-0.200	0.027	-7.280	1.620E-07	-0.250	-0.140
QSW % To	-0.560	0.068	-8.210	2.007E-08	-0.700	-0.420

The F-test indicates that the null hypothesis should be rejected and that at least one input variable significantly contributes to the variability within the response. The small P-

values indicate that both the output coupler reflectivity and the Q-switch initial transmission produce a statistically significant contribution to the output pulse energy variability. The data shows a significant increase in the output pulse energy when both the output coupler reflectivity and the Q-switch initial transmission values are decreased. The ouput pulse energy increases with decreasing output coupler reflectivity because less feedback is given to the gain medium during the pumping process. The lower feedback results in fewer stimulated emission events, therefore it takes more time for the system to reach the lasing threshold. This additional time allows for greater optical storage and subsequent higher output pulse energies when lasing occurs. The optical energy storage is primarily a function of pump power and pump time until the media is saturated. When the output coupler reflectivity is increased the additional feedback causes the laser media to produce more stimulated emissions and thereby saturate the Q-switch faster. The quicker saturation induces lasing with a shorter pump time therefore the stored optical energy is much lower than if the lasing were held off for a longer period of time. This explains the negative slope of the curves in Figures 5.1-5.3.

The reduction of the Q-switch initial transmission also holds off lasing due to the increased optical density. The increased opacity requires more time for a given optical combination to reach the lasing threshold at a given pump level. Therefore the lower the Q-switch initial transmission the more energy that is stored in the gain medium at the onset of lasing. This explains the spacing between the curves in Figures 5.1-5.3 where the lower Q-switch initial transmission results in higher output pulse energy.

Figure 5.2 indicates an operation range of 17.49-27.93 mJ. Twenty five of the twenty seven test points produced sparks. The lowest level of output coupler reflectivity produces

significantly different output pulse energy for all three levels of Q-switch initial transmission. At the higher two levels of output couple reflectivity, two values of Q-switch initial transmission produce statistically identical values of output pulse energy. Table 5.2 shows the results of the regression analysis of the data plotted in Figure 5.2. The results indicate that the linear model was a good fit and that both independent variables contribute significantly to the model. The plotted trend lines from the regression also indicate the significance of the contributions from each variable. The slope of the trend lines indicates the significance of the output coupler reflectivity. The spacing of the trend lines is an indication of a significant dependence of the output on the Q-switch initial transmission value.

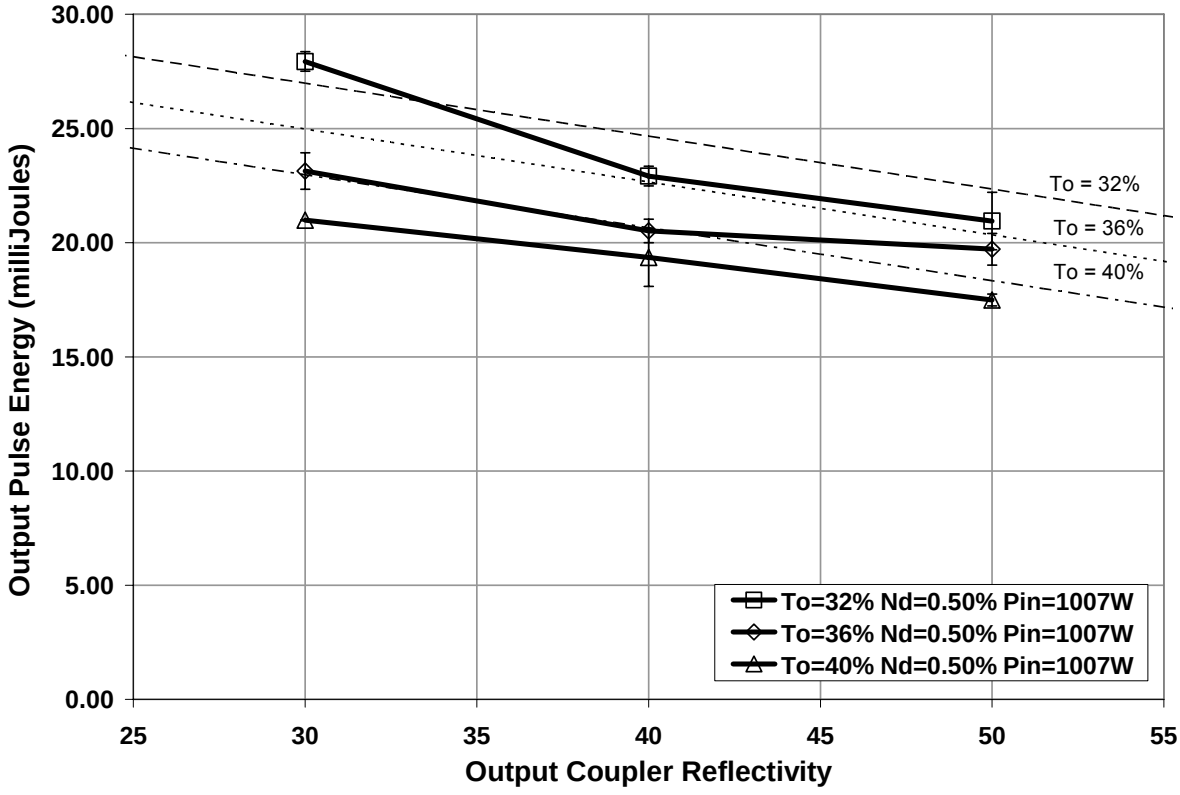

Figure 5.2: Output pulse energy response as a function of output coupler reflectivity and Q-switch initial transmission with Nd concentration of 0.50% at an input power of 1007 Watts

Table 5.2: Regression analysis of data plotted in Figure 5.2

Regression Statistics	
Multiple R	0.901
R Square	0.813
Adj. R Square	0.797
Standard Error	1.274
Observations	27

ANOVA

	df	SS	MS	F	Significance F
Regression	2	169.000	84.510	52.060	1.868E-09
Residual	24	38.960	1.623		
Total	26	208.000			

	Coefficients	Standard Error	t Stat	P-value	Lower 95%	Upper 95%
Intercept	48.970	2.968	16.500	1.339E-14	42.850	55.100
OC % Reflect.	-0.230	0.030	-7.720	5.923E-08	-0.290	-0.170
QSW % To	-0.500	0.075	-6.670	6.650E-07	-0.660	-0.350

Figure 5.3 shows a range of operation between 14.18-26.70 mJ and all but two of the twenty seven data points produced sparks. The settings of the Q-switch initial transmission produce significantly different results for all values of the output coupler reflectivity except 40%. Table 5.3 shows the results of the regression analysis of the data plotted in Figure 5.3. The results indicate that the linear model was a good fit and that both independent variables contribute significantly to the model. The plotted trend lines from the regression also indicate the significance of the contributions from each variable. The slope of the trend lines indicates the significance of the output coupler reflectivity. The spacing of the trend lines is an indication of a significant dependence of the output on the Q-switch initial transmission value.

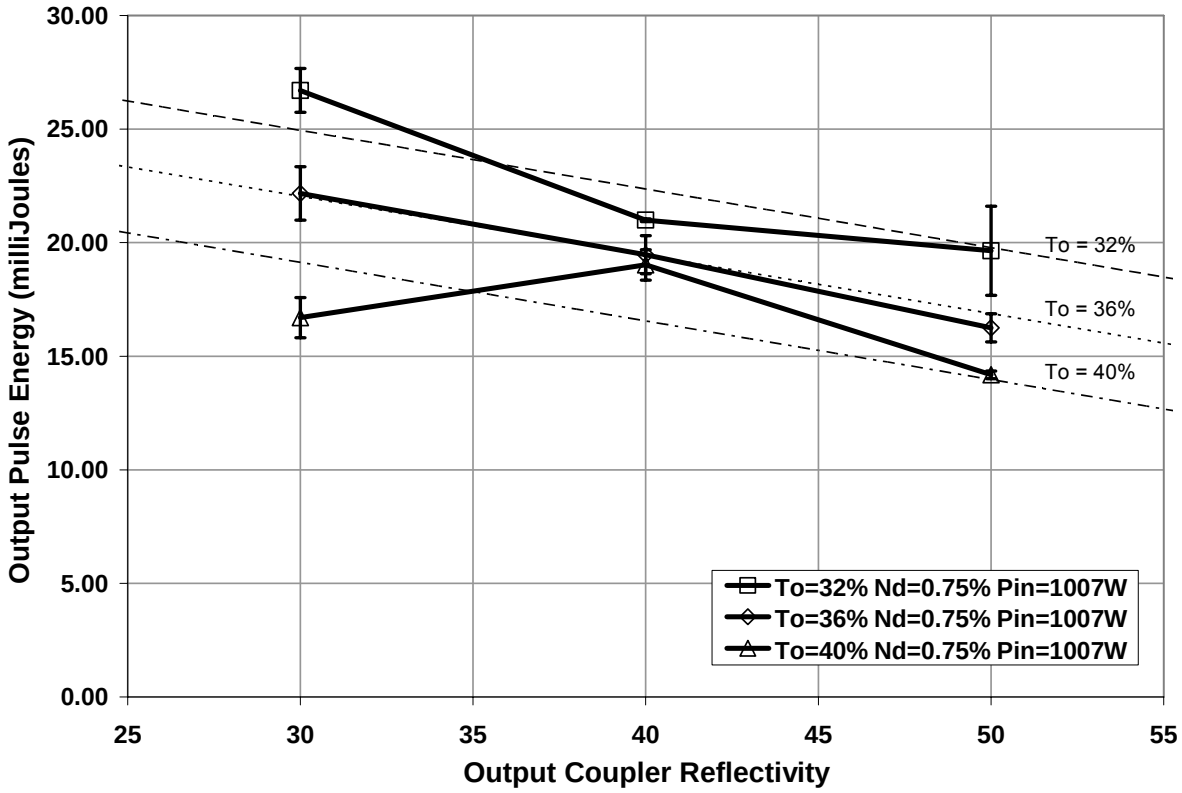

Figure 5.3: Output pulse energy response as a function of output coupler reflectivity and Q-switch initial transmission with Nd concentration of 0.75% at an input power of 1007 Watts

Table 5.3: Regression analysis of data plotted in Figure 5.3

Regression Statistics	
Multiple R	0.898
R Square	0.806
Adj. R Square	0.789
Standard Error	1.654
Observations	27

ANOVA

	df	SS	MS	F	Significance F
Regression	2	271.900	135.900	49.700	2.930E-09
Residual	24	65.640	2.735		
Total	26	337.500			

	Coefficients	Standard Error	t Stat	P-value	Lower 95%	Upper 95%
Intercept	55.930	3.852	14.520	2.205E-13	47.980	63.880
OC % Reflect.	-0.260	0.039	-6.620	7.522E-07	-0.340	-0.180
QSW % To	-0.730	0.097	-7.450	1.082E-07	-0.930	-0.530

Figure 5.4 shows the output pulse energy as a function of the output coupler reflectivity for three different values of Nd concentration. The output pulse energy values

are not easily distintuished at a 0.05 level of significance for the varying values of Nd concentration. Table 5.4 shows the results of the regression analysis of the data plotted in Figure 5.4. The results indicate that the linear model was a good fit and that both independent variables contribute significantly to the model. The plotted trend lines from the regression also indicate the significance of the contributions from each variable. The slope of the trend lines indicates the significance of the output coupler reflectivity. The spacing of the trend lines is an indication of a significant dependence of the output on the Nd concentration values.

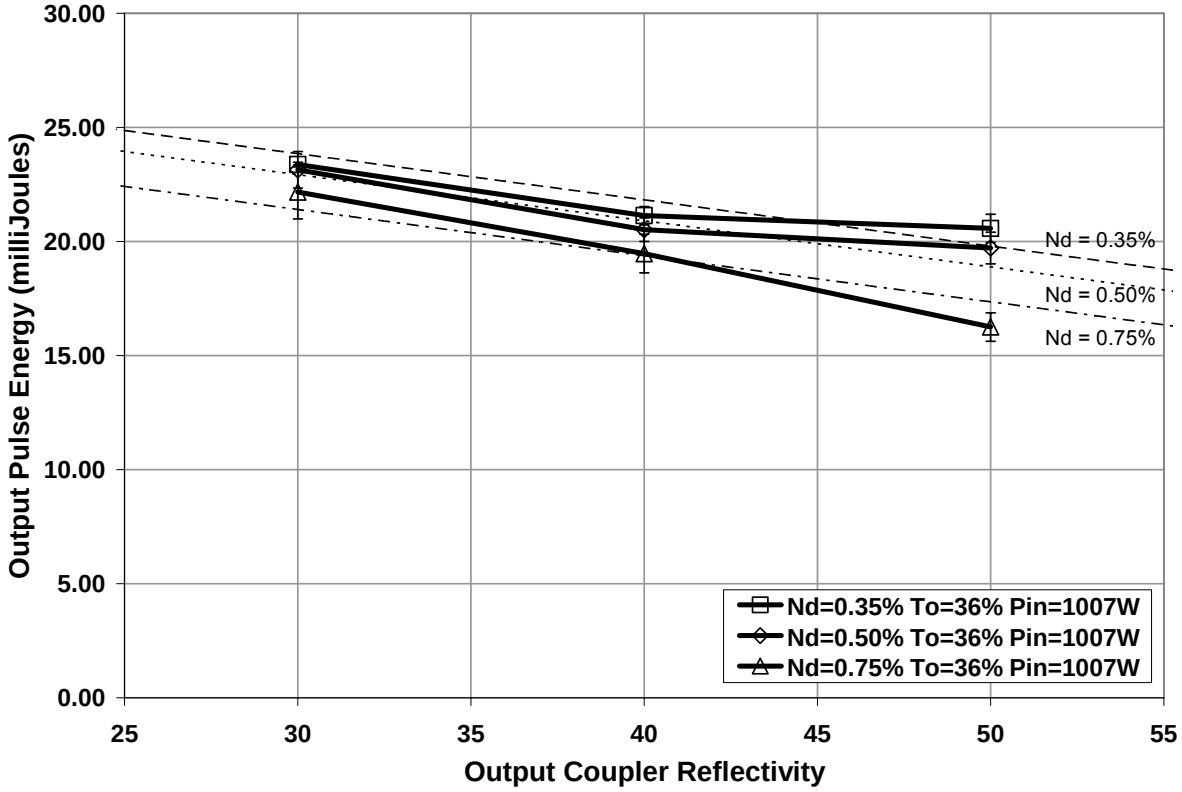

Figure 5.4: Output pulse energy response as a function of output coupler reflectivity and Nd concentration with a constant Q-switch initial transmission of 36% and an input power of 1007 Watts

Table 5.4: Regression analysis of data plotted in Figure 5.4

Regression Statistics	
Multiple R	0.918
R Square	0.843
Adj. R Square	0.830
Standard Error	0.887
Observations	27

ANOVA

	df	SS	MS	F	Significance F
Regression	2	101.300	50.640	64.290	2.295E-10
Residual	24	18.900	0.788		
Total	26	120.200			

	Coefficients	Standard Error	t Stat	P-value	Lower 95%	Upper 95%
Intercept	32.060	1.017	31.530	4.798E-21	29.960	34.160
Nd % Conc.	-6.120	1.035	-5.910	4.220E-06	-8.260	-3.980
OC % Reflect.	-0.200	0.021	-9.700	9.332E-10	-0.250	-0.160

The dependence of the output pulse energy in Figure 5.4 on the output coupler reflectivity is primarily due to the degree of feedback each reflectivity value provides to the laser system when building up to the lasing threshold. For a given Q-switch initial transmission and input pump power the lower reflectivity requires more time to build up the suitable photon flux to begin the process. The consequence of this additional build up time is larger optical storage and subsequent increase in output pulse energy when lasing occurs. This explains the slope of the curves in Figure 5.4, the lower the output coupler reflectivity the higher the output pulse energy.

The dependence of the output pulse energy in Figure 5.4 on the Nd concentration is primarily due to the absorption and stimulated re-emission that a particular concentration is capable of generating. The higher concentration laser rods more readily absorb the pump radiation thereby producing excited states that can be emitted either by stimulation or spontaneously to contribute to the photon flux when building up the lasing threshold. The more excited states that are created and subsequently stimulated for a given set of optical and pump parameters will lead to a shorter pump time before lasing onset. A consequence of the

reduction in time is a lower output pulse energy. This explains the spacing between the curves in Figure 5.4, the lower the concentration the higher the output pulse energy.

Figure 5.5 shows the dependence of the output pulse energy on the input pump power for three levels of Nd concentration. All data points are statistically equivalent with the application of a 95% confidence interval. Table 5.5 shows the results of the regression analysis of the data plotted in Figure 5.5. The results indicate that the linear model was a poor fit however at least one of the independent variables contributes significantly to the model. The plotted trend lines from the regression also indicate the significance of the contributions from each variable. The slope of the trend lines in conjunction with the regression data indicates no significant dependence of the output pulse energy on the input power in this scenario. The spacing of the trend lines indicates little or no significance of the Nd concentration on the output pulse energy, although the regression analysis does indicate significance.

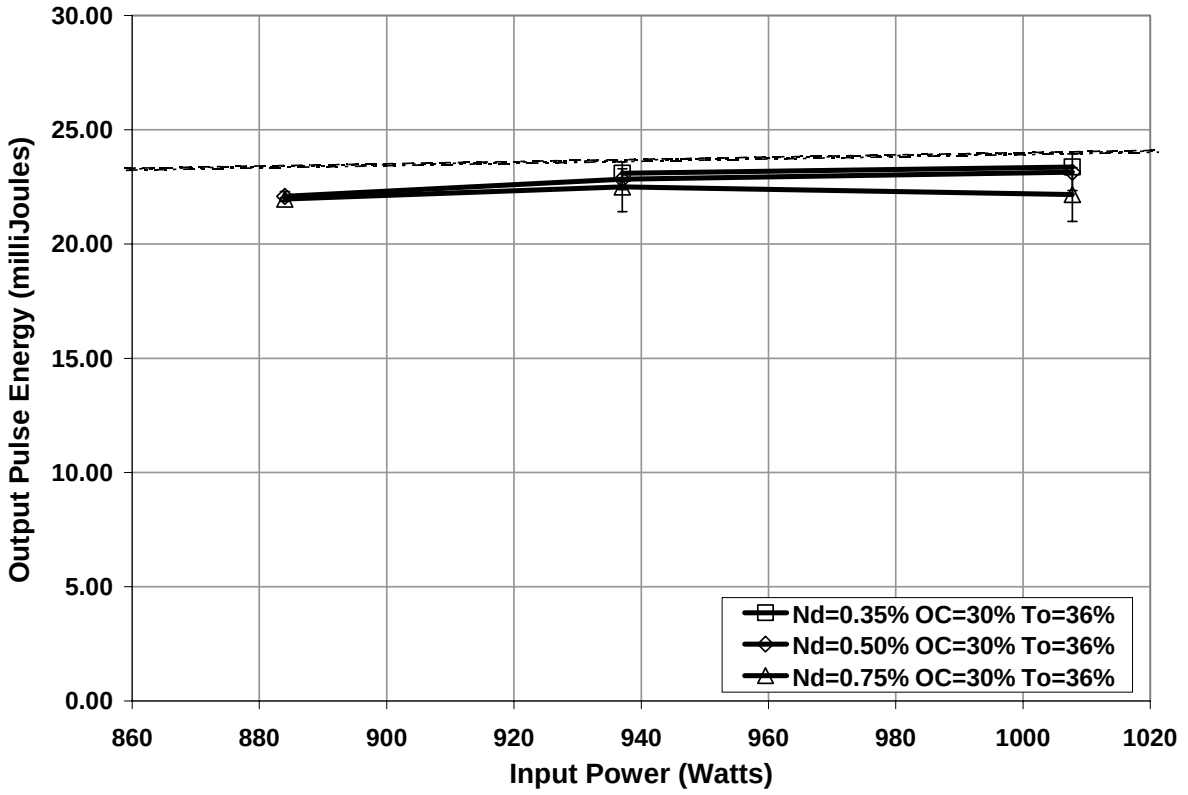

Figure 5.5: Output pulse energy as a function of optical pump power and Nd concentration with constant output coupler reflectivity and Q-switch initial transmission

Table 5.5: Regression analysis of raw data plotted in Figure 5.5

Regression Statistics	
Multiple R	0.652
R Square	0.425
Adj. R Square	0.370
Standard Error	0.563
Observations	24

ANOVA

	df	SS	MS	F	Significance F
Regression	2	4.925	2.462	7.756	3.005E-03
Residual	24	6.667	0.317		
Total	26	11.590			

	Coefficients	Standard Error	t Stat	P-value	Lower 95%	Upper 95%
Intercept	19.220	2.401	8.002	8.194E-08	14.220	24.210
Nd % Conc.	-2.130	0.728	-2.930	8.014E-03	-3.650	-0.620
Pin Optical	0.005	0.002	2.018	5.659E-02	0.000	0.010

It is evident that the input pump power has no influence on the output pulse energy from Figure 5.5. This is due to the self-regulation performed by the combination of the

output coupler reflectivity and the Q-switch initial transmission. This optical combination predetermines the output pulse energy of a given passively Q-switched laser system. The input pump power can have an effect on the output pulse energy but it seems to only be noticable when the input power is modified on order of magnitude scales which was not examined in this work.

It is also evident that for a given combination of output coupler reflectivity and Q-switch initial transmission the Nd concentration has little effect on the output pulse energy. Although it was evident in previous plots that the Nd concentration can have a significant effect on the output pulse energy Figure 5.5 provides a good example that shows the output coupler reflectivity and the Q-switch initial transmission as the limiting factors in determining output pulse energy for a range of input power levels and ion concentrations.

Figure 5.6 shows the output pulse energy as a function of pump power for three different output coupler reflectivities and fixed Q-switch initial transmission and Nd concentration. Table 5.6 shows the results of the regression analysis of the data plotted in Figure 5.6. The results indicate that the linear model was a good fit and that at least one of the independent variables contributes significantly to the model. The plotted trend lines from the regression also indicate the significance of the contributions from each variable. The slope of the trend lines, as well as the regression analysis, indicates no significance of the input pump power on the output pulse energy. The spacing of the trend lines is an indication of a significant dependence of the output on the output coupler reflectivity.

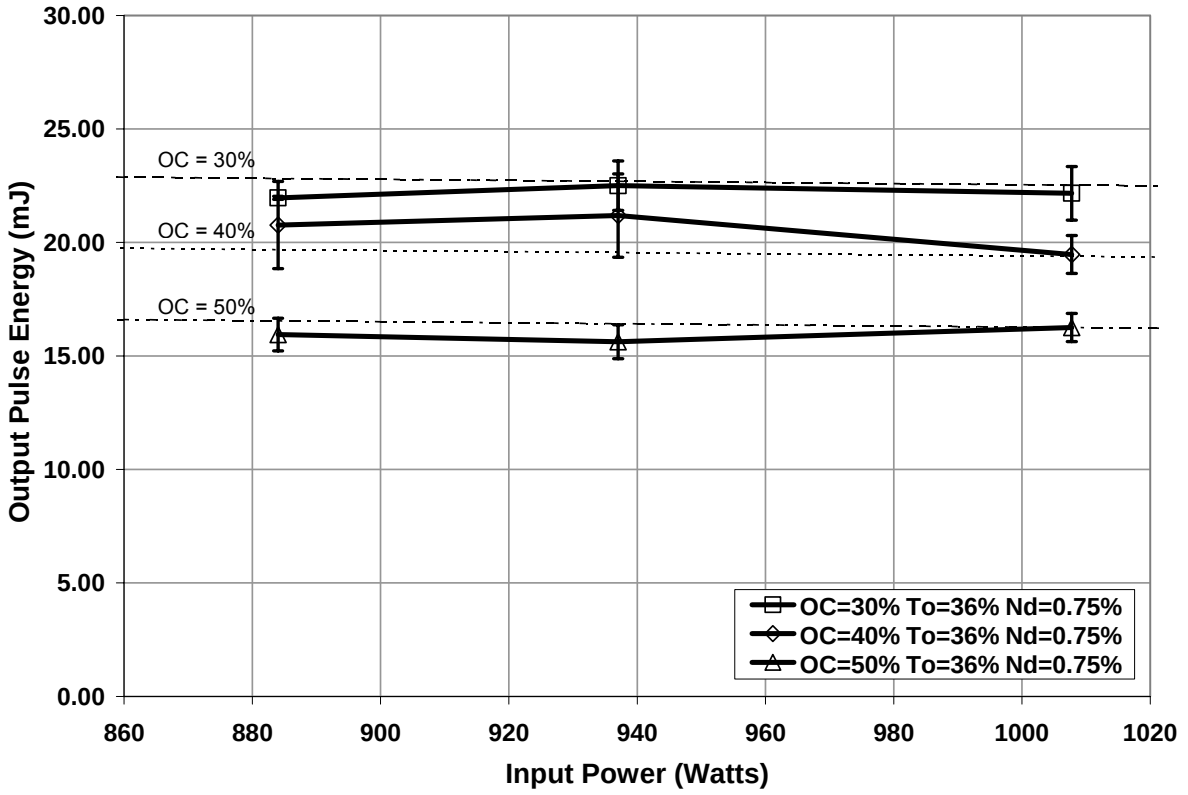

Figure 5.6: Output pulse energy versus pump power for three output coupler reflectivities and fixed Q-switch initial transmission and Nd concentration

Table 5.6: Regression analysis of raw data plotted in Figure 5.6

Regression Statistics	
Multiple R	0.913
R Square	0.833
Adj. R Square	0.819
Standard Error	1.218
Observations	27

ANOVA

	df	SS	MS	F	Significance F
Regression	2	177.400	88.710	59.780	4.763E-10
Residual	24	35.610	1.484		
Total	26	213.000			

	Coefficients	Standard Error	t Stat	P-value	Lower 95%	Upper 95%
Intercept	34.320	4.541	7.559	8.491E-08	24.950	43.690
OC % Reflect.	-0.310	0.029	-10.900	8.534E-11	-0.370	-0.250
Pin Optical	0.000	0.005	-0.510	6.148E-01	-0.010	0.007

Figure 5.6 again indicates that the input pump power has no influence on the output pulse energy for a given combination of output coupler reflectivity, Q-switch initial

transmission, and Nd concentration. The output pulse energy is shown to be strongly dependent on the output coupler reflectivity for a given combination of Nd concentration and Q-switch initial transmission regardless of the input power level for this combination of variable values. Once again this relates directly to the degree of feedback the output coupler provides the system. As will be seen in a following section the input power level does significantly effect the amount of time it takes to produce a particular output. However, in this experiment the combination of the output coupler reflectivity, Q-switch initial transmission, and the Nd concentration appear to predetermine a certain output energy level.

Figure 5.7 shows the output pulse energy as a function of pump power for three different Q-switch initial transmission values with fixed output coupler reflectivity and Nd concentration. Table 5.7 shows the results of the regression analysis of the data plotted in Figure 5.7. The results indicate that the linear model was a good fit and that both independent variables contribute significantly to the model. The plotted trend lines from the regression also indicate the significance of the contributions from each variable. The slope of the trend lines indicates the relative insignificance of the input pump power. The spacing of the trend lines is an indication of a significant dependence of the output on the Q-switch initial transmission.

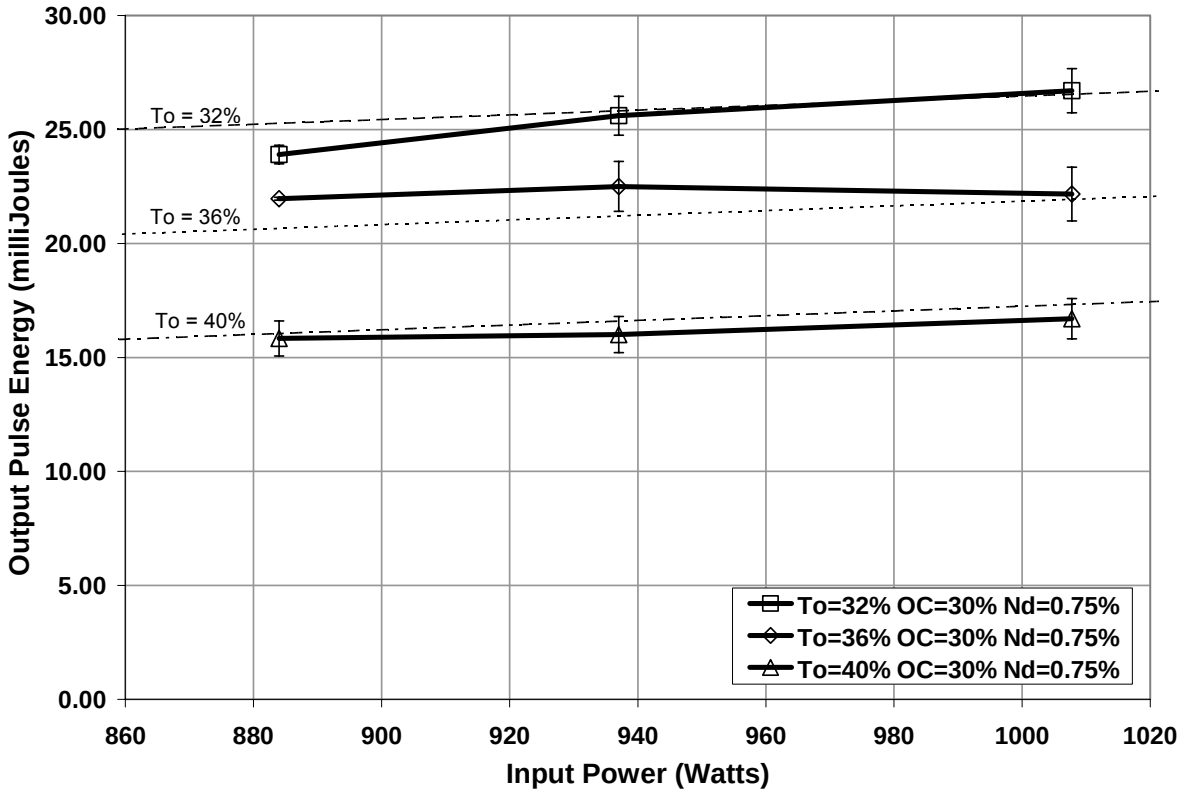

Figure 5.7: Output pulse energy versus pump power for three Q-switch initial transmission values and fixed output coupler reflectivities and Nd concentration

Table 5.7: Regression analysis of data plotted in Figure 5.7

Regression Statistics	
Multiple R	0.965
R Square	0.932
Adj. R Square	0.926
Standard Error	1.090
Observations	27

ANOVA

	df	SS	MS	F	Significance F
Regression	2	390.000	195.000	164.000	1.010E-14
Residual	24	28.540	1.189		
Total	26	418.500			

	Coefficients	Standard Error	t Stat	P-value	Lower 95%	Upper 95%
Intercept	53.060	4.562	11.630	2.388E-11	43.640	62.470
QSW % To	-1.150	0.064	-17.900	2.076E-15	-1.290	-1.020
Pin Optical	0.010	0.004	2.472	2.093E-02	0.002	0.019

Figure 5.7, along with the regression data, suggests that there may be a marginal dependence of the output pulse energy on the input pump power for this scenario.

Considering the previous plots and explanations in this section this seems unlikely. At first sight the curves look as if they follow the same patterns produced by varying the output coupler reflectivity in previous plots where the input power has little or no effect on the output. This is the case for the most part in Figure 5.7. This plot does show a strong dependence of the output pulse energy on the Q-switch initial transmission. This is another example of how the combination of output coupler reflectivity, Nd concentration, and Q-switch initial transmission act to predetermine the operational output of the laser system.

Table 5.8 shows the results of the regression analysis encompassing all of the data with respect to the output pulse energy. The regression analysis indicates a good linear fit and the rejection of the null hypothesis. The analysis also indicates that all of the independent variables contribute significantly.

Table 5.8: Regression analysis of the output pulse energy data

Regression Statistics	
Multiple R	0.872
R Square	0.760
Adj. R Square	0.756
Standard Error	1.389
Observations	228

ANOVA

	df	SS	MS	F	Significance F
Regression	2	1364.000	341.000	176.700	6.185E-68
Residual	24	430.300	1.930		
Total	26	1794.000			

	Coefficients	Standard Error	t Stat	P-value	Lower 95%	Upper 95%
Intercept	47.120	2.208	21.340	8.409E-56	42.770	51.470
Nd % Conc.	-5.780	0.556	-10.400	7.308E-21	-6.870	-4.680
OC % Reflect.	-0.200	0.012	-17.700	3.187E-44	-0.230	-0.180
QSW % To	-0.540	0.029	-18.900	2.418E-48	-0.600	-0.490
Pin Optical	0.005	0.002	2.485	1.370E-02	0.001	0.008

5.1.2 Output Pulse Width

Section 5.1.2 examines the dependence of the output pulse width on the values of the Q-switch initial transmission, the output coupler reflectivity, Neodymium concentration, and

the input power level. Figures 5.8-5.10 show the relationship between the output pulse width on the output coupler reflectivity and the Q-switch initial transmission each with fixed values of Nd concentrations of 0.35%, 0.50%, and 0.75%, respectively. Figure 5.8 shows an operational range between 8.2-11.4 ns. Table 5.9 shows the results of the regression analysis of the data plotted in Figure 5.8. The results indicate that the linear model was able to explain approximately 3% of the variability in the output pulse width, a very poor fit overall. Considering the large P-value, the null hypothesis would not be rejected in this scenario verifying that neither variable provides a significant contribution to the model. The slope of the trend lines, as well as the regression data, indicates no significance of the output coupler reflectivity on the output pulse width. The spacing of the trend lines, as well as the regression data, indicates that the output pulse width is not dependent on the Q-switch initial transmission.

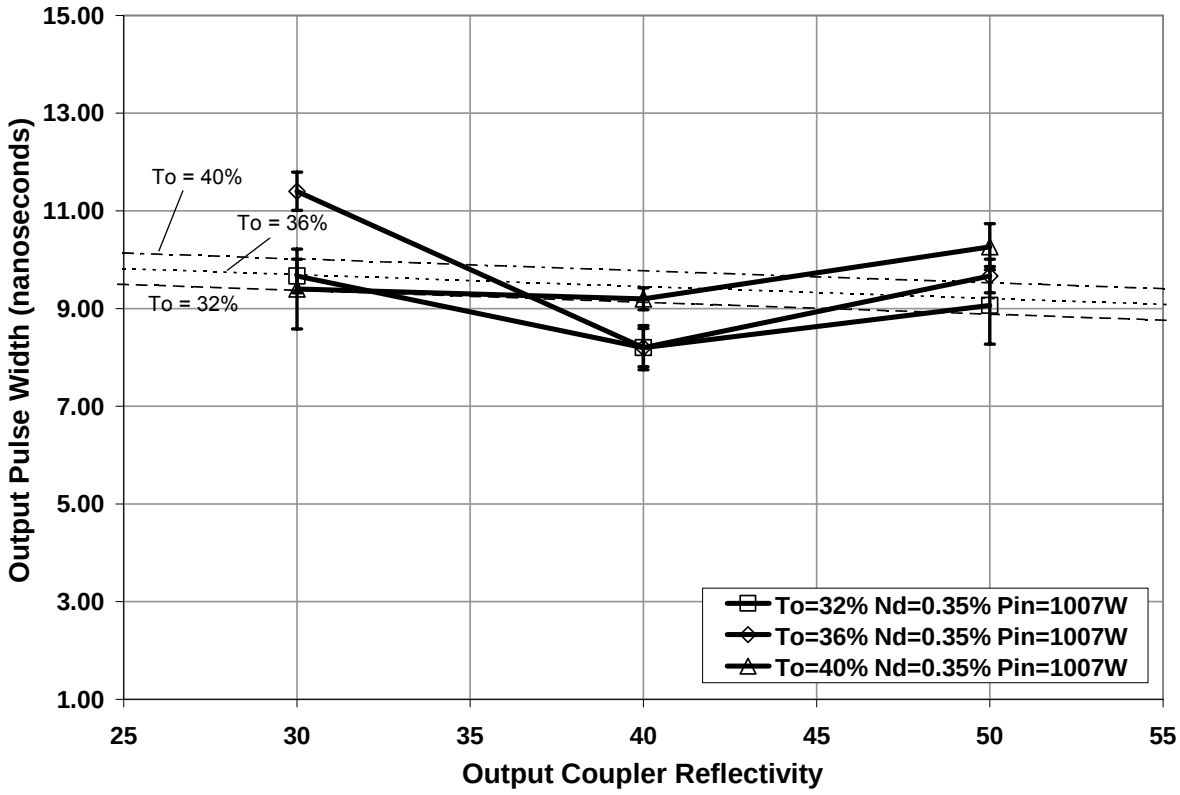

Figure 5.8: Output pulse width response as a function of output coupler reflectivity and Q-switch initial transmission with Nd concentration of 0.35% at an input power of 1007 Watts

Table 5.9: Regression analysis of data plotted in Figure 5.8

Regression Statistics	
Multiple R	0.328
R Square	0.108
Adj. R Square	0.033
Standard Error	1.008
Observations	27

ANOVA

	df	SS	MS	F	Significance F
Regression	2	2.944	1.472	1.449	2.546E-01
Residual	24	24.380	1.016		
Total	26	27.330			

	Coefficients	Standard Error	t Stat	P-value	Lower 95%	Upper 95%
Intercept	7.530	2.348	3.207	3.776E-03	2.684	12.380
OC % Reflect.	-0.020	0.024	-1.030	3.138E-01	-0.070	0.025
QSW % To	0.081	0.059	1.356	1.876E-01	-0.040	0.203

The output pulse width is largely dictated by the cavity geometry and Q-switch operational parameters but can exhibit minor variations due to cavity alignment. The data in

Figures 5.5-5.7 suggests no dependences in output pulse width due to either the Q-switch initial transmission or the output coupler reflectivity. It is not clear if any effect is present due to the optical parameters or if the data simply shows alignment variation which could not be measured or recorded with the equipment available.

Figure 5.9 shows an operational range between 7.33-9.73 ns. Table 5.10 shows the results of the regression analysis of the data plotted in Figure 5.9. The results indicate that the linear model was able to explain approximately 65% of the variability in the output pulsewidth, a poor fit overall. Unlike Table 5.9 this analysis indicates that both variables contribute significantly to the model. The slope of the trend lines indicates significance of the output coupler reflectivity on the output pulse width. The spacing of the trend lines indicates that the output pulse width is significantly dependent on the Q-switch initial transmission for this scenario.

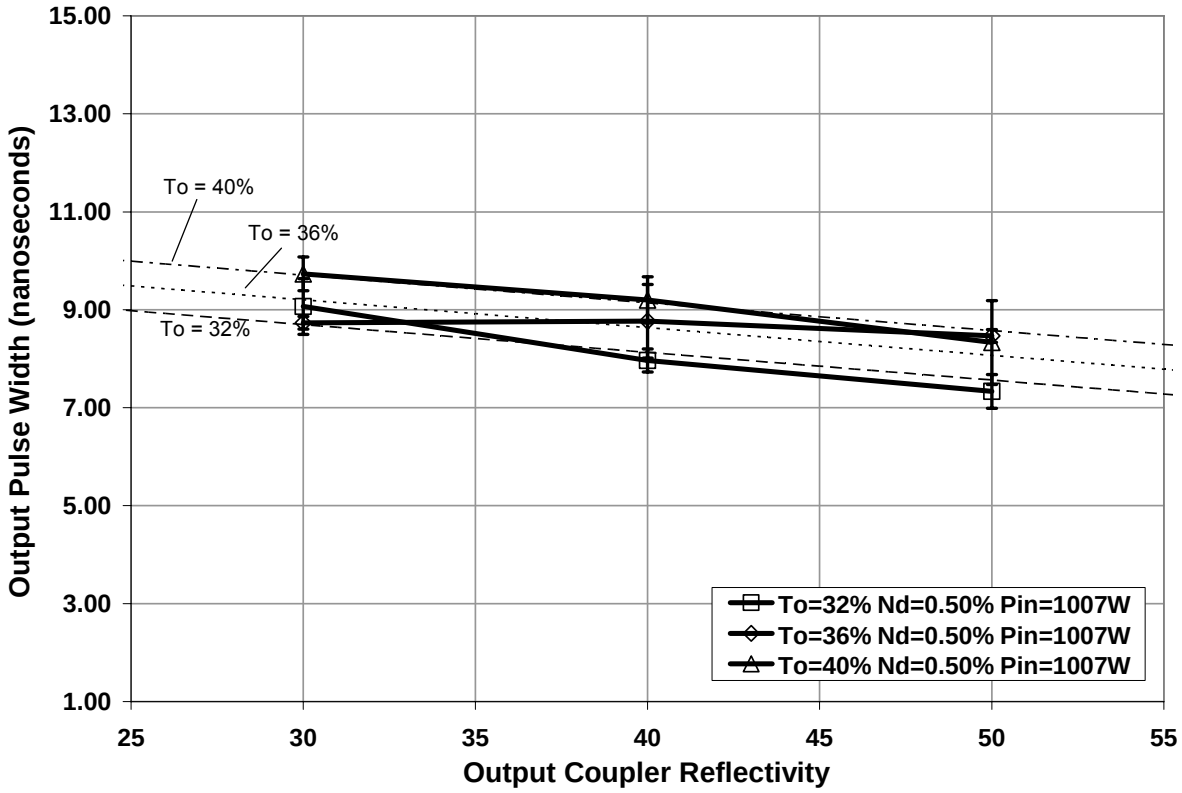

Figure 5.9: Output pulse width response as a function of output coupler reflectivity and Q-switch initial transmission with Nd concentration of 0.50% at an input power of 1007 Watts

Table 5.10: Regression analysis of data plotted in Figure 5.9

Regression Statistics	
Multiple R	0.808
R Square	0.653
Adj. R Square	0.624
Standard Error	0.480
Observations	27

ANOVA

	df	SS	MS	F	Significance F
Regression	2	10.380	5.190	22.560	3.075E-06
Residual	24	5.522	0.230		
Total	26	15.900			

	Coefficients	Standard Error	t Stat	P-value	Lower 95%	Upper 95%
Intercept	6.354	1.117	5.686	7.404E-06	4.048	8.660
OC % Reflect.	-0.060	0.011	-5.010	4.033E-05	-0.080	-0.030
QSW % To	0.126	0.028	4.471	1.593E-04	0.068	0.185

Figure 5.9, along with the regression data, show a significant dependence of the output pulse energy on the Q-switch initial transmission and output coupler reflectivity.

However this is most likely due to minor variations in the output and/or measurement technique. The output pulsewidth was not expected to vary significantly with any of the independent variables, however it is known to vary somewhat with the excited state density within the laser material. In other words the higher the excited state density the shorter the pulse width can potentially be if the cavity, the laser rod and the Q-switch are all properly aligned.

Figure 5.10 shows an operational range between 7.93-11.13 ns. Table 5.11 shows the results of the regression analysis of the data plotted in Figure 5.10. The results indicate that the linear model was able to explain approximately 42% of the variability in the output pulsewidth, a poor fit overall. The P-values for the tests of the independent variables indicate that only one of the variables contributes significantly to the model. The slope of the trend lines indicates no significance of the output coupler reflectivity on the output pulse width. The spacing of the trend lines, as well as the regression data, indicates that the output pulse width is significantly different for varying values of Q-switch initial transmission.

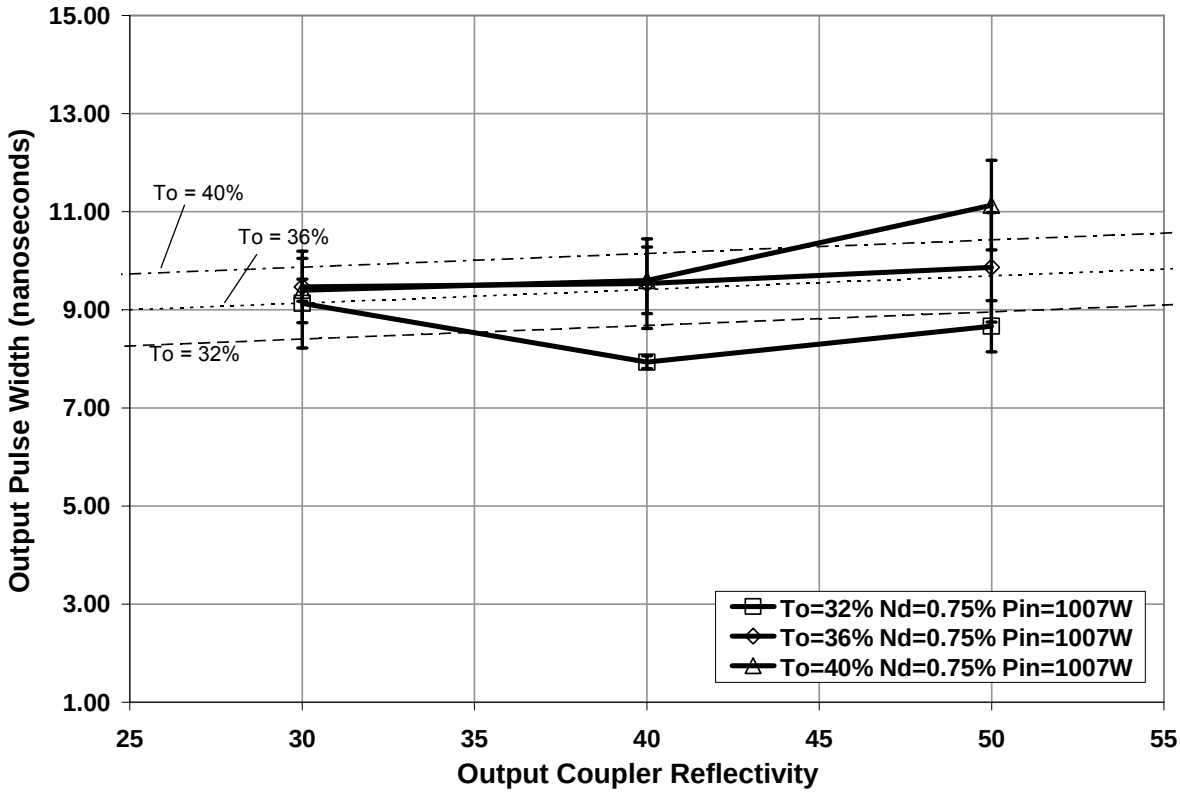

Figure 5.10: Output pulse width response as a function of output coupler reflectivity and Q-switch initial transmission with Nd concentration of 0.75% at an input power of 1007 Watts

Table 5.11: Regression analysis of data plotted in Figure 5.10

Regression Statistics	
Multiple R	0.652
R Square	0.425
Adj. R Square	0.377
Standard Error	0.791
Observations	27

ANOVA

	df	SS	MS	F	Significance F
Regression	2	11.070	5.534	8.852	1.319E-03
Residual	24	15.010	0.625		
Total	26	26.070			

	Coefficients	Standard Error	t Stat	P-value	Lower 95%	Upper 95%
Intercept	1.704	1.842	0.925	3.642E-01	-2.100	5.505
OC % Reflect.	0.028	0.019	1.490	1.491E-01	-0.010	0.066
QSW % To	0.183	0.047	3.935	6.212E-04	0.087	0.279

Figure 5.10 along with the regression data show a significant dependence of the output pulse energy on the Q-switch initial transmission; refer to the previous discussion for

possible causes of this dependence Figure 5.11 shows the output pulse width as a function of the output coupler reflectivity for three different values of Nd concentration. Table 5.12 shows the results of the regression analysis of the data plotted in Figure 5.11. The adjusted R-squared value indicates that the linear model was a poor fit and does not explain any of the variability in the dependent variable. Considering the outcome of the F test, the null hypothesis would not be rejected indicating that neither variable provides a significant contribution to the model. The plotted trend lines as well as the listed p-values for each of the variables verifies no significant contribution.

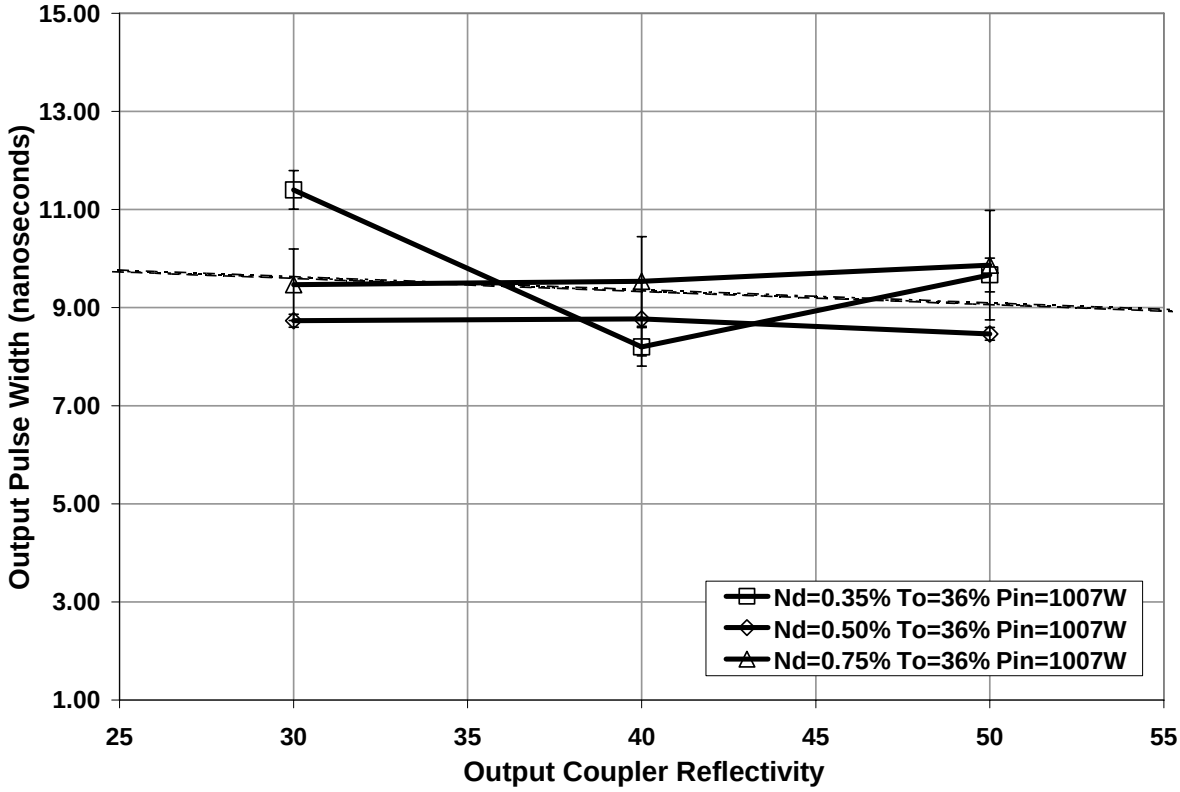

Figure 5.11: Output pulse width response as a function of output coupler reflectivity and Nd concentration with a fixed Q-switch initial transmission value of 36% at an input power of 1007 Watts

Table 5.12: Regression analysis of data plotted in Figure 5.11

Regression Statistics	
Multiple R	0.214
R Square	0.046
Adj. R Square	-0.030
Standard Error	1.055
Observations	27

ANOVA

	df	SS	MS	F	Significance F
Regression	2	1.287	0.643	0.578	5.687E-01
Residual	24	26.720	1.113		
Total	26	28.010			

	Coefficients	Standard Error	t Stat	P-value	Lower 95%	Upper 95%
Intercept	10.360	1.209	8.569	9.153E-09	7.865	12.860
Nd % Conc.	0.095	1.231	0.077	9.390E-01	-2.440	2.635
OC % Reflect.	-0.030	0.025	-1.070	2.943E-01	-0.080	0.025

Figure 5.11 indicates no dependences of the output pulse width on either the Nd concentration or the output coupler reflectivity. As stated previously the output pulse width is primarily dependent on cavity geometry, Q-switch properties, and alignment, therefore no significant dependencies are expected with fixed Q-switch initial transmission values.

Figure 5.12 shows the output pulse width as a function of the input pump power for three values of Nd concentration with constant output coupler reflectivity and Q-switch initial transmission. The data point at the lowest input power level for the 0.35% Nd concentration test did not produce output and therefore was not plotted. The data for the 0.35% Nd concentration is completely indistinguishible from the rest of the data which is statistically equivalent at a 95% confidence level. Table 5.13 shows the results of the regression analysis of the data plotted in Figure 5.12. The adjested R-squared value indicates that the linear model was a poor fit to the present data. Considering the outcome of the F test, the null hypothesis would fail to be rejected in this scenario verifying that neither variable provides a significant contribution to the model.

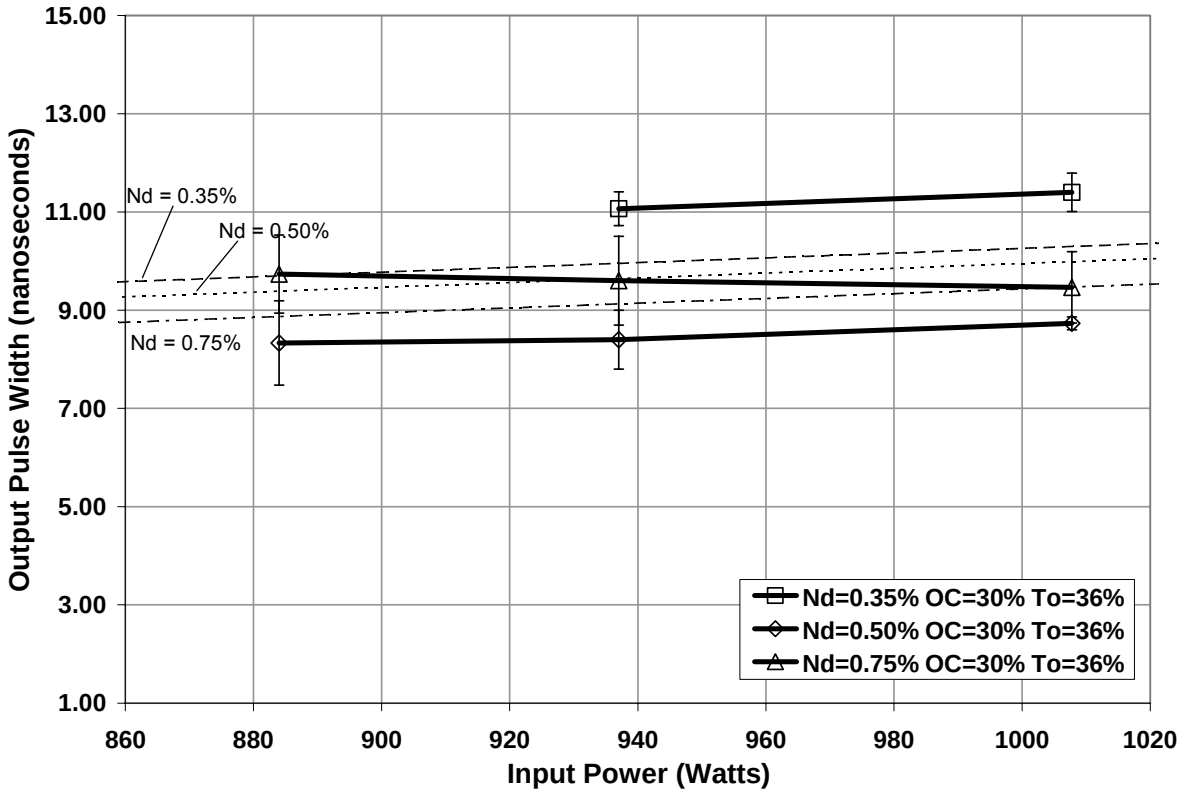

Figure 5.12: Output pulse width as a function of optical pump power and Nd concentration with constant output coupler reflectivity and Q-switch initial transmission

Table 5.13: Regression analysis of data plotted in Figure 5.12

Regression Statistics	
Multiple R	0.378
R Square	0.143
Adj. R Square	0.062
Standard Error	1.159
Observations	24

ANOVA

	df	SS	MS	F	Significance F
Regression	2	4.711	2.356	1.754	1.975E-01
Residual	24	28.210	1.343		
Total	26	32.920			

	Coefficients	Standard Error	t Stat	P-value	Lower 95%	Upper 95%
Intercept	6.133	4.939	1.242	2.280E-01	-4.140	16.400
Nd % Conc.	-2.060	1.498	-1.380	1.829E-01	-5.180	1.052
Pin Optical	0.005	0.005	0.979	3.386E-01	-0.010	0.015

Figure 5.12 indicates no dependences of the output pulse width on either the Nd concentration or the input pump power. Figure 5.13 shows the output pulse width as a

function of the input pump power for three different values of output coupler reflectivity with fixed values for Nd concentration and Q-switch initial transmission. Table 5.14 shows the results of the regression analysis of the data plotted in Figure 5.13. The results indicate that the linear model was a poor fit and does not explain any of the variability in the data. Considering the outcome of the F test, the null hypothesis would not be rejected in this scenario indicating that neither variable provides a significant contribution to the model. The plotted trend lines as well as the listed P-values for each of the variables varifies no significant contribution.

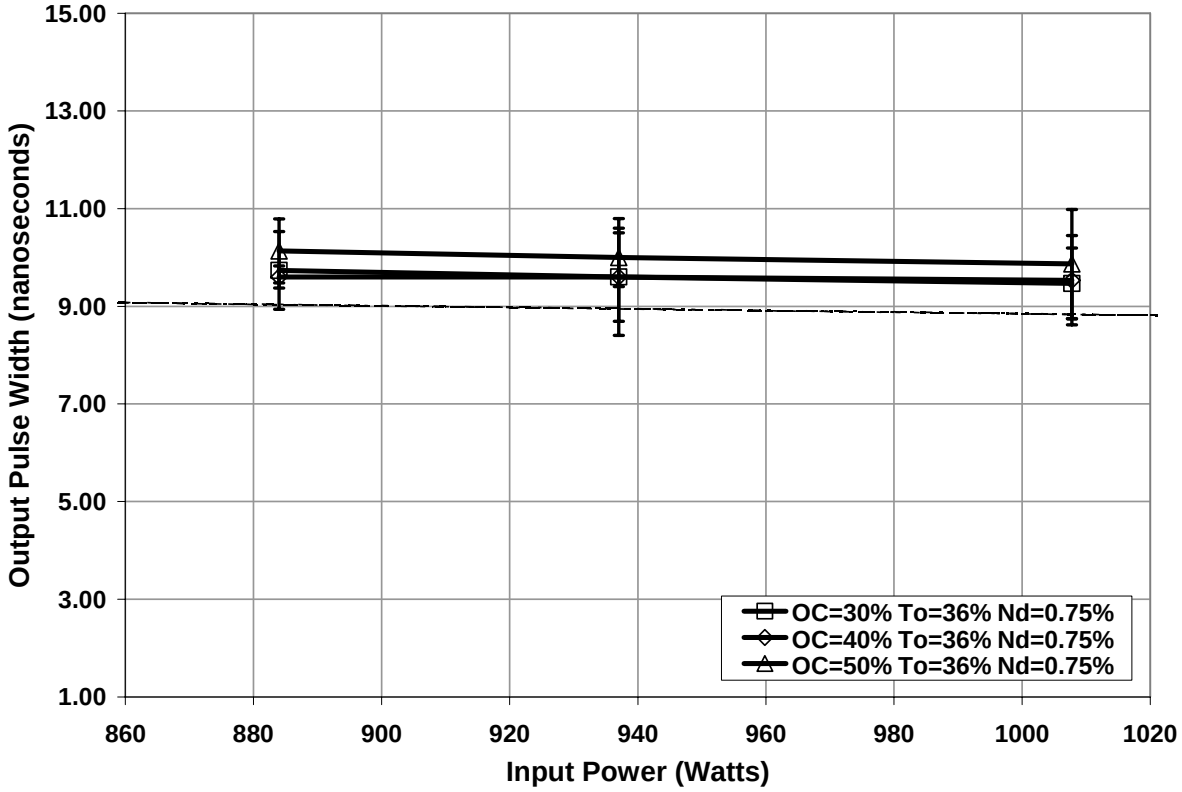

Figure 5.13: Output pulse width versus pump power for three output coupler reflectivities and fixed Q-switch initial transmission and Nd concentration

Table 5.14: Regression analysis of data plotted in Figure 5.13

Regression Statistics	
Multiple R	0.284
R Square	0.081
Adj. R Square	0.004
Standard Error	0.653
Observations	27

ANOVA

	df	SS	MS	F	Significance F
Regression	2	0.901	0.450	1.056	3.633E-01
Residual	24	10.230	0.426		
Total	26	11.130			

	Coefficients	Standard Error	t Stat	P-value	Lower 95%	Upper 95%
Intercept	10.460	2.434	4.296	2.486E-04	5.434	15.480
OC % Reflect.	0.020	0.015	1.300	2.061E-01	-0.010	0.052
Pin Optical	0.000	0.002	-0.650	5.212E-01	-0.010	0.004

Figure 5.13 indicates no dependences of the output pulse width on either the input pump power or the output coupler reflectivity. Figure 5.14 shows the output pulse width as a function of the input pump power for three different values of Q-switch initial transmission with constant Nd concentration and output coupler reflectivity values. No data groups are distinguishible with the application of a 95% confidence interal. Table 5.15 shows the results of the regression analysis of the data plotted in Figure 5.14. The results indicate that the linear model was a poor fit and does not explain any of the variability in the data. Considering the outcome of the F test, the null hypothesis would be accepted in this scenario verifying that neither variable provides a significant contribution to the model. The plotted trend lines as well as the listed P-values for each of the variables indicates no significant contribution.

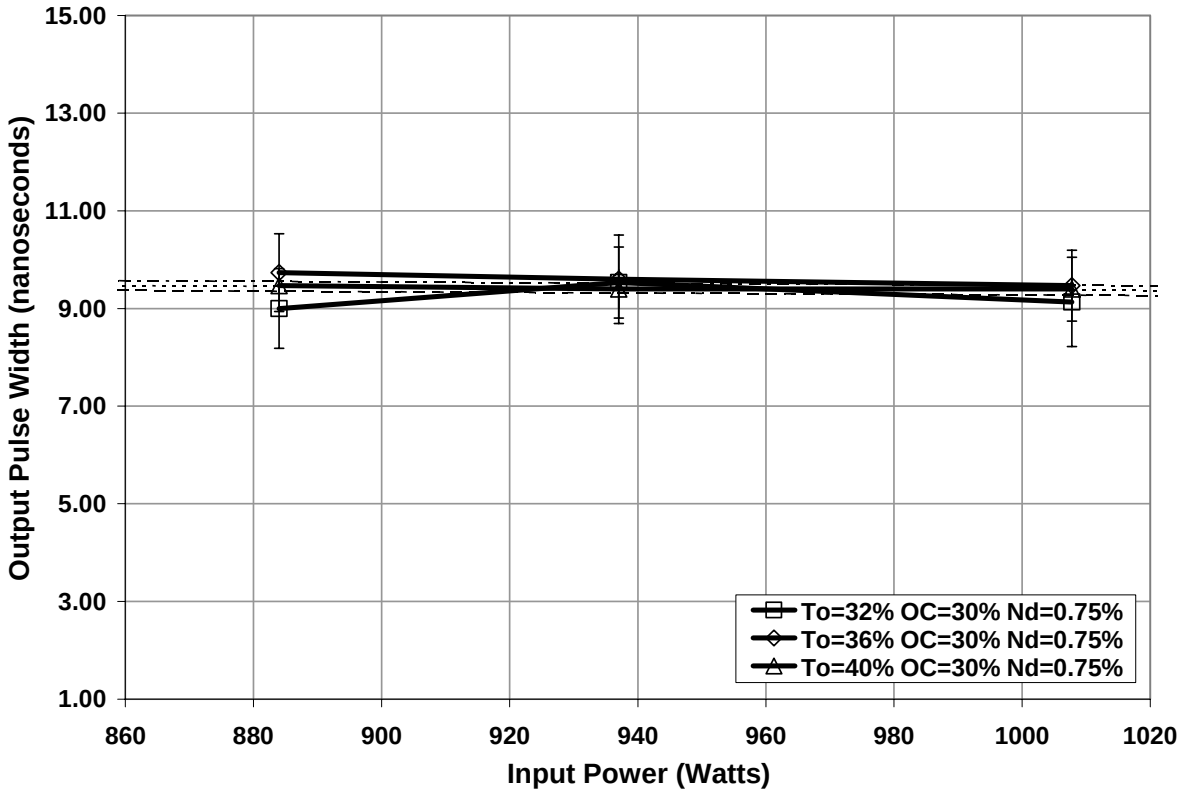

Figure 5.14: Output pulse width versus pump power for three Q-switch values and fixed output coupler reflectivity and Nd concentration

Table 5.15: Regression analysis of data plotted in Figure 5.14

Regression Statistics	
Multiple R	0.163
R Square	0.027
Adj. R Square	-0.050
Standard Error	0.564
Observations	27

ANOVA

	df	SS	MS	F	Significance F
Regression	2	0.209	0.104	0.328	7.234E-01
Residual	24	7.625	0.318		
Total	26	7.834			

	Coefficients	Standard Error	t Stat	P-value	Lower 95%	Upper 95%
Intercept	9.124	2.358	3.869	7.341E-04	4.256	13.990
QSW % To	0.025	0.033	0.753	4.590E-01	-0.040	0.094
Pin Optical	0.000	0.002	-0.300	7.667E-01	-0.010	0.004

Figure 5.14 indicates no dependences of the output pulse width on either the input pump power or the Q-switch initial transmission in this scenario. Table 5.16 shows the

results of the regression analysis encompassing all of the data with respect to the output pulse width. The regression data shows a poor linear fit however the F test indicates an excellent probability for the rejection of the null hypothesis. This indicates that at least one of the independent variables provides a significant contribution to the model. The data also indicates that only the Q-switch initial transmission contributes significantly when considering all of the variables. Referring to the discussion of Figure 5.9, Siegman [145] reports that for a passively Q-switched laser system the output pulse width can vary substantially depending on the inversion ratio that is achieved in the active laser medium prior to Q-switching. The inversion ratio is the ratio between the excited state population density just before and just after Q-switching. The larger the difference the shorter the output pulse can be with the primary limitation being the cavity length and geometry.

Table 5.16: Regression analysis of the output pulse width data

Regression Statistics	
Multiple R	0.435
R Square	0.189
Adj. R Square	0.175
Standard Error	0.958
Observations	228

ANOVA

	df	SS	MS	F	Significance F
Regression	2	47.870	11.970	13.030	1.504E-09
Residual	24	204.900	0.919		
Total	26	252.700			

	Coefficients	Standard Error	t Stat	P-value	Lower 95%	Upper 95%
Intercept	4.254	1.523	2.793	5.682E-03	1.252	7.256
Nd % Conc.	0.378	0.384	0.985	3.257E-01	-0.380	1.135
OC % Reflect.	0.001	0.008	0.159	8.735E-01	-0.010	0.017
QSW % To	0.141	0.020	7.138	1.315E-11	0.102	0.180
Pin Optical	0.000	0.001	-0.320	7.487E-01	0.000	0.002

5.1.3 Q-Switch Delay

Figures 5.15-5.17 show the response of the Q-switch delay as a function of the output coupler reflectivity and the Q-switch initial transmission each with respect to Nd

concentration. Figure 5.15 shows a Q-switch delay range between 214-484 μs. All except one of the data groupings can be distinguished when a 95% confidence level is applied to the data. Table 5.17 shows the results of the regression analysis of the data plotted in Figure 5.15. The results indicate that the linear model was able to explain approximately 83% of the variability in the data set, a good fit overall. Considering the outcome of the F test, the null hypothesis would be rejected in this scenario verifying that at least one of the variables provides a significant contribution to the model. This analysis indicates that both of the variables contribute significantly to the model. The slope of the trend lines, as well as the regression data, indicates a strong significance of the output coupler reflectivity on the Q-switch delay. The spacing of the trend lines, as well as the regression data, indicates that the Q-switch delay is significantly dependent on the Q-switch initial transmission.

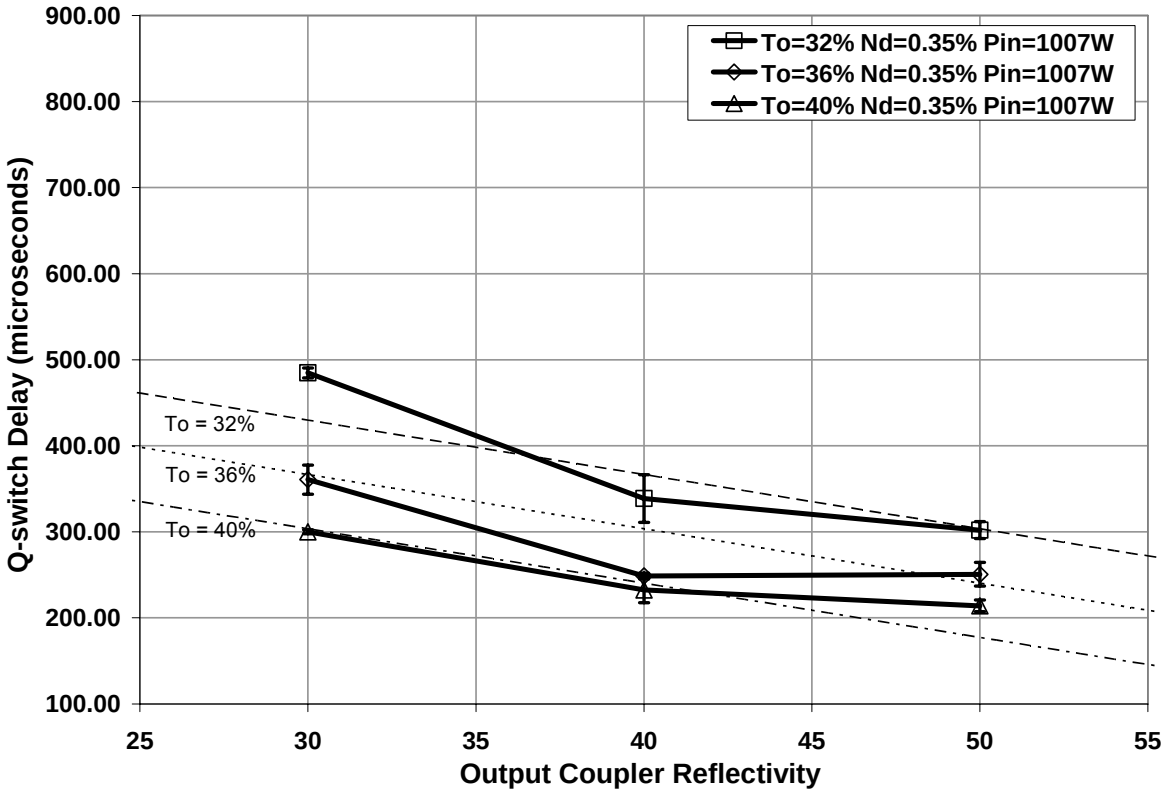

Figure 5.15: Q-switch delay response as a function of output coupler reflectivity and Q-switch initial transmission with Nd concentration of 0.35% at an input power of 1007 Watts

Table 5.17: Regression analysis of data plotted in Figure 5.15

Regression Statistics	
Multiple R	0.915
R Square	0.838
Adj. R Square	0.825
Standard Error	33.980
Observations	27

ANOVA

	df	SS	MS	F	Significance F
Regression	2	143400.000	71690.000	62.090	3.256E-10
Residual	24	27710.000	1155.000		
Total	26	171100.000			

	Coefficients	Standard Error	t Stat	P-value	Lower 95%	Upper 95%
Intercept	1124.000	79.150	14.200	3.554E-13	960.600	1287.000
OC % Reflect.	-6.310	0.801	-7.880	4.119E-08	-7.960	-4.660
QSW % To	-15.800	2.002	-7.880	4.119E-08	-19.900	-11.600

The data from Figure 5.15 shows a significant increase in the Q-switch delay with decreasing output coupler reflectivity and Q-switch initial transmission. The increase in the

output pulse energy, as shown in Section 5.1.1, is directly proportional to the Q-switch delay data. As the Q-switch delay becomes larger the output pulse energy increases proportionally. This is due to the losses that are added to the system by the decreasing output coupler reflectivity and the decreasing Q-switch initial transmission. The increased losses within the system slows the build up of a sufficient photon flux within the cavity to induce lasing, therefore more energy is stored and released as a consequence. The same holds true for Figures 5.16 and 5.17.

Figure 5.16 shows a Q-switch delay range between 232-585 μs. All of the data groupings can be distinguished when a 95% confidence level is applied to the data. Table 5.18 shows the results of the regression analysis of the data plotted in Figure 5.16. The results indicate that the linear model was able to explain approximately 71% of the variability in the data set, a satisfactory fit overall. Considering the outcome of the F test, the null hypothesis would be rejected in this scenario verifying that at least one of the variables provides a significant contribution to the model. The slope of the trend lines, as well as the regression data, indicates a strong significance of the output coupler reflectivity on the Q-switch delay. The spacing of the trend lines, as well as the regression analysis, indicates that the Q-switch delay is significantly dependent on the Q-switch initial transmission.

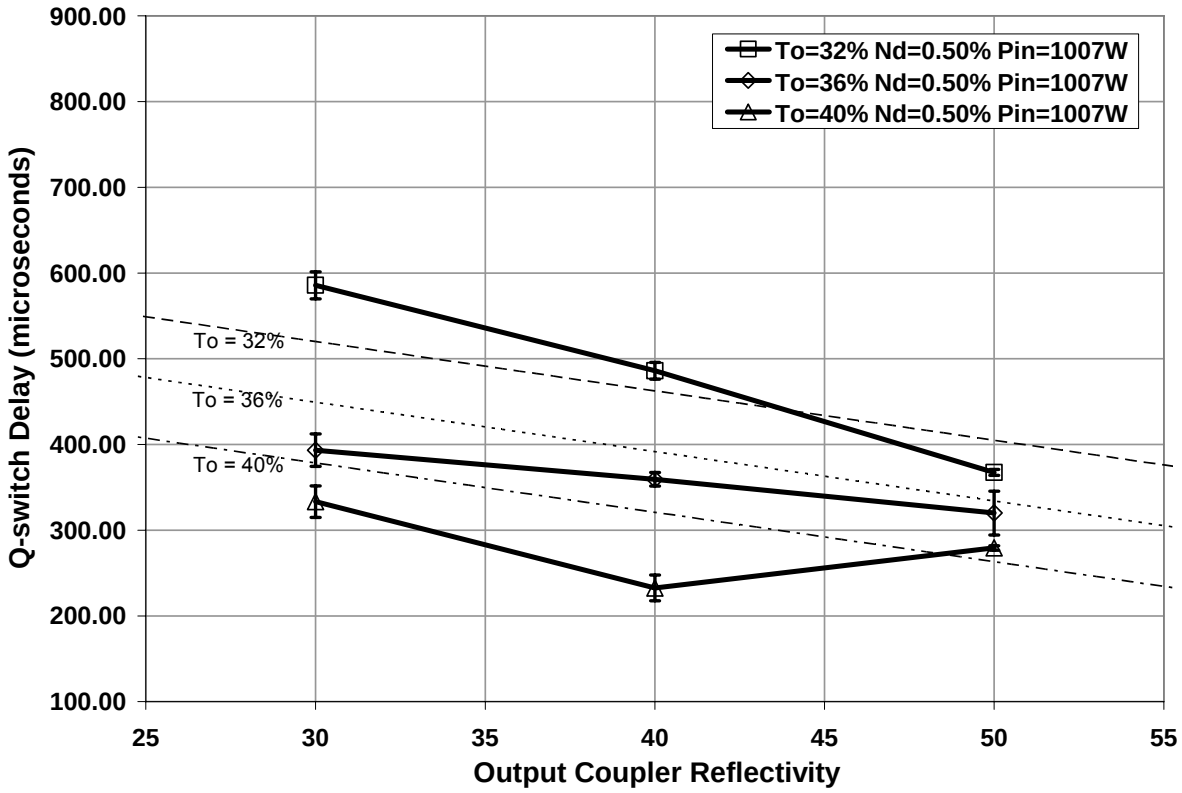

Figure 5.16: Q-switch delay response as a function of output coupler reflectivity and Q-switch initial transmission with Nd concentration of 0.50% at an input power of 1007 Watts

Table 5.18: Regression analysis of data plotted in Figure 5.16

Regression Statistics	
Multiple R	0.842
R Square	0.710
Adj. R Square	0.686
Standard Error	50.560
Observations	27

ANOVA

	df	SS	MS	F	Significance F
Regression	2	150100.000	75030.000	29.350	3.573E-07
Residual	24	61360.000	2557.000		
Total	26	211400.000			

	Coefficients	Standard Error	t Stat	P-value	Lower 95%	Upper 95%
Intercept	1260.000	117.800	10.700	1.302E-10	1017.000	1503.000
OC % Reflect.	-5.760	1.192	-4.830	6.334E-05	-8.220	-3.300
QSW % To	-17.700	2.979	-5.940	3.916E-06	-23.900	-11.600

Figure 5.17 shows a Q-switch delay range between 207-374 µs. All of the data groupings can be distinguished when a 95% confidence level is applied to the data. Table

5.19 shows the results of the regression analysis of the data plotted in Figure 5.17. The results indicate that the linear model was able to explain approximately 83% of the variability in the data set, a good fit overall. Considering the outcome of the F test, the null hypothesis would be rejected in this scenario verifying that at least one of the variables provides a significant contribution to the model. This analysis indicates that both of the variables contribute significantly to the model. The slope of the trend lines, as well as the regression analysis, indicates a strong significance of the output coupler reflectivity on the Q-switch delay. The spacing of the trend lines, as well as the regression analysis, indicates that the Q-switch delay is significantly dependent on the Q-switch initial transmission.

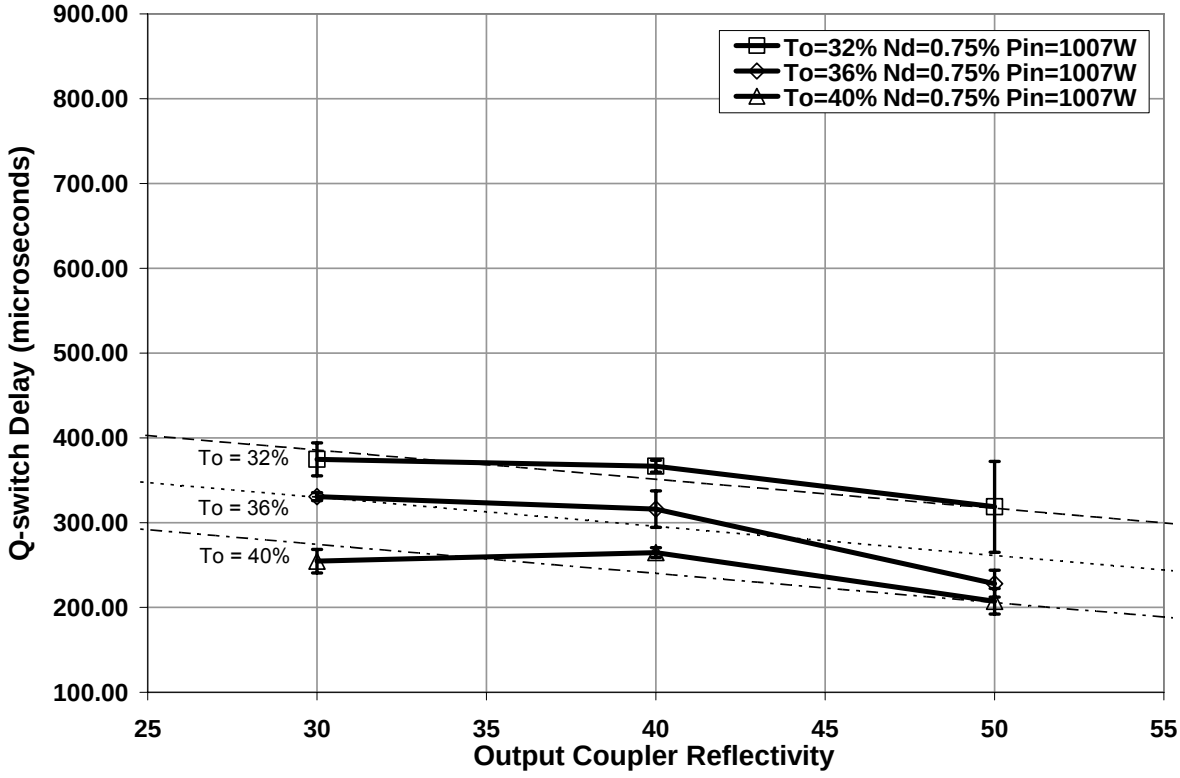

Figure 5.17: Q-switch delay response as a function of output coupler reflectivity and Q-switch initial transmission with Nd concentration of 0.75% at an input power of 1007 Watts

Table 5.19: Regression analysis of data plotted in Figure 5.17

Regression Statistics	
Multiple R	0.911
R Square	0.831
Adj. R Square	0.817
Standard Error	25.540
Observations	27

ANOVA

	df	SS	MS	F	Significance F
Regression	2	76770.000	38390.000	58.850	5.578E-10
Residual	24	15660.000	652.300		
Total	26	92430.000			

	Coefficients	Standard Error	t Stat	P-value	Lower 95%	Upper 95%
Intercept	933.000	59.490	15.680	4.102E-14	810.200	1056.000
OC % Reflect.	-3.430	0.602	-5.700	7.100E-06	-4.680	-2.190
QSW % To	-13.900	1.505	-9.200	2.303E-09	-17.000	-10.800

Figure 5.18 shows the output pulse width as a function of the output coupler reflectivity for three different values of Nd concentration. Only two of the data groups are indistinguishible with the application of a 95% confidence interal. Table 5.20 shows the results of the regression analysis of the data plotted in Figure 5.18. The results indicate that the linear model was a poor fit and does not explain the variability in the data. Considering the outcome of the F test, the null hypothesis would be rejected in this scenario verifying that at least one of the variables provides a significant contribution to the model. The plotted trend lines as well as the listed P-values for each of the variables indicates that the Nd concentration does not provide significant contribution to the model whereas the output coupler reflectivity does.

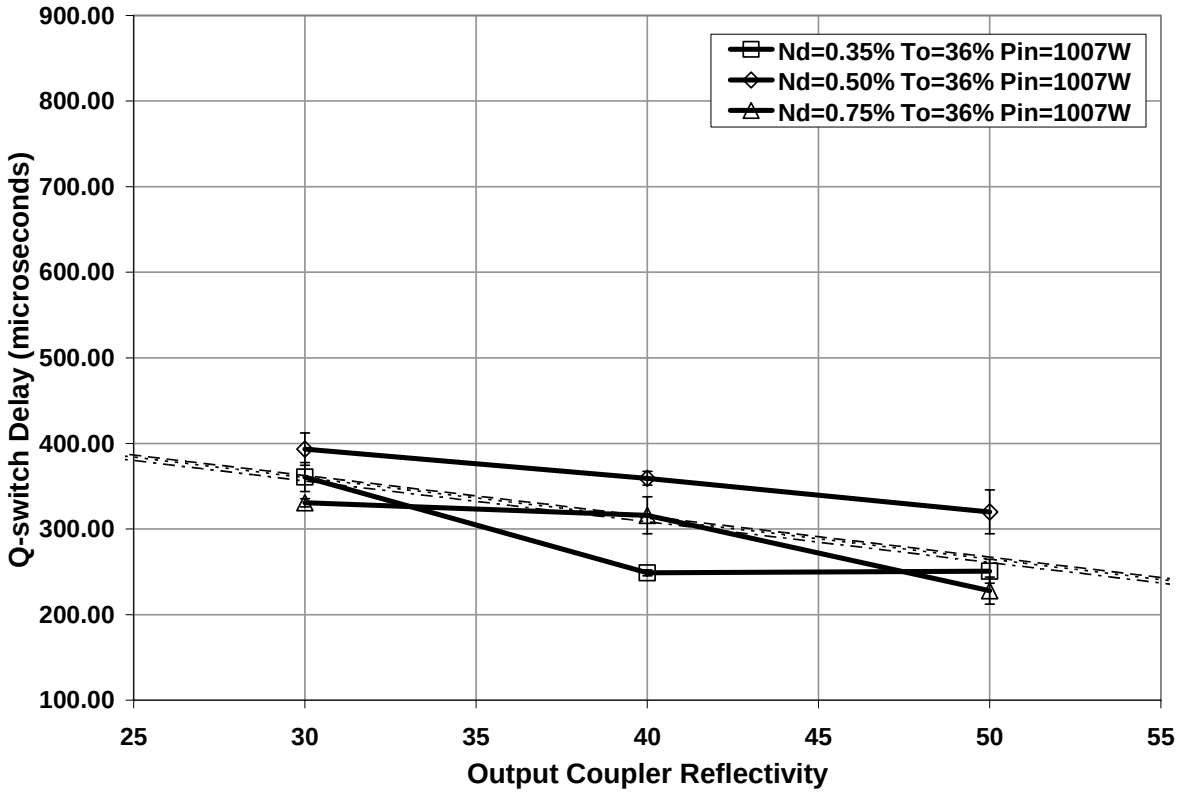

Figure 5.18: Q-switch delay response as a function of output coupler reflectivity and Nd concentration with a Q-switch initial transmission with of 36% at an input power of 1007 Watts

Table 5.20: Regression analysis of data plotted in Figure 5.18

Regression Statistics	
Multiple R	0.703
R Square	0.495
Adj. R Square	0.453
Standard Error	41.820
Observations	27

ANOVA

	df	SS	MS	F	Significance F
Regression	2	41090.000	20540.000	11.750	2.771E-04
Residual	24	41970.000	1749.000		
Total	26	83050.000			

	Coefficients	Standard Error	t Stat	P-value	Lower 95%	Upper 95%
Intercept	511.100	47.910	10.670	1.372E-10	412.200	610.000
Nd % Conc.	-16.000	48.780	-0.330	7.463E-01	-117.000	84.700
OC % Reflect.	-4.770	0.986	-4.840	6.299E-05	-6.800	-2.730

Figure 5.18 and the associated regression data indicates a strong dependence of the Q-switch delay on the output coupler reflectivity. The increasing output coupler reflectivity

provides additional feedback causing the Q-switch to saturate faster, and the consequence is lower output energy levels. The data indicates no significant dependence of the Q-switch delay on the Nd concentration. It was hypothesized that the Nd concentration may play a small role in the determination of the Q-switch delay. As the dopant concentration increased it was thought that the additional absorption and subsequent excited states would act to shorted the Q-switch delay. The Q-switch delay may depend more on the input power than the Nd concentration.

Figure 5.19 shows the Q-switch delay as a function of the input pump power for three values of Nd concentration with constant output coupler reflectivity and Q-switch initial transmission. All data groups but one are completely distinguishible from the rest of the data when a 95% confidence interval is applied. Table 5.21 shows the results of the regression analysis of the data plotted in Figure 5.19. The results indicate that the linear model was a mediocre fit of the present data. Considering the outcome of the F test, the null hypothesis would be rejected in this scenario verifying that at least one of the variables provides a significant contribution to the model. Looking at the regression analysis it is evident that both variables contribute significantly to the model. The slope of the trend lines, as well as the regression analysis, indicates a strong significance of the input pump power on the Q-switch delay. The spacing of the trend lines, as well as the regression data, indicates that the Q-switch delay is significantly dependent on the Nd concentration for this scenario.

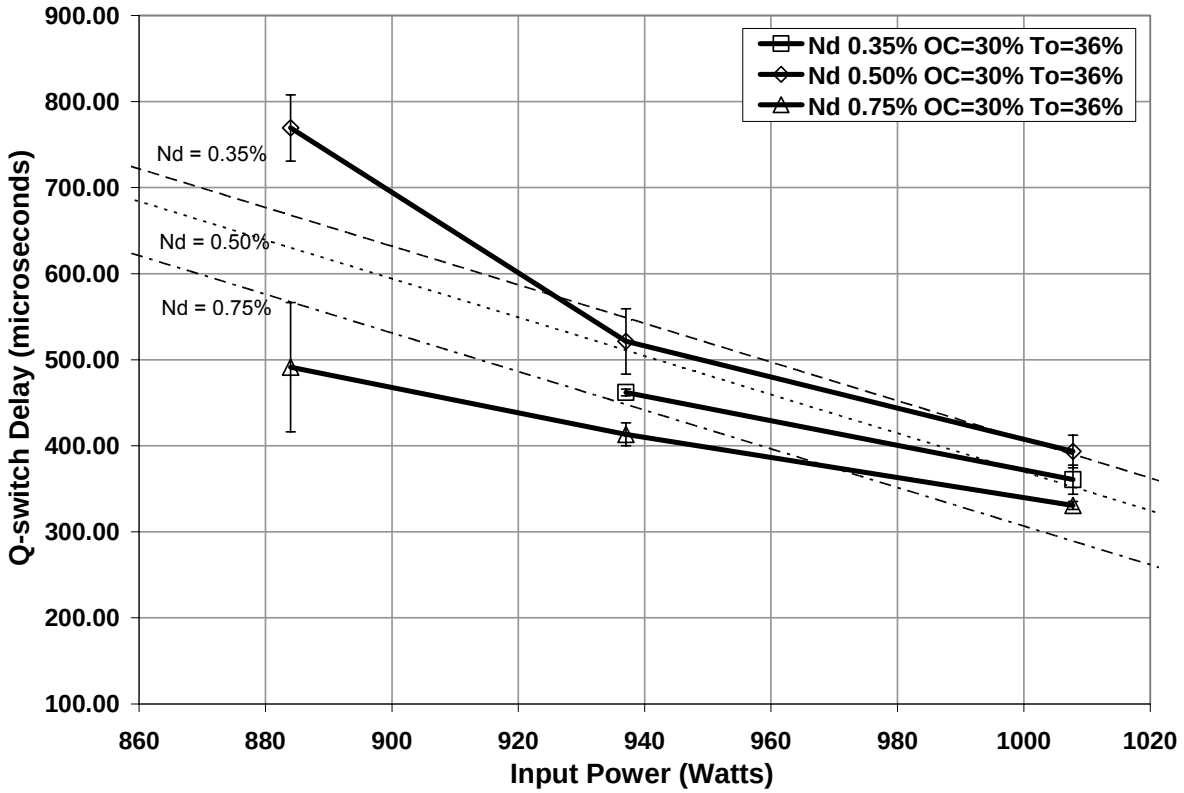

Figure 5.19: Q-switch delay versus optical pump power as a function of Nd concentration with fixed output coupler and Q-switch initial transmission

Table 5.21: Regression analysis of data plotted in Figure 5.19

Regression Statistics	
Multiple R	0.830
R Square	0.689
Adj. R Square	0.659
Standard Error	78.370
Observations	24

ANOVA

	df	SS	MS	F	Significance F
Regression	2	285200.000	142600.000	23.220	4.778E-06
Residual	24	129000.000	6141.000		
Total	26	414200.000			

	Coefficients	Standard Error	t Stat	P-value	Lower 95%	Upper 95%
Intercept	2741.000	334.000	8.207	5.451E-08	2046.000	3436.000
Nd % Conc.	-252.000	101.300	-2.490	2.132E-02	-463.000	-41.400
Pin Optical	-2.250	0.335	-6.710	1.233E-06	-2.940	-1.550

Figure 5.19 and the associated regression results in Table 5.21 indicates a significant dependence of the Q-switch delay on the Nd concentration and the input power. The Nd

concentration affects the volumetric absorption properties of the laser rod and modifies the beam overlap efficiency between the pumped volume and the resonator modes. A more pronounced effect was estimated for the Q-switch delay as a function of the Nd concetration. The differences between the Nd concentration test conditions may not have been sufficient to produce a suitable convincing effect. The Q-switch delay, as expected, decreases rapidly with increasing pump power.

Figure 5.20 shows the Q-switch delay as a function of the input pump power for three values of output coupler reflectivity with constant Q-switch initial transmission and Nd concentration. All data groups but two are completely distinguishible from the rest of the data when a 95% confidence interval is applied. Table 5.22 shows the results of the regression analysis of the data plotted in Figure 5.20. The results indicate that the linear model was a good fit of the experimental data. Considering the outcome of the F test, the null hypothesis would be rejected in this scenario verifying that at least one of the variables provides a significant contribution to the model. Looking at the regression analysis it is evident that both variables contribute significantly to the model. The slope of the trend lines, as well as the regression data, indicates a strong significance of the input pump power on the Q-switch delay. The spacing of the trend lines, as well as the regression results, indicates that the Q-switch delay is significantly dependent on the output coupler reflectivity for this scenario.

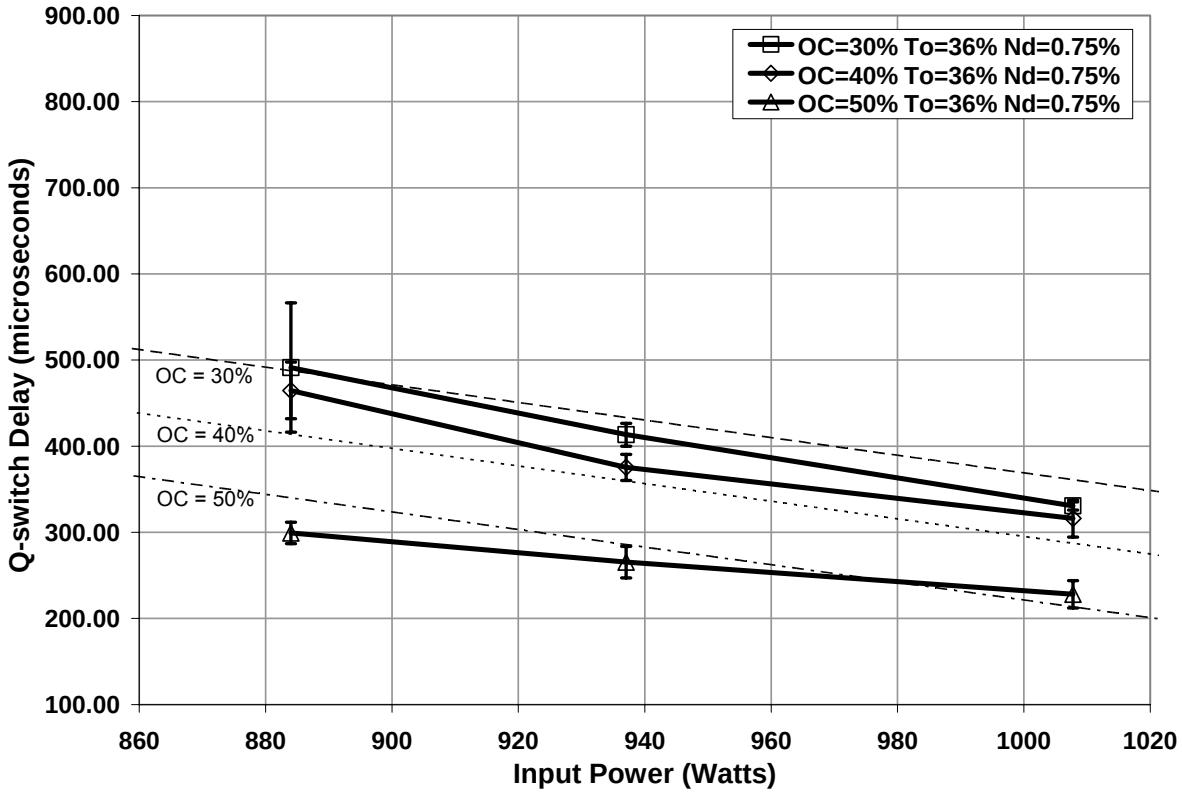

Figure 5.20: Q-switch delay versus optical pump power as a function of output coupler reflectivity with fixed Q-switch initial transmission and Nd concentration

Table 5.22: Regression analysis of data plotted in Figure 5.20

Regression Statistics	
Multiple R	0.911
R Square	0.830
Adj. R Square	0.815
Standard Error	38.100
Observations	27

ANOVA

	df	SS	MS	F	Significance F
Regression	2	169600.000	84790.000	58.420	6.000E-10
Residual	24	34840.000	1452.000		
Total	26	204400.000			

	Coefficients	Standard Error	t Stat	P-value	Lower 95%	Upper 95%
Intercept	1613.000	142.000	11.350	3.890E-11	1320.000	1906.000
OC % Reflect.	-7.380	0.898	-8.220	1.964E-08	-9.200	-5.520
Pin Optical	-1.020	0.146	-7.020	2.914E-07	-1.320	-0.720

Figure 5.20 along with Table 5.22 indicates significant contributions from both the output coupler reflectivity and the input power on the Q-switch delay. The Q-switch delay, as

expected, decreases rapidly with increasing pump power. The higher reflectivity allows the laser cavity to retain more photons which induce subsequent stimulated events that contribute to useful output. The more photons that are retained within the cavity equates to a quicker output pulse usually at a lower energy level as shown in the previous section.

Figure 5.21 shows the Q-switch delay as a function of the input pump power for three values of Q-switch initial transmission with constant output coupler reflectivity and Nd concentration. All data groups are completely distinguishible from the rest of the data when a 95% confidence interval is applied. Table 5.23 shows the results of the regression analysis of the data plotted in Figure 5.21. The results indicate that the linear model was a good fit of the present data. Considering the outcome of the F test, the null hypothesis would be rejected in this scenario verifying that at least one of the variables provides a significant contribution to the model. Looking at the regression data it is evident that both variables contribute significantly to the model. The slope of the trend lines, as well as the regression data, indicates a strong significance of the input pump power on the Q-switch delay. The spacing of the trend lines, as well as the regression data, indicates that the Q-switch delay is significantly dependent on the Q-switch initial transmission for this scenario.

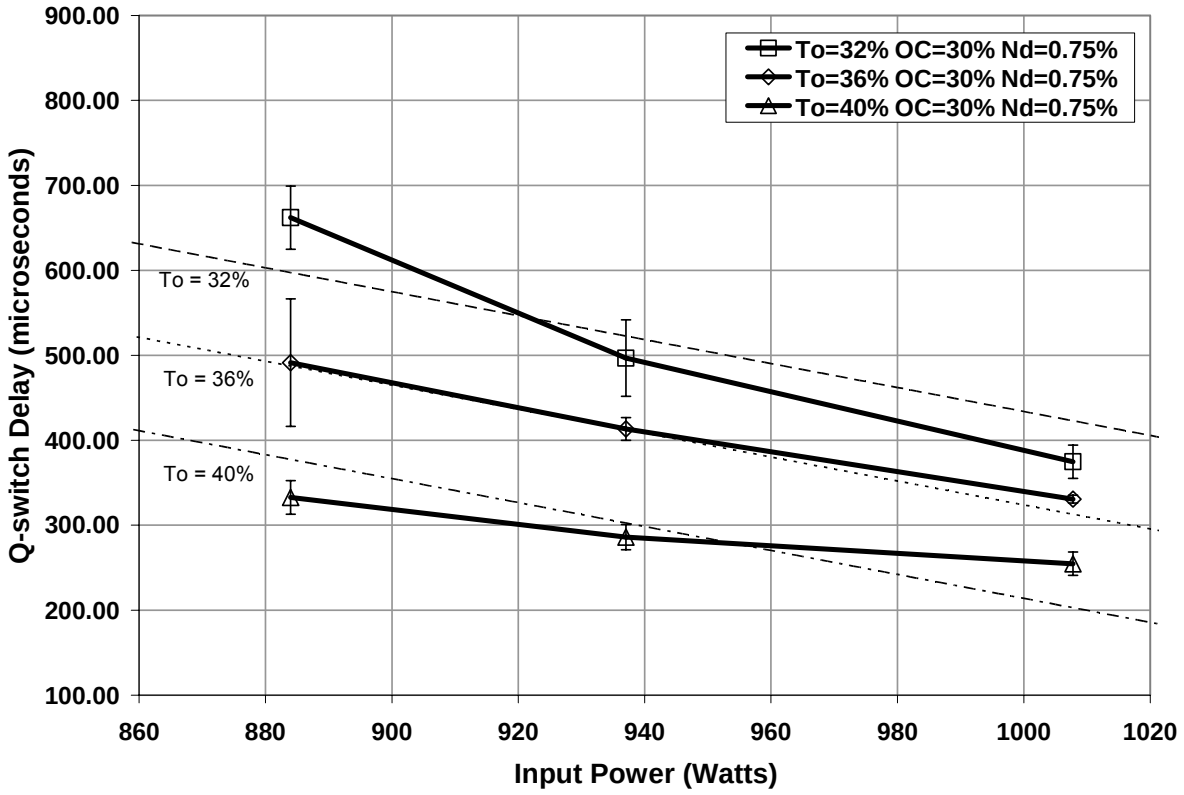

Figure 5.21: Q-switch delay versus optical pump power as a function of Q-switch initial transmission with fixed output coupler and Nd concentration

Table 5.23: Regression analysis of data plotted in Figure 5.21

Regression Statistics	
Multiple R	0.932
R Square	0.869
Adj. R Square	0.858
Standard Error	47.240
Observations	27

ANOVA

	df	SS	MS	F	Significance F
Regression	2	354000.000	177000.000	79.310	2.653E-11
Residual	24	53550.000	2231.000		
Total	26	407500.000			

	Coefficients	Standard Error	t Stat	P-value	Lower 95%	Upper 95%
Intercept	2724.000	197.700	13.780	6.783E-13	2316.000	3132.000
QSW % To	-27.500	2.784	-9.900	6.225E-10	-33.200	-21.800
Pin Optical	-1.410	0.180	-7.810	4.799E-08	-1.780	-1.040

A significant dependence of the Q-switch delay on the input pump power and the Q-switch initial transmission can be seen in Figure 5.21. The decrease of the delay is directly

due to the higher photon density that is provided by the increased pump power which fosters quicker development of the output pulses. The overall difference between each of the Q-switch initial transmission values is due to the variation in optical density of each crystal. The higher the initial transmission the more photons that are allowed through the crystal to induce secondary stimulated transitions in the gain medium and the quicker the Q-switch saturates and initiates the production of an output pulse. Therefore the lower the initial transmission the longer the Q-switch delay.

Table 5.24 shows the results of the regression analysis encompassing all of the data with respect to the Q-switch delay as a dependent variable. The regression data shows a poor linear fit, however the F test indicates a rejection of the null hypothesis. This indicates that at least one of the independent variables provides a significant contribution to the model. The data also indicates that the Nd concentration is the only independent variable that does not contribute significantly to the model when considering all of the variables. The Q-switch delay is strongly dependent on the intracavity flux density, therefore only the variables that strongly effect the flux density were found to have a significant influence on the Q-switch delay.

Table 5.24: Regression analysis of the output pulse delay data

Regression Statistics	
Multiple R	0.746
R Square	0.556
Adj. R Square	0.548
Standard Error	86.280
Observations	228

ANOVA

	df	SS	MS	F	Significance F
Regression	2	2082000.000	520400.000	69.910	2.792E-38
Residual	24	1660000.000	7444.000		
Total	26	3742000.000			

	Coefficients	Standard Error	t Stat	P-value	Lower 95%	Upper 95%
Intercept	2574.000	137.100	18.770	8.629E-48	2304.000	2844.000
Nd % Conc.	-34.500	34.560	-1.000	3.189E-01	-103.000	33.580
OC % Reflect.	-6.090	0.720	-8.460	3.572E-15	-7.510	-4.670
QSW % To	-19.200	1.776	-10.800	3.429E-22	-22.700	-15.700
Pin Optical	-1.290	0.113	-11.400	7.024E-24	-1.510	-1.060

5.1.4 Beam Quality

Figures 5.22-5.24 show the dependence of the output pulse beam quality as a function of the Q-switch initial transmission and the output coupler reflectivity each with respect to Nd concentration. Figure 5.22 shows that three of the data groupings can be distinguished when a 95% confidence level is applied to the data. Table 5.25 shows the results of the regression analysis of the data plotted in Figure 5.22. The results indicate that the linear model was a poor fit to the data overall. Considering the outcome of the F test, the null hypothesis would be rejected in this scenario verifying that at least one of the variables provides a significant contribution to the model. This analysis indicates that the Q-switch initial transmission contributes significantly to the model. The slope of the trend lines, as well as the regression data, indicates little to no significance of the output coupler reflectivity on the M^2 value. The spacing of the trend lines, as well as the regression data, indicates that the M^2 is significantly dependent on the Q-switch initial transmission.

The wide degree of variation seen in the M^2 data is primarily due to heat removal issues within the laser rod. The thermal gradients produced by the slight asymmetry in the

pumping arrangement induce a minor thermal lens effect which is highly dependent on the optical pump power and repetition rate. The thermal lensing is thought to affect every output pulse producing minor variations in each output pulse leading to the high degree of variance found in the data. This is compounded by the aparatus used to measure the beam quality. The beam quality measurement software that calculates the beam width of the output pulse at multiple locations along an artificial beam waist. Minor vairations in the beam waist can have a significant effect on the artificial beam waist parameters producing a large degree of variation in the measured beam quality parameters.

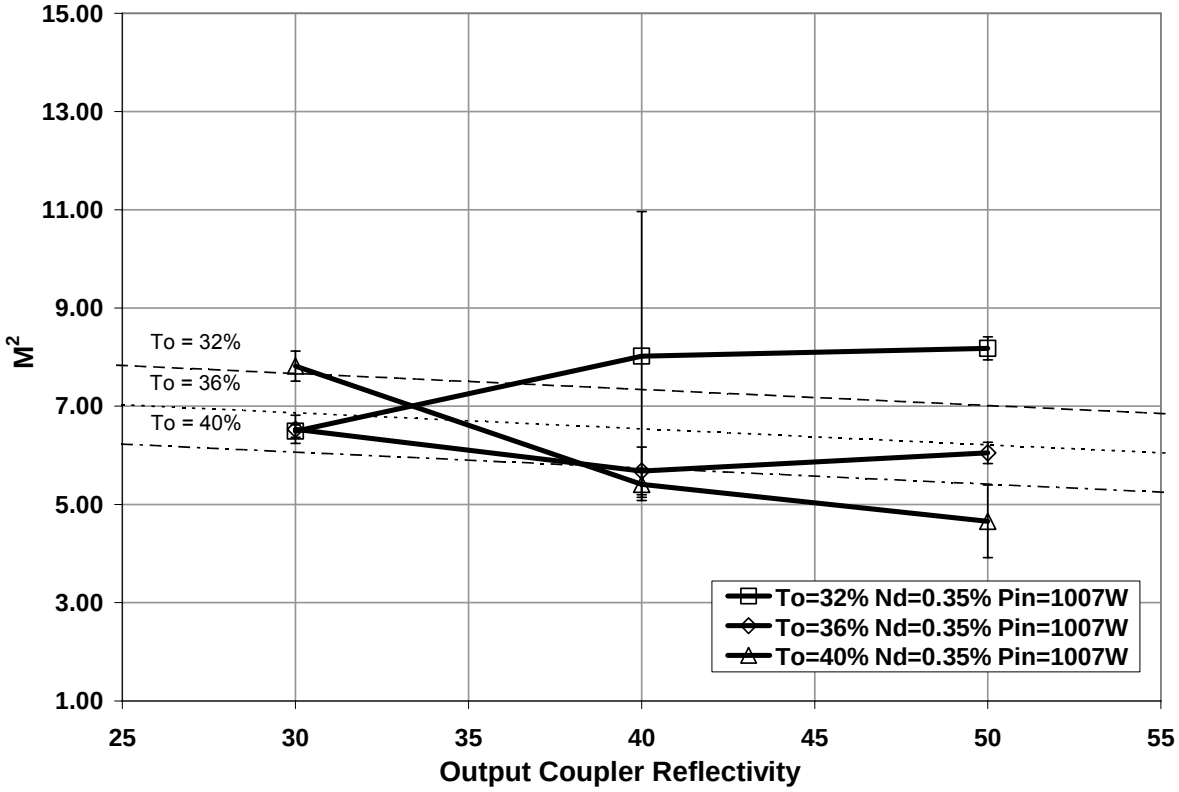

Figure 5.22: M^2 response as a function of output coupler reflectivity and Q-switch initial transmission with Nd concentration of 0.35% at an input power of 1007 Watts

Table 5.25: Regression analysis of data plotted in Figure 5.22

Regression Statistics	
Multiple R	0.508
R Square	0.258
Adj. R Square	0.196
Standard Error	1.271
Observations	27

ANOVA

	df	SS	MS	F	Significance F
Regression	2	13.470	6.733	4.171	2.788E-02
Residual	24	38.740	1.614		
Total	26	52.210			

	Coefficients	Standard Error	t Stat	P-value	Lower 95%	Upper 95%
Intercept	15.050	2.959	5.086	3.344E-05	8.943	21.160
OC % Reflect.	-0.030	0.030	-1.090	2.870E-01	-0.090	0.029
QSW % To	-0.200	0.075	-2.680	1.324E-02	-0.350	-0.050

The results from Figures 5.22 through 5.24 were not consistent in showing any significant dependence of any variable for all three tests. Although Figures 5.22 and 5.23 show Q-switch initial transmission as a significant influence on the beam quality, however Figure 5.24 does not show this dependence. Only Figure 5.23 indicates that the output coupler reflectivity contributes significantly to the beam quality. Considering the prior analysis of the dependent variables there is greater variability in the beam quality data.

Figure 5.23 shows that three of the data groupings can be distinguished when a 95% confidence level is applied to the data. Table 5.26 shows the results of the regression analysis of the data plotted in Figure 5.23. The results indicate that the linear model was a poor fit to the data overall. Considering the outcome of the F test, the null hypothesis would be rejected in this scenario verifying that at least one of the variables provides a significant contribution to the model. This analysis indicates that the Q-switch initial transmission contributes significantly to the model. The slope of the trend lines, as well as the regression data, indicates little to no significance of the output coupler reflectivity on the M^2 value. The

spacing of the trend lines, as well as the regression data, indicates that the M^2 is significantly dependent on the Q-switch initial transmission.

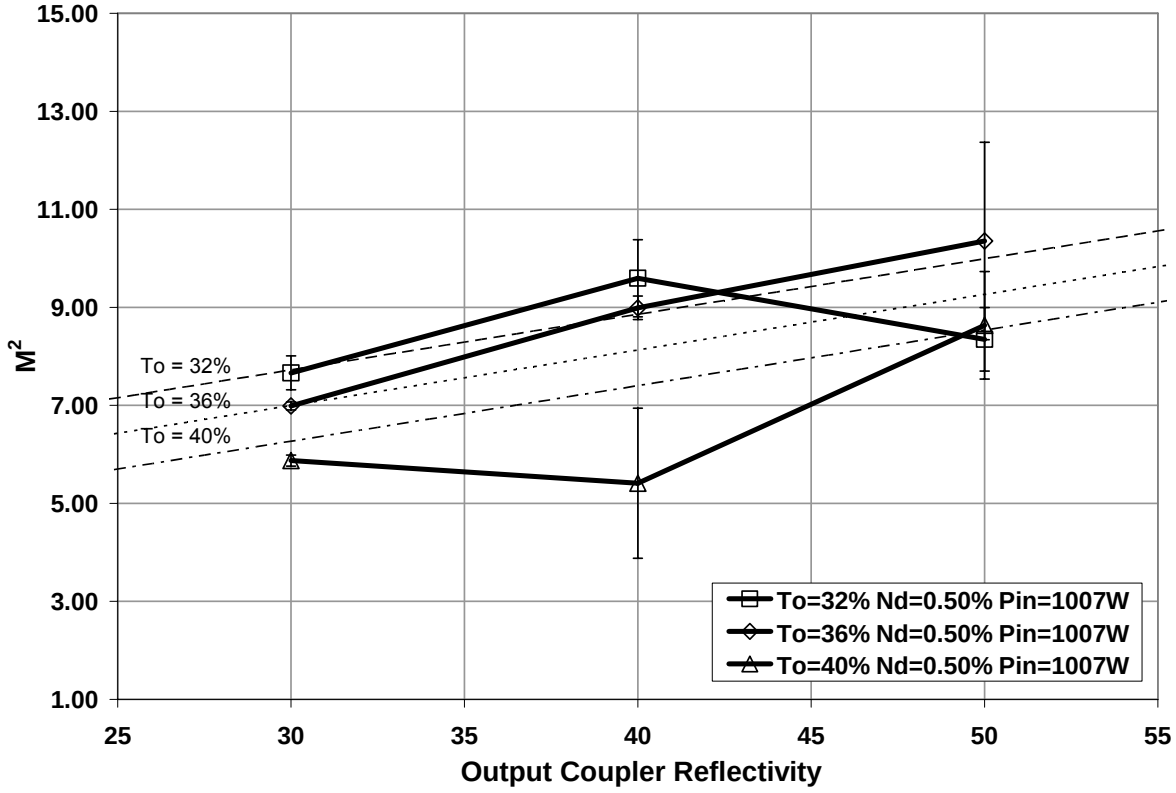

Figure 5.23: Output beam quality response as a function of output coupler reflectivity and Q-switch initial transmission with Nd concentration of 0.50% at an input power of 1007 Watts

Table 5.26: Regression analysis of data plotted in Figure 5.23

Regression Statistics	
Multiple R	0.715
R Square	0.512
Adj. R Square	0.471
Standard Error	1.140
Observations	27

ANOVA

	df	SS	MS	F	Significance F
Regression	2	32.700	16.350	12.580	1.834E-04
Residual	24	31.200	1.300		
Total	26	63.890			

	Coefficients	Standard Error	t Stat	P-value	Lower 95%	Upper 95%
Intercept	10.140	2.656	3.819	8.310E-04	4.662	15.620
OC % Reflect.	0.113	0.027	4.222	3.005E-04	0.058	0.169
QSW % To	-0.180	0.067	-2.710	1.227E-02	-0.320	-0.040

Figure 5.24 shows that all data groupings are indistinguishable when a 95% confidence level is applied to the data. Table 5.27 shows the results of the regression analysis of the data plotted in Figure 5.24. The results indicate that the linear model was a poor fit to the data overall. Considering the outcome of the F test, the null hypothesis would fail to be rejected in this scenario verifying that neither of the variables provides a significant contribution to the model. The slope of the trend lines, as well as the regression data, indicates no significance of the output coupler reflectivity on the M^2 value. The spacing of the trend lines, as well as the regression data, indicates that the M^2 has no significant dependence on the Q-switch initial transmission.

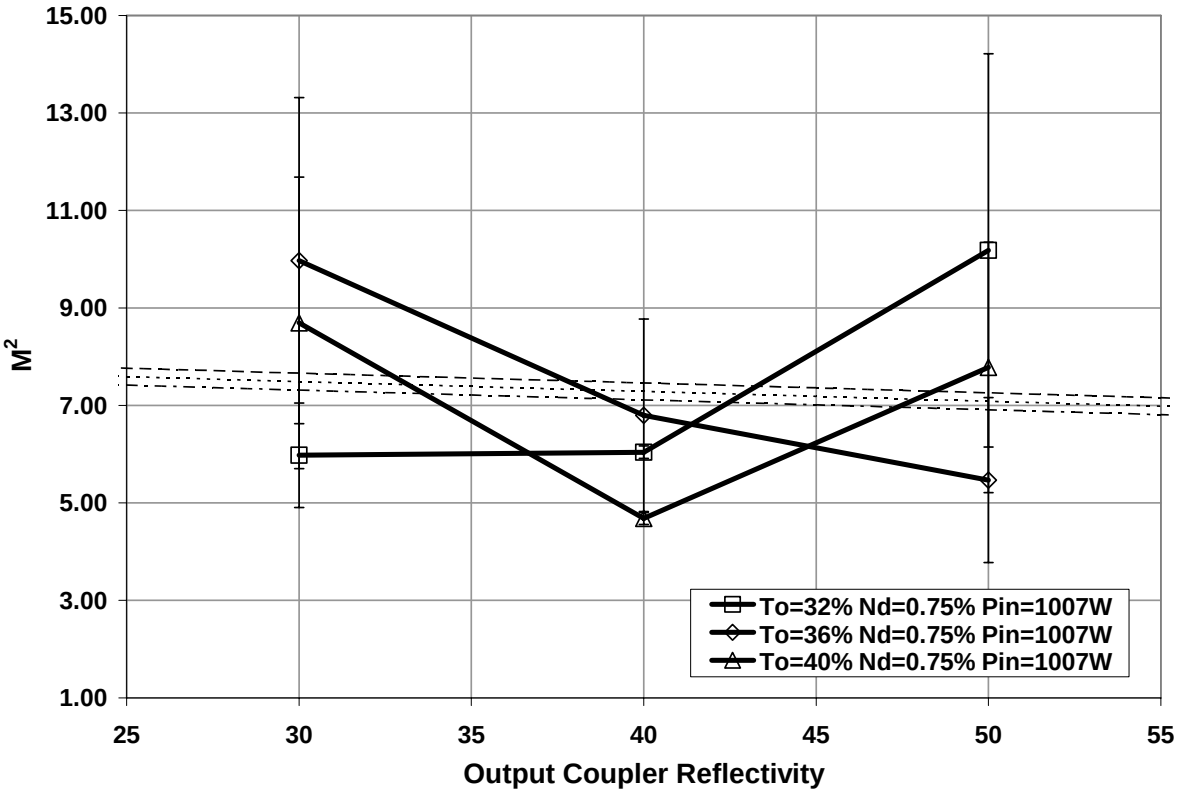

Figure 5.24: Output beam quality response as a function of output coupler reflectivity and Q-switch initial transmission with Nd concentration of 0.75% at an input power of 1007 Watts

Table 5.27: Regression analysis of data plotted in Figure 5.24

Regression Statistics	
Multiple R	0.086
R Square	0.007
Adj. R Square	-0.080
Standard Error	2.681
Observations	27

ANOVA

	df	SS	MS	F	Significance F
Regression	2	1.280	0.640	0.089	9.151E-01
Residual	24	172.500	7.189		
Total	26	173.800			

	Coefficients	Standard Error	t Stat	P-value	Lower 95%	Upper 95%
Intercept	9.661	6.246	1.547	1.350E-01	-3.230	22.550
OC % Reflect.	-0.020	0.063	-0.320	7.518E-01	-0.150	0.110
QSW % To	-0.040	0.158	-0.280	7.856E-01	-0.370	0.283

Figure 5.25 shows that few of the data groupings are distinguishable when a 95% confidence level is applied to the data. Table 5.28 shows the results of the regression analysis

of the data plotted in Figure 5.25. The results indicate that the linear model was a poor fit to the data overall. Considering the outcome of the F test, the null hypothesis would fail to be rejected in this scenario verifying that neither of the variables provides a significant contribution to the model. The slope of the trend lines, as well as the regression data, indicates no significance of the output coupler reflectivity on the M^2 value. The spacing of the trend lines, as well as the regression data, indicates that the M^2 has no significant dependence on the Nd concentration.

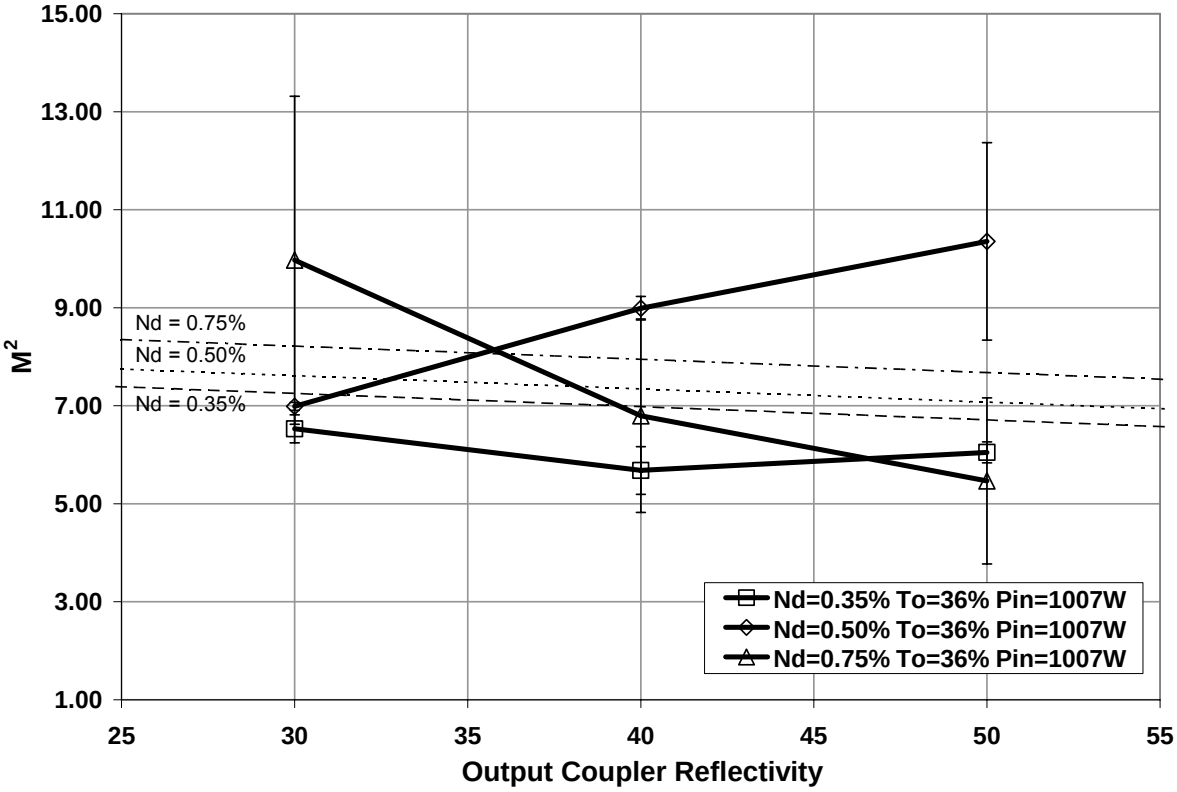

Figure 5.25: M^2 response as a function of output coupler reflectivity and Nd concentration with Q-switch initial transmission of 36% and input pump power of 1007W

Table 5.28: Regression analysis of data plotted in Figure 5.25

Regression Statistics	
Multiple R	0.218
R Square	0.047
Adj. R Square	-0.030
Standard Error	2.164
Observations	27

ANOVA

	df	SS	MS	F	Significance F
Regression	2	5.600	2.800	0.598	5.580E-01
Residual	24	112.400	4.684		
Total	26	118.000			

	Coefficients	Standard Error	t Stat	P-value	Lower 95%	Upper 95%
Intercept	7.217	2.480	2.910	7.675E-03	2.099	12.340
Nd % Conc.	2.415	2.525	0.957	3.482E-01	-2.790	7.626
OC % Reflect.	-0.030	0.051	-0.530	6.015E-01	-0.130	0.078

It was hypothesized that both the Nd concentration and the output coupler reflectivity would have a significant effect on the beam quality. The Nd concentration effects the volumetric absorption properties of the laser rod and modifies the beam overlap efficiency between the pumped volume and the resonator modes. It was thought that the beam quality would be modified with respect to the Nd concentration because of the differences in the amount of absorption and subsequent heat deposition in the laser rod. The deposition of heat due to uneven pumping, absorption, or lasing can have a significant effect on the beam quality due to thermal lensing. The output coupler reflectvity was also anticipated to have a strong affect on the beam quality due to increases in the intracavity flux from increasing reflectivity. It was also thought that if the output coupler reflectivity was lower that the increased pump time for lasing to occur this could possibly induce stronger thermal lensing due to the absorption and time scales involved. Unfortunately for this scenario neither variable was found to have a significant effect on the M^2.

Figure 5.26 shows M^2 as a function of pump power for three Nd concentrations with fixed output coupler reflectivity and Q-switch initial transmission. The data point at the

lowest input power level for the 0.35% Nd concentration test did not produce output and therefore was not plotted. The data shows no dependence of the beam quality on the pump power. Figure 5.26 shows that few of the data groupings are distinguishable when a 95% confidence level is applied to the data. Table 5.29 shows the results of the regression analysis of the data plotted in Figure 5.26. The results indicate that the linear model was a poor fit to the data overall. Considering the outcome of the F test, the null hypothesis would be rejected in this scenario verifying that at least one of the variables provides a significant contribution to the model. The slope of the trend lines, as well as the regression data, indicates no significance of the input pump power on the M^2 value. The spacing of the trend lines, as well as the regression data, indicates that the M^2 has a significant dependence on the Nd concentration in this scenario.

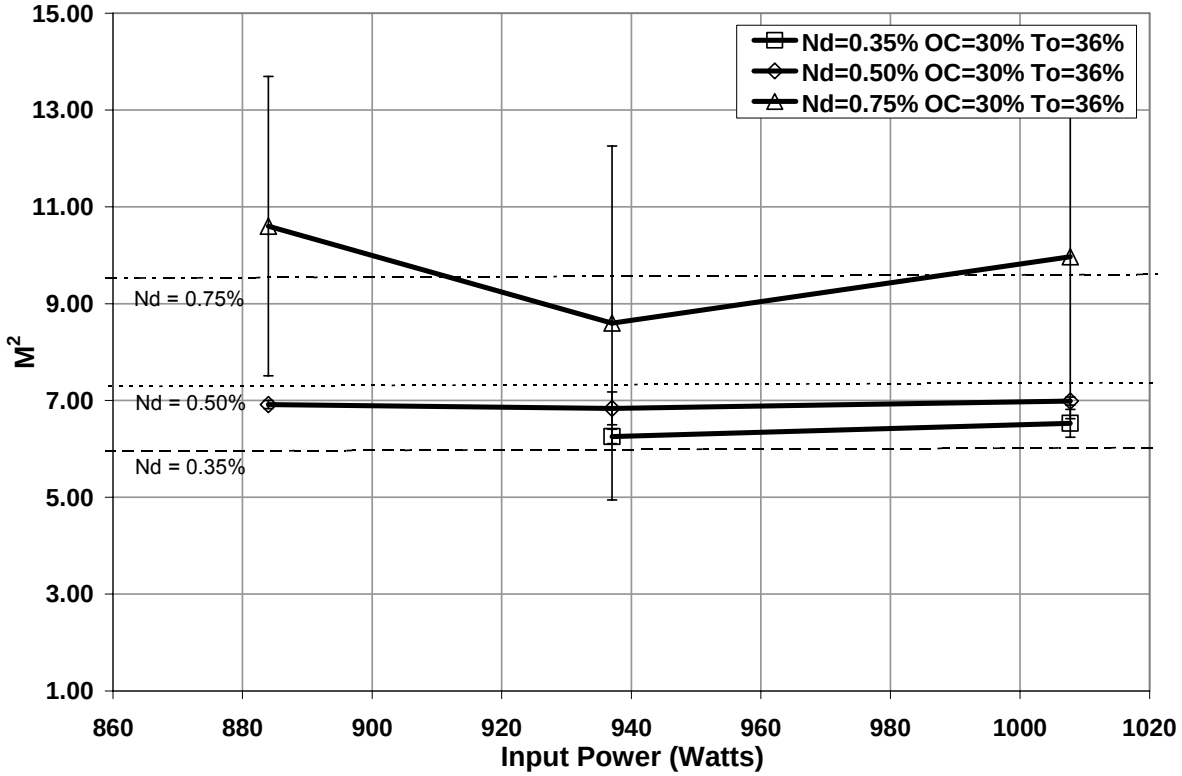

Figure 5.26: M^2 versus pump power for all three Nd concentrations with fixed output coupler and Q-switch values

Table 5.29: Regression analysis of data plotted in Figure 5.26

Regression Statistics	
Multiple R	0.664
R Square	0.440
Adj. R Square	0.387
Standard Error	1.730
Observations	24

ANOVA

	df	SS	MS	F	Significance F
Regression	2	49.440	24.720	8.263	2.254E-03
Residual	24	62.830	2.992		
Total	26	112.300			

	Coefficients	Standard Error	t Stat	P-value	Lower 95%	Upper 95%
Intercept	2.408	7.371	0.327	7.472E-01	-12.900	17.740
Nd % Conc.	8.946	2.236	4.001	6.487E-04	4.295	13.600
Pin Optical	0.000	0.007	0.065	9.491E-01	-0.010	0.016

The data in Figure 5.26 along with the regression analysis from Table 5.29 shows that the beam quality degrades as the dopant level is increased. This is primarily due to thermal

lensing caused by the higher absorption rate of the higher dopant levels. More energy is transferred to the gain medium in a given amount of time in the form of waste heat which effects the index of refraction of the laser rod causing it to act like a weak lens. It was thought that the beam quality would also degrade as a function of the input power due to excess waste heat being transferred to the laser gain medium. This was not the case for this scenario; however, the range of input power levels tested may not have been extreme enough to discern such an effect.

Figure 5.27 shows that none of the data groupings are distinguishable when a 95% confidence level is applied to the data. Table 5.30 shows the results of the regression analysis of the data plotted in Figure 5.27. The results indicate that the linear model was a poor fit to the data overall. Considering the outcome of the F test, the null hypothesis would fail to be rejected in this scenario verifying that neither of the variables provides a significant contribution to the model. The slope of the trend lines, as well as the regression data, indicates no significance of the input pump power on the M^2 value. The spacing of the trend lines, as well as the regression data, indicates that the M^2 has no significant dependence on the Q-switch initial transmission.

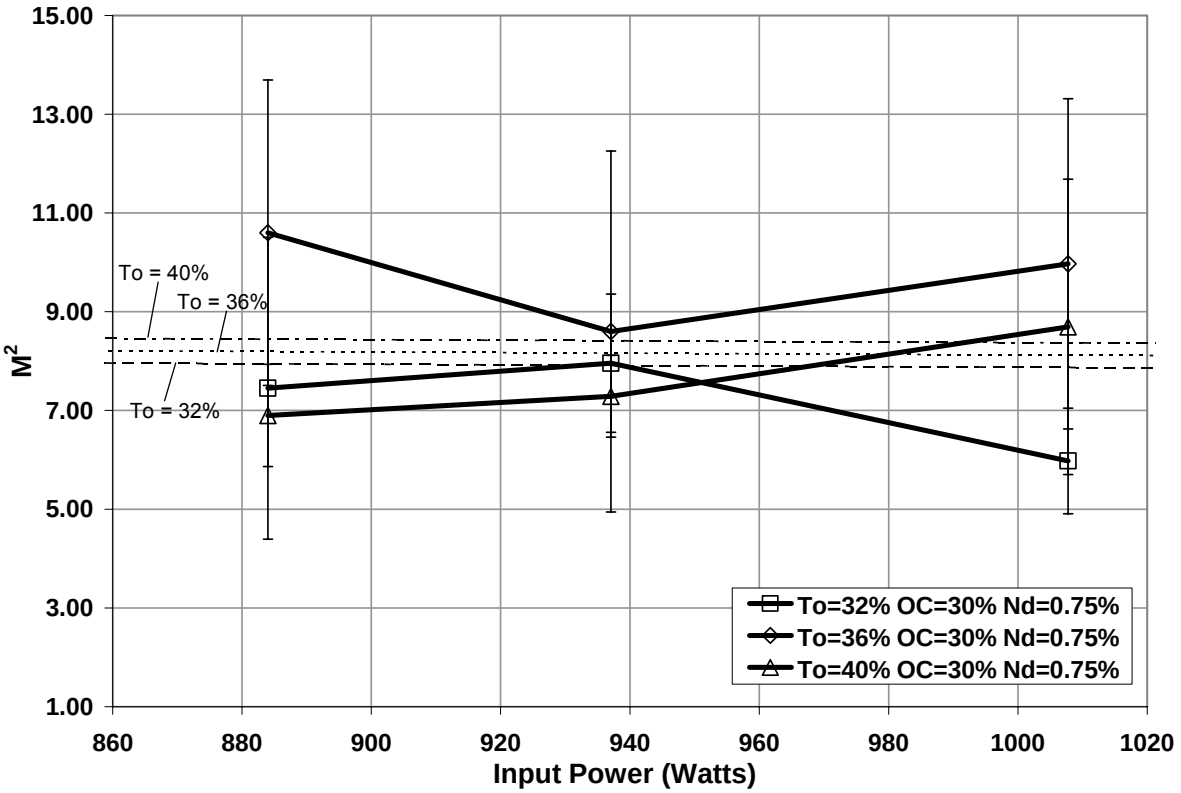

Figure 5.27: M^2 versus pump power for three Q-switch values with fixed output coupler and Nd concentration values

Table 5.30: Regression analysis of data plotted in Figure 5.27

Regression Statistics	
Multiple R	0.090
R Square	0.008
Adj. R Square	-0.070
Standard Error	2.419
Observations	27

ANOVA

	df	SS	MS	F	Significance F
Regression	2	1.145	0.572	0.098	9.072E-01
Residual	24	140.400	5.852		
Total	26	141.600			

	Coefficients	Standard Error	t Stat	P-value	Lower 95%	Upper 95%
Intercept	6.479	10.120	0.640	5.282E-01	-14.400	27.370
QSW % To	0.062	0.143	0.437	6.657E-01	-0.230	0.357
Pin Optical	0.000	0.009	-0.060	9.489E-01	-0.020	0.018

The data from Figure 5.27 shows no dependence on the Q-switch initial transmission. This was expected because the beam quality should be primarily dependent on the

parameters that effect the excited state distribution within the gain medium, i.e. waste heat distribution. The effect of the input power was discussed previously.

Figure 5.28 shows that a few of the data groupings are distinguishable when a 95% confidence level is applied to the data. Table 5.31 shows the results of the regression analysis of the data plotted in Figure 5.28. The results indicate that the linear model was a poor fit to the data overall. Considering the outcome of the F test, the null hypothesis would be rejected in this scenario verifying that at least one of the variables provides a significant contribution to the model. The slope of the trend lines, as well as the regression data, indicates no significance of the input pump power on the M^2 value. The spacing of the trend lines, as well as the regression data, indicates that the M^2 has a significant dependence on the output coupler reflectivity.

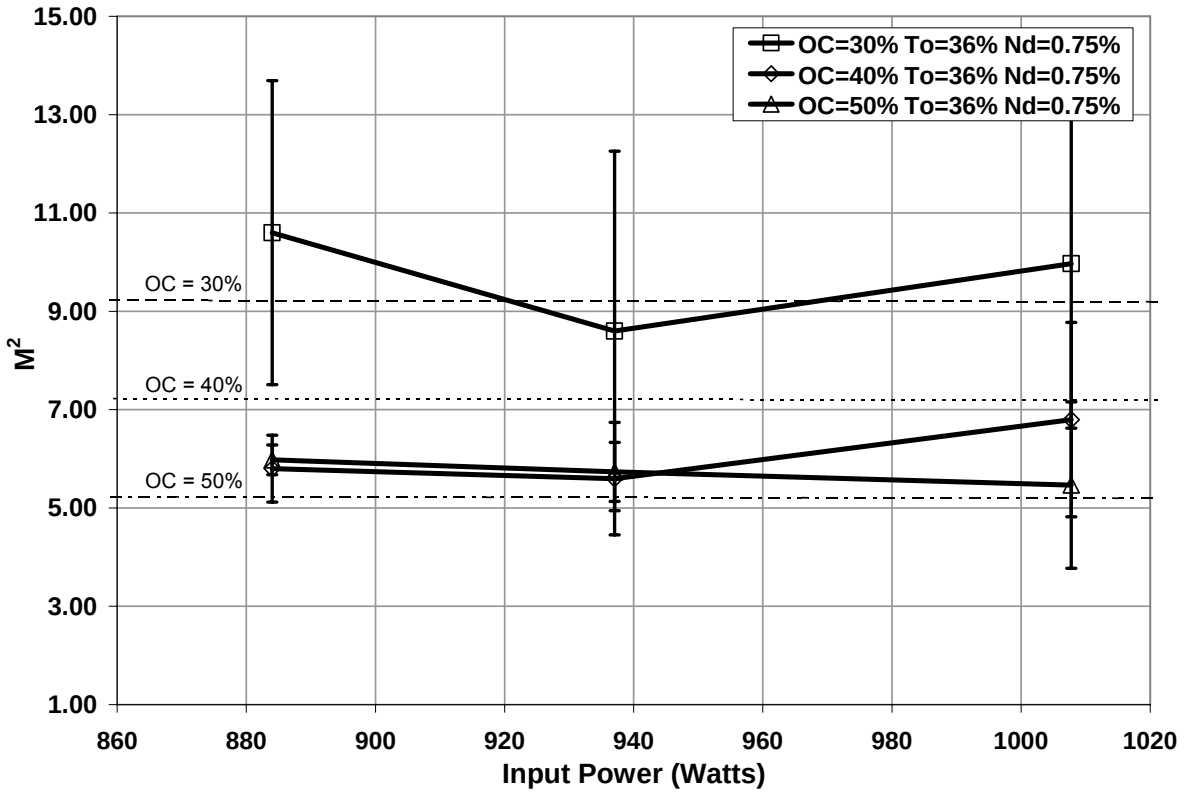

Figure 5.28: M^2 versus pump power for three output coupler reflectivities with fixed Q-switch initial transmission and Nd concentration

Table 5.31: Regression analysis of data plotted in Figure 5.28

Regression Statistics	
Multiple R	0.666
R Square	0.444
Adj. R Square	0.397
Standard Error	1.937
Observations	27

ANOVA

	df	SS	MS	F	Significance F
Regression	2	71.880	35.940	9.577	8.757E-04
Residual	24	90.070	3.753		
Total	26	162.000			

	Coefficients	Standard Error	t Stat	P-value	Lower 95%	Upper 95%
Intercept	15.370	7.222	2.128	4.378E-02	0.465	30.270
OC % Reflect.	-0.200	0.046	-4.380	2.028E-04	-0.290	-0.110
Pin Optical	0.000	0.007	-0.020	9.812E-01	-0.020	0.015

Figure 5.28 along with the regression data from Table 5.31 indicate a significant contribution of the output coupler reflectivity to the beam quality. The variance of the data

does not make this conclusion clear without the regression analysis. The output coupler reflectivity directly affects the intracavity photon flux density by determining how many photons are retained within the cavity and how many are released as leakage, prior to lasing, or as output during lasing. As shown in previous data sets the input pump power has no significant affect on the beam quality in this scenario.

Table 5.32 shows the results of the regression analysis encompassing all of the data with respect to the M^2 beam quality product. The regression data shows a poor linear fit, however the F test indicates a probability for the rejection of the null hypothesis. This indicates that at least one of the independent variables provides a significant contribution to the model. The data also indicates that the Q-switch initial transmission is the only independent variable that contributes significantly to the model when considering all of the variables.

Table 5.32: Regression analysis of the output beam M^2 data

Regression Statistics	
Multiple R	0.286
R Square	0.082
Adj. R Square	0.065
Standard Error	1.881
Observations	228

ANOVA

	df	SS	MS	F	Significance F
Regression	2	70.380	17.590	4.971	7.407E-04
Residual	24	789.300	3.540		
Total	26	859.700			

	Coefficients	Standard Error	t Stat	P-value	Lower 95%	Upper 95%
Intercept	12.380	2.990	4.139	4.941E-05	6.484	18.270
Nd % Conc.	1.067	0.754	1.416	1.581E-01	-0.420	2.552
OC % Reflect.	0.019	0.016	1.214	2.262E-01	-0.010	0.050
QSW % To	-0.150	0.039	-3.860	1.468E-04	-0.230	-0.070
Pin Optical	0.000	0.002	-0.410	6.831E-01	-0.010	0.004

5.1.5 Output Peak Power

Figures 5.29-5.31 show the dependence of the output peak power on the Q-switch initial transmission and output coupler reflectivity each with varying fixed values of Nd concentration. Figure 5.29 shows that all but two of the data groupings can be distinguished when a 95% confidence level is applied to the data. Table 5.33 shows the results of the regression analysis of the data plotted in Figure 5.29. The results indicate that the linear model was a mediocre fit to the data overall. Considering the outcome of the F test, the null hypothesis would be rejected in this scenario verifying that at least one of the variables provides a significant contribution to the model. This analysis indicates that both variables contribute significantly to the model. The slope of the trend lines, as well as the regression data, indicates a significant contribution of the output coupler reflectivity on the output peak power. The spacing of the trend lines, as well as the regression data, indicates that the output peak power is significantly dependent on the Q-switch initial transmission.

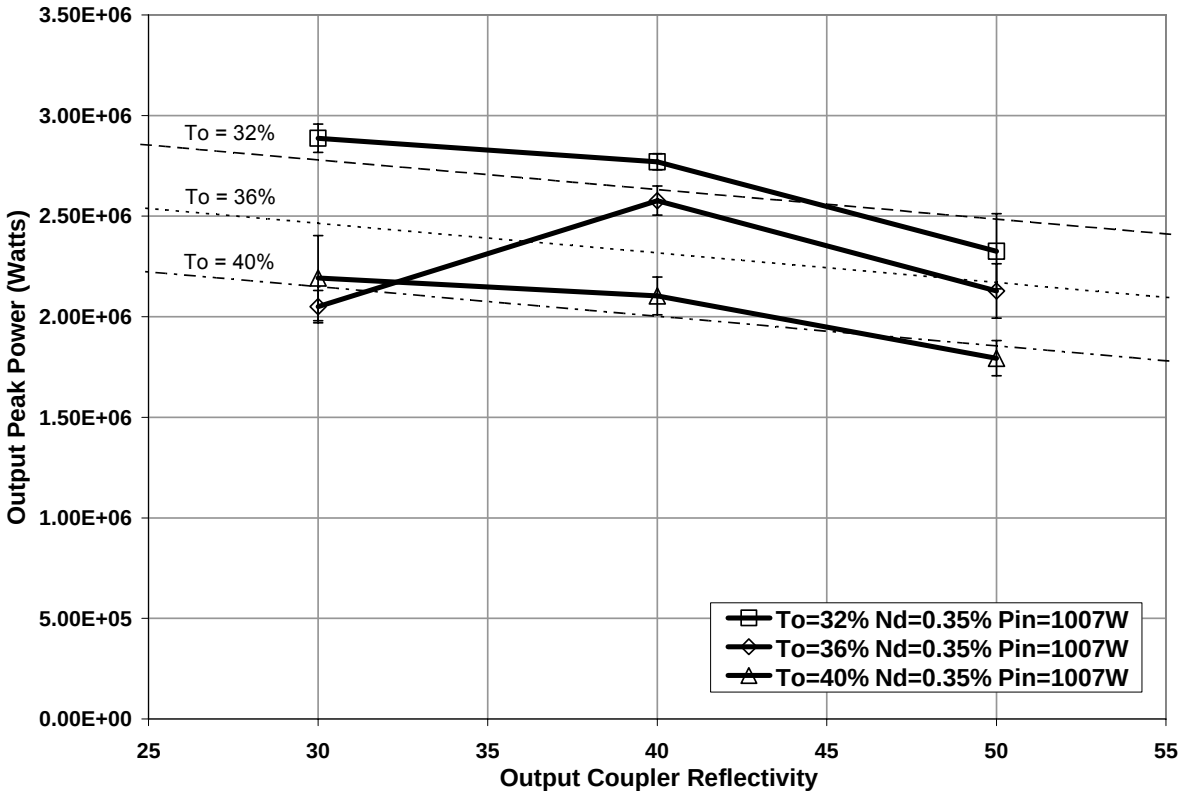

Figure 5.29: Output peak power response as a function of output coupler reflectivity and Q-switch initial transmission with Nd concentration of 0.35% at an input power of 1007 Watts

Table 5.33: Regression analysis of data plotted in Figure 5.29

Regression Statistics	
Multiple R	0.810
R Square	0.656
Adj. R Square	0.627
Standard Error	218200.000
Observations	27

ANOVA

	df	SS	MS	F	Significance F
Regression	2	2.177E+12	1.089E+12	22.870	2.759E-06
Residual	24	1.142E+12	4.760E+10		
Total	26	3.320E+12			

	Coefficients	Standard Error	t Stat	P-value	Lower 95%	Upper 95%
Intercept	5742000.000	508200.000	11.300	4.306E-11	4693000.000	6791000.000
OC % Reflect.	-14700.000	5142.000	-2.860	8.577E-03	-25300.000	-4110.000
QSW % To	-78800.000	12860.000	-6.130	2.494E-06	-105000.000	-52200.000

The output peak power data for all Nd concentration levels, Figures 5.29 through 5.31, tends to increase as both the output coupler reflectivity and the Q-switch initial

transmission are decreased. The output peak power is derived by dividing the output pulse energy in joules by the output pulse width in seconds. The peak power follows the same trend as the output pulse energy due to the relatively constant output pulse width data.

Figure 5.30 shows that all but one of the data groupings can be distinguished when a 95% confidence level is applied to the data. Table 5.34 shows the results of the regression analysis of the data plotted in Figure 5.30. The results indicate that the linear model was a good fit to the data overall. Considering the outcome of the F test, the null hypothesis would be rejected in this scenario verifying that at least one of the variables provides a significant contribution to the model. This analysis indicates that both variables contribute significantly to the model. The slope of the trend lines, as well as the regression data, indicates a significant contribution of the output coupler reflectivity on the output peak power. The spacing of the trend lines, as well as the regression data, indicates that the output peak power is also significantly dependent on the Q-switch initial transmission.

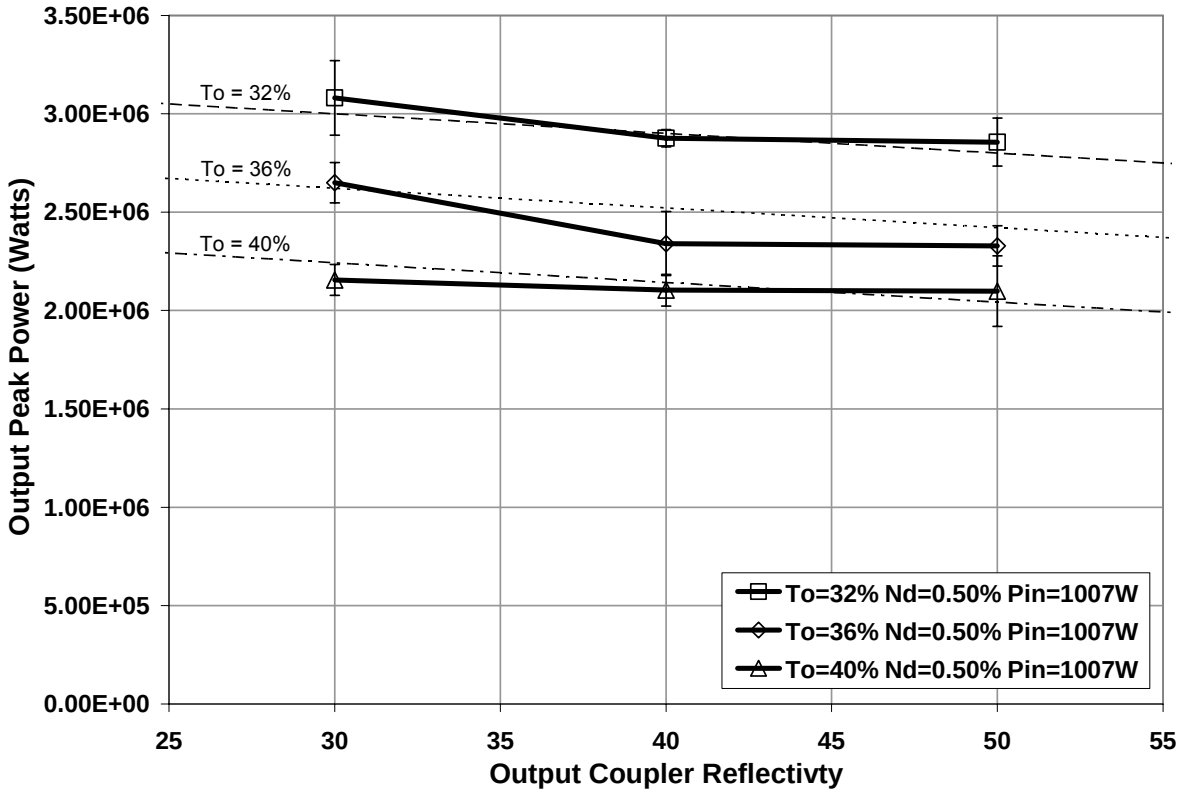

Figure 5.30: Output peak power response as a function of output coupler reflectivity and Q-switch initial transmission with Nd concentration of 0.50% at an input power of 1007 Watts

Table 5.34: Regression analysis of data plotted in Figure 5.30

Regression Statistics	
Multiple R	0.924
R Square	0.854
Adj. R Square	0.842
Standard Error	140300.000
Observations	27

ANOVA

	df	SS	MS	F	Significance F
Regression	2	2.764E+12	1.382E+12	70.210	9.359E-11
Residual	24	4.724E+11	1.968E+10		
Total	26	3.236E+12			

	Coefficients	Standard Error	t Stat	P-value	Lower 95%	Upper 95%
Intercept	6331000.000	326800.000	19.370	3.679E-16	5657000.000	7006000.000
OC % Reflect.	-10000.000	3307.000	-3.020	5.856E-03	-16800.000	-3180.000
QSW % To	-94700.000	8267.000	-11.500	3.238E-11	-112000.000	-77700.000

Figure 5.31 shows that all but two of the data groupings can be distinguished when a 95% confidence level is applied to the data. Table 3.35 shows the results of the regression

analysis of the data plotted in Figure 5.31. The results indicate that the linear model was a good fit to the data overall. Considering the outcome of the F test, the null hypothesis would be rejected in this scenario verifying that at least one of the variables provides a significant contribution to the model. This analysis indicates that both variables contribute significantly to the model. The slope of the trend lines, as well as the regression data, indicates a significant contribution of the output coupler reflectivity on the output peak power. The spacing of the trend lines, as well as the regression data, indicates that the output peak power is also significantly dependent on the Q-switch initial transmission.

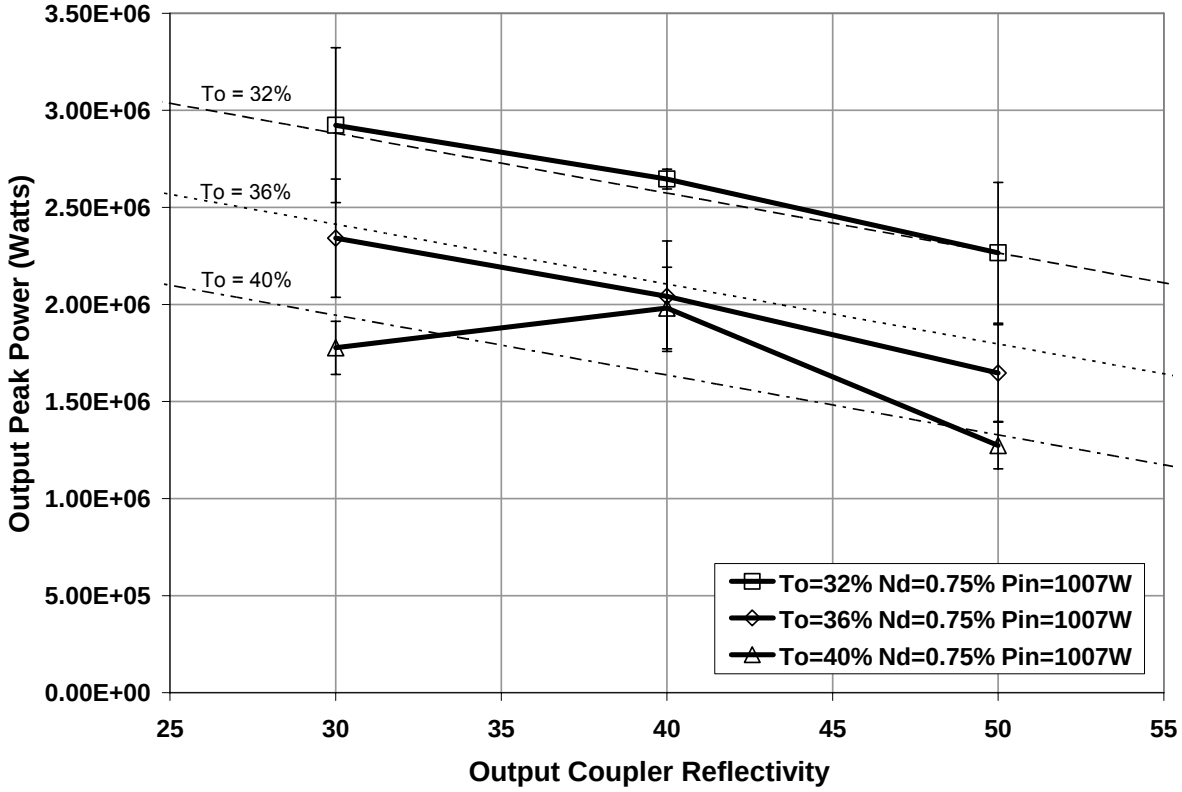

Figure 5.31: Output peak power response as a function of output coupler reflectivity and Q-switch initial transmission with Nd concentration of 0.75% at an input power of 1007 Watts

Table 3.35: Regression analysis of data plotted in Figure 5.31

Regression Statistics	
Multiple R	0.924
R Square	0.854
Adj. R Square	0.842
Standard Error	200500.000
Observations	27

ANOVA

	df	SS	MS	F	Significance F
Regression	2	5.665E+12	2.832E+12	70.420	9.073E-11
Residual	24	9.653E+11	4.022E+10		
Total	26	6.630E+12			

	Coefficients	Standard Error	t Stat	P-value	Lower 95%	Upper 95%
Intercept	7556000.000	467200.000	16.170	2.079E-14	6592000.000	8520000.000
OC % Reflect.	-30800.000	4727.000	-6.530	9.503E-07	-40600.000	-21100.000
QSW % To	-117000.000	11820.000	-9.900	5.832E-10	-142000.000	-92800.000

Figure 5.32 shows that few of the data groupings can be distinguished when a 95% confidence level is applied to the data. Table 5.36 shows the results of the regression analysis of the data plotted in Figure 5.32. The results indicate that the linear model was a poor fit to the data overall. Considering the outcome of the F test, the null hypothesis would be rejected in this scenario verifying that at least one of the variables provides a significant contribution to the model. This analysis indicates that both variables contribute significantly to the model. The slope of the trend lines, as well as the regression data, indicates a significant contribution of the output coupler reflectivity on the output peak power. The spacing of the trend lines, as well as the regression data, indicates that the output peak power is also significantly dependent on the Nd concentration.

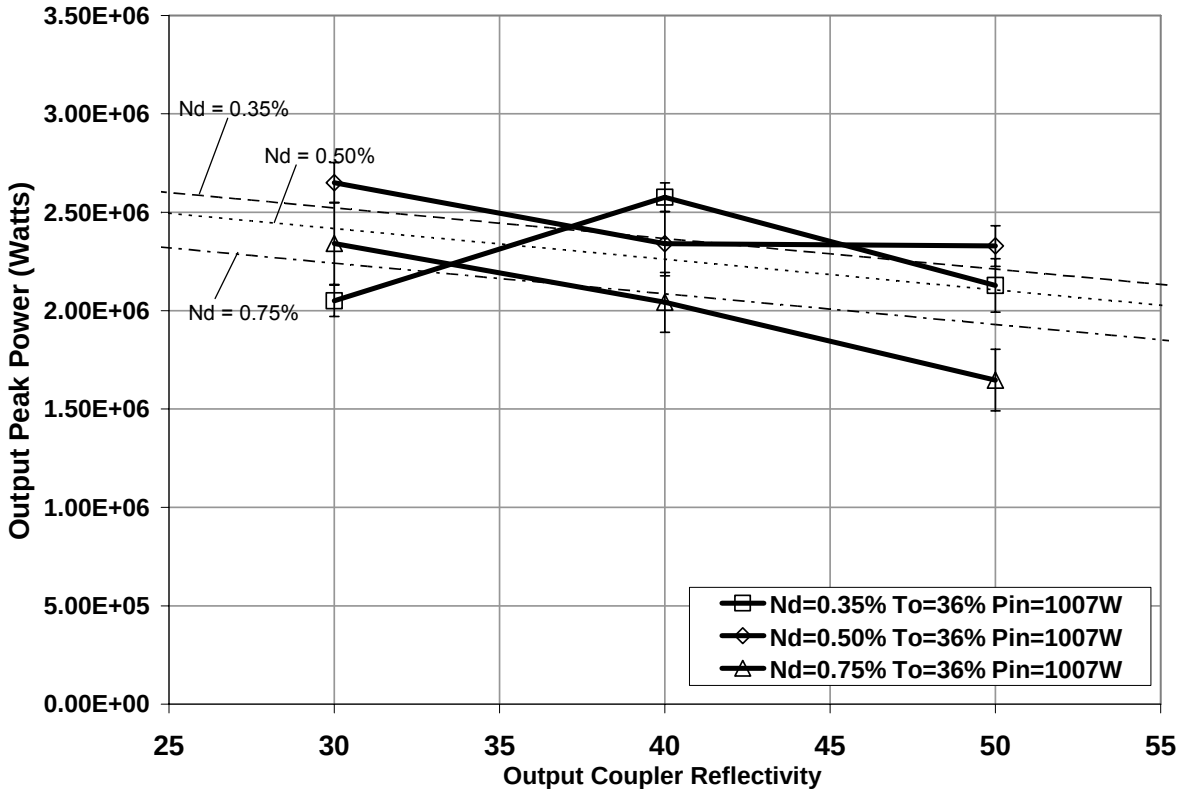

Figure 5.32: Output peak power as a function of output coupler reflectivity for three Nd concentration levles for a fixed Q-switch initial transmission and input pump power

Table 5.36: Regression analysis of data plotted in Figure 5.32

Regression Statistics	
Multiple R	0.568
R Square	0.322
Adj. R Square	0.266
Standard Error	264700.000
Observations	27

ANOVA

	df	SS	MS	F	Significance F
Regression	2	7.997E+11	3.999E+11	5.707	9.385E-03
Residual	24	1.682E+12	7.007E+10		
Total	26	2.481E+12			

	Coefficients	Standard Error	t Stat	P-value	Lower 95%	Upper 95%
Intercept	3236000.000	303300.000	10.670	1.370E-10	2610000.000	3862000.000
Nd % Conc.	-703000.000	308800.000	-2.280	3.204E-02	-1340000.000	-65600.000
OC % Reflect.	-15600.000	6239.000	-2.500	1.981E-02	-28500.000	-2700.000

Figure 5.32 and the associated regression data in Table 5.36 indicate signficant dependencies of the output peak power on both the output coupler reflectivity and the Nd

concentration. The dependence of the output peak power on the output coupler reflectivity is primarily due to the combination of the indirect relationship between the output pulse energy and the output coupler reflectivity and the relatively constant output pulse width. The decrease in the output coupler reflectivity acts to prolong the lasing process allowing for a greater energy storage and release. This is also the case with the reduction of the Nd concentration. As the concentration is reduced the lasing process is prolonged allowing for greater energy storage and release.

Figure 5.33 shows that none of the data groupings can be distinguished when a 95% confidence level is applied to the data. Table 5.37 shows the results of the regression analysis of the data plotted in Figure 5.33. The results indicate that the linear model was a poor fit to the data overall. Considering the outcome of the F test, the null hypothesis would fail to be rejected in this scenario verifying that neither of the variables provides a significant contribution to the model. The slope of the trend lines, as well as the regression data, indicates no significant contribution of the input pump power on the output peak power. The spacing of the trend lines, as well as the regression data, indicates that the output peak power is not dependent on the Nd concentration. The data point at the lowest input power level for the 0.35% Nd concentration test did not produce output and therefore was not plotted.

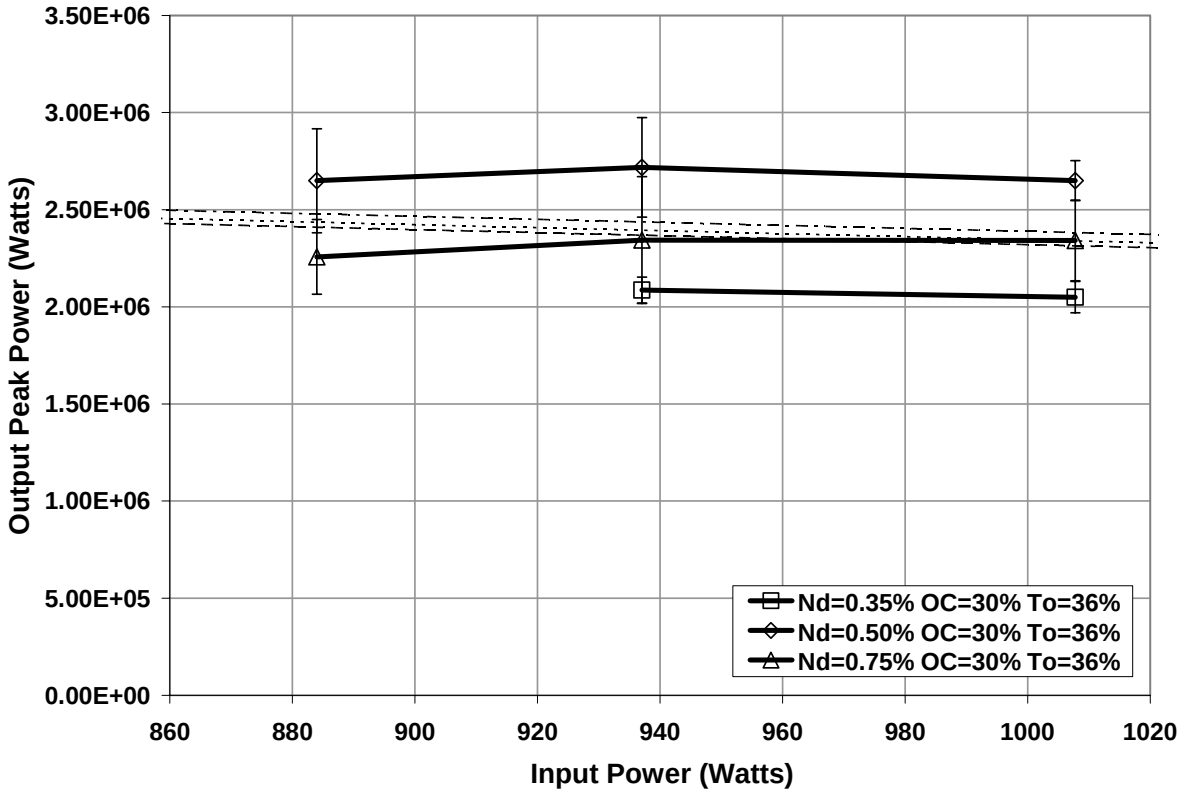

Figure 5.33: Output peak power versus pump power for all Nd concentration values with fixed output coupler and Q-switch values

Table 5.37: Regression analysis of data plotted in Figure 5.33

Regression Statistics	
Multiple R	0.177
R Square	0.031
Adj. R Square	-0.060
Standard Error	302400.000
Observations	24

ANOVA

	df	SS	MS	F	Significance F
Regression	2	6.195E+10	3.098E+10	0.339	7.165E-01
Residual	24	1.921E+12	9.147E+10		
Total	26	1.983E+12			

	Coefficients	Standard Error	t Stat	P-value	Lower 95%	Upper 95%
Intercept	3035000.000	1289000.000	2.355	2.834E-02	354600.000	5715000.000
Nd % Conc.	171100.000	391000.000	0.438	6.662E-01	-642000.000	984100.000
Pin Optical	-775.000	1292.000	-0.600	5.553E-01	-3460.000	1913.000

The data in Figure 5.33 shows no dependence of the output peak power on the input pump power or the Nd concentration. The input power was not expected to have any affect

on the output peak power due to the fact that the input power had no affect on the output pulse energy or the output pulse width. It is not clear why the Nd concentration shows no effect in Figure 5.33 when a significant affect was found in Figure 5.32. This difference is probably due to the wide variation seen in the Figure 5.33 data.

Figure 5.34 shows that all but one of the data groupings can be distinguished when a 95% confidence level is applied to the data. Table 5.38 shows the results of the regression analysis of the data plotted in Figure 5.34. The results indicate that the linear model was a good fit to the data overall. Considering the outcome of the F test, the null hypothesis would be rejected in this scenario verifying that at least one of the variables provides a significant contribution to the model. The slope of the trend lines, as well as the regression data, indicates no significant contribution of the input pump power on the output peak power. The spacing of the trend lines, as well as the regression data, indicates that the output peak power is significantly dependent on the Q-switch initial transmission.

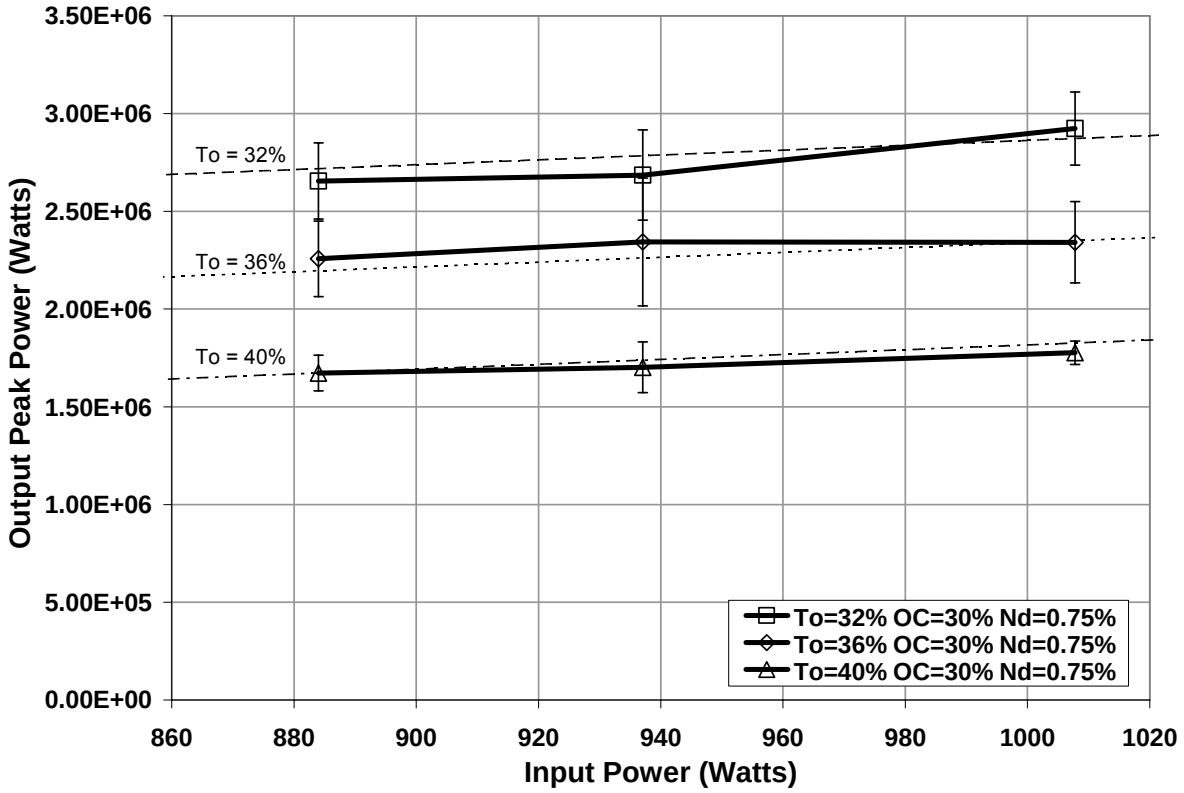

Figure 5.34: Output peak power versus pump power for three different Q-switch initial transmissions for a fixed output coupler reflectivity and Nd concentration

Table 5.38: Regression analysis of data plotted in Figure 5.34

Regression Statistics	
Multiple R	0.942
R Square	0.888
Adj. R Square	0.879
Standard Error	162400.000
Observations	27

ANOVA

	df	SS	MS	F	Significance F
Regression	2	5.030E+12	2.515E+12	95.330	3.814E-12
Residual	24	6.332E+11	2.638E+10		
Total	26	5.663E+12			

	Coefficients	Standard Error	t Stat	P-value	Lower 95%	Upper 95%
Intercept	5805000.000	679600.000	8.542	9.697E-09	4403000.000	7208000.000
Nd % Conc.	-131000.000	9571.000	-13.700	8.147E-13	-151000.000	-111000.000
Pin Optical	1242.000	620.500	2.001	5.680E-02	-38.900	2523.000

The data plotted in Figure 5.34 along with the regression data from Table 5.38 indicates a very strong relationship between the Q-switch initial transmission and the output

peak power. This is most likely due to the additional energy that is able to be stored and released with lower Q-switch initial transmission values. The data indicated that the output peak power has no dependence on the input pump power which was expected and has been seen throughout this analysis.

Figure 5.35 shows that few of the data groupings can be distinguished when a 95% confidence level is applied to the data. Table 5.39 shows the results of the regression analysis of the data plotted in Figure 5.35. The results indicate that the linear model was a poor fit to the data overall. Considering the outcome of the F test, the null hypothesis would be rejected in this scenario verifying that at least one of the variables provides a significant contribution to the model. The slope of the trend lines, as well as the regression data, indicates no significant contribution of the input pump power on the output peak power. The spacing of the trend lines, as well as the regression data, indicates that the output peak power is significantly dependent on the output coupler reflectivity.

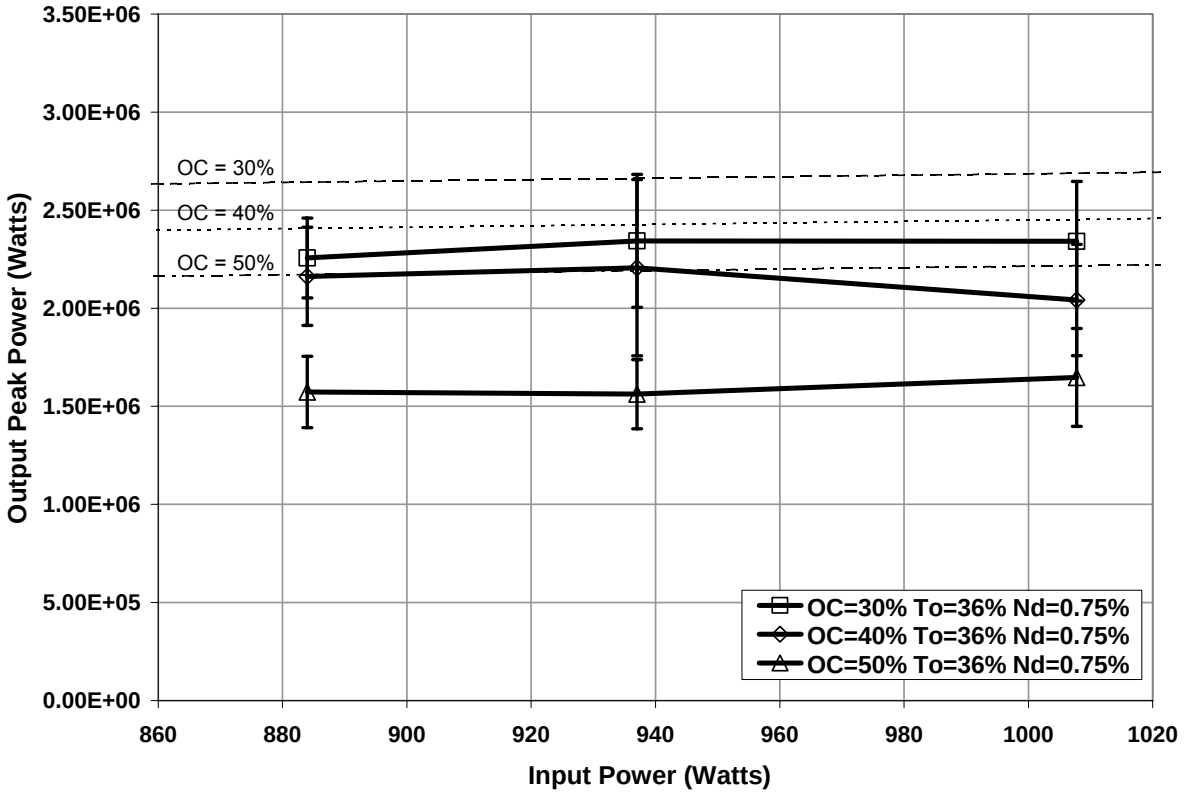

Figure 5.35: Output peak power versus pump power for three different output coupler reflectivities for fixed Q-switch initial transmission and Nd concentration

Table 5.39: Regression analysis of data plotted in Figure 5.35

Regression Statistics	
Multiple R	0.726
R Square	0.526
Adj. R Square	0.487
Standard Error	194300.000
Observations	27

ANOVA

	df	SS	MS	F	Significance F
Regression	2	1.007E+12	5.034E+11	13.340	1.274E-04
Residual	24	9.058E+11	3.774E+10		
Total	26	1.913E+12			

	Coefficients	Standard Error	t Stat	P-value	Lower 95%	Upper 95%
Intercept	3025000.000	724200.000	4.177	3.366E-04	1530000.000	4520000.000
OC % Reflect.	-23500.000	4579.000	-5.140	2.909E-05	-33000.000	-14100.000
Pin Optical	366.800	742.200	0.494	6.257E-01	-1170.000	1899.000

The data plotted in Figure 5.35 along with the regression data from Table 5.39 indicates a very strong relationship between the output coupler reflectivity and the output

peak power. This is most likely due to the additional energy that is able to be stored and released with lower output coupler reflectivity values. The data indicated that the output peak power has no dependence on the input pump power which was expected.

Table 5.40 shows the results of the regression analysis encompassing all of the data with respect to the output peak power. The regression data shows a poor linear fit however the F test indicates a probability for the rejection of the null hypothesis. This indicates that at least one of the independent variables provides a significant contribution to the model. The data also indicates that the input pump power is the only independent variable that does not contribute significantly to the model when considering all of the variables.

Table 5.40: Regression analysis of the output peak power data

Regression Statistics	
Multiple R	0.797
R Square	0.635
Adj. R Square	0.629
Standard Error	259700.000
Observations	228

ANOVA

	df	SS	MS	F	Significance F
Regression	2	2.621E+13	6.553E+12	97.120	1.026E-47
Residual	24	1.505E+13	6.747E+10		
Total	26	4.126E+13			

	Coefficients	Standard Error	t Stat	P-value	Lower 95%	Upper 95%
Intercept	6211000.000	412800.000	15.050	8.802E-36	5398000.000	7025000.000
Nd % Conc.	-656000.000	104000.000	-6.300	1.530E-09	-861000.000	-451000.000
OC % Reflect.	-20100.000	2169.000	-9.300	1.662E-17	-24400.000	-15800.000
QSW % To	-91800.000	5348.000	-17.200	1.153E-42	-102000.000	-81300.000
Pin Optical	555.600	341.400	1.627	1.051E-01	-117.000	1228.000

5.1.6 Focal Intensity

Figures 5.36-5.38 show the dependence of the output focal intensity produced by a 10 mm focal length lens as a function of Q-switch initial transmission and output coupler reflectivity each with respect to Nd concentration. Figure 5.36 shows that all of the data groupings can be distinguished when a 95% confidence level is applied to the data. Table

5.41 shows the results of the regression analysis of the data plotted in Figure 5.36. The results indicate that the linear model was a poor fit to the data overall. Considering the outcome of the F test, the null hypothesis would be accepted in this scenario verifying that neither of the variables provides a significant contribution to the model. The slope of the trend lines, as well as the regression data, indicates no significant contribution of the output coupler reflectivity on the focal intensity. The spacing of the trend lines, as well as the regression data, indicates that the focal intensity is not dependent on the Q-switch initial transmission.

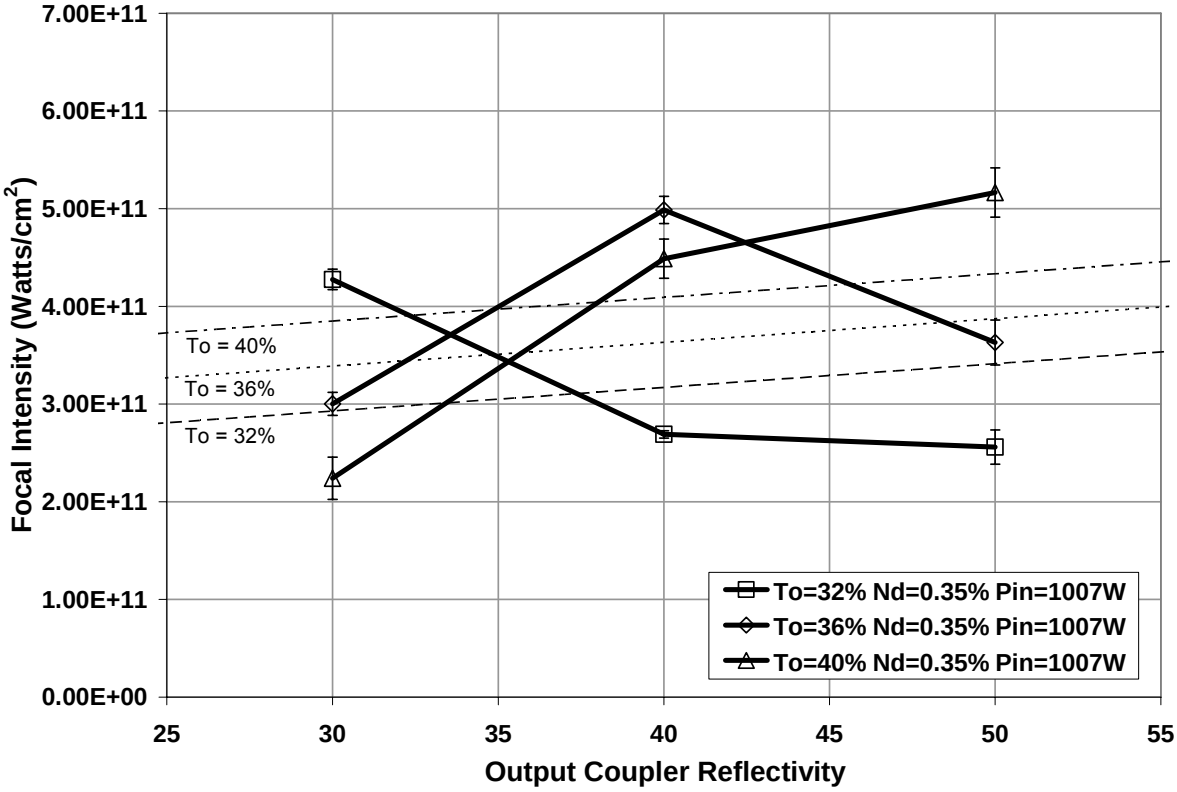

Figure 5.36: Output focal intensity response as a function of output coupler reflectivity and Q-switch initial transmission with Nd concentration of 0.35% at an input power of 1007 Watts

Table 5.41: Regression analysis of data plotted in Figure 5.36

Regression Statistics	
Multiple R	0.388
R Square	0.150
Adj. R Square	0.079
Standard Error	1.072E+11
Observations	27

ANOVA

	df	SS	MS	F	Significance F
Regression	2	4.872E+22	2.436E+22	2.121	1.419E-01
Residual	24	2.757E+23	1.149E+22		
Total	26	3.245E+23			

	Coefficients	Standard Error	t Stat	P-value	Lower 95%	Upper 95%
Intercept	-1.480E+11	2.497E+11	-0.590	5.584E-01	-6.630E+11	3.671E+11
OC % Reflect.	2.419E+09	2.526E+09	0.958	3.478E-01	-2.790E+09	7.633E+09
QSW % To	1.152E+10	6.316E+09	1.823	8.075E-02	-1.520E+09	2.455E+10

The focal intensity is a very important figure of merit of a high peak power laser system when designing for gaseous spark breakdown. The focal intensity is a product of the peak power and the beam quality and is defined as the peak power divided by the cross sectional area produced by a lens of a given focal length and a laser beam of a given beam quality or M^2. Figures 5.36-5.38 do not seem to follow any logical trends. Figure 5.37 does indicate a significant contribution of the output coupler reflectivity to the focal intensity. However when considering the two other data sets plotted in Figures 5.36 and 5.38 the significance of the output coupler reflectivity seems questionable. The variation in the focal intensity data is directly proportional to the variation in the beam quality data.

Figure 5.37 shows that all except two of the data groupings can be distinguished when a 95% confidence level is applied to the data. Table 5.42 shows the results of the regression analysis of the data plotted in Figure 5.37. The results indicate that the linear model was a mediocre fit to the data overall. Considering the outcome of the F test, the null hypothesis would be rejected in this scenario verifying that at least one of the variables provides a significant contribution to the model. The slope of the trend lines, as well as the

regression data, indicates a significant contribution of the output coupler reflectivity on the focal intensity. The spacing of the trend lines, as well as the regression data, indicates that the focal intensity is not dependent on the Q-switch initial transmission.

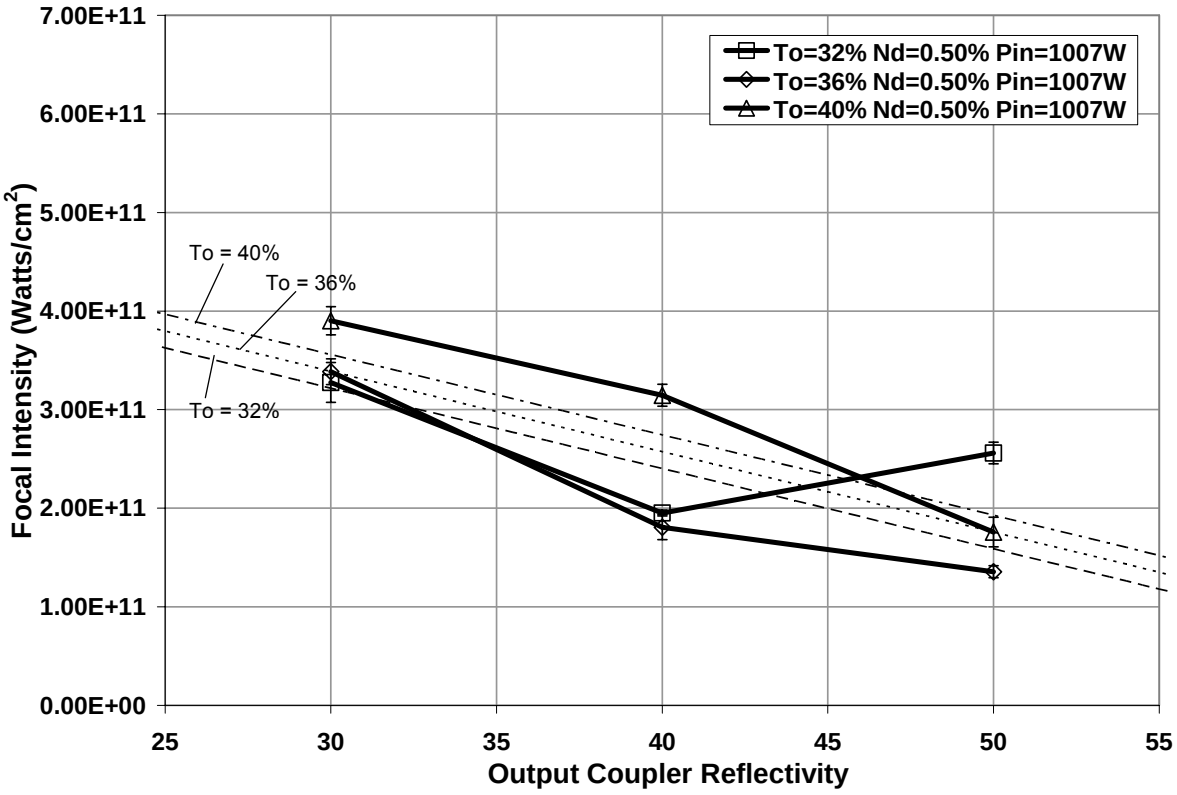

Figure 5.37: Output focal intensity response as a function of output coupler reflectivity and Q-switch initial transmission with Nd concentration of 0.50% at an input power of 1007 Watts

Table 5.42: Regression analysis of data plotted in Figure 5.37

Regression Statistics	
Multiple R	0.804
R Square	0.646
Adj. R Square	0.617
Standard Error	5.333E+10
Observations	27

ANOVA

	df	SS	MS	F	Significance F
Regression	2	1.248E+23	6.239E+22	21.940	3.818E-06
Residual	24	6.825E+22	2.844E+21		
Total	26	1.930E+23			

	Coefficients	Standard Error	t Stat	P-value	Lower 95%	Upper 95%
Intercept	4.300E+11	1.242E+11	3.462	2.024E-03	1.737E+11	6.864E+11
OC % Reflect.	-8.150E+09	1.257E+09	-6.480	1.050E-06	-1.070E+10	-5.560E+09
QSW % To	4.260E+09	3.142E+09	1.356	1.878E-01	-2.230E+09	1.075E+10

Figure 5.38 shows that three of the data groupings can be distinguished when a 95% confidence level is applied to the data. Table 5.43 shows the results of the regression analysis of the data plotted in Figure 5.38. The results indicate that the linear model was a poor fit to the data overall. Considering the outcome of the F test, the null hypothesis would fail to be rejected in this scenario verifying that neither of the variables provides a significant contribution to the model. The slope of the trend lines, as well as the regression data, indicates no significant contribution of the output coupler reflectivity on the focal intensity. The spacing of the trend lines, as well as the regression data, indicates that the focal intensity is not dependent on the Q-switch initial transmission.

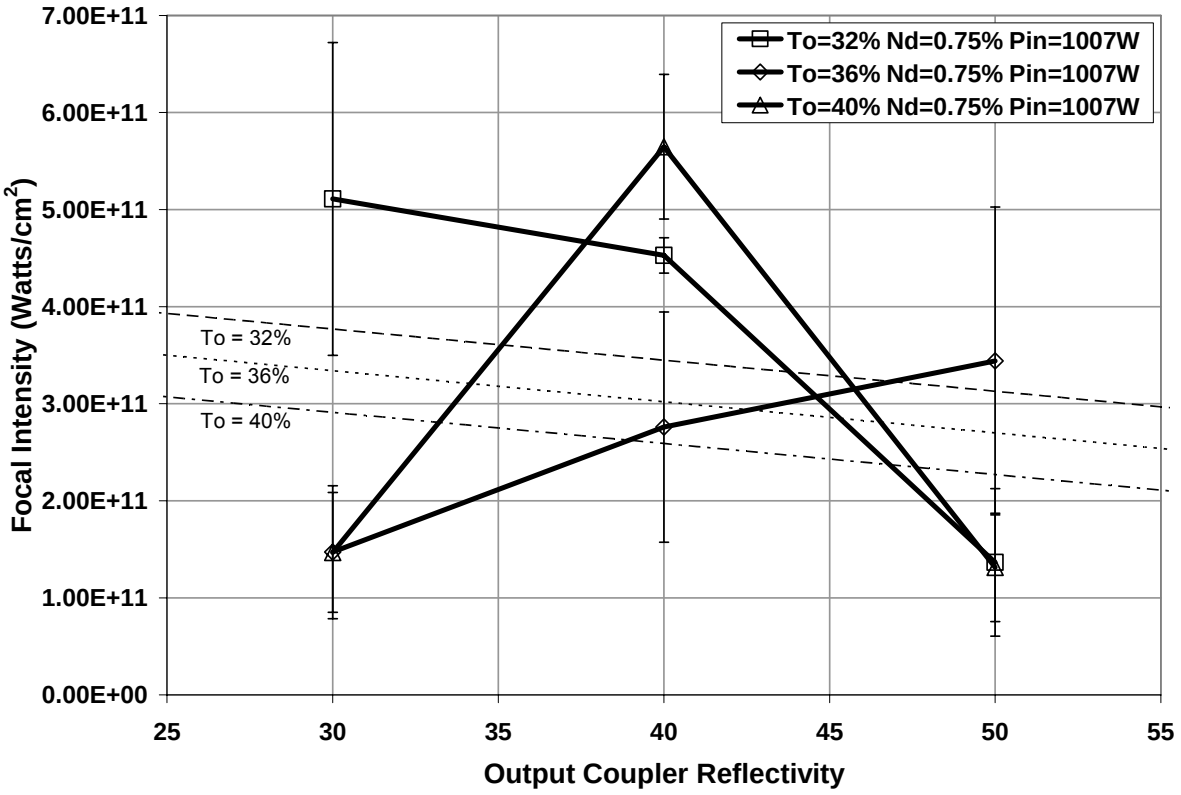

Figure 5.38: Output focal intensity response as a function of output coupler reflectivity and Q-switch initial transmission with Nd concentration of 0.75% at an input power of 1007 Watts

Table 5.43: Regression analysis of data plotted in Figure 5.38

Regression Statistics	
Multiple R	0.264
R Square	0.070
Adj. R Square	-0.010
Standard Error	1.693E+11
Observations	27

ANOVA

	df	SS	MS	F	Significance F
Regression	2	5.166E+22	2.583E+22	0.901	4.194E-01
Residual	24	6.879E+23	2.866E+22		
Total	26	7.396E+23			

	Coefficients	Standard Error	t Stat	P-value	Lower 95%	Upper 95%
Intercept	8.166E+11	3.944E+11	2.071	4.933E-02	2.610E+09	1.630E+12
OC % Reflect.	-3.200E+09	3.991E+09	-0.800	4.299E-01	-1.140E+10	5.032E+09
QSW % To	-1.070E+10	9.976E+09	-1.080	2.927E-01	-3.130E+10	9.856E+09

Figure 5.39 shows that all except one of the data groupings can be distinguished when a 95% confidence level is applied to the data. Table 5.44 shows the results of the regression

analysis of the data plotted in Figure 5.39. The results indicate that the linear model was a poor fit to the data overall. Considering the outcome of the F test, the null hypothesis would fail to be rejected in this scenario verifying that neither of the variables provides a significant contribution to the model. The slope of the trend lines, as well as the regression data, indicates no significant contribution of the output coupler reflectivity on the focal intensity. However, the spacing of the trend lines, as well as the regression data, indicates that the focal intensity may be dependent on the Nd concentration.

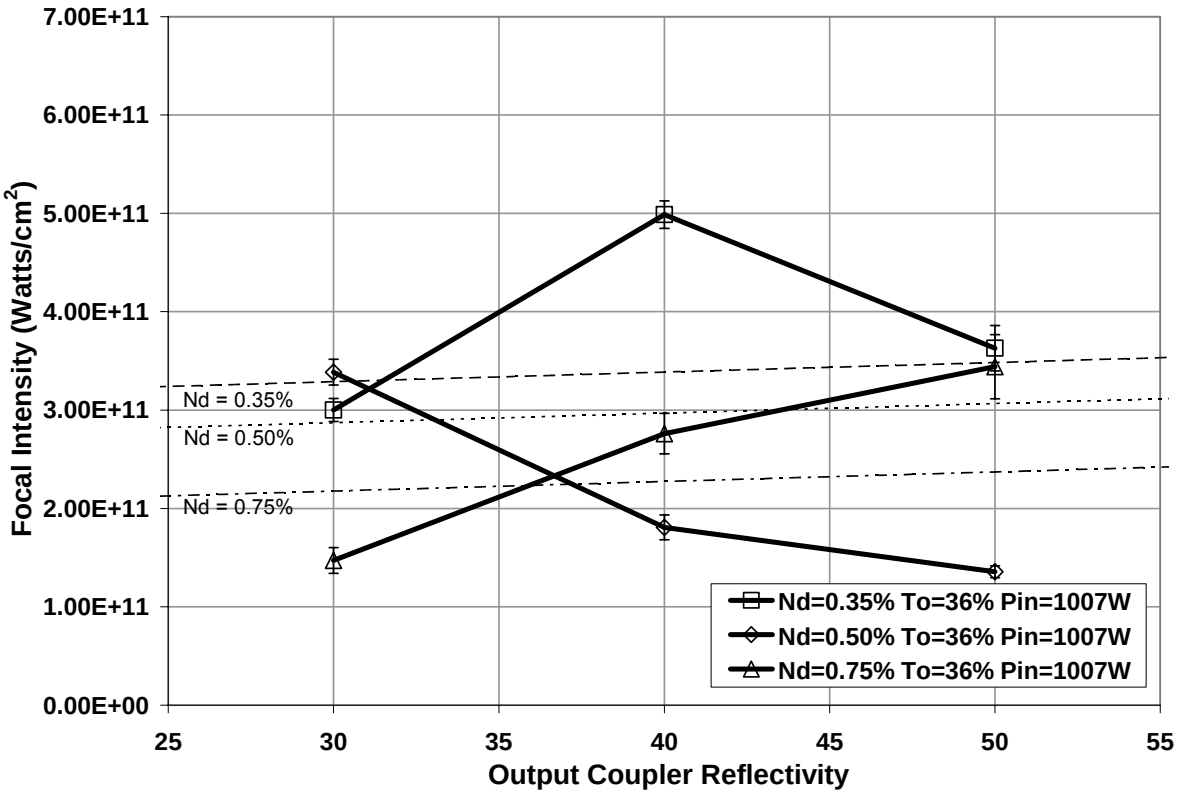

Figure 5.39: Focal Intensity as a function of output coupler reflectivity and Nd concentration for a fixed Q-switch initial transmission of 36% and input pump power of 1007W

Table 5.44: Regression analysis of data plotted in Figure 5.39

Regression Statistics	
Multiple R	0.417
R Square	0.174
Adj. R Square	0.105
Standard Error	1.077E+11
Observations	27

ANOVA

	df	SS	MS	F	Significance F
Regression	2	5.854E+22	2.927E+22	2.525	1.011E-01
Residual	24	2.782E+23	1.159E+22		
Total	26	3.368E+23			

	Coefficients	Standard Error	t Stat	P-value	Lower 95%	Upper 95%
Intercept	3.970E+11	1.234E+11	3.218	3.678E-03	1.424E+11	6.516E+11
Nd % Conc.	-2.780E+11	1.256E+11	-2.210	3.656E-02	-5.370E+11	-1.890E+10
OC % Reflect.	9.742E+08	2.538E+09	0.384	7.044E-01	-4.260E+09	6.212E+09

Figure 5.40 shows the focal intensity as a function of the pump power for three different Nd concentrations for a fixed output coupler reflectivity and Q-switch initial transmission. Figure 5.40 shows that all except one of the data groupings can be distinguished when a 95% confidence level is applied to the data. Table 5.45 shows the results of the regression analysis of the data plotted in Figure 5.40. The results indicate that the linear model was a mediocre fit to the data overall. Considering the outcome of the F test, the null hypothesis would be rejected in this scenario verifying that at least one of the variables provides a significant contribution to the model. The slope of the trend lines, as well as the regression data, indicates no significant contribution of the input pump power on the focal intensity. The spacing of the trend lines, as well as the regression data, indicates that the focal intensity is significantly dependent on the Nd concentration. The data point at the lowest input power level for the 0.35% Nd concentration test did not produce output and therefore was not plotted.

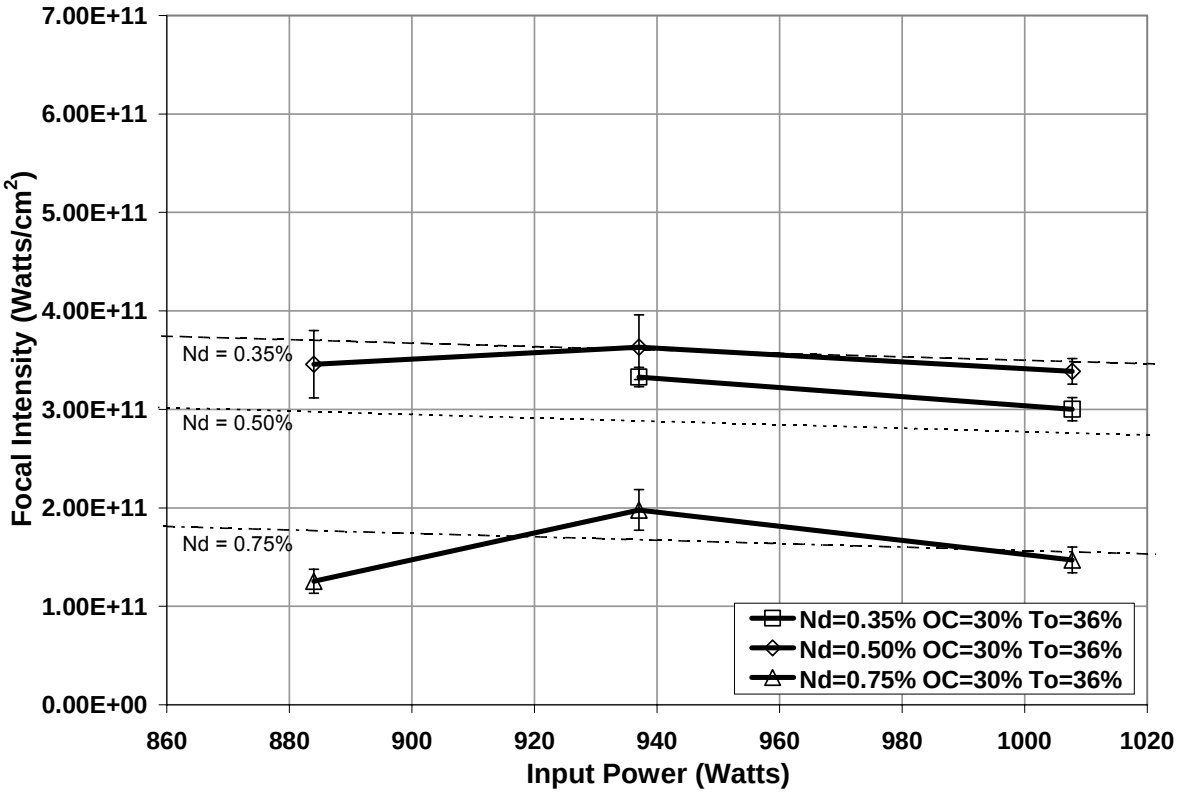

Figure 5.40: Focal intensity versus pump power for four different Nd concentrations with fixed output coupler reflectivity and Q-switch initial transmission

Table 5.45: Regression analysis of data plotted in Figure 5.40

Regression Statistics	
Multiple R	0.849
R Square	0.721
Adj. R Square	0.695
Standard Error	5.088E+10
Observations	24

ANOVA

	df	SS	MS	F	Significance F
Regression	2	1.406E+23	7.030E+22	27.150	1.501E-06
Residual	24	5.437E+22	2.589E+21		
Total	26	1.950E+23			

	Coefficients	Standard Error	t Stat	P-value	Lower 95%	Upper 95%
Intercept	6.930E+11	2.168E+11	3.196	4.343E-03	2.421E+11	1.144E+12
Nd % Conc.	-4.830E+11	6.578E+10	-7.340	3.165E-07	-6.200E+11	-3.460E+11
Pin Optical	-1.740E+08	2.174E+08	-0.800	4.321E-01	-6.260E+08	2.780E+08

The data from Figure 5.40 and the analysis shown in Table 5.45 indicates a significant contribution by the Nd concentration to the output focal intensity. It is not clear

why the focal intentisy is showing a dependence on the Nd concentration. The focal intensity is a function of the output energy, pulse width, and beam quality all of which have varying degrees of dependence on the Nd concentration. There is a great deal of variance with the output pulse width and beam quality measurements that could explain the fact that the 0.5% concentration data produces the highest focal intensity. The focal intensity does not respond as a function of the input power.

Figure 5.41 shows the focal intensity as a function of the pump power for three different Q-switch values with fixed output coupler reflectivity and Nd concentration. Figure 5.41 shows that all but two of the data groupings can be distinguished when a 95% confidence level is applied to the data. Table 5.46 shows the results of the regression analysis of the data plotted in Figure 5.41. The results indicate that the linear model was a good fit to the data overall. Considering the outcome of the F test, the null hypothesis would be rejected in this scenario verifying that at least one of the variables provides a significant contribution to the model. The slope of the trend lines, as well as the regression data, indicates no significant contribution of the input pump power on the focal intensity. The spacing of the trend lines, as well as the regression data, indicates that the focal intensity is significantly dependent on the Q-switch initial transmission.

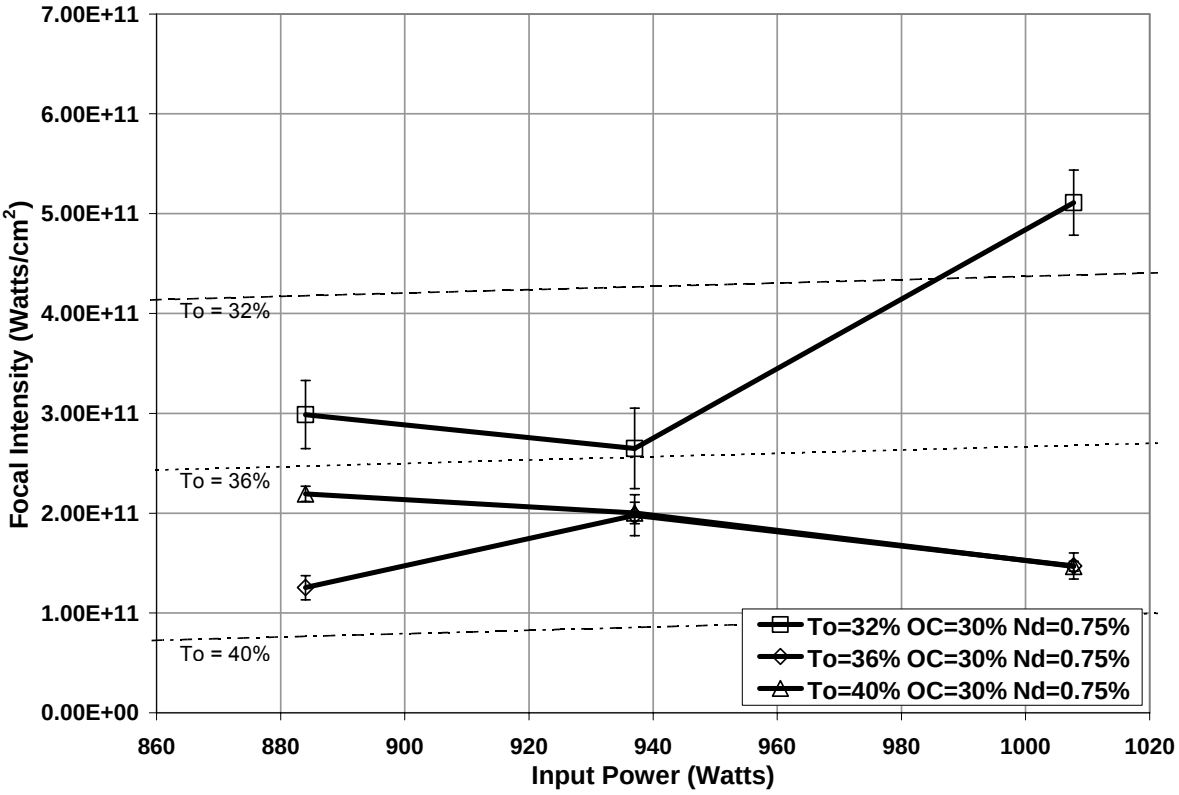

Figure 5.41: Focal intensity versus pump power for three different Q-switch values with fixed output coupler reflectivity and Nd concentration

Table 5.46: Regression analysis of data plotted in Figure 5.41

Regression Statistics	
Multiple R	0.865
R Square	0.749
Adj. R Square	0.728
Standard Error	8.566E+10
Observations	27

ANOVA

	df	SS	MS	F	Significance F
Regression	2	5.258E+23	2.629E+23	35.820	6.228E-08
Residual	24	1.761E+23	7.338E+21		
Total	26	7.019E+23			

	Coefficients	Standard Error	t Stat	P-value	Lower 95%	Upper 95%
Intercept	1.635E+12	3.584E+11	4.560	1.270E-04	8.948E+11	2.374E+12
QSW % To	-4.260E+10	5.048E+09	-8.450	1.184E-08	-5.310E+10	-3.220E+10
Pin Optical	1.674E+08	3.273E+08	0.512	6.136E-01	-5.080E+08	8.429E+08

The regression data in Table 5.46 indicates a significant contribution to the focal intensity by the Q-switch initial transmission. This contribution is not clearly shown by the

data plotted in Figure 5.41. A dependence like the one shown by the regression data was expected because the lower Q-switch initial transmission values produced higher output pulse energies. The higher output pulse energy values in conjunction with relatively constant output pulse width values produced output peak power values that were dependent on the Q-switch initial transmission.

Figure 5.42 shows the focal intensity as a function of the pump power for three different output coupler reflectivities with fixed Q-switch initial transmission and Nd concentration. Figure 5.42 shows that none of the data groupings can be distinguished when a 95% confidence level is applied to the data. Table 5.47 shows the results of the regression analysis of the data plotted in Figure 5.42. The results indicate that the linear model was a good fit to the data overall. Considering the outcome of the F test, the null hypothesis would be rejected in this scenario verifying that at least one of the variables provides a significant contribution to the model. The slope of the trend lines, as well as the regression data, indicates no significant contribution of the input pump power on the focal intensity. The spacing of the trend lines, as well as the regression data, indicates that the focal intensity is significantly dependent on the output coupler reflectivity.

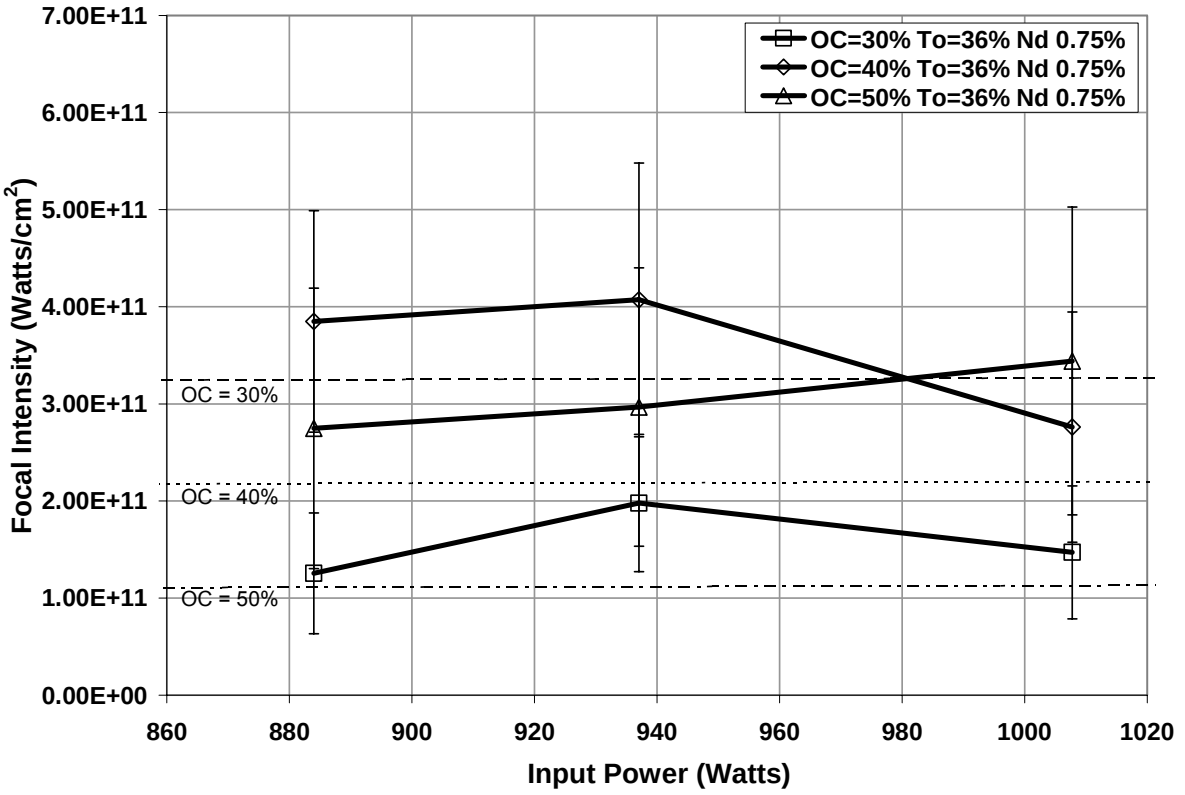

Figure 5.42: Focal intensity versus pump power for three different output coupler reflectivities with fixed Q-switch initial transmission and Nd concentration

Table 5.47: Regression analysis of data plotted in Figure 5.42

Regression Statistics	
Multiple R	0.950
R Square	0.903
Adj. R Square	0.895
Standard Error	3.031E+10
Observations	27

ANOVA

	df	SS	MS	F	Significance F
Regression	2	2.058E+23	1.029E+23	112.000	6.773E-13
Residual	24	2.205E+22	9.189E+20		
Total	26	2.278E+23			

	Coefficients	Standard Error	t Stat	P-value	Lower 95%	Upper 95%
Intercept	6.336E+11	1.130E+11	5.607	9.031E-06	4.003E+11	8.668E+11
OC % Reflect.	-1.070E+10	7.145E+08	-15.000	1.145E-13	-1.220E+10	-9.220E+09
Pin Optical	1.370E+07	1.158E+08	0.118	9.068E-01	-2.250E+08	2.527E+08

Considering the laser theory and past experimentation one would expect to find a linear increase in the focal intensity as the output coupler reflectivity is lowered. However

the beam quality was a significant factor contributing to a large degree of variation of the data plotted in Figure 5.42. Table 5.47 indicates a significant contribution by the output coupler reflectivity to the focal intensity values. However when examining the data plotted in Figure 5.42 there is a great deal of variation that makes any visual analysis difficult.

Table 5.48 shows the results of the regression analysis encompassing all of the data with respect to the focal intensity. The regression data shows a poor linear fit however the F test indicates a probability for the rejection of the null hypothesis. This indicates that at least one of the independent variables provides a significant contribution to the model. The data also indicates that the output coupler reflectivity is the only independent variable that contributes significantly to the model when considering all of the variables.

Table 5.48: Regression analysis of the focal intensity data

Regression Statistics	
Multiple R	0.228
R Square	0.052
Adj. R Square	0.035
Standard Error	1.302E+11
Observations	228

ANOVA

	df	SS	MS	F	Significance F
Regression	2	2.071E+23	5.178E+22	3.055	1.773E-02
Residual	24	3.780E+24	1.695E+22		
Total	26	3.987E+24			

	Coefficients	Standard Error	t Stat	P-value	Lower 95%	Upper 95%
Intercept	2.345E+11	2.069E+11	1.134	2.582E-01	-1.730E+11	6.423E+11
Nd % Conc.	-9.780E+10	5.215E+10	-1.880	6.196E-02	-2.010E+11	4.934E+09
OC % Reflect.	-2.710E+09	1.087E+09	-2.500	1.330E-02	-4.850E+09	-5.700E+08
QSW % To	3.259E+09	2.680E+09	1.216	2.254E-01	-2.020E+09	8.541E+09
Pin Optical	1.149E+08	1.711E+08	0.671	5.026E-01	-2.220E+08	4.521E+08

Table 5.49 provides a graphical summary of the significance, or not, of the independent variable on the dependent variables. As the output coupler reflectivity is decreased the output pulse energy increases, the Q-switch delay increases, and the output peak power increases. The output pulse width, beam quality, and focal intensity were not

significantly affected by the variation of output coupler reflectivity. As the Q-switch initial transmission is decreased the output pulse energy increases, the Q-switch delay increases, the output peak power increases as well as the output focal intensity. The output pulse width and beam quality were not significantly affected by the variation of the Q-switch initial transmission. As the Neodymium concentration is lowered the output pulse energy increases, the Q-switch delay increases, the beam quality improves and the output focal intensity increases. The output pulse width as well as the output peak power were not significantly affected by the variation of the Neodymium concentration. The optical input power only had a significant affect on the Q-switch delay all other variables were not significantly affected.

Table 5.49: Qualitative comparison of experimental laser data

		E_o	t_p	Q_d	Beam Quality	P_{peak}	I_o
OC	30%	↗	—	↘	—	↗	—
	40 %						
	50 %						
QSW - T_o	32 %	↗	—	↘	—	↗	↗
	36 %						
	40 %						
Nd	0.35%	↗	—	↘	↗	—	↗
	0.50%						
	0.75%						
P_{in}	884 W	—	—	↘	—	—	—
	937 W						
	1007 W						

5.2 Engine Testing Results

5.2.1 Characteristic Engine Data

The engine testing for each laser system was performed on nonconsecutive days. The test laser data was taken Febuary 28, 2007 and the commercial laser data was taken March 8, 2007. Table 5.50 lists the engine operational parameters collected during the engine testing.

Due to technical problems encountered on numerous occasions throughout testing not enough care was taken to ensure that certain engine operational parameters were kept constant and consistent from test to test. This was particularly the case during the commercial laser testing where the operators neglected to save crucial data files, hence NO DATA was listed where this occurred. This problem affected measured quantities, such as the complete natural gas composition, as well as calculated quantities, such as BMEP and thermal efficiency.

Table 5.50: Engine operational parameters

Parameter	Test Laser	Commercial Laser
Humidity (g/m^3)	3.85 – 3.97	2.53 – 2.67
Thermal Efficiency	24.15 – 27.56	NO DATA
Volumetric Efficiency	76.95 – 80.76	NO DATA
Engine Speed (rev/s)	9.96 – 10.06	9.55 – 10.20
Intake Temperature (˚C)	35.56-37.56	38.56-39.81
Intake Pressure	Naturally Aspirated	Naturally Aspirated
Oil Temperature (˚C)	59.49 +/- 2.56	45.76 +/- 5.24
Coolant Temperature (˚C)	80.58 +/- 2.29	63.20 +/- 5.86
BMEP (bar)	4.81 – 6.73	NO DATA
IMEP (bar)	6.16 – 8.24	6.21 – 8.47
COV IMEP (%)	1.14 – 2.84	1.18 – 2.87

The coefficient of variation (COV) of the IMEP is used as an indication of how smooth or rough the combustion is over a period of time. The lower the COV the less variation in the in-cylinder pressure data therefore, the smoother the combustion. Once the

COV of IMEP value exceeds 10% [10] the engine is considered to be misfiring. The COV of IMEP for both the test laser and the commercial laser are relatively low indicating smooth combustion. The IMEP COV values are approximately equal indicating a high degree of similarity in the combustion conditions that are produced by the two ignition systems. Table 5.51 lists the average domestic natural gas composition for each engine test; unfortunately the higher hydrocarbon concentrations for the commercial laser tests were lost due to the aforementioned problems. Table 5.52 lists the target and average measured equivalence ratio values for each engine test.

Table 5.51: Domestic natural gas composition

Constituent	Test Laser Conditions	Comm. Laser Conditions
Methane	92.12 %	90.24 %
Ethane	5.42 %	NO DATA
Propane	0.76 %	NO DATA
Butane	0.30 %	NO DATA
Pentane	0.11 %	NO DATA
N_2	0.91 %	0.93 %
CO_2	0.31 %	NO DATA

Table 5.52: Average measured equivalence ratio for each test condition

Test #	TL Φ Target	TL Φ Measured	CL Φ Target	CL Φ Estimated
1	0.8	0.806	1.0	1.008
2	0.9	0.910	0.8	0.790
3	0.9	0.912	0.9	0.915
4	0.8	0.798	0.9	0.904
5	1.0	1.028	1.0	1.023
6	0.9	0.913	0.8	0.804
7	1.0	1.008	1.0	1.022
8	0.8	0.802	0.9	0.884
9	1.0	1.036	0.8	0.807

5.2.2 In-Cylinder Data

In-cylinder pressure and heat release rate data were recorded so that the combustion characteristics produced by each ignition system could be analyzed and compared. Figures 5.43 through 5.47 show representative pressure traces and calculated heat release rates (HRR) as a function of crank angle degrees. Figure 5.43 shows the pressure curves and HRR waveforms produced by the test laser at three different equivalence ratios. An increase in Φ advances the HRR as well as the peak pressure. The extremely long ignition delay is primarily due to the shortening of the focal length of the focusing optics. Shrouding the ignition spark, as explained in Chapter 4, restricts the expansion of the flame front. Top dead center (TDC) is reached before the initial flame kernel has expanded sufficiently to induce ignition at or near TDC

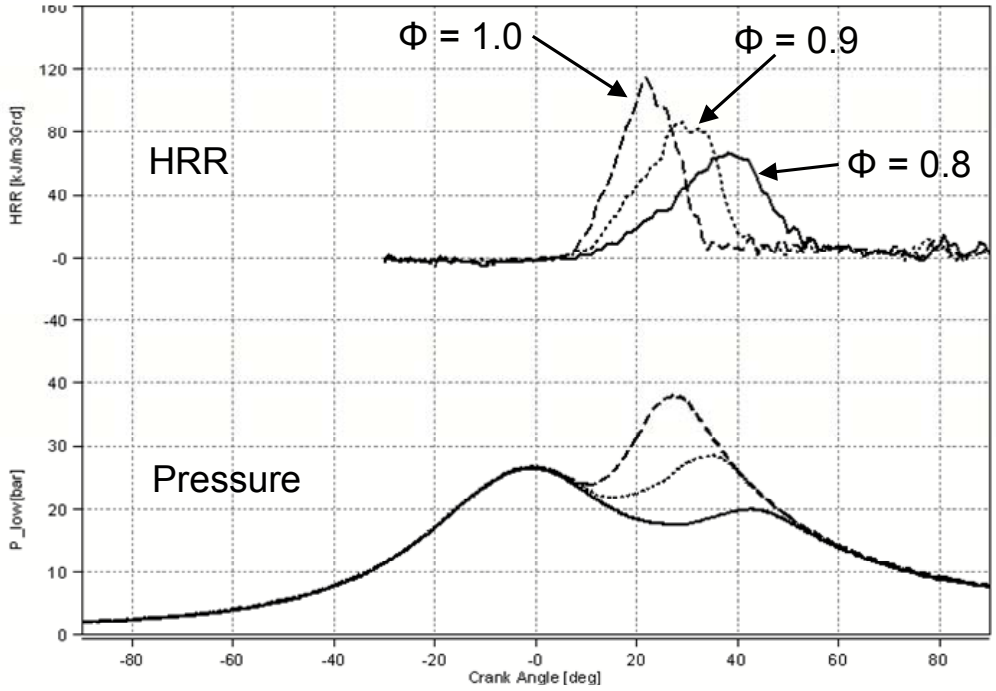

Figure 5.43: Test laser pressure and heat release rate waveforms for varying phi. Solid line Φ=0.8, Dotted line Φ=0.9, Dashed line Φ=1.0

Figure 5.44 shows the pressure curves and HRR waveforms produced by the commercial laser system at three different equivalence ratios. A comparison between Figures 5.43 and 5.44 show that the in-cylinder data produced by both the test laser and the commercial laser are virtially identical. This comparison is also shown in Figures 5.45 through 5.47 where the pressure curves and HRR traces for both lasers are compared for each equivalence ratio.

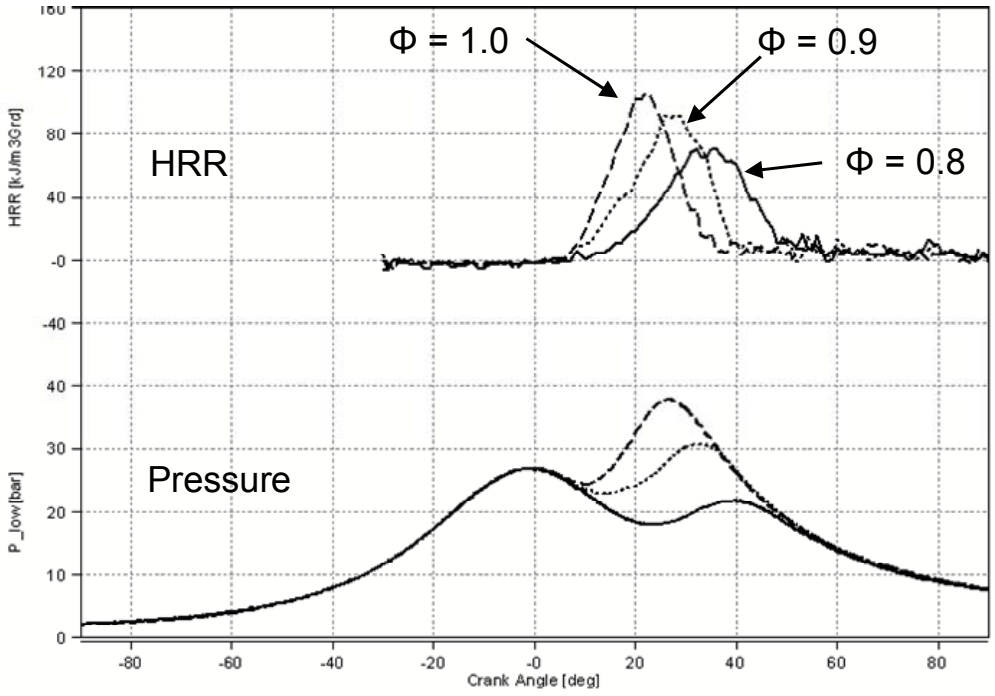

Figure 5.44: Commercial laser pressure and heat release rate waveforms for varying phi. Solid line Φ=0.8, Dotted line Φ=0.9, Dashed line Φ=1.0

Figures 5.45 through 5.47 compare the cylinder pressure and heat release rate data for each laser system at a fixed equivalence ratio. Figure 5.45 shows the data for for each laser system for an equivalence ratio of Φ=0.8. Figure 5.46 shows the data for for each laser system for an equivalence ratio of Φ=0.9. Figure 5.47 shows the data for for each laser system for an equivalence ratio of Φ=1.0. For each equivalence ratio it can be seen that the ignition delay, peak pressure and heat release waveforms are all virtually identical.

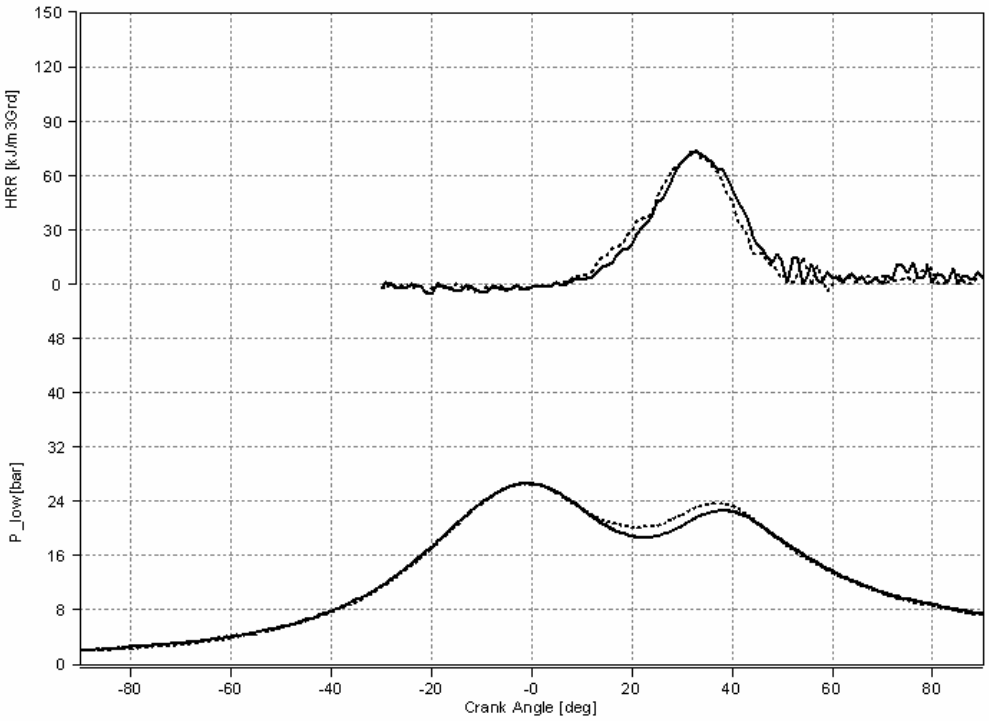

Figure 5.45: Comparison of pressure and heat release rate waveforms for Φ=0.8, solid Test Laser, dotted Commercial Laser

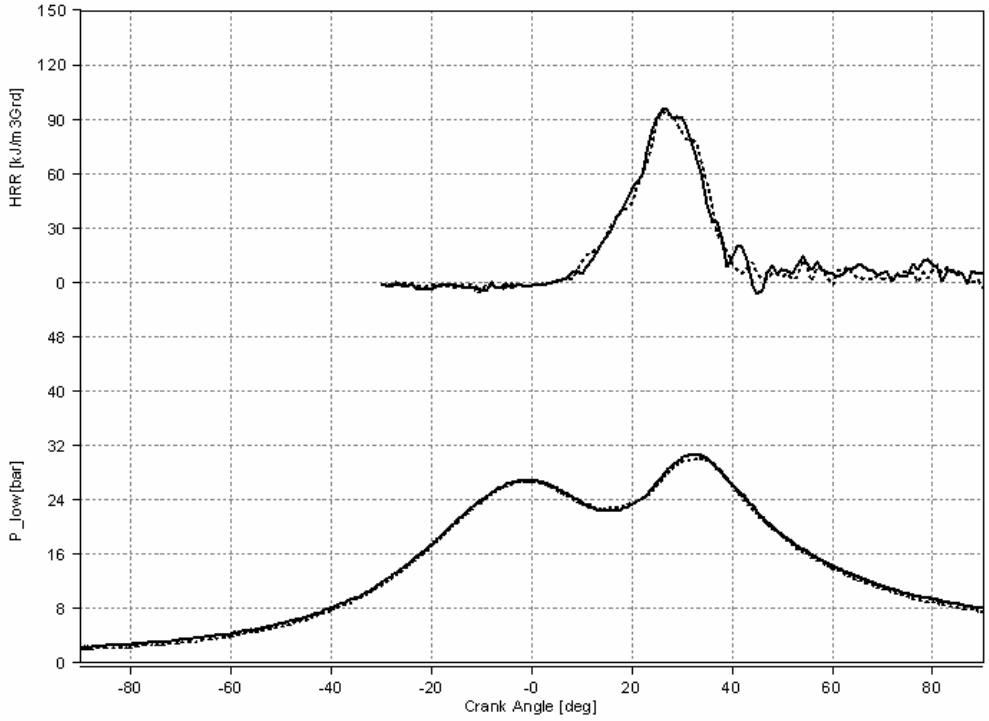

Figure 5.46: Comparison of pressure and heat release rate waveforms for Φ=0.9, solid Test Laser, dotted Commercial Laser

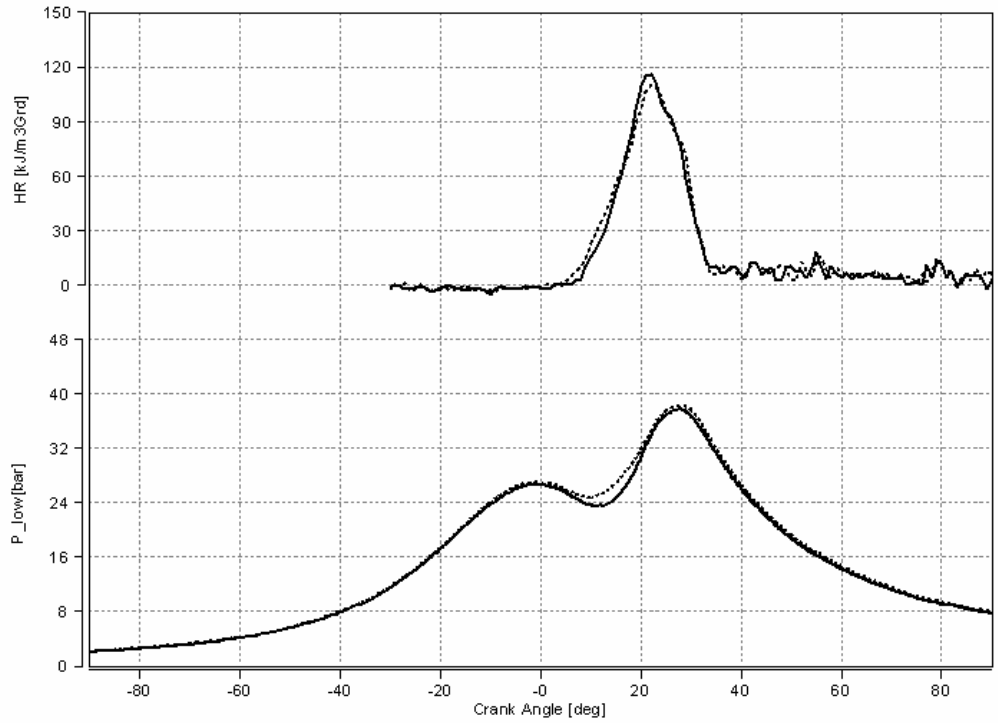

Figure 5.47: Comparison of pressure and heat release rate waveforms for Φ=1.0, solid Test Laser, dotted Commercial Laser

Figure 5.48 shows the ignition delay produced by each laser system for each equivalence ratio. The ignition delay data simply confirms the trends in the pressure and HRR data shown in Figures 5.43 and 5.44. The ignition delay decreases as the equivalence ratio is increased toward stoichiometry. The data for each laser system is statistically identical for the cases where Φ=0.8 and Φ=0.9. Overall there is little difference in the ignition delay produced by each laser system.

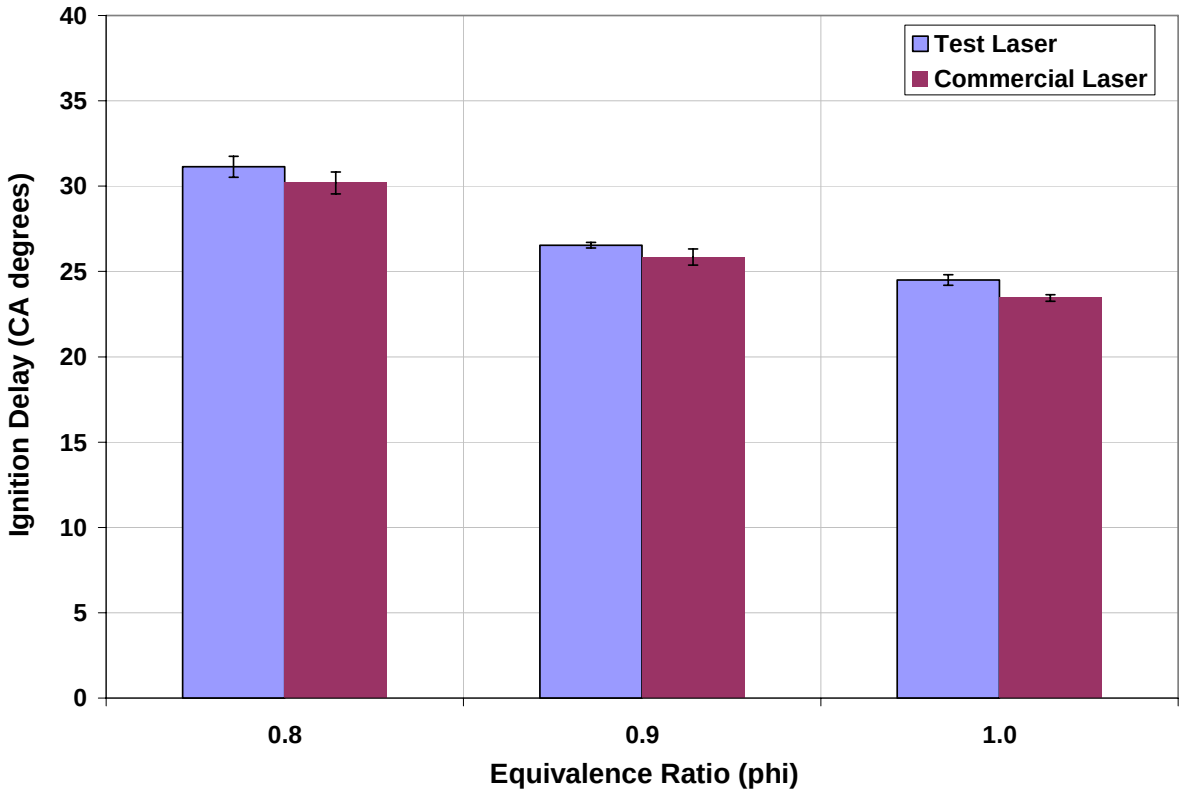

Figure 5.48: Ignition delay comparison between the test laser and the commercial laser for varying Phi

5.2.3 Engine Emissions Data

Engine emissions data was taken to determine what level of a difference, if any, in the exhaust emissions concentrations from the operation of each laser system. Figures 5.49 through 5.52 show the measured NO_x, CO, CO_2, and total hydrocarbon emissions, respectively, with respect to equivalence ratio. Figure 5.49 illustrates the NO_x emissions for both ignition systems at each equivalence ratio. The data shows a significant decrease in the NO_x emissions as the equivalence ratio is decreased. NO_x production is highly temperature depdendent and as the equivalence ratio is lowered the combustion temperature decreases. This reduction in combustion temperature significantly lowers the NO_x production. The change in load as well as the dilution of the charge are contributors to the differences in the

NO_x emissions. The NO_x emissions data was normalized to the equivalence ratio to account for the differences in the raw exhaust due to the variations in fueling to vary the equivalence ratio. All emission data, except the CO_2 data, is normalized to the equivalence ratio. The data error bars depict a single standard deviation. NO_x emissions from the test laser and the commercial laser results are statistically identical.

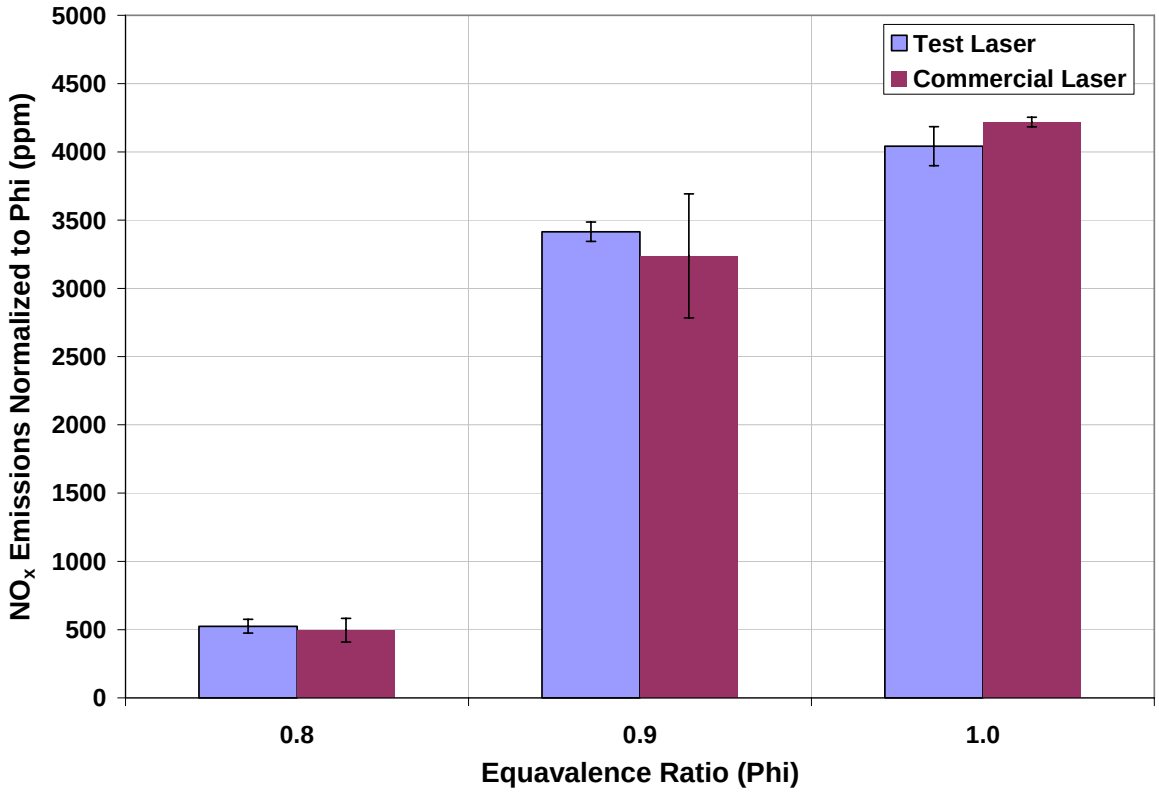

Figure 5.49: Comparison of NOx emissions normalized to Phi

Figure 5.50 illustrates the CO emissions for both ignition systems at each equivalence ratio. The data show a steady increase in the CO emission as the equivalence ratio is decreased. This increase in CO is primarily due to incomplete combustion most likely due to the large ignition delay produced by the shorter focal length. Also the flame front does not see the higher pressures that occur near TDC due to the ignition delay. This is indicated by the decrease in CO emissions as the equivalence ratio is increased to stoichiometric

conditions thereby advancing the timing and shortening the ignition delay as seen in the previous section. The change in load could also be a contributor to the difference in the CO emissions. Overall the test laser and commercial laser performed relatively the same except when Φ=0.8. At this operating point the commercial laser ignition system produced a consistently larger amount of CO.

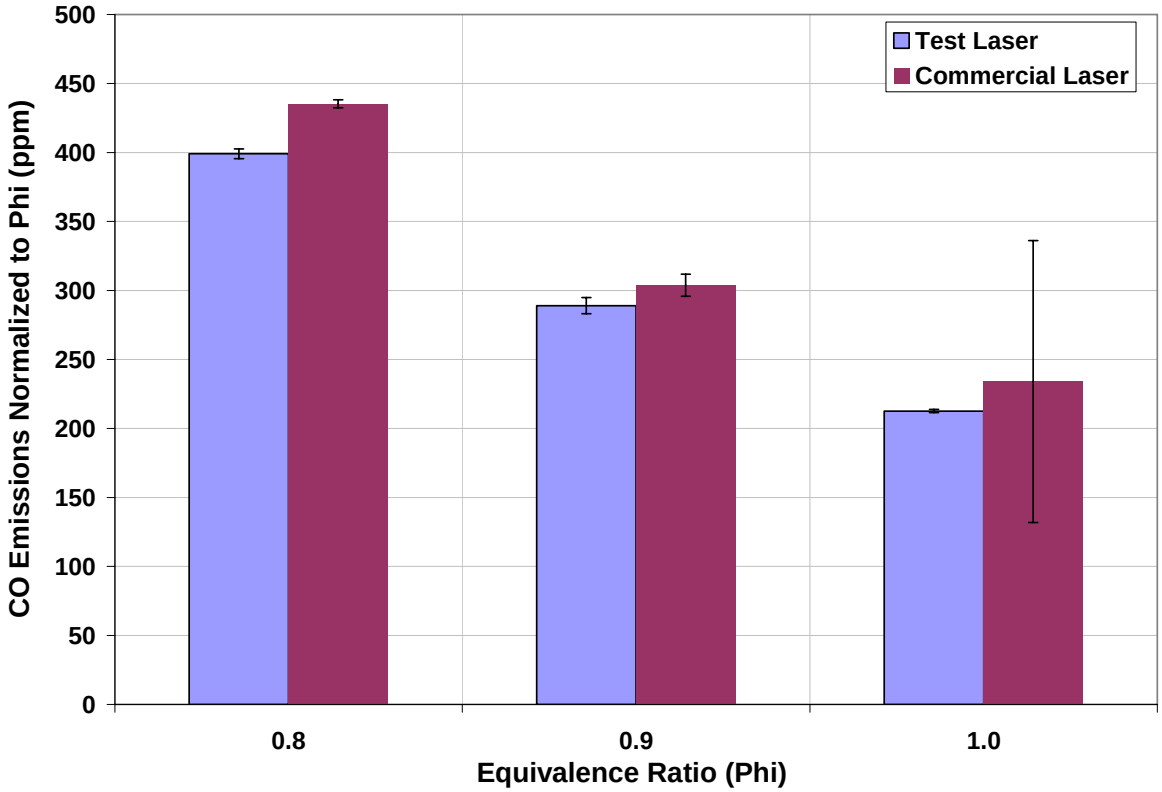

Figure 5.50: Comparison of CO emissions normalized to Phi

Figure 5.51 shows the CO_2 emissions for both ignition systems at each equivalence ratio. The data for a Φ=1.0 will be ignored because it was clipped by the analyzer due to the fact that the data exceeded the operating range of the instrument. It can, however, be assumed that the CO_2 emission exceed 10% when Φ=1.0. Assuming that the stoichiometric data is greater than or equal to 10% indicates a trend where the CO_2 concentration steadily increases as the equivalence ratio increases. This is an expected outcome because the CO_2 emissions

are being less diluted at the higher equivalence ratio values. The change in load could also be a contributor to the difference in the CO_2 emissions. These data in conjunction with the CO data indicates that the combustion is more complete with increasing equivalence ratio. The CO_2 emissions data is statistically identical at Φ=0.8 and Φ=0.9 between the two laser systems as evidenced by the overlap between their error bars.

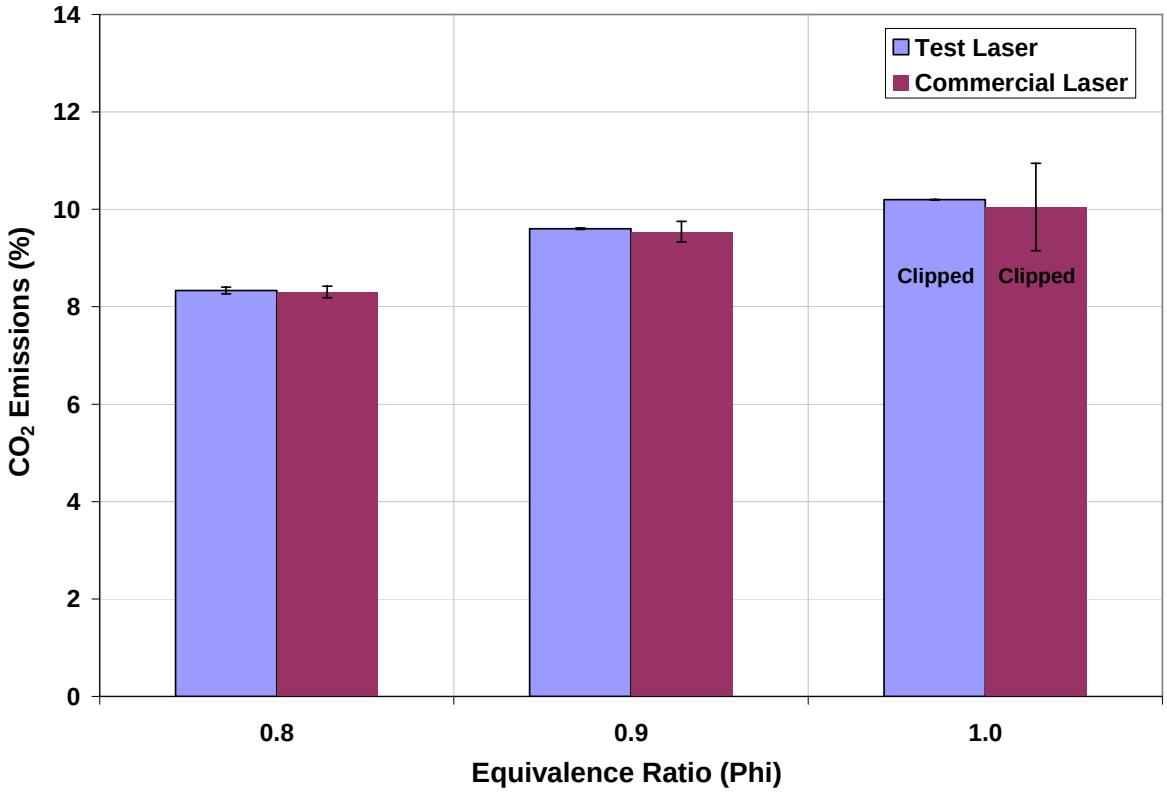

Figure 5.51: Comparison of CO_2 emissions with varying Phi

Figure 5.52 shows the total hydrocarbon (THC) emissions for both ignition systems at each equivalence ratio. There are no noticable trends in the THC data because overall the combustion was poor at all equivalence ratios. The poor combustion was primarily due to the shrouded spark and the ignition delay that it produced. The ignition delay meant that the bulk of the combustion happened on the down stroke of the piston and not at the top of the stroke where more rapid chemical heat release is expected and where the greatest amount of power

is developed by the power stroke. The ignition delay allowed for a significant amount of unburned fuel to be passed into the exhaust because of the poor and incomplete combustion that it fostered. The data indicates that the THC emissions are statistically identical between the two laser systems and relatively constant and similar with changing equivalence ratio. The consistency of the THC emission data could possibly be due to the fact that the combustion was poor and incomplete in each case. However the more incomplete combustion at the lower equivalence ratio values contributed more HC emissions which happed to be similar to the emissions produced by the higher equivalence ratio values with more complete combustion. This is evidenced in the heat release rate data discussed earlier in this chapter. The data acquired during engine testing cannot be compared to the previous laser ignition work performed at NETL due to the vastly different operating conditions. The previous research was conducted at a higher engine speed with lower equivalence ratio values with a boosted intake pressure.

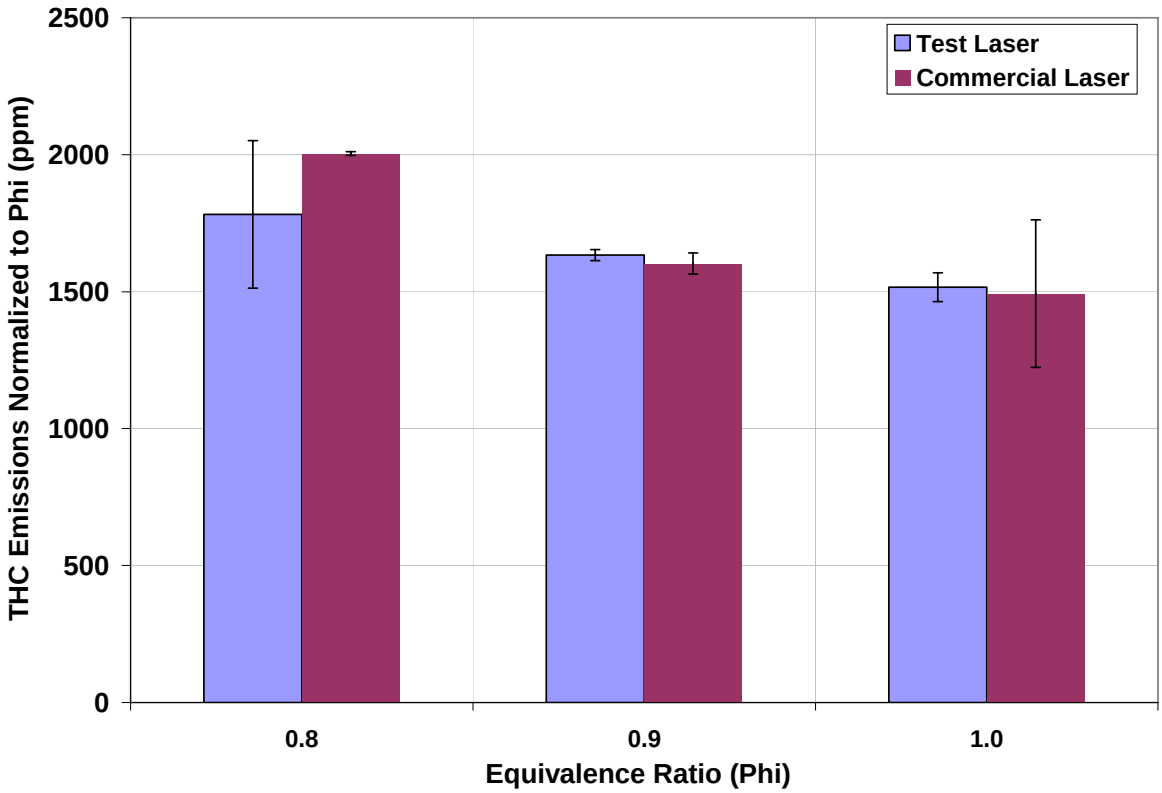

Figure 5.52: Comparison of total hydrocarbon emissions normalized to Phi

6 Conclusions and Recommendations

The primary goal of this work was to research, design, fabricate, test, and prove engine operation of a miniaturized, diode pumped, passively Q-switched, solid state laser as an ignition source for a stationary, single cylinder, natural gas fired, lean burn, reciprocating engine. The development of a miniaturized laser ignition source was an attempt to provide a more durable and cost effective ignition source for large bore stationary natural gas engines that are used for gas pipeline pumping and electrical power generation. The state of the art electrical ignition systems have reached a boundary with both ignitability and durability at the engine conditions that produce the lowest NO_x exhaust emissions and a higher engine thermal efficiency. Previous laser ignition studies, using costly commercial lasers, have shown that the low emission, high efficiency engine operating conditions can be met using laser ignition.

The laser optical component and parameter testing was performed to find a set of independent design variables that when combined and applied to an engine could reliably induce laser sparks and subsequently consistent and reliable ignition. These independent variables dealt with the laser optical components such as the output coupler reflectivity, the Q-switch initial transmission, and the active ion concentration within the laser active medium, and the optical input power to the laser system. The dependent variables were the output pulse energy, the output pulsewidth, the output delay, the output beam quality, the output peak power of the laser pulse, and the estimated intensity of the focused laser pulse. The novelty of this work lies in the combination of the laser parameters to create a single high peak power laser output pulse for use as a spark ignition source. Similar configurations have been investigated in the literature but for different applications such as multiple output

pulse trains for various industrial and communications applications. Another point of novelty is the investigation of the laser medium concentration on the output characteristics of a passively Q-switched laser system. This work has shown that lowering the Neodymium concentration in the active media within a passively Q-switched laser produces higher output energy values. This is significant because an actively Q-switched laser shows the opposite affect when the active ion concentration is varied.

The output coupler reflectivity was varied between three values, 30%, 40%, and 50%. The Q-switch initial transmission was varied between 32%, 36%, and 40%. The Neodymium concentration within the laser medium was varied between 0.35%, 0.5%, and 0.75%. Finally the optical input power was varied between 884.00 W, 937.04 W, and 1007.76 W. Of the 243 individual data points collected over the range of all of the input parameter and replications, 228 combinations produced output and 189 combinations produced laser sparks in air with a 10 mm focal length lens.

The output pulse energy (E_o) varied between 13.84 – 28.20 mJ over all optical parameter and input combinations. The output pulse energy increased the most as the output coupler reflectivity and the Q-switch initial transmission were lowered. The pulse energy varied somewhat as a function of the Nd concentration peaking with Nd = 0.5%. The output pulse energy did not significantly vary as a function of the optical input power over the range studied.

The output pulsewidth (t_p) varied between 7.00 – 14.00 ns over all optical parameter and input combinations. Overall the pulsewidth varied little with respect to each input parameter. However the pulsewidth did decrease slightly toward the optical parameter and input combinations that fostered the fastest buildup of excited state population density. These

combinations consisted of the higher values of each of the input parameters. Although these parameter combinations produced the quicker buildup in the population inversion they were not optimal for creating the larger output pulse energy levels. This leads to a trade-off in the design because the higher parameter values produce a shorter delay times in addition to the shorter pulsewidths. The designer is faced with the decision of higher output pulse energy with a longer delay time with a lower M^2 or a slightly lower output pulse energy in a shorter amount of time with a slightly higher M^2.

The output pulse delay (Qd) varied between 192 – 804 μs over all optical parameter and input combinations. The output delay varied significantly as a function of all of the input parameters. The output delay tended to decrease as the input parameter combination values were increased. The input parameter combinations that fostered the quickest build up in the excited state population density tended to produce the shortest output delay times.

The beam quality or M^2 varied between 4.02 – 13.27 over all optical parameter and input combinations. The beam quality did not follow any noticable trend as a function of the output coupler reflectivity or the optical pump power. However the beam quality did vary significantly as a function of the Nd concentration and the Q-switch initial transmission. The M^2 tended to increase as the Nd concentration was increased. This is due to the additional absorption and subsequent heat deposition within the laser rod. The additional heat deposition contributes to additional thermal lensing and distortion of the lasing photons within the laser cavity. The M^2 tended to increase as the Q-switch initial transmission was decreased. This was primarily due to the variation in the output beam profile that is dictated by the excited state population density cross section with in the laser rod and the degree of transmission that is caused as a function of time and space within the Q-switch by the excited

state population distribution. As the thermal lens changes within the laser rod, due to Nd concentration or pump power level or pump rate or asymmetry, the output beam profile and divergence changes. The excited state density distribution as well as the thermal lens it creates dictate the shape of the highly transmissive area within the Q-switch and therefore the output beam profile and divergence.

The output peak power (P_p) varied between 1.19 – 3.08 MW over all optical parameter and input combinations. The peak power is a calculated parameter and depends on the ratio of the output pulse energy to the output pulsewidth. The peak power tended to increase with decreasing output coupler reflectivity and Q-switch initial transmission. The input pump power did not seem to have an effect due to the fact that both the output pulse energy and the output pulse width do not strictly depend on the input pump power. The peak power does tend higher as a function of decreasing Nd concentration.

The focal intensity (I_o) varied between 135 – 560 GW/cm^2 over all optical parameter and input combinations. The focal intensity is a calculated value that depends on the peak power, the beam quality, the focusing lens and the laser wavelength. The focal intensity did not vary with respect to any one given input parameter. It did vary according to the peak power and the beam quality. The parameters that maximize the output peak power and minimize the M^2 value tended to produce the highest focal intensities.

The goal of the engine testing was to show that the test laser performs identically to the commercially available flashlamp pumped actively Q-switched laser used in previous laser ignition testing. The engine testing consisted of a comparison of the in-cylinder, and emissions behavior of the engine using each of the lasers as an ignition system. All engine parameters were kept as constant as possilbe while the equivalence ratio, and hence the

engine load, was varied between 0.8, 0.9, and 1.0. The test laser was constructed with a 30% output coupler, 32% Q-switch initial transmission, and a 0.5% Nd concentration rod all pumped by approximately 1000 Watts of optical power. The test laser single mode output pulse had an energy of approximately 23 mJ, with a pulsewidth of approximately 10 ns, and an M^2 value of 6.55. This output produced focal intensity of approximately 270 GW/cm^2 with the 11 mm modified on-engine optical arrangement. The commercial laser had similar output parameters and both laser systems operated the engine with similar results. Due to the shortening of the focal length of the on-engine optical setup both laser systems produced a spark well within the optical transfer cavity of the laser optics to spark plug adaptor. This shrouded spark led to a very long ignition delay and retarded combustion timing for all three values of equivalence ratio. This was evidenced by the in-cylinder pressure traces and the HRR waveforms. The emissions data indicate that both lasers produced very similar combustion. The ignition delay caused by the shrouded spark cause most of the combustion to happen after TDC which lead to poor combustion that produced high levels of CO and THC.

The recommendations are divided into two sections. The first section will deal with the current laser design and configuration and what steps need to be taken to improve the overall design and performance. The second section will deal with a subtle change in the laser design that could have a significant affect on its output performance as a laser system and as a multi-cylinder ignition system. There are four primary recommendations for future work with the current laser design and arrangement. The first suggested modification is to work to improve the output of the laser so that the long focal length optical arrangement could be used. This would allow the test laser to be directly compared to the commercial

laser and the standard electrical ignition system, at least at the low speed conditions tested in this research effort. These improvements could be approached by ensuring that the laser rod is being symmetrically pumped. Slight variations in the current design have proven troublesome. Another approach would be to provide a symmetrical waste heat removal system for both the laser rod and the laser chassis. The uneven heat distribution within the laser rod was partially suspected for some of the multimode output issues during engine testing. Significant thermal distributions are tolerable within the YAG substrate due to its substantial physical properties however, to minimize the impact of the thermal distributions on the optical performance they must be symmetric and as steady as possible.

The second suggested modification for the current laser design is to choose a more appropriate material for the laser chassis. The current configuration employed an aluminum chassis that was low cost and easily machined. The use of aluminum posed a significant problem during the engine testing when the laser was operated at five hertz. The optical testing was done at one hertz and produced an average waste heat power of approximately 1 Watt. The average waste power produced at five hertz is approximately 5 Watts. The thermoelectric coolers were specified to handle this level of heat load and performed well keeping the emission wavelength of the laser diodes centered on the absorption band of the Nd:YAG. When designing the laser system and the cooling setup it was assumed that the heat would flow from the diode mounts to the chassis and to the optics table. This was the case however, the flow of heat through the aluminum chassis caused unwanted expansion in the chassis. This expansion was substantial enough to misalign the laser to where it did not produce output. If the repetition rate of the system was brought up slowly this was not a significant issue however, slight adjustments to the alignment had to be made constantly

during this warming up process. The use of a material with a much smaller thermal expansion coefficient would greatly reduce this problem. The addition of an independent cooling system would also alleveate this problem but add unwanted complexity to the laser system.

The third general recommendation is to ruggedize the current laser assembly for on-engine use. On-engine use was not possible with the current setup due to thermal and vibrational sensitivities. When the test laser output was directed through the long focal length optical arrangement, in the laboratory, consistent robust sparks were produced. Under these well controlled conditions the laser output was sufficient for use with the 31 mm sapphire lens. The decision was made not to connect the laser directly to the engine due to concerns about the excess heat removal and the vibrations that the engine produced. When the laser was placed on the optics bench for engine testing the thermal and vibrational problems were solved. By separating the laser from the engine additional problems were encountered. The first problem was the additional optical losses imposed by the three high power laser mirrors. The second was the additional divergence allowed by the long path length between the laser and the engine. Ruggedization of the current laser design to withstand the heat and vibration would allow for on-engine operation which is another step toward a complete laser ignition system. Ruggedization in concert with a thermal management system would allow for full speed on-engine testing.

The fourth and final general recommendation would be to keep the current laser system as it is and modify the optical coupling arrangment on the engine. The current design could be modified to place the short focal length optics closer to the combustion chamber

thereby placing the spark out into the combustion chamber. This approach would require the least amount of effort but the operating speed would still be limited to 5 Hz.

The future design of the laser ignition system will involve the rearrangement of the side pumped laser into an end pumped laser. An end pumped laser calls for the injection of the pump energy longitudinally along the optical axis. In this arrangment the portion of the laser rod being excited is the portion of the laser rod that will be participating on the lasing action. In the side pumped arrangement serious problems arose due to uneven pump energy distributions within the laser rod cross section. The side pumped arrangement also involves pumping a significant volume of laser medium that does not participate in subsequent laser action and output beam production. This problem is eliminated with an end pumped arrangement where only the portion of the gain medium that is involved in the lasing action is pumped. This arrangement will allow for the centralization of the pump diodes to a location where they can be isolated from excessive heat and vibration. The output of the laser diodes can then be coupled into an optical fiber for easy delivery and distribution to one or more monolithic laser oscillators. The output from the optical fiber is focused through the laser oscillator high reflector and into the end of the laser gain medium. From this point on the laser operation is identical to the test laser presented in this work. The deposition of the pump energy down the central axis of the does provide for the symmetric removal of excess heat radially along the length of the laser rod. Figure 6.1 shows a block diagram of the recommended optically distributed end pumped multicylinder laser system.

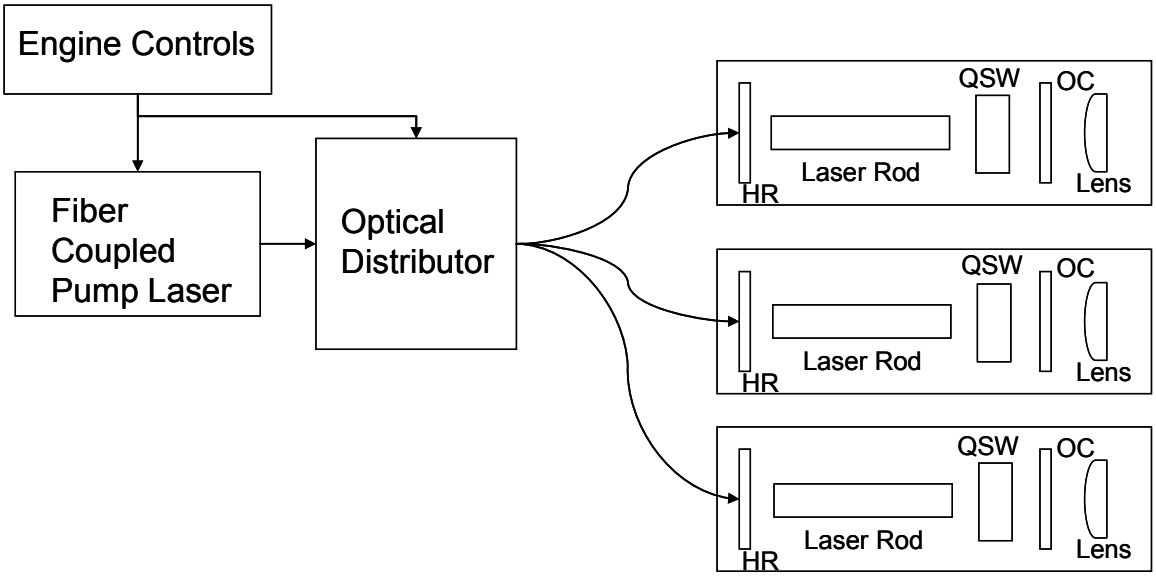

Figure 6.1: Optically distributed end pumped laser spark ignition system

7 References

1. Kopecek, H., Wintner, E., Pischinger, R., Herdin, G.R., Klausner, J., "Basics for Future Laser Ignition System for Gas Engines," Paper No. 2000-ICE-316, ICE-Vol. 35-2, Internal Combustion Engine Fall Technical Conference, ASME 2000.
2. http://www.energy.ca.gov/pier/arice/documents/2001-07_workshop/ARICE PerformanceTarget Table.pdf
3. http://www.eere.energy.gov/de/gas_fired/information_resources.html
4. Robert Bosch GmbH. Gasoline-Engine Management. Stuttgart, Germany: Robert Bosch GmbH, 1999.
5. Tran, P.X., White, F.P., "Laser-Induced Spark Ignition of CH_4/Air Mixtures," Combustion and Flame Vol. 119, pp. 203-216, 1999.
6. Weinrotter, M., Ast, G., Kopecek, H., Wintner, E., "An Extensive Comparison of Laser-Induced Plasma Ignition and Conventional Spark Ignition of Lean Methane-Air Mixtures Under Engine-Like Conditions," SAE Paper 2005-01-0248, 2005.
7. Kopecek, H., Charareh, S., Lackner, M., Forsich, C., Winter, F., Klausner, J., Herdin, G., Wintner, E., "Laser Ignition of Methane-Air Mixtures at High Pressures and Diagnostics," Proceedings of ICES03, Spring Technical Conference of the ASME Internal Combustion Engine Division, Salzburg, Austria, May 11-14, 2003.
8. Aherns, D.L., Yalin, A.P., Olsen, D.B., Kim, G.H., "Development of an Open Path Laser Ignition System for a Large Bore Natural Gas Engine: Part 1 System Design," Paper Number ICEF2005-1060, Proceedings of ASME Internal Combustion Engine Division Spring Technical Conference, April 5-7, 2005, Chicago, Illinois, USA.
9. McMillian, M.H., Woodruff, S.D., Ontko, J.S., Richardson, S.W., McIntyre, D.L., "Laser-Spark Ignition for Natural Gas Fueled Reciprocating Engines," Natural Gas Technologies Conference and Exposition, Orlando, Florida, Sept. 29 – Oct. 2, 2002.
10. McMillian, M.H., Richardson, S., Woodruff, S.D., McIntyre, D.L., "Laser-Spark Ignition Testing in a Natural Gas-Fueled Single-Cylinder Engine," SAE Paper 2004-01-0980, 2004.
11. Richardson, S., McMillian, M.H., Woodruff, S.D., McIntyre, D.L., "Misfire, Knock and NOx Mapping of a Laser Spark Ignited Single Cylinder Lean Burn Natural Gas Engine," SAE paper 2004-01-1853, June 2004.
12. McMillian, M.H., Woodruff, S.D., Richardson, S.W., McIntyre, D.L., "Laser Spark Ignition: Laser Development and Engine Testing," Paper Number ICEF2004-917, Proceedings of ICEF04 Fall Technical Conference of the ASME Internal Combustion Engine Division, October 24-27, 2004, Long Beach, California, USA.
13. Ma, J.X., Ryan III, T.W., Buckingham, J.P., "Nd:YAG Laser Ignition of Natural Gas," ASME Book G1074C-1998 pp. 117-125, 1998.
14. Hickling, R., Smith, W.R., "Combustion Bomb Tests of Laser Ignition," SAE Paper 740114, 1974.
15. Tran, P.X., "Laser Spark Ignition: Experimental Determination of Laser-Induced Breakdown Thresholds of Combustion Gases," Optics Communications Vol. 175 pp. 419-423, 2000.
16. Phouc, T.X., White, F.P., "Laser-Induced Spark Ignition of CH_4/Air Mixtures," Combustion and Flame Vol. 119 pp. 203-216, 1999.
17. Ready, J.F., Effects of High-Power Laser Radiation, Academic Press, New York, 1971.

18. Buscher, H.T., Tomlinson, R.G., Damon, E.K., "Frequency Dependence of Optically Induced Gas Breakdown," Physical Review Letters, Vol. 15, No. 22, November 29, 1965.
19. Tomlinson, R.G., Damon, E.K., Buscher, H.T., "The Breakdown of Noble and Atmospheric Gases by Ruby and Neodymium Laser Pulses," Physics of Quantum Electronics, Eds. P.L. Kelley, B. Lax, and P.E. Tannenwald, McGraw-Hill, New York, 1966.
20. Bihari, B., Gupta, S.B., Sekar, R.R., Gingrich, J., Smith, J., "Development of Advanced Laser Ignition System for Stationary Natural Gas Reciprocating Engines," Proceedings of ASME Internal Combustion Engine Division, ICEF2005-1325, Fall Technical Conference, September 11-14, 2005, Ottawa, Canada.
21. Richardson, S.W., McMillian, M.H., Woodruff, S.D., Worstell, T., McIntyre, D.L., "Laser Spark Ignition of a Blended Hydrogen-Natural Gas Fueled Single Cylinder Engine," Proceedings of ASME ICE Division, ICES2006-1397, Spring Technical Conference, May 2006, Aachen, Germany.
22. Heywood, J. B., Internal Combustion Engine Fundamentals, McGraw-Hill, New York, 1988.
23. Ivanic, Z., Ayala, F., Goldwitz, J.A., Heywood, J.B., "Effects of Hydrogen Enhancement on Efficiency and NOx Emissions of Lean and EGR-Diluted Mixtures in a SI Engine," SAE Paper 2005-01-0253, 2005.
24. "Capacitive Discharge Ignition" Application Note, AN819, ST Microelectronics, 2004.
25. Soldera, F.A., Mucklich, F.T., Hrastnik, K., Kaiser, T., "Description of the Discharge Process in Spark Plugs and its Correlation with Electrode Erosion Patterns," IEEE Transactions on Vehicular Technology, Vol. 53, No. 4, July 2004.
26. Maly, R., "Spark Ignition: Its Physics and Effects on the Internal Combustion Engine," in *Fuel Economy: Road Vehicles Powered by Spark Ignition Engines*, Eds. J.C. Hilliard and G.S. Springer, Plenum, New York, 1984.
27. Raizer, Y.P., *Gas Discharge Physics*, 1st edition, Springer-Verlag, Berlin, Germany, 1991.
28. Paschen, F., "Ueber die zum funkenubergang in luft, wasserstoff und kohlensaure, beiverschiedenen drucken erforderliche potentialdifferenz," Ann. Phys. Chem., Vol. 37, pp. 69-96, 1889.
29. http://www.du.edu/~jcalvert/phys/dischg.htm#Brea
30. Nishida, M., Hattori, T., Mukainakano, S., Mizuno, T., Goto, T., "Laser Ignition Apparatus for an Internal Combustion Engine," U.S. Patent 4,416,226 Nov. 22, 1983.
31. Vowles, R.W., "Laser Energy Ignition System," U.S. Patent 4,852,529 Aug. 1, 1989.
32. Geiger, A.R., "Method and Apparatus for Controlling a Combustion Process," U.S. Patent 5,328,665 Jul. 12, 1994.
33. Feichtinger, G., Tschetsch, H., "Internal Combustion Engine with Externally Supplied Ignition," U.S. Patent 6,053,140 Apr. 25, 2000.
34. Molina, R.W., Cortina, M., Bertolina, R., Balsa, L.H., "Rotative Combustion Chamber Engine," U.S. Patent 4,944,262 Jul. 31, 1990.
35. Mukainakano, S., Hattori, T., Nishida, M., Mizuno, T., Goto, T., "Ignition System for Engine," U.S. Patent 4,523,552 Jun. 18, 1985.
36. Mukainakano, S., Hattori, T., Nishida, M., Mizuno, T., Goto, T., "Ignition Apparatus for Internal Combustion Engine," U.S. Patent 4,434,753 Mar. 6, 1984.

37. Chung, S.H., Morsy, M.H., Ko, Y.S., "Laser-Induced Ignition System Using a Cavity," U.S. Patent 6,305,929 Oct. 23, 2001.
38. Ronney, "Laser Versus Conventional Ignition of Flames," Optical Engineering, Vol. 33 pp. 510-521, 1994.
39. Ma, J.X., Alexander, D.R., Poulain, D.E., "Laser Spark Ignition and Combustion Characteristics of Methane-Air Mixtures," Combustion and Flame Vol. 112 pp. 492-506, 1998.
40. Smith, J.R., "Comparison of Ignition Locations in a High Swirl Engine," Sandia Labs. SAND-79-8715, 1979.
41. Ronney, P.D., "Laser Versus Conventional Ignition of Flames," SPIE Vol. 1862 pp. 2-22, 2003.
42. Gupta, S., Sekar, R., "Laser and Conventional Ignition In Natural Gas Reciprocating Engines: Literature Review," Argonne National Lab. Cost Code: 49751-NG-155, October 2001.
43. Graf, J., Weinrotter, M., Kopecek, H., Wintner, E., "Laser Ignition, Optics and Contamination of Optics in an I.C. Engine," Paper Number ICEF2004-833, Proceedings of ICEF04 Fall Technical Conference of the ASME Internal Combustion Engine Division, October 24-27, 2004, Long Beach, California, USA.
44. Lackner, M., Winter, F., Charareh, S., Iskra, K., Neger, T., Kopecek, H., Wintner, E., Klausner, J., Herdin, G., "Optical Diagnostics of Laser Ignition for Future Advanced Engines," Paper Number ICEF2004-872, Proceedings of ICEF04 Fall Technical Conference of the ASME Internal Combustion Engine Division, October 24-27, 2004, Long Beach, California, USA.
45. Yang, L.C., Menichelli, V.J., "Detonation of Insensitive High Explosives by a Q-Switched Ruby Laser," Applied Physics Letters, Vol. 19, No. 11, 1 Dec. 1971.
46. Menichelli, V.J., Yang, L.C., "Laser System to Detonate Explosive Devices," NASA Tech Brief, Nov. 1974, B74-10194.
47. Yang, L.C., Menichelli, V.J., Earnest, J.E., "Laser Initiation of Explosive Devices," Weapons Technology, Jan.-Feb. 1974, pp. 344-347.
48. Lavid, M., Gulati, S.K., Lempert, W.R., "Laser Ignition of Ball Powder (Nitrocellulose Base)," SPIE vol. 2112 pp. 129-143, 1994.
49. Piltch, M.S., "Explosive Laser Light Initiation of Propellants," U.S. Patent 5,212,339 May 18, 1993.
50. Nielsen, F.B., "Laser Initiated Rocket Type Igniter," U.S. Patent 3,296,795 Jan. 10, 1967.
51. Folsom, M., "Explosive Initiator with Angled Fiber Optic Input," U.S. Patent 5,010,822 Apr. 30, 1991.
52. Gallaghan, J.A., Benson, R.W., Carlson, B.V., "Laser Stimulated Ordnance Initiation Device," U.S. Patent 3,724,383 Apr. 3, 1973.
53. Platt, W.G., "Laser Ignition System," U.S. Patent 3,685,392 Aug. 22, 1972.
54. Platt, W.G., "Laser Ignition System for Firearms," U.S. Patent 3,631,623 Jan. 4, 1972.
55. Stuckle, G., "Restraint System for Vehicle Occupants Having Laser Ignition for an Air Bag Gas Generator," U.S. Patent 5,460,407 Oct. 24, 1995.
56. Loughry, B., Ulrich, O.E., "Laser Ignition of Explosives," U.S. Patent 4,917,014 Apr. 17, 1990.
57. Streifer, W., Scifres, D.R., Klein, J.R., "Method of Initiating a Sequence of Pyrotechnic Events," U.S. Patent 4,862,802 Sep. 5, 1989.

58. Baker, R.L., “Pyrotechnic Pumped Laser for Remote Ordnance Initiation System,” U.S. Patent 3,618,526 Nov. 9, 1971.
59. Josse, A.P., “Pyrotechnic Priming Device Having a Microlens Set by a Shape Memory Material and Pyrotechnic Chain Utilizing Said Device,” U.S. Patent 5,052,300 Oct. 1, 1991.
60. Yang, L.C., Menichelli, V.J., “Optically Detonated Explosive Device,” U.S. Patent 3,812,783 May 28, 1974.
61. Lewis, D.J., Gardner, F.H., “Explosive Detonating Device,” U.S. Patent 3,528,372 Sept. 15, 1970.
62. Hawley, J.D., “Optically Initiated Detonator,” U.S. Patent 5,179,247 Jan. 12, 1993.
63. Letendre, G.R., Chandler, V.E., Monk, D.B., “Direct Laser Ignition of Ignition Products,” U.S. Patent 5,406,889 Apr. 18, 1995.
64. Beyer, R.A., “Multi-Point Fiber Optic Igniter,” U.S. Patent 5,191,167 Mar. 2,1993.
65. Shann, P.C. “Detonation of Explosive Charges and Equipment Therefore,” U.S. Patent 4,391,195 Jul. 5, 1983.
66. Williams, M.S., Durrell, R.R., Kokoshvili, S.M., Moore, C.J., Moser, J.M., Netoff, T.J., “Laser Initiated Ordnance Systems,” U.S. Patent 5,206,455 Apr. 27, 1993.
67. Lewis, D.J., Coombs, I.G., “Light Energized Explosive Device,” U.S. Patent 3,408,937 Nov. 5, 1968.
68. Carel, C., Josse, A., “Photopyrotechnical Detonation Device and Photopyrotechnical Chain Using This Device,” U.S. Patent 4,870,903 Oct. 3, 1989.
69. Nilsson, N., Larsson, L., Hafstrand, A., “Method of Initiating Artillery Propellant Powder Charges, Artillery Propellant Powder Charge Module and Artillery Powder Charge,” U.S. Patent 6,415,715 B1 Jul. 9, 2002.
70. Winch, P.C., Blackledge, M., “Electro-Optical Control of Solid Fuel Rocket Burn Rate,” U.S. Patent 4,587,805 May 13, 1986.
71. Lawrence, H.R., “Laser Ignition,” U.S. Patent 3,177,651 April 13, 1965.
72. Williams, N.P., “Initiator for Use in Laser Beam Ignition of Solid Propellants,” U.S. Patent 4,047,483 Sept. 13, 1977.
73. Hoskins, R.H., “Method for Inducing Chemical Reactions with Lasers,” U.S. Patent 3,405,045 Oct. 8, 1968.
74. Lemelson, J.H., “Chemical Reaction Apparatus and Method,” U.S. Patent 4,702,808 Oct. 27, 1987.
75. Rich, J.W., Raymonda, J.W., “Method and Apparatus for the Initiation of Chemical Reactions,” U.S. Patent 4,012,301 Mar. 15, 1977.
76. Few, J.D., Lewis, J.W.L., “Laser Initiated Non-Linear Fuel Droplet Ignition,” U.S. Patent 5,404,712 Apr. 11, 1995.
77. Few, J.D., Lewis, J.W.L., “Laser Initiated Non-Linear Fuel Droplet Ignition,” U.S. Patent 5,673,550 Oct. 7, 1997.
78. Few, J.D., Lewis, J.W.L., “Laser Initiated Non-Linear Fuel Droplet Ignition,” U.S. Patent 5,524,429 Jun. 11, 1996.
79. Few, J.D., Lewis, J.W.L., “Laser Initiated Non-Linear Fuel Droplet Ignition,” U.S. Patent 5,485,720 Jan. 23, 1996.
80. Few, J.D., Lewis, J.W.L., “Laser Initiated Non-Linear Fuel Droplet Ignition Apparatus,” U.S. Patent 5,598,699 Feb. 4, 1997.

81. Few, J.D., Lewis, J.W.L., “Laser Initiated Non-Linear Fuel Droplet Ignition Method,” U.S. Patent 5,497,612 Mar. 12, 1996.
82. Early, J.W., “Multiple-Laser Pulse Ignition Method and Apparatus,” U.S. Patent 5,756,924 May 26, 1998.
83. Early, J.W., “Laser Preheat Enhanced Ignition,” U.S. Patent 5,876,195 Mar. 2, 1999.
84. Early, J.W., Lester, C.S., “Laser Ignition,” U.S. Patent 6,428,307 B1 Aug. 6, 2002.
85. Early, J.W., “Laser Ablation Based Fuel Ignition,” U.S. Patent 5,769,621 Jun. 23, 1998.
86. Early, J.W., Lester, C.S., “Laser Ignition,” U.S. Patent 6,413,077 B1 Jul. 2, 2002.
87. Early, J.W., Lester, C.S., “Laser Ignition,” U.S. Patent 6,394,788 B1 May 28, 2002.
88. Early, J.W., Lester, C.S., “Laser Ignition,” U.S. Patent 6,382,957 B1 May 7, 2002.
89. Early, J.W., Lester, C.S., “Laser Ignition,” U.S. Patent 6,514,069 B1 Feb. 4, 2003.
90. Few, J.D., Lewis, J.W.L., “Gas Turbine Engine Photon Ignition System,” U.S. Patent 4,947,640 Aug. 14, 1990.
91. DeFreitas, D.M., Migliori, A., “Ignition Methods and Apparatus Using Microwave and Laser Energy,” U.S. Patent 5,845,480 Dec. 8, 1998.
92. DeFreitas, D.M., “Laser Ignition Methods and Apparatus for Combustors,” U.S. Patent 5,367,869 Nov. 29, 1994.
93. DeFreitas, D.M., “Electrostatic Fuel Injector Body with Igniter Electrodes Formed in the Housing,” U.S. Patent 5,588,299 Dec. 31, 1996.
94. Early, J.W., Thomas, M.E., “Laser Controlled Flame Stabilization,” U.S. Patent 6,302,682 B1 Oct. 16, 2001.
95. Andress, B., Kuchelbacher, L., “Ignition Device for Oil-Fired Boilers,” U.S. Patent 3,427,118 Feb. 11, 1969.
96. Berberich, B., “Shock Wave Burner,” U.S. Patent 3,473,879 Oct. 21, 1969.
97. Smith, M.M., “Jet Engine Augmenter Operation at High Altitudes,” U.S. Patent 4,302,933 Dec. 1, 1981.
98. Hirsch, R.L., “Method of Mounting a Fuel Pellet in a Laser-Excited Fusion Reactor,” U.S. Patent 4,142,088 Feb. 27, 1979.
99. Whittlesey, J.R.B., “Apparatus Using Lasers to Trigger Thermonuclear Reactions,” U.S. Patent 3,378,446 April 16, 1968.
100. Daiber, J.W., Hertzberg, A., Wittliff, C.E., “Method of Creating a Controlled Nuclear Fusion Reaction,” U.S. Patent 3,489,645 Jan. 13, 1970.
101. Patrick, R., Schoenborn, P., Franklin, M., Bose, F., “Plasma Initiating Assembly,” U.S. Patent 6,062,163 May 16, 2000.
102. Patrick, R., Schoenborn, P., Franklin, M., Bose, F., “Method for Igniting Low Pressure Inductively Coupled Plasma,” U.S. Patent 5,639,519 Jun. 17, 1997.
103. Patrick, R., Schoenborn, P., Franklin, M., Bose, F., “Apparatus for Igniting Low Pressure Inductively Coupled Plasma,” U.S. Patent 5,468,296 Nov. 21, 1995.
104. Bovino, L.J., Wright, W.H., “Triggering Technique for Multi-Electrode Spark Gap Switch,” U.S. Patent 5,153,460 Oct. 6, 1992.
105. Borisov, M.F., Gromovenko, V.M., Lapshin, V.A., Rezunkov, Y.A., Saveleva, V.P., Stepanov, V.V., “Long Laser Spark for Controlling the Trajectory of an Atmospheric Electric Discharge,” J. Opt. Technol. Vol. 66, No. 3, pp. 203-209, 1999.
106. Borisov, M.F., Gromovenko, V.M., Danilov, M.F., Lapshin, V.A., “Interaction of a Long Laser Spark with an Atmospheric Electric Field,” J. Opt. Technol. Vol. 66, No. 3, pp. 210-214, 1999.

107. Aleksandrov, G.N., Kadzov, G.D., "Possibility of Using a Laser Spark to Enhance the Reliability of Lightning Protection," J. Opt. Technol. Vol. 66, No. 3, pp. 183-186, 1999.
108. Shelobolin, A.V., "Long Laser Spark and Electric Gas Breakdown," Plasma Physics Reports, Vol. 26, No. 4, pp. 320-327, 2000.
109. Danilov, O.B., Tul'skii, S.A., "An Electrical Discharge Initiated by a Long Laser Spark," J. Opt. Technol. Vol. 66, No. 3, pp. 187-189, 1999.
110. Isberg, J., Skytt, P., Ekberg, M., Sunesson, A., Bergkvist, M., Gustafsson, A., Bernhoff, H., "A Laser Triggered Plasma Switch," 12th IEEE Intl. Pulsed Power Conf. Cat. No. 99CH36358, Vol. 1 pp. 138-41, 1999.
111. Homan, H.S., Sirignano, W.A., "Minimum Mass of Burning Aluminum Particles for Ignition of Methane Air and Propane Air Mixtures," 18th Symposium (International) on Combustion, Combustion Institute, Pittsburgh, pp. 1709-1717, 1981.
112. Kingdon, R.G., Weinberg, F.J., "The Effect of Plasma Constitution on Laser Ignition Energies," 16th Symposium (International) on Combustion, Combustion Institute, Pittsburgh, pp. 747-756, 1976.
113. Lavid, M., Poulos, A.T., Gulati, S.K., "Infrared Multiphoton Ignition and Combustion Enhancement of Natural Gas," SPIE Vol. 1862, pp. 33-44, 1993.
114. Hill. R.A., Laguna, G.A., "Laser Initiated Combustion of $CH_4 + O_2$ Mixtures," Optics Comm. Vol. 32, No. 3, pp.435-439, March 1980.
115. Chou, M.S., Zukowski, T.J., "Ignition of $H_2/O_2/NH_3$, $H_2/AIR/NH_3$ and $CH_4/O_2/NH_3$ Mixtures by Excimer-Laser Photolysis of NH_3," Combustion and Flame Vol. 87, pp. 191-202, 1991.
116. Witriol, N.M., Forch, B.E., Miziolek, A.W., "Modeling Laser Ignition of Combustible Gases," 27th JANNAF Combustion Meeting, pp. 213-217, 1990.
117. Early, J.W., "Laser Ablation Based Fuel Ignition," U.S. Patent 5,769,621 Jun. 23, 1998.
118. Forch, B.E., Miziolek, A.W., "Ultraviolet Laser Ignition of Premixed Gases by Efficient and Resonant Multiphoton Photochemical Formation of Microplasmas," Combustion Science and Technology, Vol. 52, pp. 151-159, 1987.
119. Lim, E.H., McIlroy, A., Ronney, P.D., Syage, J.A., "Detailed Characterization of Minimum Ignition Energies of Combustible Gases Using Laser Ignition Sources," Transport phenomena in combustion; Proceedings of the 8th International Symposium on Transport Phenomena in Combustion (ISTP-VIII), San Francisco, CA; UNITED STATES; 16-20 July 1995. pp. 176-184, 1996.
120. Norrish, R.G.W., "The Study of Combustion by Photochemical Methods," 10th Symposium (International) on Combustion, pp. 1-18, 1965.
121. Lucas, D., Dunn-Rankin, D., Hom, K., Brown, N.J., "Ignition by Excimer Laser Photolysis of Ozone," Combustion and Flame Vol. 69, pp. 171-184, 1987.
122. Lavid and Stevens, "Photochemical Ignition of Premixed Hydrogen/Oxidizer Mixtures with Excimer Lasers," Combustion and Flame Vol. 60, pp. 195-202, 1985.
123. Lavid, M., Nachshon, Y., Gulati, S.K., Stevens, J.G., "Photochemical Ignition of Premixed Hydrogen/Oxygen Mixtures with ArF Laser," Combustion Science and Technology, Vol. 96, pp. 231-245, 1994.
124. Forch, B.E., Miziolek, A.W., "Oxygen-Atom Two-Photon Resonance Effects in Multiphoton Photochemical Ignition of Premixed H_2/O_2 Flows," Optics Letters, Vol. 11, No. 3, March 1986.

125. Forch, B.E., Miziolek, A.W., "Laser-Based Ignition of H_2/O_2 and D_2/O_2 Premixed Gases Through Resonant Multiphoton Excitation of H and D Atoms Near 243 nm," Combustion and Flame Vol. 85, pp. 254-262, 1991.
126. Forch, B.E., "Resonant Laser Ignition of Reactive Gases," SPIE Vol. 2122, pp. 118-128, 1994.
127. Weyl, G.M., Laser-Induced Plasmas and Applications, Eds. Radziemski, L.J., Cremers, D.A., Marcel Dekker, Inc., New York, 1989.
128. Morgan, C.G., "Laser-Induced Breakdown of Gases," Rep. Prog. Phys., Vol. 38, pp. 621-665, 1975.
129. Morgan, C.G., "Laser-Induced Electrical Breakdown of Gases," In: Meek, J.M., Crags, J.D., editors. Electrical Breakdown of Gases. New York: Wiley, 1978, pp. 717-752.
130. Durbin, E. J., and Tsal, K. C., "Extending the Lean Limit Operation of an SI Engine with a Multiple Electrode Spark Plug," SAE Paper 830476, 1983.
131. DeMichelis, C., "Laser Induced Gas Breakdown: A Bibliographical Review," IEEE Journal of Quantum Electronics, Vol. QE-5, No. 4, April 1969.
132. Ho, C.M., "An Experimental Study on the Growth of Laser Spark and Electric Spark Ignited Flame Kernels" Dissertation, Pennsylvania State University, 1995.
133. Dale, J.D., Smy, P.R., Clements, R.M., "Laser Ignited Internal Combustion Engine – An Experimental Study," SAE Paper 780329, 1978.
134. Kopecek, H., Charareh, S., Lackner, M., Forsich, C., Winter, F., Klausner, J., Herdin, G., Weinrotter, M., Wintner, E., "Laser Ignition of Methane-Air Mixtures at High Pressures and Diagnostics," Journal of Engineering for Gas Turbines and Power, Vol. 127, pp. 213-219, Jan. 2005.
135. Herdin, G., Klausner, J., Wintner, E., Weinrotter, M., Graf, J., "Laser Ignition a New Concept to Use and Increase the Potentials of the Gas Engines," ICEF2005-1352, ASME Internal Combustion Engine Division Fall Technical Conference, September 11-14, 2005, Ottawa, Canada.
136. Alger, T., Mehta, D., Chadwell, C., Roberts, C., "Laser Ignition in a Pre-Mixed Engine: The Effect of Focal Volume and Energy Density on Stability and the Lean Operating Limit," SAE Paper 2005-01-3752, 2005.
137. Ahrens, D.L., Olsen, D.B., Yalin, A.P., "Development of an Open Path Laser Ignition System for a Large Bore Natural Gas Engine: Part 2 Single Cylinder Demonstration," Proceedings of ASME ICE Division, ICES2005-1317, Fall Technical Conference, September 11-14, 2005, Ottawa, Canada.
138. Yalin, A.P., Defoort, M.W., Joshi, S., Olsen, D., Willson, B., Matsuura, Y., Miyagi, M., "Laser Ignition of Natural Gas Engines Using Fiber Delivery," Proceedings of ASME ICE Division, ICEF2005-1336, Fall Technical Conference, September 11-14, 2005, Ottawa, Canada.
139. Yalin, A.P., Defoort, M.W., Willson, B., Matsuura, Y., Miyagi, M., "Use of Hollow-Core-Fibers to Deliver Nanosecond Nd:YAG Laser Pulses to Form Sparks in Gases," Optics Letters, Vol. 30, No. 16, August 15, 2005.
140. Yalin, A.P., Reynolds, A.R., Joshi, S., Defoort, M.W., Willson, B., Matsuura, Y., Miyagi, M., "Development of a Fiber Delivered Laser Ignition System for Natural Gas Engines," Proceedings of ASME ICE Division, ICEF2006-1370, Spring Technical Conference, May 7-10, 2006, Aachen, Germany.

141. Smith, J.R., "Comparison of Ignition Locations in a High Swirl Engine," Sandia Labs. SAND-79 -8715, 1979.
142. Koechner, W., Bass, M., Solid-State Lasers: A Graduate Text, Springer-Verlag, New York, 2003.
143. Svelto, O., Principles of Lasers, 4th Edition, Hanna, D.C., Translator, Editor, Plenum Press, New York, London, 1998.
144. Kuhn, K.J., Laser Engineering, Prentice-Hall, Inc., Upper Saddle River, New Jersey, 1998.
145. Siegman, A.E., Lasers, University Science Books, Sausalito, California, 1986.
146. Verdeyen, J.T., Laser Electronics, 3rd Edition, Prentice-Hall, Inc., Upper Saddle River, New Jersey, 1995.
147. Applied Laser Safety, Laser Professionals Inc., 2620 S. Maryland Parkway, #749, Las Vegas, NV 89109, 2005.
148. BeamCAD: Laser Beam Analysis Software, Instruction Manual, Coherent, 1992.
149. Chen, Y.F., Lan, Y.P., Chang, H.L., "Analytical model for design criteria of passively Q-switched lasers," IEEE Journal of Quantum Electronics, Vol. 37, No. 3, March 2001.
150. Dong, J., "Numerical Modeling of CW-Pumped Repetitively Passively Q-Switched Yb-YAG Lasers with Cr:YAG as Saturable Absorber," Optics Communications Vol. 226, pp. 337-344, 2003.
151. Xiao, G., Bass, M., "A Generalized Model for Passively Q-Switched Lasers Including Excited State Absorption in the Saturable Absorber," IEEE Journal of Quantum Electronics, Vol. 33, No. 1, January 1997.
152. Degnan, J., "Optimization of Passively Q-Switched Lasers," IEEE Journal of Quantum Electronics, Vol. 31, No. 11, November 1995.
153. Conant, L., Reno, C., "GaAs Laser Diode Pumped Nd:YAG Laser," Applied Optics, Vol. 13, No. 11, Nov. 1974.
154. Rosenkrantz, L., "GaAs Diode-Pumped Nd:YAG Laser," J. Appl. Phys., Vol. 43, No. 11, Nov. 1972.
155. Farmer, G., Kiang, Y., "Low-Current-Density LED-Pumped Nd:YAG Laser Using a Solid Cylindrical Reflector," Journal of Applied Physics, Vol. 45, No. 3, March 1974.
156. Zendzian, W., Jabczynski, J.K., Mierczyk, Z., "Passively Q-Switched, 5 mJ, Nd:YAG Triangle Slab Laser Pumped by 300 W Quasi CW Diode Array," WJ6, CLEO, Pacific Rim 1999, pp. 223-224, 1999.
157. Agnesi, A., Dell'Acqua, S., Morello, C., Piccinno, G., Reali, G., Sun, Z., "Diode-Pumped Neodymium Lasers Repetitively Q-Switched by Cr^{4+}:YAG Solid-State Saturable Absorbers," IEEE Journal of Selected Topics in Quantum Electronics, Vol. 3, No. 1, Feb. 1997.
158. Pavel, N., Saikawa, J., Kurimura, S., Taira, T., "High Average Power Diode End-Pumped Composite Nd:YAG Laser Passively Q-Switched by Cr^{4+}:YAG Saturable Absorber," Jpn. J. Appl. Phys., Vol. 40, Part 1, No. 3A, pp. 1253-1259, March 2001.
159. Lam, P.K., Freitag, I., Bode, M., Tunnermann, A., Welling, H., "High Average Power Q-Switched Second Harmonic Generation with Diode-Pumped Nd:YAG Laser," Electronics Letters, Vol. 34, No. 7, April 2, 1998.
160. Afzal, R., Yu, A., Zayhowski, J., Fan, T., "Single-Mode High-Peak-Power Passively Q-Switched Diode-Pumped Nd:YAG," Optics Letters Vol. 22, No. 17, Sept. 1, 1997.

161. Agnesi, A., Dell'Acqua, S., Piccinini, E., Reali, G., Piccinno, G., "Efficient Wavelength Conversion with High-Power Passively Q-Switched Diode-Pumped Neodymium Lasers," IEEE Journal of Quantum Electronics, Vol. 34, No. 8, Aug. 1998.
162. Aniolek, K.W., Schmitt, R.L., Kulp, T.J., Richman, B.A., Bisson, S.E., Powers, P.E., "Microlaser-Pumped Periodically Poled Lithium Niobate Optical Parametric Generator-Optical Parametric Amplifier," Optics Letters, Vol. 25, No. 8, April 15, 2000.
163. Isyanova, Y., Manni, J.G., Welford, D., Jaspan, M., Russell, J.A., "High-Power, Passively Q-switched Microlaser-Power Amplifier System," OSA TOPS Vol. 50, Advanced Solid-State Lasers, 2001 Optical Society of America.
164. Zayhowski, J.J., "Passively Q-Switched Microchip Lasers and Applications," The Review of Laser Engineering, Vol. 26, No. 12, Dec. 1998.
165. Proteus Single Cylinder Research Engine No. 102 Instruction and Operating Manual, 1986.
166. McMillian, M.H., "Combustion Analysis and Particulate Mutagenicity Characterization for a Single-Cylinder Diesel Engine Fueled by Fischer-Tropsch Derived Liquids" Dissertation, West Virginia University, 2002.
167. Tidona, R.J., Nuzami, A.A., and Cernansky, N.P., "Reducing Interference Effects in the Chemiluminescent Measurement of Nitric Oxides from Combustion Systems," JAPCA Vol. 38, pp. 806-911, 1988.
168. Matthews, R.D., Sawyer, R.F., and Schefer, R.W., "Interferences in Chemiluminescent Measurement of NO and NO_2 Emissions from Combustion Systems," Environmental Science and Technology, Vol. 11, No. 12, November 1977.
169. Procedures for Operating the Proteus Diesel Engine, National Energy Technology Laboratory Document No. 0555-0001-3-02-0, Attachment 5, August 3, 2006.

Appendix A – Advanced Ignition System Functional Requirements

Functional Requirement for Advanced Natural Gas Recip Ignition System

Version 1.0

This spec is based on the collective input from the three engine manufacturers responsible for commercializing products based on ARES program goals. Refer to the DOE DEER website "http://www.eren.doe.gov/der/gas_fired/gas_fired.html " for information concerning the ARES program.

Ignition systems play a critical role in advancing state of the art combustion systems for improved efficiency and reduced emissions in natural gas engines. The attached specification outlines some of the critical aspects of advanced ignition, but is not meant as an all-inclusive list. While electric ignition systems are the most common system available today, future systems may or may not use this approach. However, the key ingredients of cost, reliability, and serviceability must be maintained to satisfy our broad customer base.

This list is subject to change as technology advances, and will need to be reviewed and updated at future meetings of the Advanced Ignition System Roundtable.

Our definition of the ignition system includes the entire package required to accept an ignition signal from an external source until completion of the ignition event. Typical components today include a control module, processor, ignition distribution system, cylinder processor (coil and extender), igniter (spark plug), and limited ignition diagnostics and prognostics. Note that this ignition system requirement does not include a combustion analysis package although this would be desirable in future systems.

Gordon Gerber
Caterpillar Inc

Mark Rosswurm
Cummins Inc

Ed Reinbold
Waukesha Engine

November 06, 2002

	System Profile Element	Continuous-Duty Power Generation Requirements*	Units
1	**Cost (current dollars)**		
	- First Cost (add $1/ekw for CSA requirement)	4.00	$ / kWe
	- Life Cycle Cost (including system replacement at major)	0.25	$ / MWe-hr
	- Repair Costs to 1st Engine Overhaul	0.15	$ / MWe-hr
2	**Performance**		
	-Maximum ignition pressure (peak cylinder pressure)	220	bar
	-Minimum air/fuel ratio	0.9	λ
	-Maximum air/fuel ratio (w/swirl)	2.5	λ
	-Minimum methane number (hydrogen capable)	0	
	- Maximum methane number (landfill capable)	140	
	- Ignition timing repeatability (non-mechanical)	0.08	° crank
	- Ignition timing accuracy (non-mechanical)	0.08	° crank
	- COV (steady state, 0.5 g/bhp-hr NOx, 25 bar BMEP)	<1.0	%
	- RPM maximum (overspeed)	125	% of rated
	- RPM minimum (cranking)	50	rpm
	- Full Load range (minimum – maximum)	10 – 25	bar
3	**Ignition System Durability**		
	- Life to replacement for ignition module and harness	80,000	hrs
4	**Reliability**		
	- Ignition System (continuous duty)	6000	MTBF (hrs)
	- Ignition System Reliability (peaking / standby)	3000	MTBF (hrs)
5	**Environmental**		
	- Shock (mechanical)	20 - all three axis	G's
	- Vibration	10	G's (rms)
	- On-engine Temperature Range	-40C to 130C	°C
	- Ambient Temperature	-40C to 48C	°C
	- In-cylinder temperature	2200	°C
	- Fluids Resistance	Ethylene glycol Lube oil	
	- EMI (susceptibility)	200 (30 kHz - 1 GHz)	V/m
	- Altitude	4000	m
	- Humidity	200	grains
	- Drop	1	m
	- Thermal cycles	10,000	cycles
	- Water intrusion	Withstand steam cleaning and high-pressure spray	
	- Vertical Load (Step test)	100	kg
6	**Safety & Regulatory**	CSA Class I Div I	Elec Power
		CSA Class I Div II C&D	Petroleum
		UL Requirements	As developed
7	**Physical**		
	- Size (max of any one piece)	0.015	M^3
	- Weight (max of any one piece)	10	kg
	- Number of cylinders (scalable)	4 – 20	cylinders
	- Power source	24	VDC
8	**Mounting**		
	- System Location	All systems on engine	

	System Profile Element	Continuous-Duty Power Generation Requirements*	Units
9	**Noise**		
	- Rating	SAE J1113	
	- Rating	ISO 13766	
10	**Mean Time to Repair**		
	- Continuous duty	6000	hrs
	- Peaking / standby duty	3000	hrs
11	**Serviceability**		
	- Maximum time for scheduled service	10	minutes / cyl
12	**External Communications Interface**		
	1) Compatible with Engine Diagnostic Tools		
	2) SAE J1939 Communications		
	3) Ability to set timing via the data link		
13	**Predictive Maintenance**		
	1) Ignition system fault code generation		
	2) Prognostics on finite life devices		
14	**So we don't end on 13.**		

* 1.5 MWe engine operating at 1800 rpm.

Appendix B – Equipment Data Sheets

Laser Diode Current Driver Specification Sheet

PARAMETER	MODEL PCX150-25 Drives 1 to 12 Diodes in Series	MODEL PCX150-50 Drives 1 to 25 Diodes in Series	MODEL PCX150-100 Drives 1 to 50 Diodes in Series
PULSE OUTPUT CURRENT			
Amplitude Range	1A to 125A	1A to 150A	1A to 150A
Output Current Resolution	0.1A		
Accuracy At ≥25A Setpoint	1%		
Slow-start Ramp Resolution	0.1A		
Pulse Rise Time	<10μs (10%-90%) (1)		
Pulse Fall Time	<10μs (10%-90%) (1)		
Pulse Width	50μs to 5ms		
Pulse Recurrence Frequency Range	Single Shot to 5KHz		
Maximum Duty Cycle and Average Current	4% at 125A, 6% at 100A, 40% at 15A. The maximum average output power is 150W, and the average current cannot exceed 6A.	2% at 150A, 3% at 100A, 20% at 15A. The maximum average output power is 150W, and the average current cannot exceed 3A.	2% at 150A, 3% at 100A, 20% at 15A. The maximum average output power is 300W, and the average current cannot exceed 3A.
Output Pulse Width Stability	≤±0.5% at 1ms pulse width, 125A at maximum output voltage		
Output Pulse Amplitude Stability	≤±0.5% at 1ms pulse width, 125A at maximum output voltage		
Output Pulse Flatness	≤±0.1% at 1ms pulse width, 125A at maximum output voltage		
Over/undershoot	<5%		
Jitter	<10ns shot-to-shot		
Output Connector	Ribbon Cable, Front Panel		
COMPLIANCE VOLTAGE			
Range	1V to 25V	1V to 50V	1V to 100V
Resolution	1V		
CURRENT LIMIT			
Range	1A to 150A		
Resolution	1A		
TRIGGER IN			
Trigger Input	TTL or +5V ±1V, into 50Ω		
Minimum Trigger Pulse Width	100ns		
Input Trigger Connector	BNC, Front Panel		
SYNC MONITOR OUTPUT			
Sync Monitor	TTL output into high impedance		
Sync Monitor Connector	BNC, Front Panel		
CURRENT MONITOR OUTPUT			
CVR Monitor	50A/1V into 50Ω, typically within 1% of the displayed actual current		
CVR Monitor Connector	BNC, Front Panel		
VOLTAGE MONITOR OUTPUT			
Voltage Monitor	50V/1V into 50Ω, typically within 1% of the actual voltage		
Voltage Monitor Connector	BNC, Front Panel		
GENERAL			
Input AC Power	90-240VAC Nominal, 50/60Hz		
Dimensions (H X W X D)	3 1/4" x 17" x 21"		
Weight	Approx. 22 lbs		
Safety	Complies with CDRH US21 CFR 1040.10		

Laser Power Meter and Detector Head

Laserstar

Versatile Laser Power/Energy Meter

- Two models available: dual and single channel
- Single channel model can be upgraded to dual channel
- Compatible with all Ophir thermopile, pyroelectric, photodiode and RP heads
- Large LCD display
- Backlighting and rechargeable battery
- Screen graphics and statistics (std dev. min, max)
- Analog output
- Built-in RS232 interface
- Log every data point at >1500Hz with pyroelectric heads
- Non-volatile data storage up to 50,000 points
- Laser tuning screen and power log
- Audio sound for laser tuning and low battery
- Statistics package
- GPIB option (IEEE488.1)
- NIST traceable
- CE marked
- Soft keys, menu-driven

The dual channel model enables user to simply plug in any of Ophir's thermal, pyroelectric, photodiode or RP heads and measure two channels independently, or the ratio or difference between them in real time.
Up to 10 data files (54,000 points total) can be stored for onboard review or downloading to computer even if Laserstar has been switched off. The built-in RS232 interface and StarCom PC software allow on-line processing of data or processing previously stored data; results are displayed graphically on a PC.

Digital Power Screen

- CW industrial, medical and scientific lasers
- pW to 20KW with appropriate heads
- Can average over selected period Useful for unstable lasers
- Fast response bar graph

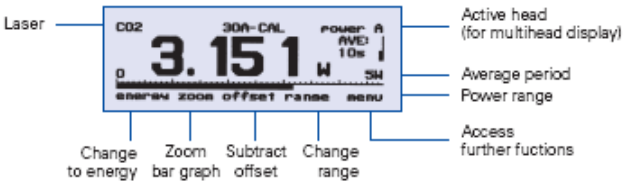

Laser Tuning Screen or Power Log Screen (not shown)

- Maximizing laser power
- User selected time periodand zoom
- Option of audio tune tone

Energy Measurement Screen

- Pyroelectric and thermal heads – single pulse
- Pyroelectric frequency measurement

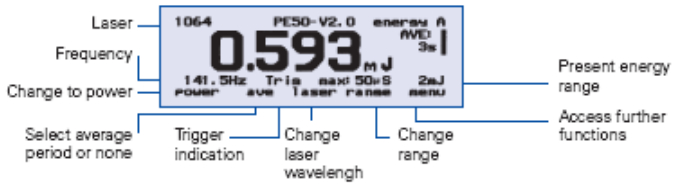

Energy Log Screen

- Pyroelectric heads
- Thermal heads – successive single pulses
- Continuous scroll
- Energy statistics

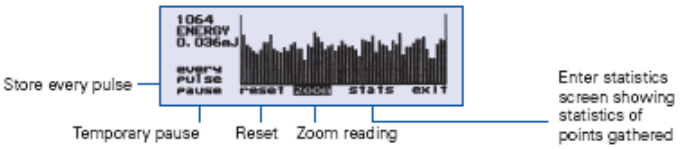

Ratio Screen

- Two independent heads
- Measure ratio, sum, difference
- Normalize one head to the other

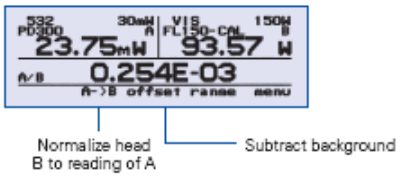

Data Storage and Transmission

- Non-volatile storage of power and energy logging data
- Store in up to 10 files and transmit to
- PC using StarCom Windows program provided

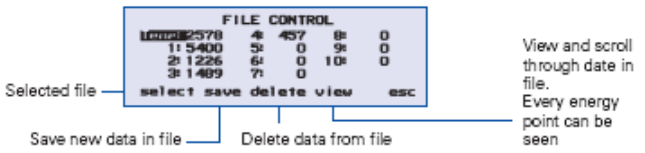

Specifications

Display	High legibility 64 x 240 pixel graphics supertwist LCD with switchable, electroluminescent backlight which operates from charger or battery. Large 17mm digits. Screen refresh 15Hz.
Features	Many screen features including: power with bargraph, energy, average, exposure, frequency, graphs and more. Analog output 1 volt F.S.
Case	Molded high-impact plastic with swivel display and EMI conductive shielding, to allow use even in proximity to pulsed lasers.
Size	Folds to a compact 228mm W x 195mm L x 54mm H.
Battery	Rechargeable 18 hours between charges. Charger (included) also functions as AC adapter.
Multihead option	Two heads can be connected and measure independently, or the ration, sum or difference of the two can be displayed.
Data handling	Built-in RS232 communications at up to 19200 baud. Non-volatile on-board data storage in 10 files of up to 54000 points total. Data can be viewed on-board or transmitted to PC.
Head features	Works with thermal, pyroelectric and photodiode heads. Automatic, continuous, background cancellation with PD300 heads. Submicrojoule and multikilohertz capability with pyroelectric heads.
Program features	User can update calibration information. Preferred startup configuration can be set by user. User can recalibrate power, energy, response time and zero offset.

Ordering Information		
Item	**Description**	**Ophir P/N**
Laserstar	Laserstar single channel universal smart head display for thermal, pyroelectric, photodiode and RP heads	1Z01600
Laserstar 2 Channel	Laserstar with dual channel capability including ration and difference measurement	1Z01601
Laserstar Hard Case	Hard case 46x35x13cm. For display and up to three heads	1Z09101
Laserstar AN adapter	Laserstar analog output adapter. Plugs into D25 output and provides analog output from BNC plug (1 unit supplied with Laserstar)	1Z11004
Laserstar 2 Ch AN Out	Laserstar AN adapter but for dual channel Laserstar (1 unit supplied with Laserstar)	1Z11005
Laserstar 2 Ch Upgrade	Upgrade single channel Laserstar to dual channel version (contact agent for details)	18121
Laserstar Battery Pack	Replacement battery pack for Laserstar	1Z14006
Laserstar RS232 Cable	D25 to D9 cable	1Z10032
Laserstar IEEE Option	IEEE GPIB adapter for Laserstar	18300
Laserstar IEEE Upgrade Kit	Upgrade for existing Laserstar	18301

PE50BB-DIF/PE50DIF-ER

Pulse Energy Measurements 60µJ to 40J, up to 400Hz

Recommended Use: PE50BB-DIF: High energy YAG lasers, general
PE50DIF-ER: High rep rate high energy lasers, Erbium lasers

Special Features: Removable diffuser for high damage threshold

Specifications	PE50BB-DIF				PE50DIF-ER			
	Diffuser out		Diffuser in		Diffuser out		Diffuser in	
Aperture:	Ø46mm		Ø33mm		Ø46mm		Ø33mm	
Spectral Response:	0.19 - 20µm		0.4 - 2.5µm		0.19 - 3µm		0.4 - 3µm	
Surface Reflectivity:	5%		15%		50%		15%	
Calibration Accuracy:	± 3%		± 3%		± 3%		± 3%	
Additional Error with Wavelength:								
193nm	±2%		N.A.		N.A.		N.A.	
248nm	±2%		N.A.		N.A.		N.A.	
400-800nm	±2%		See note a		±2%		See note b	
1064nm	0		0		0		0	
1.5-2.5µm	±2%		See note b		N.A.		See note b	
2.1µm	±2%		0		N.A.		0	
2.94µm	±2%		N.A.		N.A.		0	
10.6µm	±5%		N.A.		N.A.		N.A.	
Damage Threshold:								
<100ns	0.3J/cm²		3J/cm²		0.1J/cm²		1.5J/cm²	
1µs	0.3J/cm²		3J/cm²		0.2J/cm²		3J/cm²	
300µs	1J/cm²		10J/cm²		4J/cm²		40J/cm²	
Linearity:	±2% for>10% of full scale		±2% for >10% of full scale		±2% for >10% of full scale		±2% for >10% of full scale	
Maximum Average Power:	15W		40W		20W		40W	
Max Ave Power Density:	10W/cm²		500W/cm²		10W/cm²		500W/cm²	
Max Pulse Width Setting:	Short	Long	Short	Long	Short	Long	Short	Long
Maximum Pulse Width:	3ms	10ms	3ms	10ms	200µs	1ms	200µs	1ms
Maximum Pulse Rate:	40Hz	10Hz	40Hz	10Hz	400Hz	200Hz	400Hz	200Hz
Energy Scales:	10J to 2mJ	10J to 20mJ	40J to 8mJ	40J to 80mJ	10J to 2mJ	10J to 2mJ	30J to 6mJ	30J to 6mJ
Lowest Measurable Energy:	100µJ	1mJ	500µJ	5mJ	60µJ	100µJ	300µJ	0.5mJ
Noise on Lowest Range:	15µJ	40µJ	80µJ	200µJ	5µJ	10µJ	30µJ	50µJ
Additional Error with Frequency:	±1%	±1%	±1%	±1%	±1%	±1%	±1%	±1%
Cooling	Convection							

Notes: a: Calibrated for 532nm
b: With diffuser installed, head is not calibrated at these wavelengths but provision is made for user calibration

PE50BB-DIF/PE50DIF-ER

DIFFUSER in

DIFFUSER out

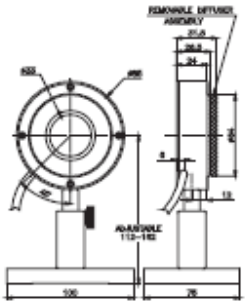

Ordering information		
Item	Description	Ophir P/N
PE50BB-DIF-V2	33/46mm aperture pyroelectric energy meter with broadband absorber and removable diffuser	1Z02866
PE50DIF-ER-V2	33/46mm aperture pyroelectric energy meter with metallic absorber and removable diffuser	1Z02867

High-speed Photo Detectors – DET Series

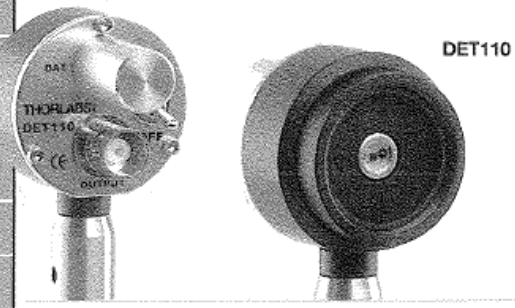

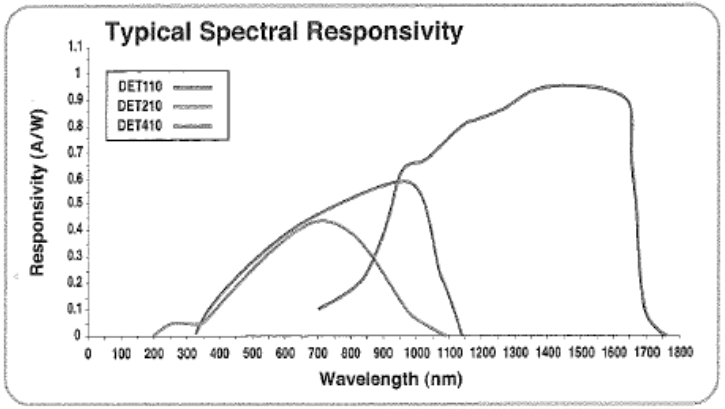

The DET-series detectors are compact, versatile, high-speed optical detectors. Each model comes complete with a fast PIN photodiode and an internal bias battery packaged in a rugged aluminum housing. With a wide bandwidth DC-coupled output, these detectors are ideal for monitoring fast-pulsed lasers as well as DC sources. The direct photodiode anode current is provided on a rear panel BNC. This output is easily converted to a positive voltage using a terminating resistor. We recommend a 50Ω load resistance for fastest response times (see the T4119 shown below).

Each DET housing includes a detachable 1" Optic Mount (SM1T1) for installing Neutral Density Filters, spectral filters and lenses. The optical head is fully compatible with Thorlabs SM1-series and cage plate accessories. Thorlabs has decreased the package diameter to better fit our cage plate assemblies. Also available are fiber optic adapters for use with connectorized fiber.

DET Series Features

- High speed response
- Responsive from 200nm to 1800nm
- Easy to use
- Internal bias battery (included)
- Low profile housings fit in cage plate assemblies
- Includes threaded mount for 1" (25mm) optics
- Compatible with SM1-Series products
- New UV version available

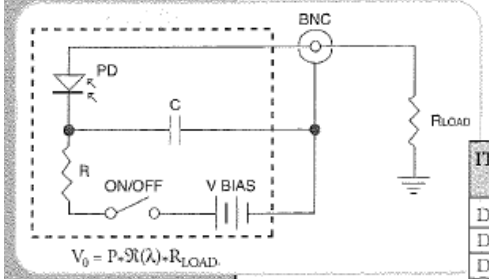

ITEM#	METRIC ITEM	$	£	€	¥	DETECTOR	RISE TIME	ACTIVE AREA	SPECTRAL RANGE
DET110	DET110/M	$ 93.00	£ 65.10	€ 93,00	¥ 15,810	Si PIN	20ns	13mm² (3.6 x 3.6mm)	350-1100nm
DET210	DET210/M	$ 129.00	£ 90.30	€ 129,00	¥ 21,930	Si PIN	1ns	0.8mm² (Ø1mm)	200-1100nm
DET410	DET410/M	$ 249.00	£ 174.30	€ 249,00	¥ 42,330	InGaAs	5ns	0.8mm² (Ø1mm)	800-1800nm
DET710	DET710/M	$ 169.00	£ 118.30	€ 169,00	¥ 28,730	GaP	1/140ns	4.8mm²	150-500nm

Oscilloscope

Digital Phosphor Oscilloscopes

TDS 3012 * TDS 3014 * TDS 3032 * TDS 3034 * TDS 3052 * TDS 3054

This product is discontinued.
View alternative products.

Check product support status.

CHARACTERISTICS

Features
› **Specs**

TDS 3000 Series Electrical Characteristics

	TDS 3012	TDS 3032	TDS 3052	TDS 3014	TDS 3034	TDS 3054
Bandwidth	100 MHz	300 MHz	500 MHz	100 MHz	300 MHz	500 MHz
Channels	2	2	2	4	4	4
Sample Rate on Each Channel	1.25 GS/s	2.5 GS/s	5 GS/s	1.25 GS/s	2.5 GS/s	5 GS/s
Maximum Record Length	10K points on all models					
Vertical Resolution	9-bits on all models					
Vertical Sensitivity (/div)	1 mV-10 V on all models					
Vertical Accuracy	±2% on all models*					
Max Input Voltage (1 megaohm)	150V RMS CAT I on all models					
Position Range	± 5 div on all models					
BW Limit	20 MHz	20, 150 MHz	20, 150 MHz	20 MHz	20, 150 MHz	20, 150 MHz
Input Coupling	AC, DC, GND on all models					
Input Impedance Selections	1 megaohm in parallel with 13 pF, or 50 Ohm					
Time Base:						
Range (/div)	4 ns - 10 s/div	2 ns - 10 s/div	1 ns - 10 s/div	4 ns - 10 s/div	2 ns - 10 s/div	1 ns - 10 s/div
Accuracy	200 ppm	200 ppm	200 ppm	200 ppm	200 ppm	200 ppm
Display Monitor	Color LCD					

* Derated at 0.07%/°C for temperatures above +28°C and below +18°C.

TEC DC Power Supply

HP / Agilent 6632-6634A/B Power Supplies

- Low-noise output
- Linear output regulation
- Precision low current measurement
- High-speed programming, 2 ms (400 µs in fast mode)
- Measured V & I readback over GPIB
- B-Models add RS-232 and rotary knob

Maximum Output	20 V / 5 A	50 V / 2 A	100 V / 1 A
Ripple & Noise (rms/p-p)	0.3 / 3 mV	0.5 / 3 mV	0.5 / 3 mV
Load Regulation	2 mV / 1 mA	4 mV / 1 mA	5 mV / 1 mA
Programming Resolution	5 mV / 1.25 mA	12.5 mV / 0.5 mA	25 mV / 0.25 mA
Model Number	**6632A**	**6633A**	**6634A**

Laser Diode Module Data Sheet

150W QCW Laser Diode Array Submodule
Part Number: ASM05P150

SILVER BULLET™

- Packaged 3 Bar Laser Diode Array
- Easily Soldered to a Heat Exchanger
- Available Wavelengths (790-1550nm)

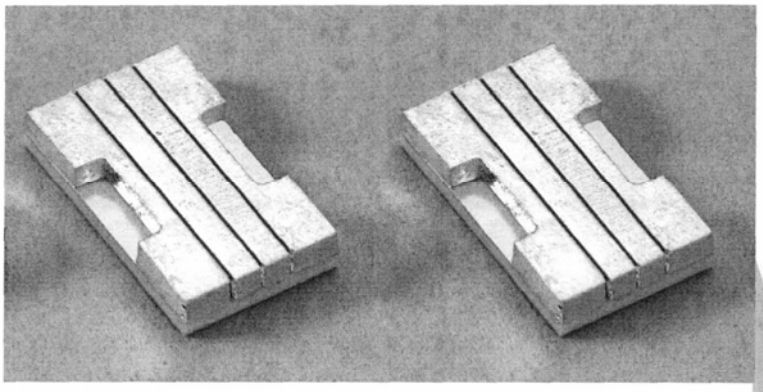

OPTICAL CHARACTERISTICS

PARAMETER	CONDITIONS	MIN	TYP	MAX	UNITS
QCW Peak Power Output	65A, 150 µsec, 1kHz	150	---	---	W
Operating Current	150W at 25°C Heat Sink	---	55	65	A
Threshold Current	25°C Heat Sink	---	13	16	A
Center Wavelength	150W at Heat Sink	---	808	---	nm
Wavelength Tolerance	150W at 25°C Heat Sink	---	± 3	---	nm
Spectral Width FWHM	150W at 25°C Heat Sink	---	2.0	2.5	nm
Wavelength Shift	---	0.23	0.25	0.27	nm/°C
Beam Divergence FWHM	---	---	40x10	42x12	° x °

ELECTRICAL CHARACTERISTICS

PARAMETER	CONDITIONS	MIN	TYP	MAX	UNITS
Series Resistance	25°C Heat Sink	---	0.018	0.030	ohms
Operating Voltage	25°C Heat Sink, 150W	---	6.6	8.1	V

ABSOLUTE MAXIMUM RATINGS

PARAMETER	CONDITIONS
Forward Current	70A
Reverse Current	25µA
Reverse Voltage	3V
Operating Temperature Range (2)	-20°C to 50°C
Storage Temperature Range	-40°C to 85°C

NOTES
(1) These specifications apply for operation at 808nm. Other wavelengths available upon request.
(2) A dry nitrogen environment should be provided by the user when storing and operating at temperatures below ambient dew point.

NORTHROP GRUMMAN
Space Technology
Cutting Edge Optronics
20 Point West Blvd. St. Charles, MO 63301 636.916.4900 p 636.916.4994 f
www.st.northropgrumman.com/ceolaser st-ceolaser-info@ngc.com

MECHANICAL CHARACTERISTICS

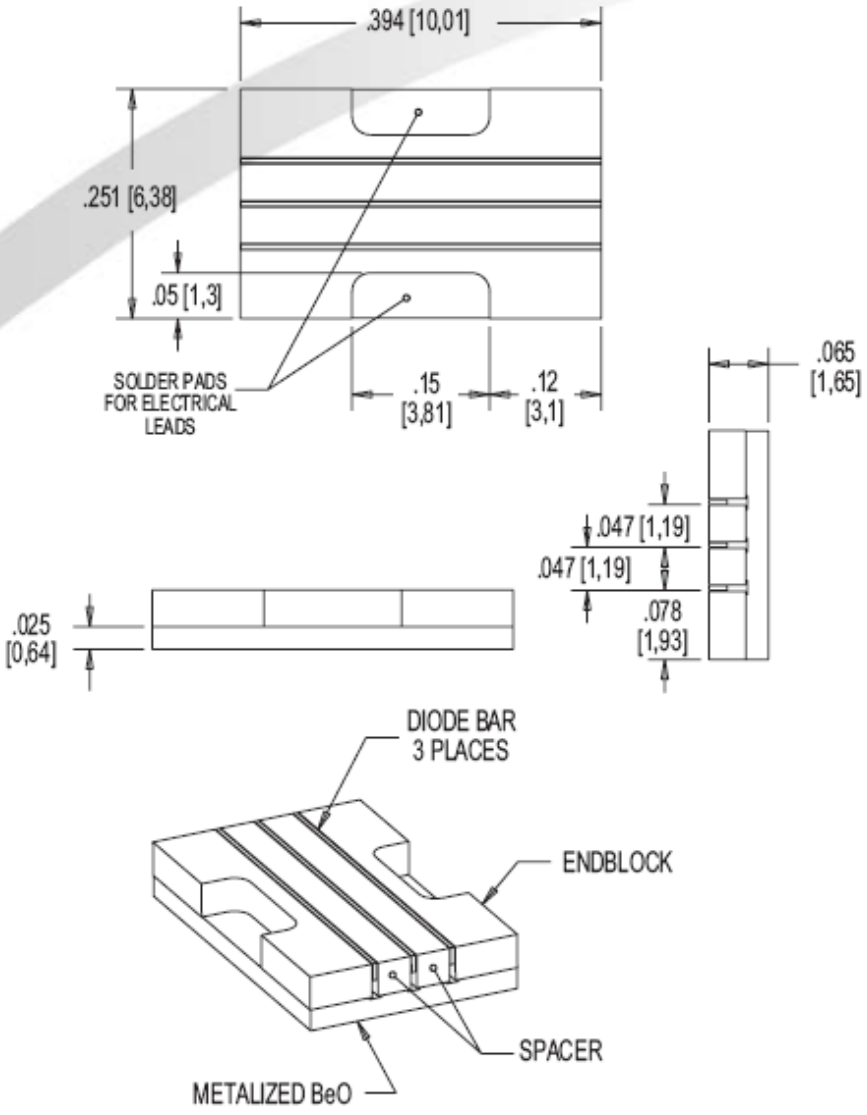

Thermoelectric Coolers

877.825.3006
1894 Highway 50E, Ste. 4304
Carson City, Nevada 89701
sales@kryotherm.com

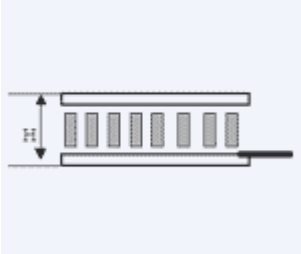

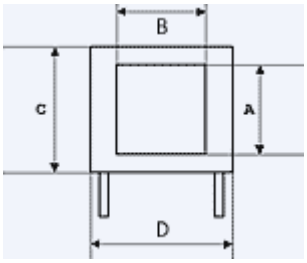

P/N	Imax (A)	Qmax (W)	Umax (V)	ΔTmax (K)	A mm	B mm	C mm	D mm	H mm
TB-35-0,6-1,0	1.7	4.4	4.3	69	6.0	12.0	6.0	12.0	2.75

Thermally Conductive Epoxy

EPOXY TECHNOLOGY

Product Information Sheet

MATERIAL ID:	**EPO-TEK® H70E-4**
Date: 04/2005	**Per:**
Rev: III	
Material Description:	A two component, thermally conductive, electrically insulating, thixotropic epoxy for circuit assembly applications at the PCB level.
Number of Components:	Two
Mix Ratio:	1:1
Cure Schedule (minimum)	120°C/15 Minutes - 80°C/1 Hour - 50°C/12 Hours
Specific Gravity:	--- Part A: 1.61 Part B: 2.02
Pot Life:	2.5 Days
Shelf Life:	One year at room temperature

NOTE: Container(s) should be kept closed when not in use. Filled systems should be stirred thoroughly before mixing and prior to use

---

MATERIAL CHARACTERISTICS: *To be used as a guide only, not as a specification. Data below is not guaranteed. Different batches, conditions and applications yield differing results; Cure condition: 150°C/1 hour*
* denotes test on lot acceptance basis

PHYSICAL PROPERTIES:			
*Color (before cure):	Part A: Dark Grey Part B: Dark Grey	Weight Loss:	
*Consistency:	Smooth thixotropic paste	@ 200°C:	0.57 %
*Viscosity (23°C):		@ 250°C:	1.49 %
@ 10 rpm	20,000 - 40,000 cPs	@ 300°C:	3.09 %
Thixotropic Index:	3.2	Operating Temp:	
*Glass Transition Temp:	≥ 80 °C (Dynamic Cure 20—200°C /ISO 25 Min; Ramp -10—200°C @ 20°C/Min)	Continuous:	- 55°C to + 200°C
		Intermittent:	- 55°C to + 300°C
Coefficient of Thermal Expansion (CTE):		Storage Modulus @ 23°C:	416,749 psi
Below Tg:	17 x 10^{-6} in/in°C	Ion Content:	
Above Tg:	77 x 10^{-6} in/in°C	Cl^-:	
Shore D Hardness:	67	NH_4^+:	
Lap Shear @ 23°C:	1,070 psi	Na^+:	
Die Shear @ 23°C:	≥ 5 Kg / 1,700 psi	K^+:	
Degradation Temp:	432 °C	*Particle Size:	≤ 20 microns

ELECTRICAL AND THERMAL PROPERTIES:			
Thermal Conductivity:	0.57 W/mK	Dielectric Constant (1kHz):	4.81
Volume Resistivity @ 23°C:	≥ 2.5x10^{13} Ohm-cm	Dissipation Factor (1kHz):	0.0179

OPTICAL PROPERTIES:			
Spectral Transmission:	N/A	Index of Refraction:	N/A

EPOXY TECHNOLOGY, INC.
14 FORTUNE DRIVE, BILLERICA, MA 01821 (978) 667-3805, FAX (978) 663-9782
WEB SITE: www.epotek.com

Nd:YAG Data Sheet (VLOC)

Nd:YAG Laser Crystals

VLOC grows large diameter neodymium doped yttrium aluminum garnet (Nd:YAG) crystals using the Czochralski technique. The use of high quality starting materials for crystal growth, whole boule interferometry, and precise measurement of Nd concentration using transmission spectroscopy and fluorescence lifetime measurements, assures that each crystal will perform to customer specifications. Full documentation is available for every shipment, and VLOC maintains traceability on all material produced, from finished laser material back to starting oxides. State-of-the-art fabrication and coating processes enable VLOC to provide consistently reliable finished product. Detailed physical and optical properties for Nd:YAG are listed on page 59.

VLOC produces a wide variety of finished laser rods, as well as supplying Nd:YAG material. Our general Nd:YAG production capabilities include:

- Rod sizes from 2mm to 12.5mm in diameter and from 1mm to 180mm in length
- Nd dopant concentrations between 0.6 and 1.3%
- Polished and AR coated barrels
- Slabs with apertures of up to 7mm X 15mm
- MIL-C-675C adhesion, abrasion and humidity resistance
- Damage threshold of over 15 J/cm^2
- A wide variety of anti-reflection, partial reflector, high reflector and dichroic coatings
- Premium grade Nd:YAG, with lower wavefront distortion, is available upon request

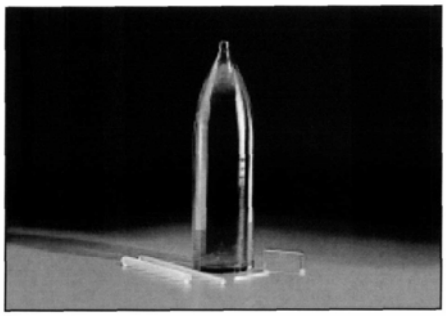

Coatings

Several different high reflector, anti-reflection and dichroic optical coatings can be applied to Nd:YAG rods, depending upon their exact configuration and use. For flashlamp-pumped lasers with external end mirrors, the anti-reflection coating #2010 (page 51) is typically specified. For end-pumped crystals the dichroic coating #1015 (page 55) is used. See page 50 for an overview of the optical coatings provided by VLOC.

To order a finished Nd:YAG laser rod, specify the parameters listed on page 38. Typical finished part specifications and tolerances are listed below.

Specifications:

Material	Nd:YAG
Dopant concentration	As specified ±0.1%
Diameter Tolerance	+0.0, -0.025mm
Length Tolerance	±0.5mm
Parallelism	<10 arc seconds
Perpendicularity	<5 arc minutes
Chamfer	0.13 ± 0.08mm @ 45°
Barrel Finish	Ground or Polished
Wavefront Distortion	
<7mm diameter	<λ/10 per inch @ 632.8nm
≥7mm diameter	<λ/8 per inch @ 632.8nm
Surface Flatness	λ/10 @ 632.8nm
Surface Quality	10/5
Clear Aperture	95%

Nd:YAG Data Sheet (Scientific Materials)

Scientific Materials Corp.

SMC Home

- > About SMC
- > Products and Services
- > Technical Sales Offices
- > Research
- > Exhibitions
- > News Releases
- > Employment
- > Contact Us

Nd:YAG

Neodymium doped Yttrium Aluminum Garnet (Nd:YAG) lases at 1064 nm. Nd:YAG is grown by the Czochralski growth process and is fabricated into laser rods, slabs and other gain media components.

Advantages

- High Efficiency, Low Threshold, High Gain
- High Optical Quality, Low Loss at 1064nm
- Good Mechanical and Thermal Properties

Applications

- These components are used in solid-state lasers for a variety of applications covering the industrial, medical, scientific and military fields.

Material Properties	
Crystal Structure	Cubic
Y_{3+} Site Symmetry	D_2
Lattice Constant	a = 12.013 A
Standard Orientation	<111>
Molecular Weight	593.7 g 1/mol
Melting Point	1965° C
Density	4.56 g /cm^3
Thermal Expansion	7.8 x 10^{-6}° C^{-1}
Thermal Conductivity	13 W m^{-1} k^{-1}
Specific Heat (Cp)	0.140 cal g^{-1}° C^{-1}
MOHS hardness	8.2
Young's Modulus	335 Gpa
Tensil Strength	2 Gpa
Thermal Shock Resistance	8 W/cm
Refractive Index @ 632.8nm	1.83
Y_{3+} Site	1.38 x 10 (20) /cm^3
Al_{3+} Site (IV)	1.38 x 10 (20) /cm^3
Al_{3+} Site (VI)	0.92 x 10 (20) /cm^3

Cr:YAG Data Sheet

Cr^{4+}:YAG

Passive Q-Switching has advantages of passive (no necessary for the input power), compact, low cost and easy to manufacture and operate. Cr:YAG is an excellent passive Q-switch crystals for Nd and Yb doped laser whose wavelength is in the range of 900-1200 nm, especially for the diode pumped or lamp pumped Nd:YAG, Nd:YLF and Yb:YAG. Due to Cr:YAG has chemically stable, durable, UV resistant, good thermal conductivity and high damage threshold (> 500 MW/cm2), it will replace traditional materials, such as, LiF, organic Dye and color centers for passive Q-switching application.

Foctek provide a wide variety of finished crystals, our general Cr^{4+}:YAG production Capabilities include:

1) Cr^{4+} Dopant Concentration: 0.5 mol% ~ 3 mol%
2) Aperture: 2x2 ~ 14x14mm
3) Length: 0.1 ~ 12mm
4) Initial Transmission: 10% ~ 99%
5) Coating: Antireflective

Typical Specification and Tolerance:

1) Dimension Tolerance: (W ± 0.1mm) x (H ± 0.1mm) x (L + 0.2mm/-0.1mm)
2) Flatness: λ/8 @ 633nm
3) Scratch/Dig Code: 10/5 Scracth/dig per MIL-O-13830A
4) Parallelism: better than 20 arc seconds
5) Perpendicularity: 5 arc minutes
6) Wavefront Distortion: less than λ/8 @ 633nm
7) Clear Aperture: > 90% central area

Notes:

To inquiry or order a finished Cr^{4+}:YAG crystals, please specify the specification listed above in particular the size, initial transmission and coatings.

Physical and Optical Properties:

Chemical Formula	$Cr^{4+}:Y_3Al_5O_{12}$
Crystal Structure	Cubic garnet
Recovery Time	8.5 μs
Hardness	Mohs 8.5
Density	4.56g/cm^3
Orientation	[100]+/-10°
Thermal Conductivity	12.13w/m/k
Refractive Index	1.82 @ 1064nm

Base state absorption cross section	$\sigma s_1=4.3x10^{-18}cm^2$
Emission state absorption cross section	$\sigma s_2=8.2x10^{-19}cm^2$
Fluorescence lifetime	3.4us

Output Coupler and High Reflection Mirror Data Sheet

Nd:YAG Laser Mirrors

Y

Optical Components and Assemblies

- Contact a CVI applications engineer for OEM mirror mounts and system integrations capabilities
- Mirror mounts are available ▶ 357

Substrate Material	UV grade fused silica if λ < 450nm BK7 glass if λ ≥ 450nm
S1 Surface Figure	λ/10 at 633nm before coating
S1 Surface Quality	10-5 CVI Laser Quality defined on page **430**
S2 Surface Quality	Commercial polish
Diameter Tolerance	+ 0.00mm, – 0.25mm
Thickness Tolerance	± 0.25mm
Wedge	≤ 5 minutes
Chamfer	0.35mm at 45° typical
Concentricity	≤ 0.05mm
Radius Tolerance	± 0.5%
Coating Technology	Electron beam multilayer dielectric
Adhesion and Durability	Per MIL-C-675C. Insoluble in lab solvents.
Clear Aperture	Exceeds central 85% of diameter
Damage Threshold	20J/cm², 20ns, 20Hz; 1MW/cm², CW at 1064nm
Coated Surface Figure	λ/10 at 633nm on select substrates

How To Order

Y1 – 1537 – 45S – 5.00CC

Product Code	Laser	Wavelength
Y1	Nd:YAG	1064nm
Y2	Nd:YAG	532nm
Y3	Nd:YAG	355nm
Y4	Nd:YAG	266nm
Y5	Nd:YAG	213nm
Y13	Nd:YAG	1319nm

Size Code	Diameter	Thickness						
0537	0.500"	0.375"	1025	1.000"	0.250"	1940	50.0mm	10.0mm
0643	15.0mm	11.0mm	1032	1.000"	8.0mm	2037	2.000"	0.375"
0737	0.750"	0.375"	1037	1.000"	0.375"	3050	3.000"	0.500"
0924	25.0mm	6.0mm	1537	1.500"	0.375"	4050	4.000"	0.500"

Angle of Incidence in Degrees with Polarization

0	Normal incidence
45S	45 degrees, S polarization
45P	45 degrees, P polarization
45UNP	45 degrees, Unpolarized

Radius of Curvature (m) (CC=concave, CX=convex, omit for flat mirror) ▶ **196, 428**

0.025	0.10	0.25	0.75	1.5	4.0	7.0	10.0
0.05	0.15	0.30	1.0	2.0	5.0	8.0	15.0
0.075	0.20	0.50	1.2	3.0	6.0	9.0	20.0

0° designs

45° designs

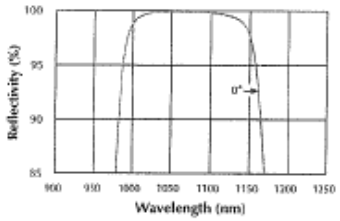

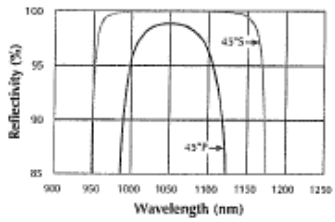

Reflectivity vs. Wavelength of Y1 Series 1064nm Nd:YAG Laser Mirror for 0° and 45° incidence angle designs.

Min. Reflectance > 99.5% at 0°
> 99.0% at 45°UNP

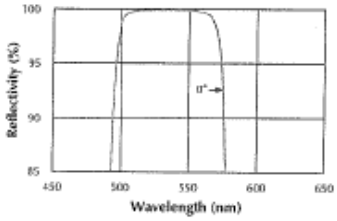

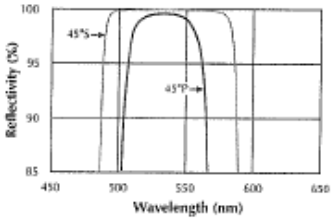

Reflectivity vs. Wavelength of Y2 Series 532nm Nd:YAG Laser Mirror for 0° and 45° incidence angle designs.

Min. Reflectance > 99.5% at 0°
> 99.0% at 45°UNP

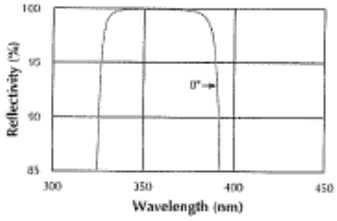

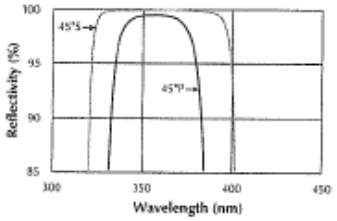

Reflectivity vs. Wavelength of Y3 Series 355nm Nd:YAG Laser Mirror for 0° and 45° incidence angle designs.

Min. Reflectance > 99.5% at 0°
> 99.0% at 45°UNP

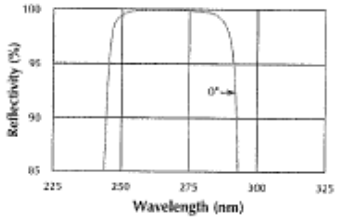

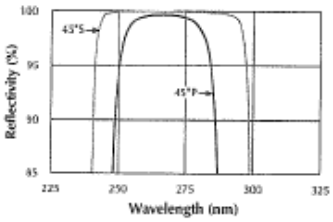

Reflectivity vs. Wavelength of Y4 Series 266nm Nd:YAG Laser Mirror for 0° and 45° incidence angle designs.

Min. Reflectance > 99.5% at 0°
> 99.0% at 45°UNP

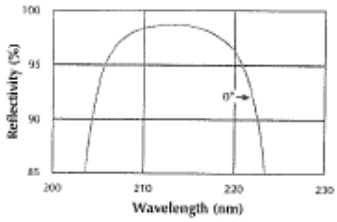

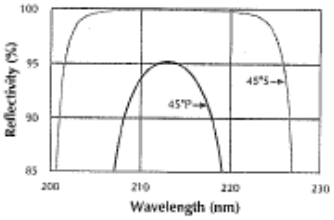

Reflectivity vs. Wavelength of Y5 Series 213nm Nd:YAG Laser Mirror for 0° and 45° incidence angle designs.

Min. Reflectance > 98.0% at 0°
> 97.0% at 45°UNP

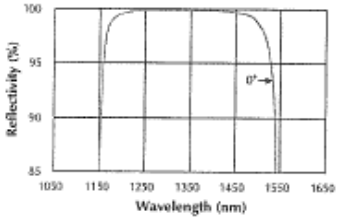

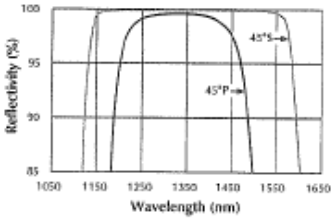

Reflectivity vs. Wavelength of Y13 Series 1319nm CW Nd:YAG Laser Mirror for 0° and 45° incidence angle designs.

Min. Reflectance > 99.5% at 0°
> 99.0% at 45°UNP

Mirror Mount Mechanical Drawing

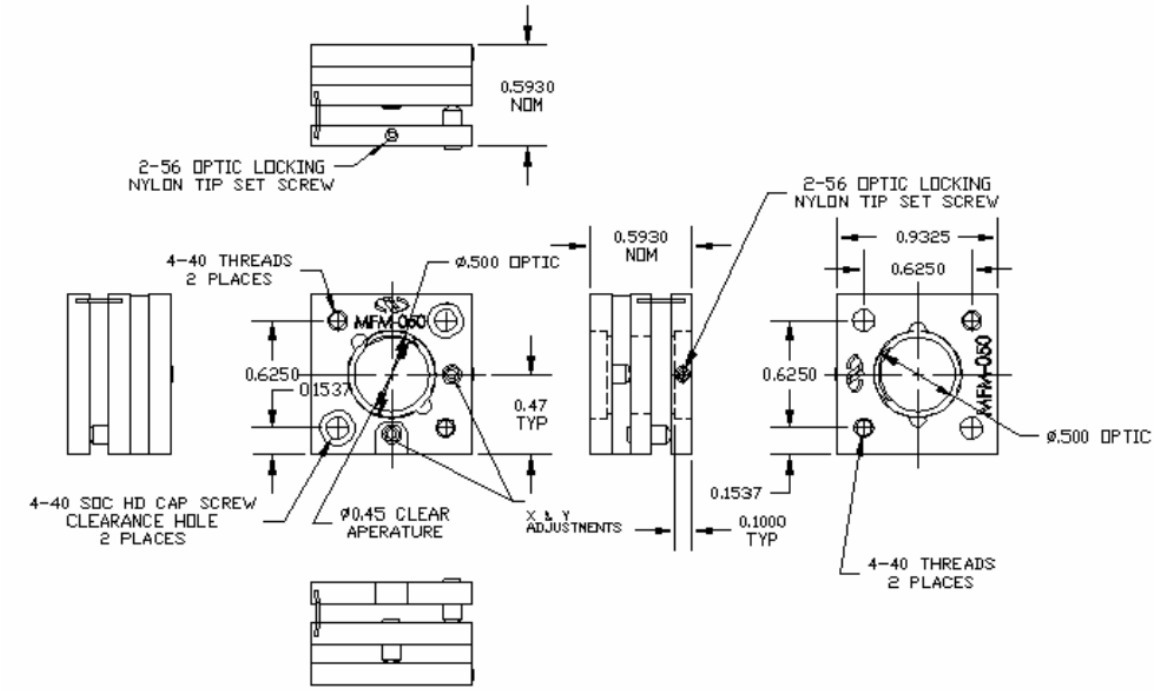

Piezoelectric Pressure Transducer

THE THRILL OF SOLUTIONS.

AVL

Sensors

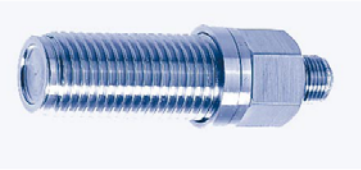

GU21D
Transducer Uncooled
Art. No. GG0558

This pressure transducer opens a new dimension for cylinder pressure transducers with an M7 thread. The GU21D's key advantage is that although it is more compact than a conventional 10mm cooled transducer, it offers almost the same measurement precision. The influence on the measurement signal due to deformation of the mounting bore has been minimised by a newly designed transducer housing.

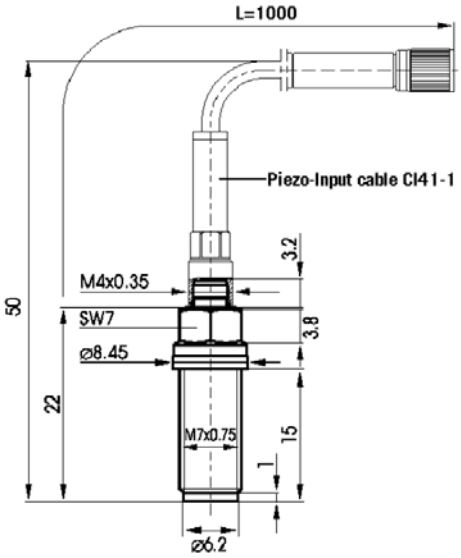

Dimensions

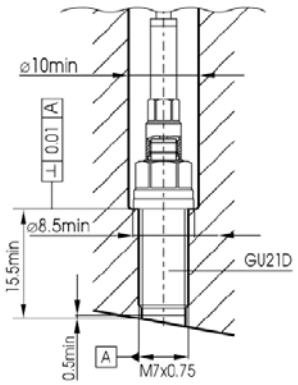

Example for direct installation

Last Update: January 2002 1

GU21D Transducer Uncooled

Standard Specifications

Measuring Range	0...250 bar (3625 psi), 25 MPa
Lifetime	> 10^8 load changes
Overload	300 bar (4350 psi), 30 MPa
Sensitivity (nominal)	35 pC/bar (2.41 pC/psi), 350 pC/MPa
Linearity	< ±0.3 (0.1)* % FSO
Natural Frequency	85 kHz
Acceleration Sensitivity	< 0.002 bar/*g*
Shock Resistance	> 2000 *g*
Operating Temperature Range	up to 400°C (750°F)
Thermal Sensitivity Shift	20...400°C <±2% 200...300°C <±0.5%
Insulation Resistance at 20°C (68°F)	> 10^{13} Ω
Capacitance	8 pF
Mass (without cable)	6 grammes
Mounting Torque	3 Nm (for adaptors refer to drawings)

Thermodynamic Specifications

Cyclic Temperature Drift	< ±0.4 (0.2)* bar
Load Change Drift	
Max. Zero-line Gradient dp/dt	1,5 mbar/ms
Permanent Zero-line Deviation	8 bar
IMEP-Stability	< 2.5 %

*) Selected transducers GU21D (Art. No. GG0682) with specifications in ( ) can be supplied upon request.

Scope of Supply

1 Transducer GU21D
1 Piezo-Input cable CI41-1 plus Coupling CC41, fitted
2 Spare O-rings for cable
1 Gasket SG03 (fitted) + 1 Spare gasket
1 Protection cap
1 Calibration sheet
1 Specification sheet
1 Brief description

GU21D Transducer Uncooled

Accessories

Cables and Couplings	CI41-1, CI42-1 (metal mesh), CC41, E124-10
Cable-Mounting Tool	TC01
Gasket	SG03
Dismounting Tool for gasket	TT17
Dummy	DG04
Removal Tool	TD01
Adaptor	AH06
Machining Tool	MS22 (MD22, MT21), MS24 (MD24, MT31)
Mounting Tool	TS03 (TT11, TT02)
Mounting Spray	SF01

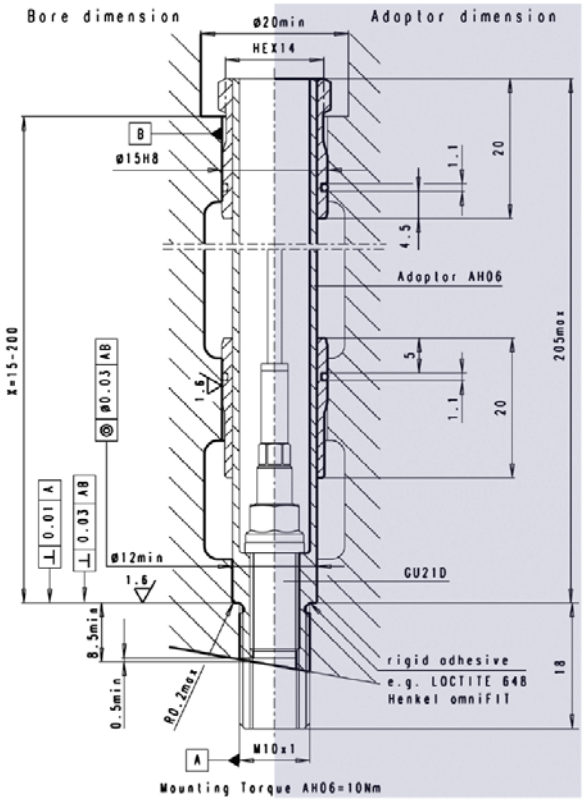

Installation by means of Adaptor AH06

Chemiluminescent NO_x Analyzer

Thermo Environmental Instruments

MODEL 42C HIGH LEVEL

Chemiluminescent NO-NO_2-NO_X Analyzer

The *Model 42C High Level* (42-HL) combines the superior optical, mechanical, and chemical characteristics of its predecessor, the *Model 42H*, with an enhanced electronics package and user interface. The outcome is a powerful, easy-to-use, chemiluminescent based analyzer capable of measuring oxides of nitrogen from parts per billion (ppb) to 5000 parts per million (ppm).

Thermo Environment Instruments design engineers have introduced a user interface which easily guides one through operation of the *Model 42C-HL*. This is accomplished via 4 line by 20 character Vacuum Fluorescent Display and simple layout of easy-to-use function keys. The end result is a combination of self explanatory display messages and intuitive function entries.

User programmable software capabilities allow individual measurement range settings to be stored in memory for subsequent recall and NO, NO_2, No_X hourly average storage for up to one month. Extended troubleshooting diagnostics now provide instantaneous indication of instrument operating parameter status including: Pressure, Flow, DC Supply Voltages, Internal Temperate, Reaction Chamber Temperature, PMT Operating Voltage and Converter Temperature.

KEY FEATURES

- Wide Dynamic Range
- Electronic Diagnostic Transducers
- Multi-Line Alpha Numeric Display
- Dedicated Communications Processor
- Remote Performance Diagnostics
- Oil-Less Vacuum Pump

MODEL 42C HIGH LEVEL SPECIFICATIONS

Range	0 - 10, 20, 50, 100, 200, 500, 1000, 2000, 5000 ppm
Noise	25 ppb
Detection Limit	50 ppb
Zero Drift (24 hour)	50 ppb
Span Drift (24 hour)	± 1% full scale
Rise Fall Times (0 - 90%)	2.5 seconds NO Mode; 5.0 seconds NO_x Mode
Linearity	+ 1% full scale
Sample Flow Rate	25 cc/min. with Bypass 2 SCFH
Vacuum	28.5" Hg
Power Requirements	90 - 110, 105 - 125, 210 - 250 VAC 500 Watts
Physical Dimensions	17" (W) x 8 3/4" (H) x 23" (D)
Weight	70 lbs., including pump
Outputs	selectable voltage 0 - 10 mv, 100 mv, 1v, 5v, 10v, 4 - 20 mA Isolated (optional)

FLEXIBLE COMMUNICATIONS

- Bidirectional Addressable RS-232 Communication Port
- Analog Data Outputs with Selectable Voltages
- Isolated Current Outputs (optional)
- Analog Status Outputs (optional)
- Instrument Diagnostics, local and remote

Model 42C High Level - FLOW SCHEME

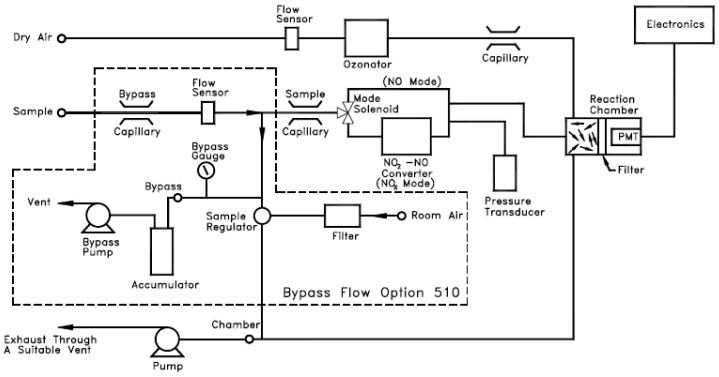

Model 42C-HL Standard Configuration

The *Model 42C-HL* standard plumbing configuration is used in applications where ample amount of sample is present. The sample should be at a continuous stable flow. The analyzer is allowed to extract the sample as needed by use of a vented manifold system (atmospheric dump).

Model 42C-HL Regulated Bypass System Option

The *Model 42C HL* regulated bypass system (enclosed by dotted lines) is used when the sample must be transported over a long distance. It is also used when an unstable flow is being provided. The regulated bypass system provides make-up air through the sample regulator in case of lack of sample to the reaction chamber. This unique feature avoids instrument drift due to pressure changes.

For Price and Delivery Information, Contact:

Thermo Environmental Instruments

8 West Forge Parkway
Franklin, MA 02038 USA

Tel: 508 520-0430 Fax: 508 520-1460
E-mail:thermo@thermoei.com Web Site: www.thermoei.com

CO, CO_2 Analyzers

HORIBA ENVIRONMENTAL AND PROCESS INSTRUMENTS

Products | Contact | Financing | Service | Company | News

VIA-510 Gas Analyzer

Features

- Selectable response time
- Selectable outputs: 0–1 VDC or 4–20 mA
- Digital outputs indicate malfunctions or calibration failure)
- Measures CO, CO_2, NO_x, SO_2, CH_4, C_2H_4, and NO_2; others upon request

Overview

The VIA-510 series of general-purpose gas analyzers provide continuous monitoring of concentrations of the specific sample gas. The analyzers can be operated from controls on the front panel or by commands from a remote computer. Measurement results are displayed on the front panel and are available to remote data logging systems through an industry-standard interface.

The VIA-510 series can be used for a wide variety of analyses and tests, such as industrial process control and composition analysis, environment-related atmospheric and fixed-source emissions monitoring, and automobile emission analysis.

These analyzers use the infrared absorption method which offers superior sensitivity, selectivity, and stability. They are compact and compatible with a variety of OEM analysis equipment.

A high level of sensitivity is achieved through the use of a dual-beam NDIR analysis method. Horiba's patented chopper motor assures continuous long-term stable monitoring. The analysis mechanism and the amplifier are combined in a single unit. The highly accurate performance makes the analyzers suitable for process monitoring and control.

Specifications

Standard Ranges

Gas	Minimum	Maximum
Carbon monoxide (CO)	0-50 ppm	0-100%
Carbon dioxide (CO_2)	0-50 ppm	0-100%
Nitrogen monoxide (NO)	0-100 ppm	0-100%
Sulfer dioxide (SO_2)	0-100 ppm	0-100%
Methane (CH_4)	0-100 ppm	0-100%
Ethene (C_2H_4)	0-100 ppm	0-100%

Nitrous Oxide (N_2O)	0-100 ppm	0-100%

Performance

Lowest detection limit:	1.0 ppm
Repeatability:	± 1% of full-scale
Response time:	Selectable
Zero drift:	< 1% (full scale) per day
Span drift:	< 2% (full scale) per week

Flame Ionization Analyzer for Total Hydrocarbon Analysis

HORIBA ENVIRONMENTAL AND PROCESS INSTRUMENTS

Products | Contact | Financing | Service | Company | News

FIA-510 Total Hydrocarbon Analyzer

Features

- Few moving parts–superior reliability
- Efficient detector reduces hydrogen fuel use to a minimum
- Sensitive and stable
- Selectable response time
- Multiple ranges available
- Digital I/O and isolated analog output

Overview

The FIA-510 provides continuous measurement of concentrations of total hydrocarbons (THC). The analyzer uses a hydrogen flame ionization detection method and has few moving parts. It performs accurate measurement for long periods and is highly stable.

The FIA-510 can be used for a wide variety of analyses and tests, such as industrial process control and composition analysis, environment-related atmospheric and fixed-source emissions monitoring, and automobile emission analysis.

The FIA-510 can be operated from controls on the front panel or by commands from a remote computer. Measurement results are displayed on the front panel and are available to remote data logging systems through an industry-standard interface.

The instrument may be calibrated automatically or manually and is packaged to fit into a standard 19-inch rack. It is designed to work with the Horiba ESF-510 sample conditioning unit.

Performance Specifications

Ranges:	0-50, 100, 200, 500, 1000, 5000, 10,000, and 30,000 ppm C as propane
Lowest detection limit:	1.0 ppm
Response time:	< 60 seconds
Zero drift:	± 1% full scale per day
Span drift:	± 2% fulle scale per day

New Wave Research Tempest-20 Nd:YAG laser

Tempest Specifications

The following table shows the Tempest specifications for the different models that are available. The specifications are subject to change without notice.

Energy[1]	1064 nm	532 nm	355 nm	266 nm
Tempest-10 Hz	200 mJ	100 mJ	50 mJ	30 mJ
Tempest-20 Hz	200 mJ	100 mJ	50 mJ	30 mJ
Tempest-30 Hz	180 mJ	90 mJ	40 mJ	20 mJ
Tempest-300-10 Hz	300 mJ	180 mJ	75 mJ	45 mJ
Tempest-300-20 Hz	200 mJ	130 mJ	NA	NA
Energy stability[2]	± 2 %	± 3.5 %	± 6 %	± 7 %
Pulse width[3]	3-5 ns	3-5 ns	3-5 ns	3-5 ns
Beam divergence[4]	< 1 mrad	< 1 mrad	< 1 mrad	< 1 mrad
Beam pointing[5]	< 200 µrad	< 200 µrad	< 200 µrad	< 200 µrad
Jitter	± 0.5 ns	± 0.5 ns	± 0.5 ns	± 0.5 ns
Beam Diameter - Tempest 10, 20, 30	~5mm	~4.5mm	~4 5mm	~4.5mm
Beam Diameter - Tempest 300-10, 20	~6mm	~5 5mm	~5.5mm	~5 5mm

1. Optical losses due to optional attenuator will reduce maximum energy by 10%
2. Pulse-to-pulse for 98% of shots after 30 minute warm up
3. Full width half maximum
4. Full angle for 86% of the energy, $1/e^2$ point
5. Full angle for 86% of the energy, $1/e^2$ point

Appendix C - Laser Assembly and Data Collection Procedure List

1. Turn on and initialize equipment (Alignment Laser, Oscilloscopes, Current Pulser, Power Meter, Beam Analyzer, Camera, Frame Grabber, and Laptop).
2. Clean laser rod optical surfaces with a swab or lens tissue saturated with spectroscopic grade acetone or methanol.
3. Install laser rod into laser chassis and tighten nylon set screws on each end of the laser rod ensuring one screw is tighter than the other to allow for linear thermal expansion.
4. Clean diode pump modules with a swab or lens tissue saturated with spectroscopic grade acetone or methanol.
5. Mount diode pump modules onto laser chassis using two screws each.
6. Secure diode module electrical interconnections.
7. Connect output cable from current pulser to diode module electrical terminals ensuring proper positive and negative orientation.
8. Mount laser chassis to optical bench.
9. Align laser spark plug with the output of the alignment laser, ensure that alignment laser beam enters and exits the center of the laser rod faces so the laser output will be collinear with the alignment laser beam.
10. Install mirror mounts.
11. Clean output coupler and high reflection mirrors with lens tissue saturated with spectroscopic grade acetone or methanol.
12. Install and align one mirror at a time ensuring the back reflections from the mirrors line up with the exit aperture of the alignment laser.

13. Set current pulse repetition rate to 1 Hz.
14. Set current pulse output pulse width to 600 microseconds.
15. Enable laser door interlock.
16. Start current pulser with highest current test set point (60A set point 57A actual).
17. Monitor output while modifying alignment for maximum CW output.
18. When maximum CW output found rotate photodiode into the beam path of the alignment laser to measure the leakage photons through the rear mirror of the test laser.
19. Insert Cr:YAG crystal(s) into Q-switch pocket.
20. Ensure optical faces of the crystal are perpendicular to the optical axis.
21. Monitor output (energy and pulse width if any produced) and rotate crystal until maximum output pulse energy is produced.
22. Make minor mirror adjustments to ensure maximum output.
23. Ensure single temporal mode output (An example of the difference between single and multiple temporal output modes is shown in Figure 8.1).

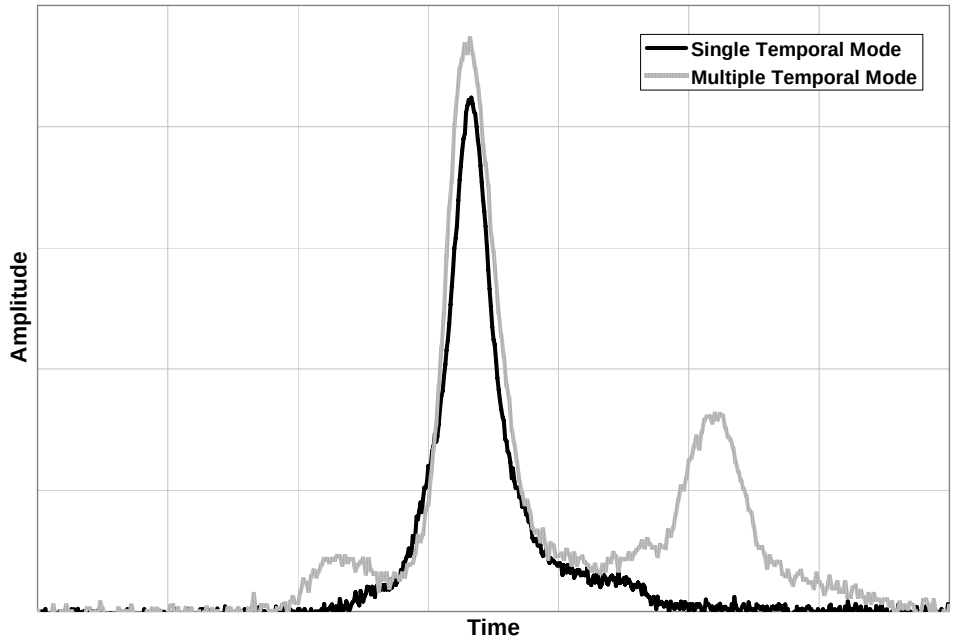

Figure B-1: Comparison of single and mutiple temporal mode output

24. Adjust alignment or crystal rotation to ensure single temporal mode output.
25. If no output is produced at this point increase the input pulse width until output is produced, do not exceed one millisecond input pulse width to avoid thermal damage to the diode pumps.
26. Check OSC2, if more than one output pulse is produced over the course of the pump cycle reduce the input pulse width to limit the output to one pulse per pump cycle.
27. Fill out optical and electrical parameters on data collection sheet.
28. Record output pulse energy.
29. Measure the maximum output pulse amplitude on OSC1, move on screen cursors to the half maximum on either side of the output pulse.
30. Record output pulse width.
31. Move the on screen cursors to the beginning of the pump cycle and to the output pulse.

32. Record output pulse delay.
33. Align and initialize beam analyzer.
34. Ensure output beam profile is aligned properly.
35. Run the automatic beam analysis software.
36. Record M^2 value.
37. Reduce input current to the next set point.
38. Adjust input pulse width if needed.
39. Repeat steps 27 through 38 until all three current set points are recorded.
40. Increase the input current to the highest setting.
41. Repeat steps 26 through 40 until all three input current replications are completed for this particular optical parameter combination.
42. Remove Q-switch.
43. Repeat steps 19 through 42 until all three Q-switch initial transmission values have been examined for this particular combination of output coupler reflectivity and laser rod Nd concentration.
44. Remove output coupler.
45. Repeat steps 12 through 44 until all Q-switch values in combination with all output coupler reflectivity values have been examined with this particular laser rod Nd concentration value.
46. Disassemble laser in reverse order and replace laser rod with next test rod.
47. Repeat steps 2 through 46 until all laser rods have been tested.

Appendix D - Laser Chassis and Spark Plug Adaptor Drawings

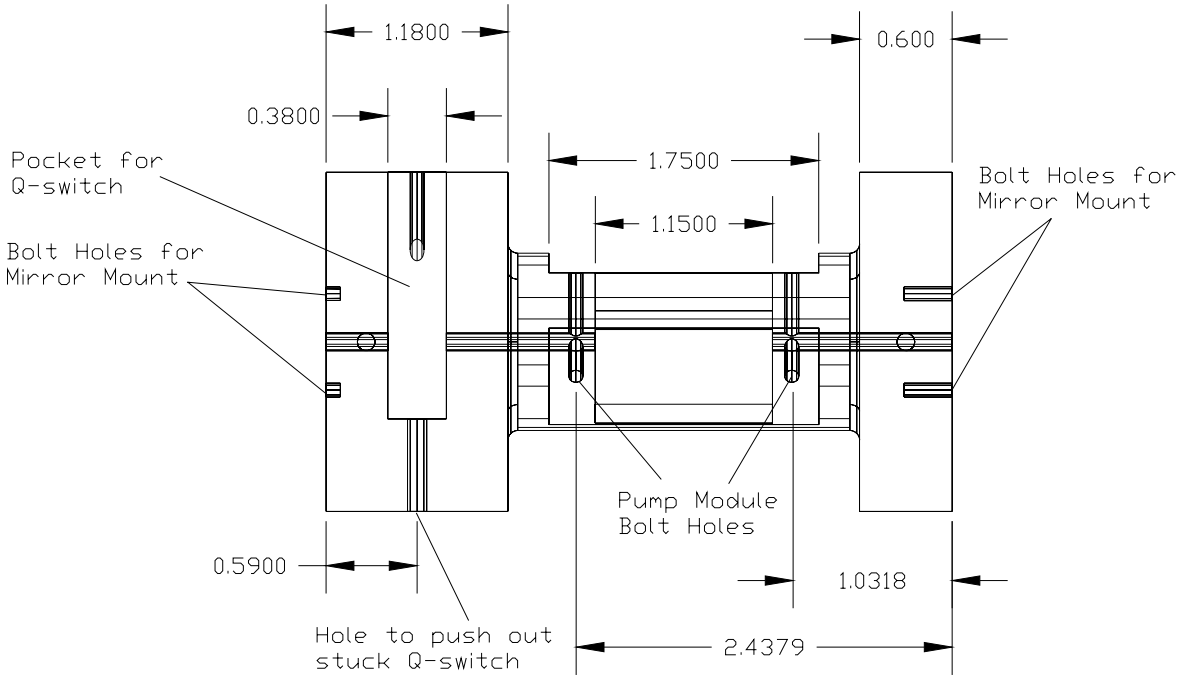

Figure C-1: Side view schematic of laser spark plug chassis (scale in inches)

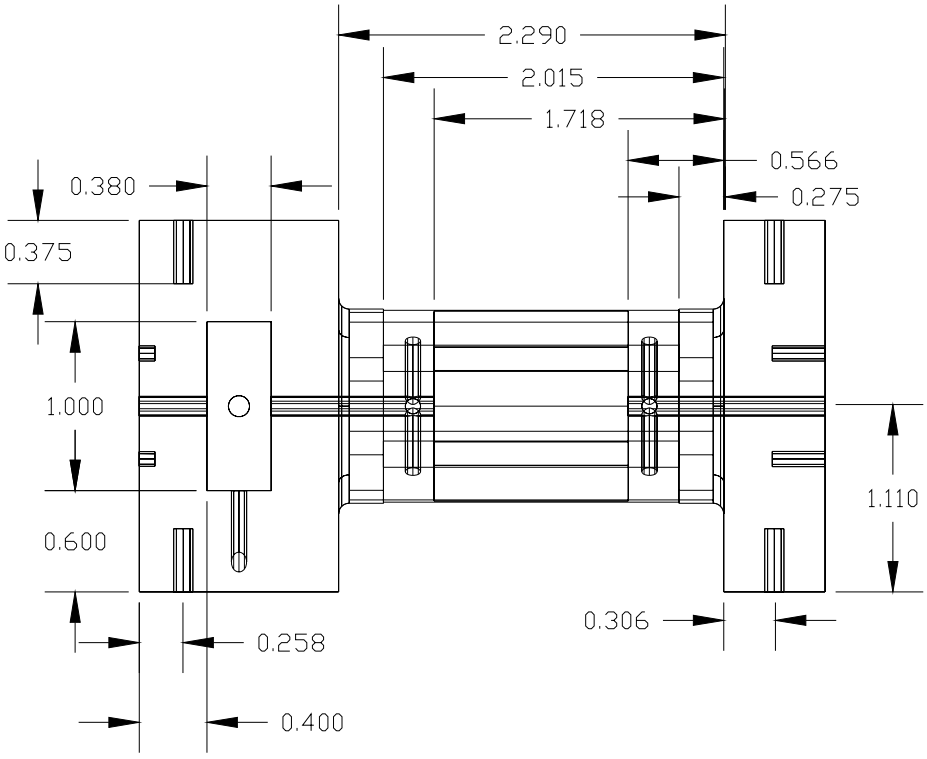

Figure C-2: Top view of the laser chassis (scale in inches)

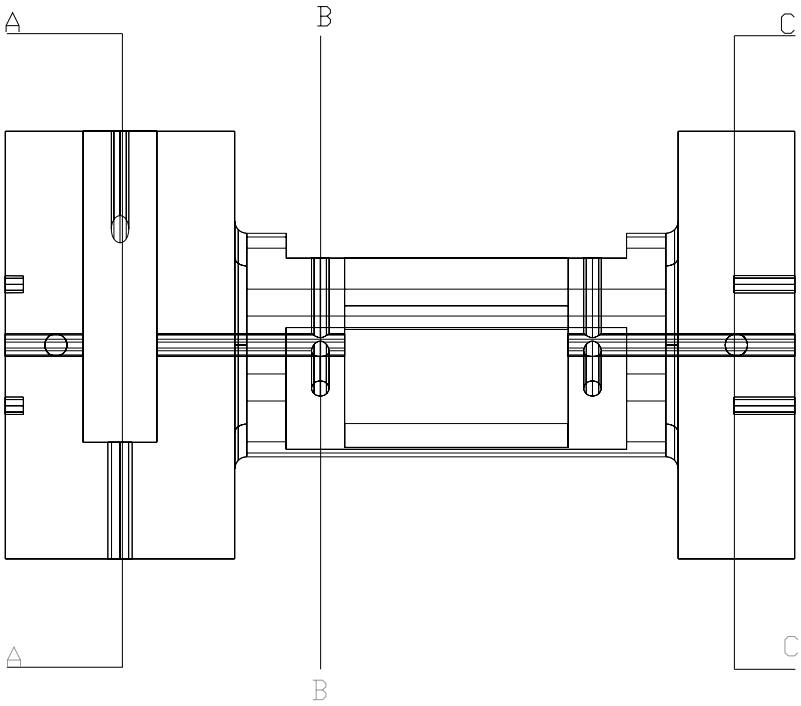

Figure C-3: Schematic showing sections of the laser chassis

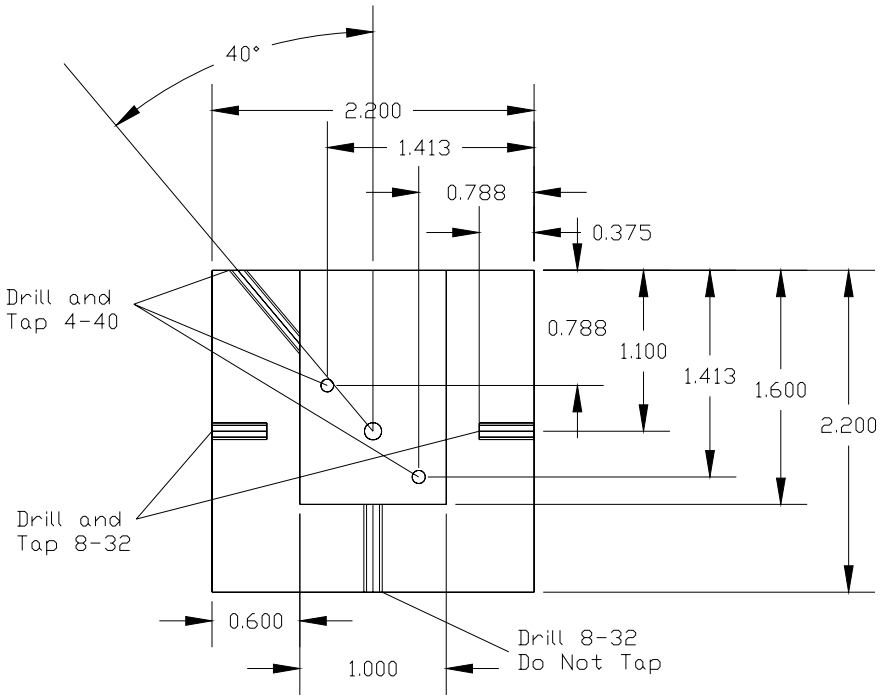

Figure C-4: Section A-A of the laser chassis (scale in inches)

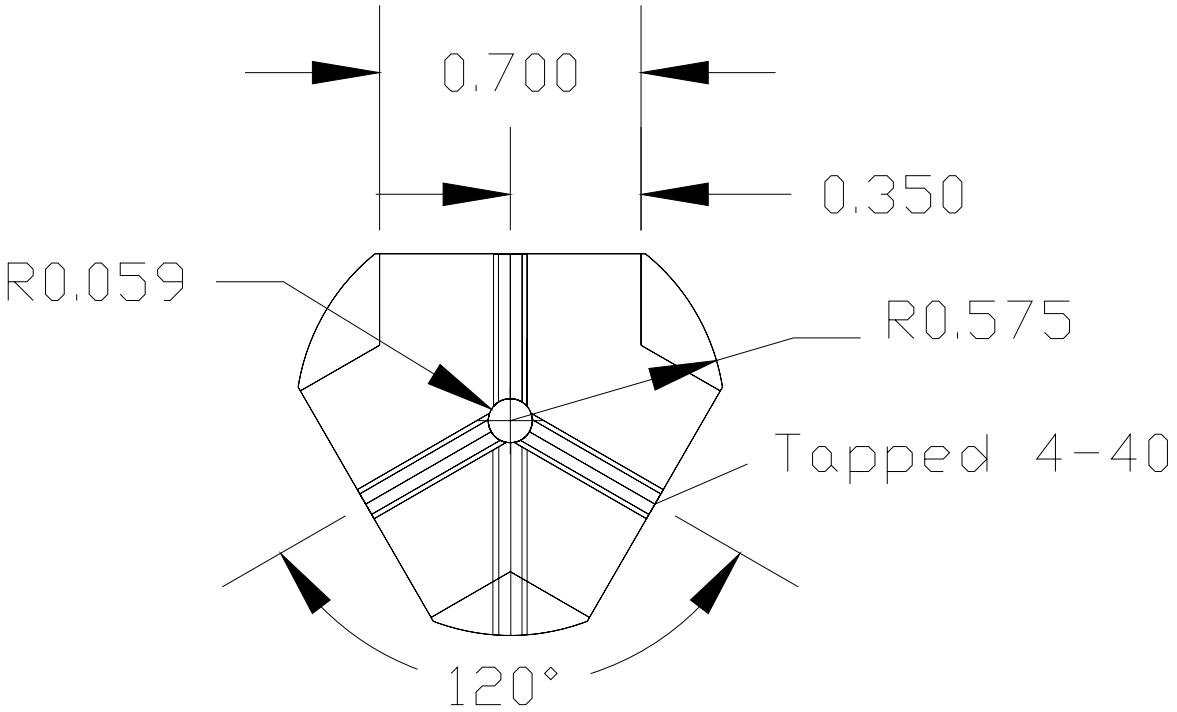

Figure C-5: Section B-B of the laser chassis (scale in inches)

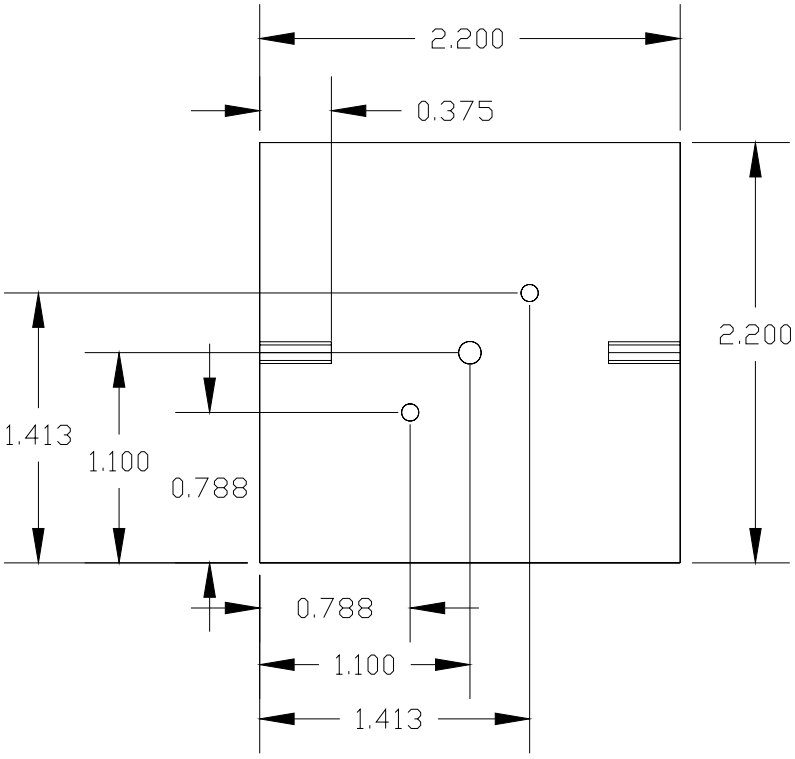

Figure C-6: Seciton C-C of the laser chassis (scale in inches)

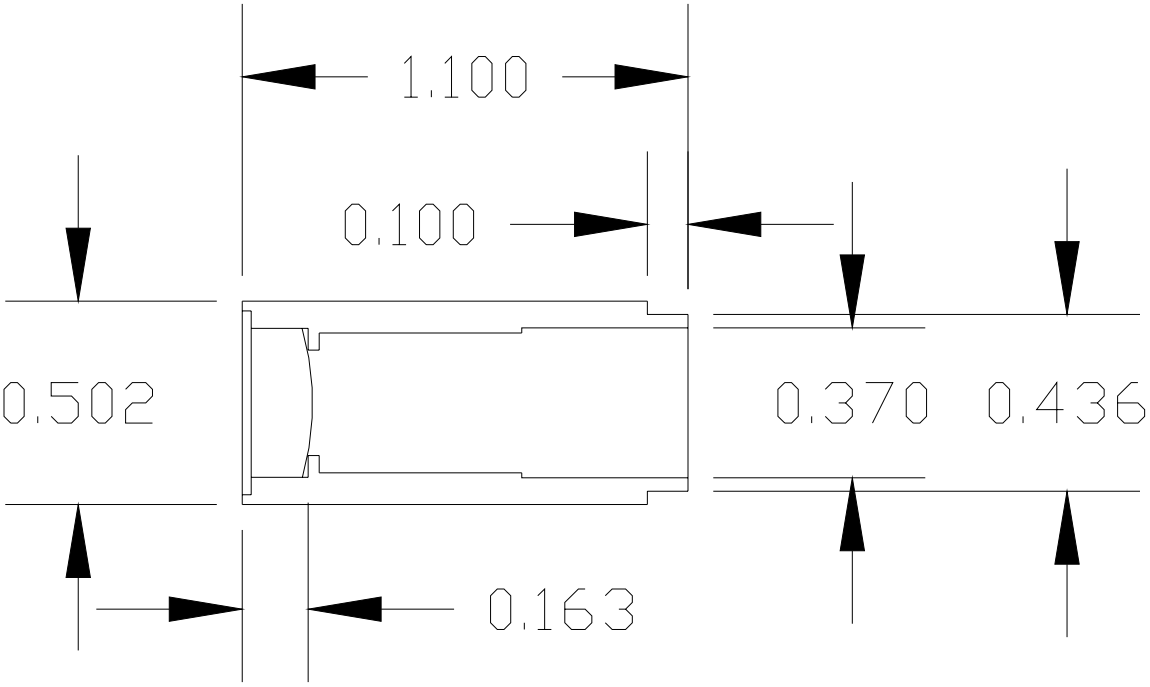

Figure C-7: Sapphire Window/Lens Assembly 3E Labs P/N SPI-150-100 (scale in inches)

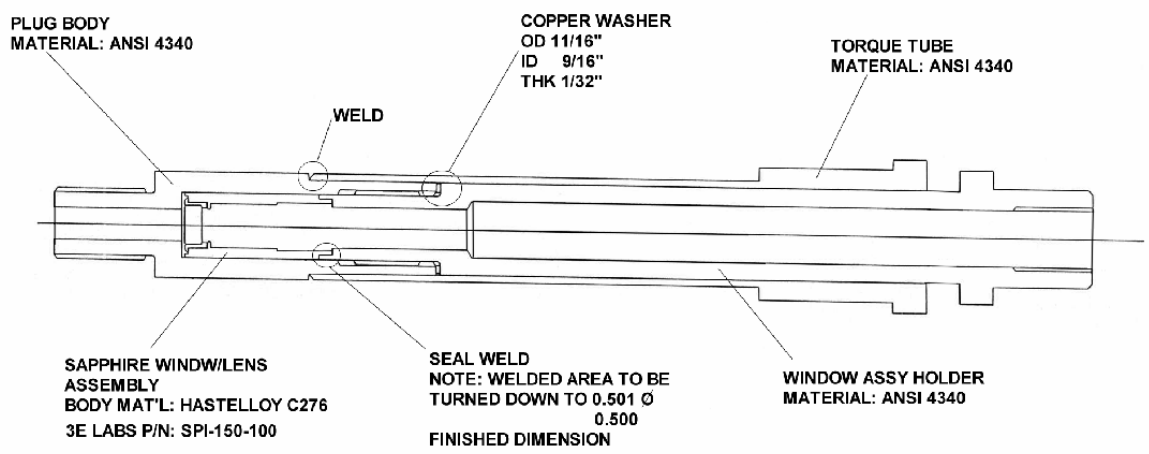

Figure C-8: Laser optical access spark plug adaptor assembly drawing (scale in inches)

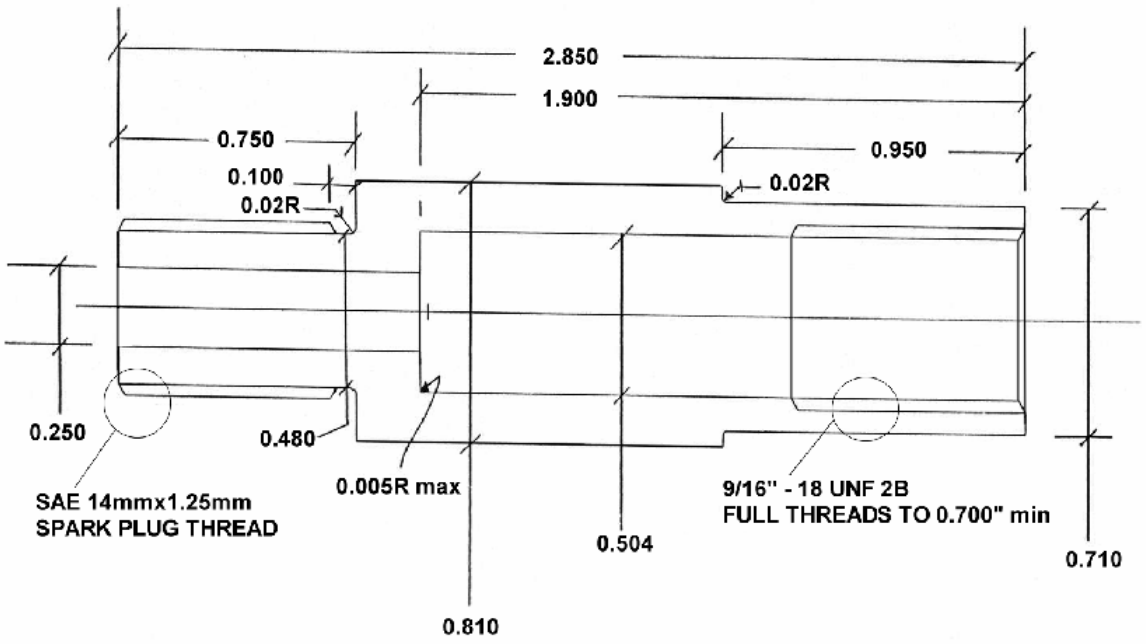

Figure C-9: Plug adaptor body, material ANSI 4340 (scale in inches)

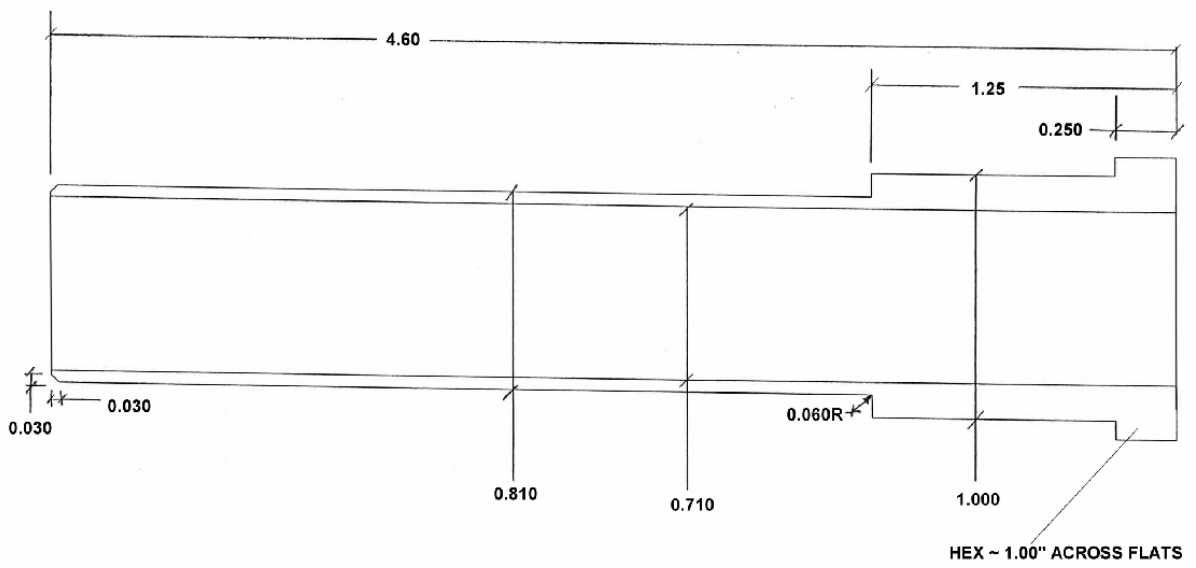

Figure C-10: Torque tube, material ANSI 4340 (scale in inches)

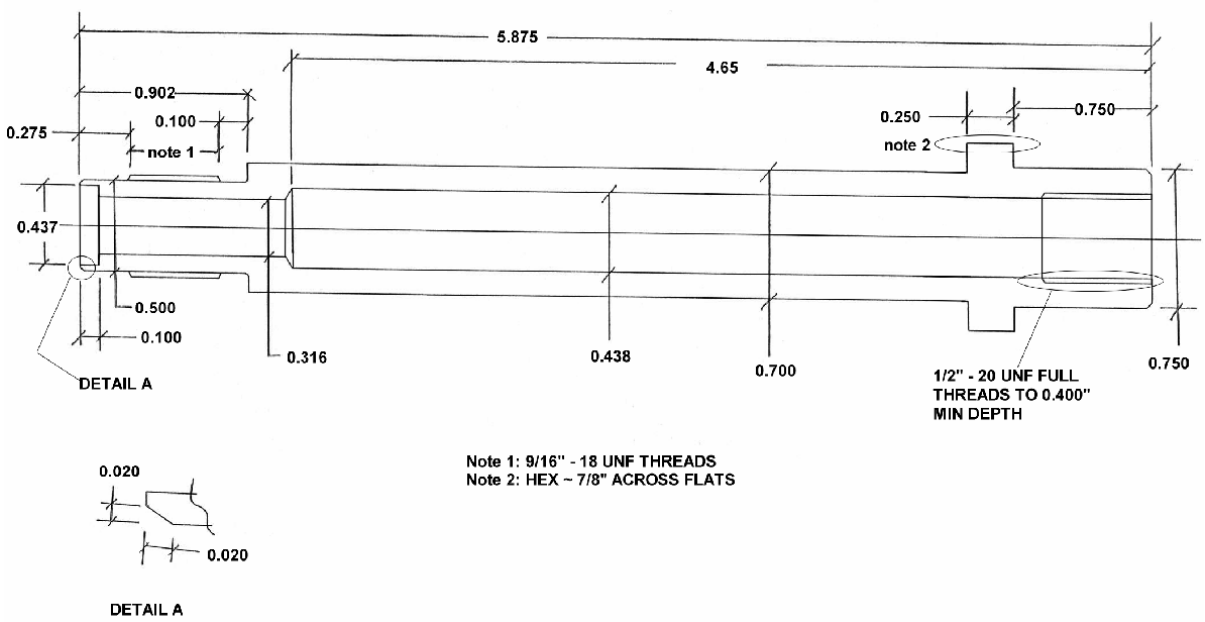

Figure C-11: Window/lens assembly holder, material ANSI 4340 (scale in inches)

Appendix E – Laser Design Experimental Data

This section lists the raw data collected during the optical experimentation. Each recorded value is listed as well as the averaged and calculated values. The dashes indicate that no output was produced.

OC	QSW	ND	Freq
flat 30	40+80=32	0.35	1

Meas. No.	Pump time	current	voltage	Eout	tp	Qd	M2-x	M2-y	spark
1	631.00	57.00	34.00	27.60	9.40	480.00	6.61	10.48	y
2	-	-	-	-	-	-	-	-	n
3	-	-	-	-	-	-	-	-	n
4	650.00	57.00	34.00	27.95	9.60	490.00	6.39	10.55	y
5	-	-	-	-	-	-	-	-	n
6	-	-	-	-	-	-	-	-	n
7	650.00	57.00	34.00	28.18	10.00	484.00	6.48	10.74	y
8	-	-	-	-	-	-	-	-	n
9	-	-	-	-	-	-	-	-	n

Averages

1	643.67	57.00	34.00	27.91	9.67	484.67	6.49	10.59
2	-	-	-	-	-	-	-	-
3	-	-	-	-	-	-	-	-

PowerE	PowerO	PeakPower	Intensity @ 10mm fL	DL Intensity @ 10mm fL
1938.00	1007.76	2887241	4.2756E+11	1.8027E+13
-	-	-	-	-
-	-	-	-	-

OC	QSW	ND	Freq
flat 30	40+90=36	0.35	1

Meas. No.	Pump time	current	voltage	Eout	tp	Qd	M2-x	M2-y	spark
1	450.00	57.00	34.00	23.47	11.00	378.00	6.74	8.15	y
2	600.00	53.00	34.00	23.01	10.80	466.00	6.29	6.69	y
3	-	-	-	-	-	-	-	-	n
4	450.00	57.00	34.00	23.32	11.60	352.00	6.60	8.56	y
5	600.00	53.00	34.00	23.24	11.00	460.00	6.11	7.43	y
6	-	-	-	-	-	-	-	-	n
7	450.00	57.00	34.00	23.32	11.60	352.00	6.25	8.21	y
8	600.00	53.00	34.00	23.03	11.40	460.00	6.37	8.92	y
9	-	-	-	-	-	-	-	-	n

Averages

1	450.00	57.00	34.00	23.37	11.40	360.67	6.53	8.31
2	600.00	53.00	34.00	23.09	11.07	462.00	6.26	7.68
3	-	-	-	-	-	-	-	-

PowerE	PowerO	PeakPower	Intensity @ 10mm fL	DL Intensity @ 10mm fL
1938.00	1007.76	2050000	3.0018E+11	1.2800E+13
1802.00	937.04	2086747	3.0556E+11	1.3029E+13
-	-	-	-	-

OC	QSW	ND	Freq
flat 30	40	0.35	1

Meas. No.	Pump time	current	voltage	Eout	tp	Qd	M2-x	M2-y	spark
1	450.00	57.00	34.00	20.73	8.60	302.00	8.12	8.42	y
2	450.00	53.00	34.00	20.10	9.20	366.00	7.63	6.39	y
3	450.00	50.00	34.00	20.16	9.00	438.00	8.16	9.03	y
4	450.00	57.00	34.00	20.59	9.60	298.00	7.60	6.67	y
5	450.00	53.00	34.00	20.22	10.00	360.00	7.90	6.81	y
6	450.00	50.00	34.00	20.19	9.20	438.00	8.05	6.51	y
7	450.00	57.00	34.00	20.50	10.00	300.00	7.73	7.28	y
8	450.00	53.00	34.00	20.56	9.60	362.00	7.98	8.87	y
9	450.00	50.00	34.00	20.22	9.60	434.00	7.93	8.14	y

Averages

1	450.00	57.00	34.00	20.61	9.40	300.00	7.82	7.46
2	450.00	53.00	34.00	20.29	9.60	362.67	7.84	7.36
3	450.00	50.00	34.00	20.19	9.27	436.67	8.05	7.89

PowerE	PowerO	PeakPower	Intensity @ 10mm fL	DL Intensity @ 10mm fL
1938.00	1007.76	2192199	2.2402E+11	1.3688E+13
1802.00	937.04	2113889	2.1602E+11	1.3199E+13
1700.00	884.00	2178777	2.2265E+11	1.3604E+13

OC	QSW	ND	Freq
flat 40	32	0.35	1

Meas. No.	Pump time	current	voltage	Eout	tp	Qd	M2-x	M2-y	spark
1	400.00	57.00	34.00	22.75	8.20	360.00	11.00	14.17	y
2	550.00	53.00	34.00	23.90	8.20	386.00	6.96	10.83	y
3	550.00	50.00	34.00	23.09	9.20	472.00	8.86	9.09	y
4	400.00	57.00	34.00	21.88	7.80	344.00	6.23	10.90	y
5	550.00	53.00	34.00	22.72	8.00	426.00	10.91	11.21	y
6	600.00	50.00	34.00	23.90	8.40	430.00	5.15	5.95	y
7	400.00	57.00	34.00	23.52	8.60	312.00	6.83	9.06	y
8	500.00	53.00	34.00	23.47	9.00	378.00	7.34	10.41	y
9	500.00	50.00	34.00	23.21	9.60	466.00	6.85	7.83	y

Averages

1	400.00	57.00	34.00	22.72	8.20	338.67	8.02	11.38
2	533.33	53.00	34.00	23.36	8.40	396.67	8.40	10.82
3	550.00	50.00	34.00	23.40	9.07	456.00	6.95	7.62

PowerE	PowerO	PeakPower	Intensity @ 10mm fL	DL Intensity @ 10mm fL
1938.00	1007.76	2770325	2.6892E+11	1.7297E+13
1802.00	937.04	2781349	2.6999E+11	1.7366E+13
1700.00	884.00	2580882	2.5053E+11	1.6115E+13

OC	QSW	ND	Freq
flat 40	36	0.35	1

Meas. No.	Pump time	current	voltage	Eout	tp	Qd	M2-x	M2-y	spark
1	400.00	57.00	34.00	21.54	8.60	252.00	5.99	7.85	y
2	400.00	53.00	34.00	20.33	8.20	296.00	5.44	8.22	y
3	500.00	50.00	34.00	21.45	8.40	334.00	6.39	9.41	y
4	400.00	57.00	34.00	20.91	8.00	246.00	5.86	8.22	y
5	400.00	53.00	34.00	20.62	8.00	290.00	5.21	7.34	y
6	400.00	50.00	34.00	20.13	9.60	336.00	5.97	9.42	y
7	400.00	57.00	34.00	20.94	8.00	248.00	5.19	7.88	y
8	400.00	53.00	34.00	20.96	9.60	290.00	5.40	8.10	y
9	400.00	50.00	34.00	19.38	10.40	354.00	5.66	8.91	y

Averages

1	400.00	57.00	34.00	21.13	8.20	248.67	5.68	7.98
2	400.00	53.00	34.00	20.64	8.60	292.00	5.35	7.89
3	433.33	50.00	34.00	20.32	9.47	341.33	6.01	9.25

PowerE	PowerO	PeakPower	Intensity @ 10mm fL	DL Intensity @ 10mm fL
1938.00	1007.76	2576829	4.9870E+11	1.6089E+13
1802.00	937.04	2399612	4.6440E+11	1.4983E+13
1700.00	884.00	2146479	4.1541E+11	1.3402E+13

OC	QSW	ND	Freq
flat 40	40	0.35	1

Meas. No.	Pump time	current	voltage	Eout	tp	Qd	M2-x	M2-y	spark
1	300.00	57.00	34.00	18.92	9.00	218.00	5.56	8.37	y
2	300.00	53.00	34.00	20.30	9.00	258.00	5.88	7.63	y
3	350.00	50.00	34.00	19.33	10.80	294.00	6.24	8.86	y
4	300.00	57.00	34.00	20.13	9.20	244.00	5.53	8.39	y
5	300.00	53.00	34.00	19.61	11.40	286.00	4.79	7.41	y
6	350.00	50.00	34.00	19.96	9.60	332.00	5.01	6.40	y
7	300.00	57.00	34.00	19.01	9.40	236.00	5.14	9.21	y
8	300.00	53.00	34.00	19.18	9.40	274.00	4.02	8.09	y
9	350.00	50.00	34.00	18.84	10.00	316.00	4.98	9.17	y

Averages

1	300.00	57.00	34.00	19.35	9.20	232.67	5.41	8.66
2	300.00	53.00	34.00	19.70	9.93	272.67	4.90	7.71
3	350.00	50.00	34.00	19.38	10.13	314.00	5.41	8.14

PowerE	PowerO	PeakPower	Intensity @ 10mm fL	DL Intensity @ 10mm fL
1938.00	1007.76	2103623	4.4877E+11	1.3135E+13
1802.00	937.04	1982886	4.2301E+11	1.2381E+13
1700.00	884.00	1912171	4.0793E+11	1.1939E+13

OC	QSW	ND	Freq
flat 50	40+80=32	0.35	1

Meas. No.	Pump time	current	voltage	Eout	tp	Qd	M2-x	M2-y	spark
1	450.00	57.00	34.00	20.22	9.00	292.00	8.36	10.12	y
2	450.00	53.00	34.00	20.94	8.40	352.00	8.03	9.35	y
3	500.00	50.00	34.00	21.02	8.20	458.00	8.39	10.80	y
4	450.00	57.00	34.00	21.19	8.40	308.00	8.22	10.31	y
5	450.00	53.00	34.00	20.02	10.20	376.00	8.50	10.80	y
6	500.00	50.00	34.00	19.01	9.80	460.00	8.34	9.94	y
7	450.00	57.00	34.00	21.83	9.80	306.00	7.95	9.27	y
8	450.00	53.00	34.00	22.09	9.40	380.00	8.20	10.72	y
9	500.00	50.00	34.00	22.23	9.60	464.00	7.97	9.39	y

Averages

1	450.00	57.00	34.00	21.08	9.07	302.00	8.18	9.90
2	450.00	53.00	34.00	21.02	9.33	369.33	8.24	10.29
3	500.00	50.00	34.00	20.75	9.20	460.67	8.23	10.04

PowerE	PowerO	PeakPower	Intensity @ 10mm fL	DL Intensity @ 10mm fL
1938.00	1007.76	2325000	2.1713E+11	1.4517E+13
1802.00	937.04	2251786	2.1029E+11	1.4060E+13
1700.00	884.00	2255797	2.1067E+11	1.4085E+13

OC	QSW	ND	Freq
flat 50	40+90=36	0.35	1

Meas. No.	Pump time	current	voltage	Eout	tp	Qd	M2-x	M2-y	spark
1	450.00	57.00	34.00	20.36	9.60	264.00	6.10	8.33	y
2	450.00	53.00	34.00	19.30	9.20	310.00	6.27	9.41	y
3	450.00	50.00	34.00	20.73	9.80	334.00	6.59	7.03	y
4	400.00	57.00	34.00	21.19	9.40	248.00	6.21	8.76	y
5	400.00	53.00	34.00	20.30	9.80	290.00	6.50	9.62	y
6	400.00	50.00	34.00	20.85	10.00	336.00	6.45	7.83	y
7	400.00	57.00	34.00	20.16	10.00	240.00	5.84	8.66	y
8	400.00	53.00	34.00	19.38	9.60	282.00	5.54	7.48	y
9	400.00	50.00	34.00	19.64	10.20	318.00	5.70	7.69	y

Averages

1	416.67	57.00	34.00	20.57	9.67	250.67	6.05	8.58
2	416.67	53.00	34.00	19.66	9.53	294.00	6.10	8.84
3	416.67	50.00	34.00	20.41	10.00	329.33	6.25	7.52

PowerE	PowerO	PeakPower	Intensity @ 10mm fL	DL Intensity @ 10mm fL
1938.00	1007.76	2127931	3.6299E+11	1.3286E+13
1802.00	937.04	2062238	3.5178E+11	1.2876E+13
1700.00	884.00	2040667	3.4810E+11	1.2742E+13

OC	QSW	ND	Freq
flat 50	40	0.35	1

Meas. No.	Pump time	current	voltage	Eout	tp	Qd	M2-x	M2-y	spark
1	350.00	57.00	34.00	18.18	10.60	208.00	5.35	7.00	y
2	350.00	53.00	34.00	18.35	10.20	240.00	4.77	6.71	y
3	350.00	50.00	34.00	18.03	11.60	270.00	5.43	7.02	y
4	350.00	57.00	34.00	18.32	9.80	214.00	4.05	6.27	y
5	350.00	53.00	34.00	18.98	9.60	256.00	5.28	8.91	y
6	350.00	50.00	34.00	19.10	10.80	292.00	4.35	7.14	y
7	350.00	57.00	34.00	18.75	10.40	220.00	4.57	7.27	y
8	350.00	53.00	34.00	17.57	10.60	254.00	4.74	8.54	y
9	350.00	50.00	34.00	18.81	9.40	298.00	4.72	6.68	y

Averages

1	350.00	57.00	34.00	18.42	10.27	214.00	4.66	6.85
2	350.00	53.00	34.00	18.30	10.13	250.00	4.93	8.05
3	350.00	50.00	34.00	18.65	10.60	286.67	4.83	6.95

PowerE	PowerO	PeakPower	Intensity @ 10mm fL	DL Intensity @ 10mm fL
1938.00	1007.76	1793831	5.1651E+11	1.1200E+13
1802.00	937.04	1805921	5.1999E+11	1.1276E+13
1700.00	884.00	1759119	5.0652E+11	1.0984E+13

OC	QSW	ND	Freq
flat 30	40+80=32	0.5	1

Meas. No.	Pump time	current	voltage	Eout	tp	Qd	M2-x	M2-y	spark
1	650.00	57.00	34.00	28.10	8.60	572.00	7.59	9.68	y
2	-	-	-	-	-	-	-	-	n
3	-	-	-	-	-	-	-	-	n
4	650.00	57.00	34.00	28.20	9.60	600.00	7.40	9.40	y
5	-	-	-	-	-	-	-	-	n
6	-	-	-	-	-	-	-	-	n
7	650.00	57.00	34.00	27.50	9.00	585.00	8.00	10.40	y
8	-	-	-	-	-	-	-	-	n
9	-	-	-	-	-	-	-	-	n

Averages

1	650.00	57.00	34.00	27.93	9.07	585.67	7.66	9.83
2	-	-	-	-	-	-	-	-
3	-	-	-	-	-	-	-	-

PowerE	PowerO	PeakPower	Intensity @ 10mm fL	DL Intensity @ 10mm fL
1938.00	1007.76	3080882	3.2756E+11	1.9236E+13
-	-	-	-	-
-	-	-	-	-

OC	QSW	ND	Freq
flat 30	40+90=36	0.5	1

Meas. No.	Pump time	current	voltage	Eout	tp	Qd	M2-x	M2-y	spark
1	707.00	57.00	34.00	23.81	8.80	412.00	7.07	9.38	y
2	707.00	53.00	34.00	23.30	7.80	560.00	7.18	10.81	y
3	900.00	50.00	34.00	21.94	7.80	804.00	6.96	8.49	y
4	707.00	57.00	34.00	23.21	8.60	388.00	6.93	8.17	y
5	707.00	53.00	34.00	22.60	8.60	500.00	6.69	8.28	y
6	900.00	50.00	34.00	22.30	8.00	768.00	6.96	8.27	y
7	707.00	57.00	34.00	22.40	8.80	380.00	6.97	8.34	y
8	707.00	53.00	34.00	22.60	8.80	504.00	6.64	7.98	y
9	900.00	50.00	34.00	22.00	9.20	736.00	6.83	8.28	y

Averages

1	707.00	57.00	34.00	23.14	8.73	393.33	6.99	8.63
2	707.00	53.00	34.00	22.83	8.40	521.33	6.84	9.02
3	900.00	50.00	34.00	22.08	8.33	769.33	6.92	8.35

PowerE	PowerO	PeakPower	Intensity @ 10mm fL	DL Intensity @ 10mm fL
1938.00	1007.76	2649618	3.3859E+11	1.6544E+13
1802.00	937.04	2718254	3.4736E+11	1.6972E+13
1700.00	884.00	2649600	3.3859E+11	1.6544E+13

OC	QSW	ND	Freq
flat 30	40	0.5	1

Meas. No.	Pump time	current	voltage	Eout	tp	Qd	M2-x	M2-y	spark
1	550.00	57.00	34.00	21.00	9.80	352.00	5.92	7.48	y
2	550.00	53.00	34.00	20.80	9.60	400.00	5.93	7.22	y
3	550.00	50.00	34.00	20.50	9.40	492.00	5.89	7.24	y
4	550.00	57.00	34.00	20.96	10.00	324.00	5.76	6.56	y
5	550.00	53.00	34.00	20.50	9.60	400.00	6.05	7.51	y
6	550.00	50.00	34.00	20.50	9.80	496.00	5.96	8.01	y
7	550.00	57.00	34.00	20.99	9.40	324.00	5.94	7.52	y
8	550.00	53.00	34.00	20.70	9.40	404.00	5.97	8.02	y
9	550.00	50.00	34.00	20.50	9.60	500.00	6.09	7.83	y

Averages

1	550.00	57.00	34.00	20.98	9.73	333.33	5.87	7.19
2	550.00	53.00	34.00	20.67	9.53	401.33	5.98	7.58
3	550.00	50.00	34.00	20.50	9.60	496.00	5.98	7.69

PowerE	PowerO	PeakPower	Intensity @ 10mm fL	DL Intensity @ 10mm fL
1938.00	1007.76	2155822	3.9020E+11	1.3461E+13
1802.00	937.04	2167832	3.9238E+11	1.3536E+13
1700.00	884.00	2135417	3.8651E+11	1.3333E+13

OC	QSW	ND	Freq
flat 40	32	0.5	1

Meas. No.	Pump time	current	voltage	Eout	tp	Qd	M2-x	M2-y	spark
1	650.00	57.00	34.00	22.50	7.80	480.00	9.45		y
2	650.00	53.00	34.00	23.00	8.10	560.00	10.10		y
3	750.00	50.00	34.00	22.85	7.50	704.00	8.42		y
4	650.00	57.00	34.00	23.25	8.20	496.00	8.98		y
5	650.00	53.00	34.00	22.20	8.00	575.00	9.05		y
6	750.00	50.00	34.00	22.30	8.40	698.00	9.54		y
7	650.00	57.00	34.00	23.00	7.90	482.00	10.35		n
8	650.00	53.00	34.00	23.10	7.50	558.00	9.21		y
9	750.00	50.00	34.00	22.75	7.80	715.00	10.09		n

Averages

1	650.00	57.00	34.00	22.92	7.97	486.00	9.59	0.00
2	650.00	53.00	34.00	22.77	7.87	564.33	9.45	0.00
3	750.00	50.00	34.00	22.63	7.90	705.67	9.35	0.00

PowerE	PowerO	PeakPower	Intensity @ 10mm fL	DL Intensity @ 10mm fL
1938.00	1007.76	2876569	1.9516E+11	1.7961E+13
1802.00	937.04	2894068	1.9634E+11	1.8070E+13
1700.00	884.00	2864979	1.9437E+11	1.7888E+13

OC	QSW	ND	Freq
flat 40	36	0.5	1

Meas. No.	Pump time	current	voltage	Eout	tp	Qd	M2-x	M2-y	spark
1	500.00	57.00	34.00	20.10	8.00	360.00	9.07		y
2	500.00	53.00	34.00	21.25	8.20	455.00	9.55		y
3	650.00	50.00	34.00	20.50	8.00	600.00	10.01		n
4	500.00	57.00	34.00	20.45	9.10	352.00	8.75		y
5	500.00	53.00	34.00	19.99	7.90	470.00	8.68		y
6	650.00	50.00	34.00	20.90	8.40	596.00	9.54		y
7	500.00	57.00	34.00	21.00	9.20	366.00	9.15		y
8	500.00	53.00	34.00	20.65	9.60	468.00	8.99		y
9	650.00	50.00	34.00	19.85	9.00	608.00	8.69		n

Averages

1	500.00	57.00	34.00	20.52	8.77	359.33	8.99	0.00
2	500.00	53.00	34.00	20.63	8.57	464.33	9.07	0.00
3	650.00	50.00	34.00	20.42	8.47	601.33	9.41	0.00

PowerE	PowerO	PeakPower	Intensity @ 10mm fL	DL Intensity @ 10mm fL
1938.00	1007.76	2340304	1.8080E+11	1.4612E+13
1802.00	937.04	2408171	1.8604E+11	1.5036E+13
1700.00	884.00	2411417	1.8630E+11	1.5056E+13

OC	QSW	ND	Freq
flat 40	40	0.5	1

Meas. No.	Pump time	current	voltage	Eout	tp	Qd	M2-x	M2-y	spark
1	600.00	57.00	34.00	22.50	9.80	416.00	8.29		y
2	600.00	53.00	34.00	20.94	9.60	558.00	8.34		y
3	850.00	50.00	34.00	20.30	9.60	686.00	12.98		n
4	600.00	57.00	34.00	20.28	9.20	398.00	5.92		y
5	600.00	53.00	34.00	21.65	9.20	512.00	5.88		y
6	800.00	50.00	34.00	21.05	9.80	748.00	6.06		y
7	600.00	57.00	34.00	21.11	9.00	390.00	5.98		y
8	600.00	53.00	34.00	20.22	9.60	500.00	6.69		n
9	800.00	50.00	34.00	19.01	10.20	680.00	5.13		n

Averages

1	600.00	57.00	34.00	21.30	9.33	401.33	6.73	0.00
2	600.00	53.00	34.00	20.94	9.47	523.33	6.97	0.00
3	816.67	50.00	34.00	20.12	9.87	704.67	8.06	0.00

PowerE	PowerO	PeakPower	Intensity @ 10mm fL	DL Intensity @ 10mm fL
1938.00	1007.76	2281786	3.1455E+11	1.4247E+13
1802.00	937.04	2211620	3.0488E+11	1.3809E+13
1700.00	884.00	2039189	2.8111E+11	1.2732E+13

OC	QSW	ND	Freq
flat 50	40+80=32	0.5	1

Meas. No.	Pump time	current	voltage	Eout	tp	Qd	M2-x	M2-y	spark
1	500.00	57.00	34.00	20.39	7.00	368.00	8.30	11.57	y
2	500.00	53.00	34.00	19.00	7.00	472.00	8.28	11.84	y
3	700.00	50.00	34.00	20.96	8.00	636.00	7.95	11.52	y
4	500.00	57.00	34.00	20.22	7.40	364.00	8.94	13.68	y
5	500.00	53.00	34.00	19.20	7.40	482.00	8.20	11.98	y
6	700.00	50.00	34.00	19.44	8.00	648.00	8.27	13.40	y
7	500.00	57.00	34.00	22.23	7.60	370.00	7.80	11.28	y
8	500.00	53.00	34.00	21.54	8.00	478.00	7.68	10.68	y
9	700.00	50.00	34.00	21.22	8.00	660.00	8.52	11.80	n

Averages

1	500.00	57.00	34.00	20.95	7.33	367.33	8.35	12.18
2	500.00	53.00	34.00	19.91	7.47	477.33	8.05	11.50
3	700.00	50.00	34.00	20.54	8.00	648.00	8.25	12.24

PowerE	PowerO	PeakPower	Intensity @ 10mm fL	DL Intensity @ 10mm fL
1938.00	1007.76	2856364	2.5600E+11	1.7835E+13
1802.00	937.04	2666964	2.3902E+11	1.6652E+13
1700.00	884.00	2567500	2.3011E+11	1.6031E+13

OC	QSW	ND	Freq
flat 50	40+90=36	0.5	1

Meas. No.	Pump time	current	voltage	Eout	tp	Qd	M2-x	M2-y	spark
1	400.00	57.00	34.00	20.42	8.40	304.00	9.37	11.99	y
2	400.00	53.00	34.00	19.61	9.80	362.00	9.68	12.57	n
3	500.00	50.00	34.00	19.62	7.80	436.00	9.31	11.58	y
4	400.00	57.00	34.00	19.31	8.40	310.00	9.28	14.39	y
5	400.00	53.00	34.00	18.98	8.40	376.00	9.69	14.20	n
6	500.00	50.00	34.00	19.10	10.00	470.00	12.26	14.53	n
7	400.00	57.00	34.00	19.41	8.60	346.00	12.41	14.47	y
8	400.00	53.00	34.00	19.70	8.40	424.00	11.48	11.57	n
9	500.00	50.00	34.00	17.20	9.20	492.00	11.39	12.05	n

Averages

1	400.00	57.00	34.00	19.71	8.47	320.00	10.35	13.62
2	400.00	53.00	34.00	19.43	8.87	387.33	10.28	12.78
3	500.00	50.00	34.00	18.64	9.00	466.00	10.99	12.72

PowerE	PowerO	PeakPower	Intensity @ 10mm fL	DL Intensity @ 10mm fL
1938.00	1007.76	2328346	1.3562E+11	1.4538E+13
1802.00	937.04	2191353	1.2764E+11	1.3682E+13
1700.00	884.00	2071111	1.2064E+11	1.2932E+13

OC	QSW	ND	Freq
flat 50	40	0.5	1

Meas. No.	Pump time	current	voltage	Eout	tp	Qd	M2-x	M2-y	spark
1	400.00	57.00	34.00	17.72	9.20	282.00	7.53	10.13	n
2	400.00	53.00	34.00	17.23	9.80	340.00	8.15	10.27	n
3	450.00	50.00	34.00	17.46	9.60	414.00	8.27	11.13	n
4	400.00	57.00	34.00	17.26	7.80	278.00	9.02	12.03	n
5	400.00	53.00	34.00	17.60	7.80	334.00	8.98	12.22	n
6	450.00	50.00	34.00	17.49	7.80	394.00	8.64	11.66	n
7	400.00	57.00	34.00	17.49	8.00	278.00	9.35	12.65	n
8	400.00	53.00	34.00	17.49	8.00	332.00	9.14	12.76	n
9	450.00	50.00	34.00	17.49	7.80	390.00	8.98	11.46	n

Averages

1	400.00	57.00	34.00	17.49	8.33	279.33	8.63	11.60
2	400.00	53.00	34.00	17.44	8.53	335.33	8.76	11.75
3	450.00	50.00	34.00	17.48	8.40	399.33	8.63	11.42

PowerE	PowerO	PeakPower	Intensity @ 10mm fL	DL Intensity @ 10mm fL
1938.00	1007.76	2098800	1.7582E+11	1.3104E+13
1802.00	937.04	2043750	1.7121E+11	1.2761E+13
1700.00	884.00	2080952	1.7432E+11	1.2993E+13

OC	QSW	ND	Freq
flat 30	40+80=32	0.75	1

Meas. No.	Pump time	current	voltage	Eout	tp	Qd	M2-x	M2-y	spark
1	500.00	57.00	34.00	27.50	10.00	390.00	4.94	6.84	y
2	682.00	53.00	34.00	26.40	9.80	542.00	8.95	11.73	y
3	881.00	50.00	34.00	24.00	8.80	700.00	5.92	8.46	y
4	500.00	57.00	34.00	26.80	9.00	378.00	6.20	9.61	y
5	682.00	53.00	34.00	25.50	8.80	480.00	6.57	8.28	y
6	881.00	50.00	34.00	24.20	9.80	644.00	5.86	8.97	y
7	500.00	57.00	34.00	25.80	8.40	356.00	6.79	7.77	y
8	682.00	53.00	34.00	24.90	10.00	468.00	8.35	14.46	y
9	881.00	50.00	34.00	23.50	8.40	642.00	10.57	15.74	y

Averages

1	500.00	57.00	34.00	26.70	9.13	374.67	5.98	8.07
2	682.00	53.00	34.00	25.60	9.53	496.67	7.96	11.49
3	881.00	50.00	34.00	23.90	9.00	662.00	7.45	11.06

PowerE	PowerO	PeakPower	Intensity @ 10mm fL	DL Intensity @ 10mm fL
1938.00	1007.76	2923358	5.1099E+11	1.8253E+13
1802.00	937.04	2685315	4.6938E+11	1.6767E+13
1700.00	884.00	2655556	4.6418E+11	1.6581E+13

OC	QSW	ND	Freq
flat 30	40+90=36	0.75	1

Meas. No.	Pump time	current	voltage	Eout	tp	Qd	M2-x	M2-y	spark
1	450.00	57.00	34.00	21.00	9.20	334.00	10.63	17.76	y
2	500.00	53.00	34.00	21.80	9.60	422.00	6.63	11.74	y
3	650.00	50.00	34.00	22.00	9.00	564.00	7.47	10.68	y
4	450.00	57.00	34.00	22.50	10.20	332.00	6.74	6.85	y
5	500.00	53.00	34.00	22.10	10.40	418.00	6.84	7.93	y
6	650.00	50.00	34.00	21.90	10.40	434.00	11.82	11.83	y
7	450.00	57.00	34.00	23.00	9.00	326.00	12.54	16.72	y
8	500.00	53.00	34.00	23.60	8.80	400.00	12.33	17.85	y
9	650.00	50.00	34.00	22.00	9.80	476.00	12.51	15.00	y

Averages

1	450.00	57.00	34.00	22.17	9.47	330.67	9.97	13.78
2	500.00	53.00	34.00	22.50	9.60	413.33	8.60	12.51
3	650.00	50.00	34.00	21.97	9.73	491.33	10.60	12.50

PowerE	PowerO	PeakPower	Intensity @ 10mm fL	DL Intensity @ 10mm fL
1938.00	1007.76	2341549	1.4708E+11	1.4620E+13
1802.00	937.04	2343750	1.4722E+11	1.4634E+13
1700.00	884.00	2256849	1.4176E+11	1.4091E+13

OC	QSW	ND	Freq
flat 30	40	0.75	1

Meas. No.	Pump time	current	voltage	Eout	tp	Qd	M2-x	M2-y	spark
1	400.00	57.00	34.00	17.20	9.60	252.00	10.67	13.15	y
2	400.00	53.00	34.00	16.50	9.60	300.00	7.81	8.07	y
3	450.00	50.00	34.00	16.60	9.40	352.00	6.80	7.85	y
4	400.00	57.00	34.00	15.80	9.20	268.00	9.72	9.78	y
5	400.00	53.00	34.00	15.20	9.60	274.00	7.60	10.29	y
6	450.00	50.00	34.00	15.60	9.60	318.00	7.86	10.26	y
7	400.00	57.00	34.00	17.10	9.40	244.00	5.69	5.53	y
8	400.00	53.00	34.00	16.30	9.00	284.00	6.45	7.56	y
9	450.00	50.00	34.00	15.30	9.40	328.00	6.04	4.57	y

Averages

1	400.00	57.00	34.00	16.70	9.40	254.67	8.69	9.49
2	400.00	53.00	34.00	16.00	9.40	286.00	7.29	8.64
3	450.00	50.00	34.00	15.83	9.47	332.67	6.90	7.56

PowerE	PowerO	PeakPower	Intensity @ 10mm fL	DL Intensity @ 10mm fL
1938.00	1007.76	1776596	1.4678E+11	1.1093E+13
1802.00	937.04	1702128	1.4063E+11	1.0628E+13
1700.00	884.00	1672535	1.3818E+11	1.0443E+13

OC	QSW	ND	Freq
flat 40	32	0.75	1

Meas. No.	Pump time	current	voltage	Eout	tp	Qd	M2-x	M2-y	spark
1	500.00	57.00	34.00	20.96	8.00	368.00	6.14	5.46	y
2	500.00	53.00	34.00	19.41	9.00	466.00	6.46	7.06	y
3	650.00	50.00	34.00	19.56	8.00	572.00	5.24	7.09	y
4	500.00	57.00	34.00	21.05	8.00	372.00	5.92	7.53	y
5	500.00	53.00	34.00	20.99	8.40	476.00	6.16	8.12	y
6	750.00	50.00	34.00	21.17	8.00	700.00	6.17	8.47	y
7	500.00	57.00	34.00	20.96	7.80	360.00	6.06	8.68	y
8	500.00	53.00	34.00	20.85	8.20	460.00	6.17	8.55	y
9	750.00	50.00	34.00	20.76	8.20	680.00	5.75	7.49	y

Averages

1	500.00	57.00	34.00	20.99	7.93	366.67	6.04	7.22
2	500.00	53.00	34.00	20.42	8.53	467.33	6.26	7.91
3	716.67	50.00	34.00	20.50	8.07	650.67	5.72	7.68

PowerE	PowerO	PeakPower	Intensity @ 10mm fL	DL Intensity @ 10mm fL
1938.00	1007.76	2645798	4.5283E+11	1.6520E+13
1802.00	937.04	2392578	4.0949E+11	1.4939E+13
1700.00	884.00	2540909	4.3487E+11	1.5865E+13

OC	QSW	ND	Freq
flat 40	36	0.75	1

Meas. No.	Pump time	current	voltage	Eout	tp	Qd	M2-x	M2-y	spark
1	400.00	57.00	34.00	18.64	8.80	336.00	8.52	9.15	y
2	500.00	53.00	34.00	22.83	9.20	372.00	6.53	7.68	y
3	600.00	50.00	34.00	22.40	9.40	494.00	6.36	7.01	y
4	400.00	57.00	34.00	19.70	10.40	314.00	6.84	7.93	y
5	500.00	53.00	34.00	19.58	10.80	390.00	6.26	7.18	y
6	600.00	50.00	34.00	20.88	9.80	464.00	6.17	7.77	y
7	400.00	57.00	34.00	20.07	9.40	298.00	5.03	6.32	y
8	500.00	53.00	34.00	21.14	8.80	364.00	4.66	5.67	y
9	600.00	50.00	34.00	19.01	9.60	436.00	5.24	8.19	y

Averages

1	400.00	57.00	34.00	19.47	9.53	316.00	6.80	7.80
2	500.00	53.00	34.00	21.18	9.60	375.33	5.82	6.84
3	600.00	50.00	34.00	20.76	9.60	464.67	5.92	7.66

PowerE	PowerO	PeakPower	Intensity @ 10mm fL	DL Intensity @ 10mm fL
1938.00	1007.76	2042308	2.7604E+11	1.2752E+13
1802.00	937.04	2206597	2.9825E+11	1.3778E+13
1700.00	884.00	2162847	2.9234E+11	1.3504E+13

OC	QSW	ND	Freq
flat 40	40	0.75	1

Meas. No.	Pump time	current	voltage	Eout	tp	Qd	M2-x	M2-y	spark
1	300.00	57.00	34.00	19.70	9.60	270.00	4.71	7.49	y
2	400.00	53.00	34.00	18.72	9.40	326.00	5.63	8.52	y
3	400.00	50.00	34.00	18.61	8.80	382.00	5.52	8.01	y
4	300.00	57.00	34.00	18.61	10.20	264.00	4.77	8.02	y
5	400.00	53.00	34.00	17.86	8.80	302.00	5.18	7.43	y
6	400.00	50.00	34.00	17.46	9.00	350.00	4.52	5.78	y
7	300.00	57.00	34.00	18.75	9.00	260.00	4.56	5.92	y
8	400.00	53.00	34.00	18.95	9.20	302.00	5.20	6.57	y
9	400.00	50.00	34.00	18.66	8.60	382.00	5.84	7.23	y

Averages

1	300.00	57.00	34.00	19.02	9.60	264.67	4.68	7.14
2	400.00	53.00	34.00	18.51	9.13	310.00	5.34	7.51
3	400.00	50.00	34.00	18.24	8.80	371.33	5.29	7.01

PowerE	PowerO	PeakPower	Intensity @ 10mm fL	DL Intensity @ 10mm fL
1938.00	1007.76	1981250	5.6480E+11	1.2371E+13
1802.00	937.04	2026642	5.7774E+11	1.2654E+13
1700.00	884.00	2073106	5.9099E+11	1.2944E+13

OC	QSW	ND	Freq
flat 50	40+80=32	0.75	1

Meas. No.	Pump time	current	voltage	Eout	tp	Qd	M2-x	M2-y	spark
1	400.00	57.00	34.00	18.32	8.40	264.00	6.28	9.70	y
2	400.00	53.00	34.00	18.38	9.20	314.00	8.34	11.34	y
3	400.00	50.00	34.00	18.46	8.80	366.00	8.39	12.43	y
4	400.00	57.00	34.00	21.60	8.40	346.00	10.99	15.92	y
5	500.00	53.00	34.00	21.22	8.00	436.00	11.61	17.30	y
6	600.00	50.00	34.00	21.60	7.60	580.00	10.00	13.67	y
7	400.00	57.00	34.00	19.01	9.20	346.00	13.27	17.73	y
8	500.00	53.00	34.00	18.64	9.40	434.00	10.19	14.50	y
9	600.00	50.00	34.00	18.41	9.20	560.00	8.49	11.54	y

Averages

1	400.00	57.00	34.00	19.64	8.67	318.67	10.18	14.45
2	466.67	53.00	34.00	19.41	8.87	394.67	10.05	14.38
3	533.33	50.00	34.00	19.49	8.53	502.00	8.96	12.55

PowerE	PowerO	PeakPower	Intensity @ 10mm fL	DL Intensity @ 10mm fL
1938.00	1007.76	2266538	1.3656E+11	1.4152E+13
1802.00	937.04	2189474	1.3191E+11	1.3671E+13
1700.00	884.00	2283984	1.3761E+11	1.4261E+13

OC	QSW	ND	Freq
flat 50	40+90=36	0.75	1

Meas. No.	Pump time	current	voltage	Eout	tp	Qd	M2-x	M2-y	spark
1	350.00	57.00	34.00	15.62	9.20	218.00	4.69	6.27	n
2	350.00	53.00	34.00	15.24	9.60	256.00	5.29	7.22	n
3	350.00	50.00	34.00	15.30	10.80	292.00	5.67	8.62	n
4	350.00	57.00	34.00	16.51	11.00	244.00	7.19	12.52	n
5	350.00	53.00	34.00	15.24	10.60	284.00	6.32	11.72	n
6	350.00	50.00	34.00	15.96	9.80	312.00	6.14	9.87	n
7	350.00	57.00	34.00	16.62	9.40	222.00	4.52	6.09	y
8	350.00	53.00	34.00	16.39	9.80	256.00	5.59	7.70	n
9	350.00	50.00	34.00	16.57	9.80	294.00	6.13	8.07	n

Averages

1	350.00	57.00	34.00	16.25	9.87	228.00	5.47	8.29
2	350.00	53.00	34.00	15.62	10.00	265.33	5.73	8.88
3	350.00	50.00	34.00	15.94	10.13	299.33	5.98	8.85

PowerE	PowerO	PeakPower	Intensity @ 10mm fL	DL Intensity @ 10mm fL
1938.00	1007.76	1646959	3.4410E+11	1.0283E+13
1802.00	937.04	1562333	3.2642E+11	9.7549E+12
1700.00	884.00	1573355	3.2872E+11	9.8237E+12

OC	QSW	ND	Freq
flat 50	40	0.75	1

Meas. No.	Pump time	current	voltage	Eout	tp	Qd	M2-x	M2-y	spark
1	250.00	57.00	34.00	14.01	10.20	192.00	5.21	7.47	n
2	250.00	53.00	34.00	14.24	9.80	228.00	8.94	11.97	n
3	300.00	50.00	34.00	14.21	9.80	256.00	8.92	10.78	n
4	250.00	57.00	34.00	14.24	11.60	214.00	9.52	14.90	n
5	300.00	53.00	34.00	13.84	11.80	246.00	6.31	10.43	n
6	350.00	50.00	34.00	14.27	11.80	280.00	7.41	11.45	n
7	250.00	57.00	34.00	14.30	11.60	216.00	8.61	11.64	n
8	300.00	53.00	34.00	14.47	12.80	252.00	9.96	14.55	n
9	300.00	50.00	34.00	13.95	14.00	276.00	9.03	12.83	n

Averages

1	250.00	57.00	34.00	14.18	11.13	207.33	7.78	11.34
2	283.33	53.00	34.00	14.18	11.47	242.00	8.40	12.32
3	316.67	50.00	34.00	14.14	11.87	270.67	8.45	11.69

PowerE	PowerO	PeakPower	Intensity @ 10mm fL	DL Intensity @ 10mm fL
1938.00	1007.76	1273952	1.3141E+11	7.9543E+12
1802.00	937.04	1236919	1.2759E+11	7.7231E+12
1700.00	884.00	1191854	1.2295E+11	7.4417E+12

[redacted]

Dustin L. McIntyre [redacted]. He attended Culloden Elementary School, Milton Junior High, and Ona Middle School. He graduated from Milton High School in June of 1994 and enrolled at West Virginia University in August of 1994. He received a Bachelor of Science in Electrical Engineering and a Bachelor of Science in Computer Engineering in December of 1998. He enrolled in graduate school in January of 1999 in the Mechanical and Aerospace Engineering Department of the College of Engineering and Mineral Resources. He graduated with a Masters Degree in Mechanical Engineering in August of 2000 with his thesis entitled "The Coaxial Cavity Resonator as a Prototype RF IC Ignition Engine." The author began his Doctoral studies in August of 2000 and took a leave of absence in May 2002 to work for the United States Department of Energy's National Energy Technology Laboratory where he is currently working as a Mechanical Engineer and finishing his Doctoral studies.

A Laser Spark Plug Ignition System for a Stationary Lean-Burn Natural Gas Reciprocating Engine

Dustin L. McIntyre

Dissertation submitted to the
College of Engineering and Mineral Resources
at West Virginia University
in partial fulfillment of the requirements for the degree of

Doctor of Philosophy
in
Mechanical Engineering

Department of Mechanical and Aerospace Engineering

APPROVAL OF THE EXAMINING COMMITTEE

Mridul Gautam, Ph.D., Chair

John M. Kuhlman, Ph.D.

Michael H. McMillian, Ph.D.

Gary J. Morris, Ph.D.

Gregory J. Thompson, Ph.D.

Date

Steven D. Woodruff, Ph.D.